

INFORMATION TO USERS

This manuscript has been reproduced from the microfilm master. UMI films the text directly from the original or copy submitted. Thus, some thesis and dissertation copies are in typewriter face, while others may be from any type of computer printer.

The quality of this reproduction is dependent upon the quality of the copy submitted. Broken or indistinct print, colored or poor quality illustrations and photographs, print bleedthrough, substandard margins, and improper alignment can adversely affect reproduction.

In the unlikely event that the author did not send UMI a complete manuscript and there are missing pages, these will be noted. Also, if unauthorized copyright material had to be removed, a note will indicate the deletion.

Oversize materials (e.g., maps, drawings, charts) are reproduced by sectioning the original, beginning at the upper left-hand corner and continuing from left to right in equal sections with small overlaps.

ProQuest Information and Learning
300 North Zeeb Road, Ann Arbor, MI 48106-1346 USA
800-521-0600

UMI[®]

University of Alberta

THE ROLE OF ULF WAVES IN ENERGY TRANSPORT IN THE MAGNETOSPHERE

by

Joe Tom Mathews



A thesis submitted to the Faculty of Graduate Studies and Research in partial fulfillment of the requirements for the degree of **Doctor Of Philosophy**.

Department of Physics

Edmonton, Alberta
Fall 2005



Library and
Archives Canada

Bibliothèque et
Archives Canada

0-494-08691-2

Published Heritage
Branch

Direction du
Patrimoine de l'édition

395 Wellington Street
Ottawa ON K1A 0N4
Canada

395, rue Wellington
Ottawa ON K1A 0N4
Canada

Your file *Votre référence*

ISBN:

Our file *Notre référence*

ISBN:

NOTICE:

The author has granted a non-exclusive license allowing Library and Archives Canada to reproduce, publish, archive, preserve, conserve, communicate to the public by telecommunication or on the Internet, loan, distribute and sell theses worldwide, for commercial or non-commercial purposes, in microform, paper, electronic and/or any other formats.

The author retains copyright ownership and moral rights in this thesis. Neither the thesis nor substantial extracts from it may be printed or otherwise reproduced without the author's permission.

In compliance with the Canadian Privacy Act some supporting forms may have been removed from this thesis.

While these forms may be included in the document page count, their removal does not represent any loss of content from the thesis.

AVIS:

L'auteur a accordé une licence non exclusive permettant à la Bibliothèque et Archives Canada de reproduire, publier, archiver, sauvegarder, conserver, transmettre au public par télécommunication ou par l'Internet, prêter, distribuer et vendre des thèses partout dans le monde, à des fins commerciales ou autres, sur support microforme, papier, électronique et/ou autres formats.

L'auteur conserve la propriété du droit d'auteur et des droits moraux qui protègent cette thèse. Ni la thèse ni des extraits substantiels de celle-ci ne doivent être imprimés ou autrement reproduits sans son autorisation.

Conformément à la loi canadienne sur la protection de la vie privée, quelques formulaires secondaires ont été enlevés de cette thèse.

Bien que ces formulaires aient inclus dans la pagination, il n'y aura aucun contenu manquant.


Canada

University of Alberta

Library Release Form

Name of Author: Joe Tom Mathews

Title of Thesis: The Role of ULF Waves in Energy Transport in the Magnetosphere

Degree: Doctor Of Philosophy

Year this Degree Granted: 2005

Permission is hereby granted to the University of Alberta Library to reproduce single copies of this thesis and to lend or sell such copies for private, scholarly or scientific research purposes only.

The author reserves all other publication and other rights in association with the copyright in the thesis, and except as hereinbefore provided, neither the thesis nor any substantial portion thereof may be printed or otherwise reproduced in any material form whatever without the author's prior written permission.

.....
Joe Tom Mathews

Edmonton, Alberta
Canada, T6G 2J1

Date:

“I am sick to death of cleverness. Everybody is clever nowadays. You can’t go anywhere without meeting clever people. The thing has become an absolute public nuisance. I wish to goodness we had a few fools left.”

“Ignorance is like a delicate exotic fruit; touch it and the bloom is gone.”

Oscar Wilde, The Importance of Being Earnest

University of Alberta

Faculty of Graduate Studies and Research

The undersigned certify that they have read, and recommend to the Faculty of Graduate Studies and Research for acceptance, a thesis entitled **The Role of ULF Waves in Energy Transport in the Magnetosphere** submitted by Joe Tom Mathews in partial fulfillment of the requirements for the degree of **Doctor Of Philosophy in Astrophysical Sciences**.

.....
Dr. M. Heimpel

.....
Dr. D. Knudsen

.....
Dr. I. Mann

.....
Dr. R. Rankin

.....
Dr. Y. Tsui

Date:

Abstract

We examine the role of ULF waves in energy transport in the Earth's magnetosphere for four distinct types of events. Firstly we present ground-based observations of an N=0 Pc5 drift resonance in the afternoon sector that is extremely well-defined and narrow-band in both frequency and azimuthal wavenumber. We also present the first characterisation of the 2-D ionospheric velocity flows of such a wave, and we explain the wave growth via in-situ observations of an unstable particle energy distribution in the Earth's ring current.

Secondly we show how field line resonance (FLR) on closed auroral field lines in the dusk sector can modulate auroral particle precipitation, and that field line stretching can overcome the typical poleward FLR phase. We argue that the flank waveguide may be excited via fast mode waves propagating sunward from the magnetotail, producing equatorward and sunward propagating east-west aligned auroral arcs via mode-conversion to Alfvén waves on stretched auroral field lines.

Thirdly we present the first EISCAT measurements of ionospheric heating rates due to auroral poleward boundary intensifications (PBIs), and show that PBIs can deposit a similar amount of energy per unit area into the ionosphere as substorms.

Finally we characterise the ground signature of PBIs in ground-based optical and magnetometer data, and show that the PBI repetition rate matches the frequency of Alfvén waves observed in-situ in the PSBL at altitudes of 5-6 R_E . The observation of identical periodicities provides definitive evidence that high altitude ULF wave activity may be a major mechanism for auroral particle precipitation, and can therefore play an important role in energy coupling between the magnetotail and the ionosphere. We also find that the observed Alfvén waves carry an Earthward directed field-aligned Poynting flux that contains enough energy to explain the heating rates due to PBIs as measured by the EISCAT Svalbard radar. Satellite measurements show that high frequency oscillations are superim-

posed on top of the ULF waves in the PSBL and these high frequency waves have kinetic scale sizes and may therefore produce appreciable parallel electric fields. We show that these high frequency waves are characteristic of Alfvénic turbulence, probably driven by a current-convective interchange instability.

Acknowledgements

This work was partially carried out with funding from PPARC, a Marie Curie EU scholarship, and under a graduate scholarship at the University of Alberta.

Many thanks to data providers: Dr R. W. Smith at the University of Alaska, Fairbanks, for meridian scanning photometer data, Dr J. Moen at the University of Oslo and UNIS for all sky camera data and Dr. F. Mozer at the University of California, Berkeley for Polar electric field data.

Thanks to everyone who helped me along the way – you know who you all are. Special thanks to Dr Ian Mann, Dr David Milling, Dr Louis Ozeke, Dr Jonathan Rae and Dr Clare Watt for many useful and insightful conversations. And of course to Kate, who showed me the light when all was dark.

Contents

1	The Sun-Earth Connection	1
1.1	The Sun	1
1.2	The Solar Wind	3
1.3	The Bow Shock	6
1.4	The Magnetosphere	7
1.5	Geomagnetic Activity	10
1.6	Geomagnetic Indices	16
1.6.1	The Planetary K_p Index	16
1.6.2	The Dst Index	17
1.7	Magnetospheric ULF Waves	17
2	Plasma Theory and ULF Waves	19
2.1	Single Particle Motion	19
2.1.1	Motion of Charged Particles in a Constant, Uniform Magnetic Field - Gyromotion	19
2.1.2	Mirroring of Charged Particles in Magnetic Fields	20
2.1.3	Drifting of Particles in a Dipolar Magnetic Field	22
2.2	Magnetohydrodynamics	23
2.2.1	Properties of MHD Plasmas	23
2.2.2	Maxwells Equations	25
2.2.3	Continuity of Mass and Momentum	25
2.2.4	Equation of State and Ohms Law	26
2.3	Waves in Cold Magnetized Plasmas	27
2.4	Waves in Warm Magnetized Plasmas	29
2.5	Mode Conversion and Field Line Resonance	31
2.6	Driving Mechanisms For Field Line Resonances	36
2.6.1	Poloidal Mode Field Line Resonance	37
2.6.2	Toroidal Mode Field Line Resonance	40
2.7	Effects of the Ionosphere on the Observation of Geomagnetic Pulsations	41
2.8	Electron Acceleration by Alfvén Waves	44
2.9	Auroral Emissions	47

3	Instrumentation and Analysis Techniques	49
3.1	Ground-Based Magnetometers	49
3.2	Coherent HF Radars	55
3.3	Incoherent Scatter Radars	57
3.4	Ground-Based Optical Instruments	61
3.5	Satellites	63
3.5.1	Polar	64
3.5.2	The Advanced Composition Explorer (ACE)	66
4	Multi-Instrument Observations of Particle Driven Field Line Resonance	67
4.1	Introduction	67
4.2	Observations	70
4.2.1	Magnetospheric Configuration	70
4.2.2	IMAGE Magnetometer Data	72
4.2.3	STARE Radar Data	82
4.2.4	Polar CAMMICE Data	88
4.3	Discussion	91
4.4	Conclusions	102
5	Quiet Time Magnetospheric Flank FLR and Waveguide Study¹	105
5.1	Introduction	105
5.2	Ground-Based Instrumentation	107
5.3	Events	107
5.3.1	3 rd January 1998	109
5.3.2	29 th December 2000	112
5.3.3	18 th January 2002	112
5.4	Detailed Study of 3 rd January 1998 Event	117
5.5	Discussion	122
5.6	Conclusions	130
6	Energy Deposition In Nightside Auroral Poleward Boundary Intensifications	132
6.1	Introduction	132
6.2	Observations	133
6.3	Discussion	138
6.4	Conclusions	143
7	Observations of Large Alfvén Wave Poynting Flux in the Plasmasheet Boundary Layer Associated with Auroral Arcs	144
7.1	Introduction	144
7.2	Observations	145

¹The work presented in this Chapter has also been published in the paper “Multi-instrument observations of ULF wave-driven discrete auroral arcs propagating sunward and equatorward from the poleward boundary of the duskside auroral oval” by J. T. Mathews, I. R. Mann, I. J. Rae, I. J. and J. Moen, (2004) *Phys. Plasma.*, Vol. 11, No. 4 p 1250.

7.3 Discussion	163
7.4 Conclusions	173
8 Further Work	175
Bibliography	177
A Coordinate Systems	185
B Derivation Of E_{\parallel} For Kinetic Alfvén Waves	186

List of Tables

1.1	Classification of ULF waves first proposed by Jacobs <i>et al.</i> (1964). Adapted from Kivelson and Russell (1995).	18
3.1	IMAGE magnetometer stations with their geographic and corrected geomagnetic (CGM) coordinates (for full details see the IMAGE website at http://www.ava.fmi.fi/image/stations.html). Magnetic coordinate transformations are calculated for an altitude of 120 km for the 1 January 2003 epoch via the online tool at http://nssdc.gsfc.nasa.gov/space/cgm/cgm.html	51
3.2	Parameters measured by IS radars. After Risbeth and Williams (1985) . . .	58
3.3	Locations of EISCAT radars. Superscripts 1 and 2 refer to the EISCAT Svalbard radar (ESR) steerable and field aligned dishes, respectively. Adapted from http://www.eiscat.com/instrumentation.html	58
3.4	The four major auroral transitions measured by optical instrumentation. The superscript * represents an excited rotational energy state. Adapted from Kivelson and Russell (1995).	63

List of Figures

1.1	The structure of the Sun, showing approximate distances, temperatures and plasma densities. Adapted from Kivelson and Russell (1995)	2
1.2	Spiral form of the solar wind showing the interplanetary magnetic field and solar wind flow. Taken from Allan and Poulter (1992).	4
1.3	Compression and rarefaction of solar wind magnetic field lines by the fast and slow solar wind. Taken from Kivelson and Russell (1995).	5
1.4	“Ballerinas skirt” model of the heliospheric current sheet, with the orbits of the solar system planets out to Jupiter shown. Taken from the website at http://pluto.space.swri.edu/IMAGE/glossary/IMF.html	6
1.5	Diagrammatic representation of the Earth’s magnetosphere with major regions labeled. Taken from the IMAGE website at Rice University, located at http://space.rice.edu/IMAGE/livefrom/sunearth.html	8
1.6	The vertical structure of the Earth’s neutral atmosphere and ionosphere. Image courtesy Center for Space Sciences, University of Texas.	11
1.7	Illustration of magnetic connection of solar wind field lines to geomagnetic field lines at the Earth’s magnetopause. From Cowley (1999).	13
1.8	The magnetospheric cycle first proposed by Dungey (1961) for a purely southward IMF. From Ozeke (2002).	15
1.9	Diagram illustrating the form of the substorm current wedge. Taken from Russell (1974).	16
2.1	Schematic of box model for dipolar field lines. Solid arrows represent magnetic field, B_0 , which is uniform across the box, and dashed lines represent the incident fast mode wave.	32
2.2	Taken from Allan and Poulter (1992). Schematic showing two fast mode waves (numbered 1 and 2) with differing values of k_y and different discrete frequencies propagating into the magnetosphere and reflecting at points x_{r1} and x_{r2} . The two fast mode waves drive field line resonant standing Alfvén waves at points x_{c1} and x_{c2}	35
2.3	Schematic of box model for magnetotail, after Wright <i>et al.</i> (1999).	35
2.4	Alfvén speed profile in the z direction used by Wright <i>et al.</i> (1999). Preferentially, traveling Alfvén waves are excited in the region of large Alfvén speed gradient in the region that represents the PSBL.	36

2.5	Representations of fundamental and second harmonic toroidal and poloidal field line resonance perturbations. ΔH and ΔD represent magnetic oscillations in the radial and azimuthal directions in the magnetosphere respectively. Taken from Hughes (1994).	37
2.6	Schematic representation of three trajectories of drift-bounce motion of protons in the rest frame of a FLR. The schematic shows a box model geometry where the magnetic field lines are directed vertically from the southern to northern hemisphere. The electric field perturbations of a standing Alfvén wave are represented by plus and minus signs, the density of the symbols reflecting the magnitude of the electric field. Solid and dashed arrowed lines represent the trajectories of the guiding centers of mirroring and drifting protons in the rest frame of the wave. Taken from Ozeke (2002).	39
2.7	Diagram of the magnetosphere illustrating sources of waves in the magnetosphere. From Allan and Poulter (1992).	42
2.8	Schematic showing the mechanism by which field aligned currents due to Alfvén waves close in the ionosphere via a Pedersen current. The electric field associated with the Pedersen current, E_x , produces a Hall current whose magnetic signature is observed on the ground.	43
2.9	Excited oxygen states that give rise to auroral emissions. Included are the green line (557.7 nm), red line (630.0 nm) and UV line (297.2 nm), with the energies of the transitions and their respective lifetimes.	48
3.1	Locations of IMAGE magnetometer stations from the IMAGE website at http://www.geo.fmi.fi/image/stations.html . Magnetometers are marked by red dots, all sky cameras by white dots and the STARE radars common field of view is also shown. Dashed lines represent lines of geographic latitude and longitude.	52
3.2	Location and field of view of the nine northern hemisphere SuperDARN radars.	56
3.3	Diagram representing the pulse transmission and reflection paths for a SuperDARN radar. A pulse is emitted from the transmitter, transmitted from the ground to reflect off an ionospheric irregularity, transmitted back to the ground on its return path and received by the radar (known as $1\frac{1}{2}$ hop scattering). Scattering can also occur at closer distances to the radar, before the ray is transmitted by the ground, and this is known as $1/2$ hop scattering. All ranges and altitudes are approximate and depend on ionospheric conditions.	57
3.4	Sample ionospheric properties measured by IS radars. Shown are electron density (top left), the shape of the received spectrum (top right), ion and electron temperature profiles (bottom left, red and yellow respectively) and the line-of-sight ion drift (bottom right). Taken from the Millstone Hill IS website at http://hyperion.haystack.edu/midas/inscal.html	59

3.5	Field of view of the CUTLASS HF radars (fans) and the EISCAT Svalbard radar (ESR) and EISCAT Tromsø UHF IS radar (circles) projected to an altitude of 110 km. Taken from the University of Leicester CUTLASS website at http://www.ion.le.ac.uk/cutlass/pictures/cutlassmap.gif	60
3.6	Location and field of view of the Longyearbyen MSP (line) and Ny Ålesund ASC (oval). Fields of view are projected to an emission altitude of 110 km.	62
3.7	Typical orbit of the Polar satellite for the 9 th May 1997, projected into the GSE X-Y, X-Z and Y-Z planes. Also included is the spacecrafts radial distance from the Sun-Earth line. Calculations were made by the online tool at SSC web (http://sscweb.gsfc.nasa.gov/).	65
4.1	ACE SWEPAM [McComas <i>et al.</i> (1998)] H^+ speed and density and MGF [Smith <i>et al.</i> (1998)] B_x , B_y and B_z magnetic field data for the 26 th August 1999. Red vertical lines indicate the solar wind conditions during the period of ULF wave activity on the ground. ACE MGF data provided courtesy of N. Ness at Bartol Research Institute, SWEPAM data provided courtesy of D. J. McComas at SWRI.	71
4.2	Hourly averages of the Dst index for the 26 th August 1999.	72
4.3	Unfiltered H-component magnetometer data from selected stations from the IMAGE array for the 26 th August 1999.	73
4.4	Unfiltered D-component magnetometer data from selected stations from the IMAGE array for the 26 th August 1999. Red vertical lines represent the interval of ULF wave activity.	74
4.5	Unfiltered H-component magnetograms from selected IMAGE magnetometer stations for the interval 1430 to 1630 UT on the 26 th August 1999. Note that the scales for the stations are independently scaled, full scale deflection being indicated on each timeseries as FSD.	75
4.6	Unfiltered D-component data for the same interval and in the same format as Figure 4.5. Red arrows illustrate the westwards phase motion of the pulsation.	76
4.7	H- (upper panel) and D -(lower panel) component power spectra for IMAGE magnetometer stations for the interval 1515 to 1600 UT. The spectra in each panel are plotted on the same scale so that the relative spectral power at differing stations may be easily compared. The red line on the D component spectra corresponds to the frequency at which the largest amplitude was observed at the station with the highest power (TRO).	77
4.8	Latitudinal power profiles for the H- and D-components of the wave (dotted and solid lines, respectively).	79
4.9	Latitudinal phase profile for the H- and D-components of the wave. Blue lines indicate uncorrected measurements, red lines represent phase measurements corrected for m value.	81

4.10	Stacked timeseries for the two STARE radars. The plotted parameter is backscatter power for alternate range gates between 10 to 24 for beam 6 of the Hankasalmi radar (upper panel), and beam 7 of the Trondheim radar (lower panel). Latitudinal coverage is 65° to 68° for the upper panel, and longitudinal range is 101° to 104° for the lower panel.	84
4.11	Power spectra for beam 6 of the Hankasalmi STARE radar (left column) and beam 7 of the Trondheim STARE radar (right column). Spectra are stacked for range gates 10 through 20, even numbered gates only, with the nearest range gates at the top and farthest at the bottom.	85
4.12	STARE merged velocities for 1545:00 UT on the 26 August 1999.	86
4.13	STARE merged velocities for 1537:20 UT on the 26 August 1999.	87
4.14	Orbital configuration of the Polar satellite for one orbit starting at 0000 UT on the 26 th August 1999. Upper left panel is the projection into the GSE x-y plane, the upper right panel is the projection into the GSE x-z plane, the lower left panel is the projection into the GSE y-z plane and the lower right panel is the radial distance of the satellite from the center of the Earth. Plot provided by SSCWEB at http://sscweb.gsfc.nasa.gov	89
4.15	Orbital configuration of the Polar satellite for the orbit immediately after that in, and in the same format as, Figure 4.14. Figure provided by SSCWEB at http://sscweb.gsfc.nasa.gov	90
4.16	Polar CAMMICE ion distribution functions (IDFs) from two consecutive orbits on the 26 August 1999. Timeseries are offset by increasing powers of 10, and the lowest trace in each panel corresponds to the lowest L-shell, as determined by the Tsyganenko 96 model (Tsyganenko and Stern, 1996a).	92
4.17	Amplitude (solid line) and phase (dashed line) profiles used to calculate model flows for a poloidal field line resonance.	96
4.18	Derivatives of amplitude (solid line) and phase (dashed line) profiles used in computing ionospheric velocity flows due to a poloidal FLR.	97
4.19	Model results for the 2D velocity flow structure in the ionosphere produced by a poloidal field line resonance.	98
4.20	Plot of N=0 and N=1 resonance curves as a function of energy, W , and L -shell, superimposed onto open-closed orbit plot for $K_P=2$ and where shaded regions indicate closed orbits (see main text and Ozeke and Mann (2001) for more details). Dashed lines represent N=0 and N=1 resonance curves with a 25 percent difference on the equatorial plasma density. For reference, the open-closed orbit boundaries for K_p values of 1, 3 and 4 are plotted as green, red and blue lines respectively.	100
4.21	Variation of resonant proton energy with K_p for $L=8.3$ and $MLT=1500$ using the model of Ozeke and Mann (2001).	102

5.1	Location of ground-based instrumentation used in this study. Locations are shown at 1400 UT on 03 January 1998. Plotted are representations of the Longyearbyen MSP (thick line), Ny Ålesund ASC (oval) and SuperDARN CUTLASS radars (fans) fields of view. The locations of the IMAGE magnetometers used in this study (Table 3.1) are plotted with + symbols.	108
5.2	WIND MFI (B_X , B_Y and B_Z in GSM coordinates; top three panels) and SWE (v_x GSM, number density and dynamic pressure; bottom three panels) solar wind parameters for 3rd January 1998. The data are time lagged by 67 minutes (the assumed travel time from Wind to the Earth).	110
5.3	Longyearbyen MSP data for 1200 to 1700 UT on the 3rd January 1998; 630.0 and 557.7 nm filters are shown. The y axis runs from 81 to 69 degrees geomagnetic latitude. The 630.0 nm field of view has been cropped to coincide with the field of view of the 557.7 nm filter.	111
5.4	ACE SWEPAM (v_x GSM and number density; top two panels) and MFI (B_X , B_Y and B_Z in GSM coordinates; lower three panels) solar wind parameters for 29th December 2000.	113
5.5	Longyearbyen MSP data for the 29th December 2000. The y axis runs from -170 to 170 degrees look angle, corresponding to 69 to 81 degrees geomagnetic latitude. All five filters from the MSP are shown. Periodic, equatorwards propagating auroral features are observed between 1400 and 1600 UT.	114
5.6	ACE SWEPAM (v_x GSM, top panel) and MFI (B_X , B_Y and B_Z in GSM coordinates; lower three panels) solar wind parameters for 18th January 2002. No number density data exists for this interval.	115
5.7	Longyearbyen MSP data for the 18th January 2002. The y axis runs from -170 to 170 degrees look angle, corresponding to 69 to 81 degrees geomagnetic latitude. All five filters from the MSP are shown. Clear, periodic equatorwards propagating auroral features are observed between 1300 and 1500 UT.	116
5.8	Ny Ålesund 557.7 nm ASC data for the interval 1429:46 to 1434:45 UT, projected to 110 km altitude with geographic overlay. The data are cut at 80° from the zenith.	117
5.9	Keogram constructed from the 557.7 nm filter of the Ny Ålesund ASC for the interval 1400 to 1500 UT.	119
5.10	Longyearbyen MSP 557.7 nm emission (top row panels) and IMAGE magnetometer (bottom three row panels) data from 1300 to 1600 UT on the 3 January 1998. Left hand stack displays 557.7 nm MSP data from the zenith (top panel) and LYR H,D,Z magnetometer data (bottom three panels). Right hand stack displays 557.7 nm MSP data corresponding to the latitude of Hopen Island (zenith angle of 136° assuming a 110 km emission altitude) and HOP magnetometer data. All time-series are unfiltered.	120

5.11	Power spectra from 557.7 nm MSP (left panel) and IMAGE magnetometer X-component (right panel) data, filtered between 1000 and 100 seconds. MSP scans were taken from the zenith southward (with 90° indicating the zenith), at intervals of ten degrees in look direction; panel labels indicate zenith angle and magnetometer stations in the left and right panels, respectively.	121
5.12	SuperDARN northern hemisphere merged velocity vectors for the intervals 1442 to 1444 UT (left panel) and 1444 to 1446 UT (right panel) on the 03 January 1998, projected onto a geographic overlay. Also plotted are the predicted location of convection cells from the APL map-potential model.	122
5.13	Tsyganenko 1996 model results for field lines corresponding to IMAGE magnetometer stations from Table 3.1, mapped into the equatorial GSM plane at 1430 UT on the 3 rd January 1998. Also plotted as a dashed line is the magnetopause location from the Shue <i>et al.</i> (1997) model.	125
5.14	Schematic of the dipolar field line geometry. The propagation time for an Alfvén wave along field lines L_1 and L_2 from the equatorial plane to the Earth (at latitudes λ_1 and λ_2) is t_1 and t_2	126
6.1	MSP data from Longyearbyen for the interval 0000 to 0700 UT on the 10 th February 2000, plotted against magnetic latitude. The polewards edge of the auroral oval, as characterised by 630.0 nm emission is seen to move throughout the interval, and there is clear activity at the polewards edge in both the 630.0 nm and 557.7 nm bands throughout the interval. Clear, equatorwards propagating auroral features are observed between 0120 and 0150 UT and also between 0430 and 0500 UT.	134
6.2	IMAGE H- and D-component magnetometer data for the interval 0000 to 0330 UT on the 10 th February 2000. Each timeseries is independently scaled, FSD indicating the full scale deflection of the trace in each panel.	136
6.3	ESR data for the interval 0000 to 0330 UT on the 10 th February 2000. Parameters plotted are electron number density (top panel), ion temperature (second panel), electron temperature (third panel) and ion velocity (lower panel).	137
6.4	Stacked timeseries from the Longyearbyen MSP (top panel), unfiltered Bear Island magnetometer (second and third panels) and the EISCAT Svalbard radar (lower three panels). Red vertical lines correspond to the maximum intensity of the three quasi-periodic auroral features.	139
6.5	Taken from Lyons <i>et al.</i> (2002). Top panel shows MSP data from Canadian sector, with PBI events. The horizontal line at 67° latitude delineates data from Rankin Inlet (above 67° latitude) and Gillam (below 67° latitude). Bottom shows Polar data where the auroral zone shows evidence of wave-like structure.	141

7.1	Data from the Longyearbyen MSP for the interval 1730 to 1930 UT on the 7 th December 1999. The top panel corresponds to the 630.0 nm filter, the bottom to the 557.7 nm emission. The vertical scale represents the look angle of the MSP in the north-south direction, and ninety degrees corresponds to the zenith. PBIs are observed to propagate equatorward from the poleward boundary of the auroral oval 1854 and 1904.	146
7.2	Solar wind magnetic field data from the ACE satellite in GSM coordinates for the interval 1700 to 2000 UT on the 7 th December 1999. The travel time from ACE to the Earth is ~40 minutes, and the red vertical line is the time of the substorm onset observed by SAMNET (see text) lagged by this amount.	147
7.3	557.7 nm Ny Ålesund all sky camera data for the interval 1900 to 1906 UT on the 7 th December 1999 superimposed onto a geographic map. Data are cut off at 170° from the zenith. Magnetic north is approximately in the north-north east direction.	148
7.4	557.7 nm Ny Ålesund all sky camera data for the interval 1906 to 1912 UT on the 7 th December 1999 superimposed onto a geographic map. Data are cut off at 170° from the zenith.	149
7.5	SAMNET magnetometer data for the interval 1800 to 2000 UT on the 7 th December 1999. The timeseries have been filtered between 200 and 20 seconds to highlight Pi2 activity, believed to be indicative of substorm onset timing.	150
7.6	Unfiltered H- and D-component data from the five northernmost IMAGE magnetometer stations for the interval 1800 - 2000 UT on the 7 th December 1999. Red vertical lines indicate the time interval for which Fourier analysis was performed.	152
7.7	Fourier transforms of the D-component data from the five northernmost IMAGE magnetometer stations for the interval 1845 to 1905 UT on the 7 th December 1999 (highlighted in Figure 7.6). Timeseries are filtered between 50 and 350s, i.e., 2.6 to 20 mHz.	153
7.8	Slice through Longyearbyen MSP data from Figure 7.1 from the zenith in the 557.7 nm filter (top panel) and unfiltered D-component Longyearbyen magnetometer data (bottom panel) for the interval 1835 to 1905 UT on the 7 th December 1999. Red vertical lines indicate auroral intensifications that correspond with magnetic deflections.	154
7.9	ESR field aligned data for the interval 1730 to 1930 UT on the 7 th December 1999. From top to bottom, panels represent the logarithm of the electron density, the ion temperature, the electron temperature and the ion velocity. Blue in the ion velocity plot corresponds to motion towards the radar, with red corresponding to anti-Earthward motion.	155

7.10	Polar ionospheric footprint for the interval 1730 to 1930 UT on the 7 th December 1999 as determined from a Tsyganenko 1996 model. The grey line represents the field of view of the Longyearbyen MSP, and land masses and the Feldstein auroral oval for $K_p = 4$ are plotted for reference. Created by Jonathan Rae at the University of Alberta.	156
7.11	Spectrograms from the HYDRA instrument on-board Polar for the interval 1730 to 1930 UT. Upper and lower panels show electron and ion fluxes between energies of 10 eV and 10 keV. Data courtesy of J. Scudder at U. of Iowa and produced via CDAWEB at http://cdaweb.gsfc.nasa.gov	157
7.12	Polar magnetic (top three panels) and electric (bottom three panels) field data from 1830 to 1930 UT on the 7 th December 1999. The data are presented in a local field-aligned coordinate system, with z representing the field aligned direction, y the approximately azimuthal direction and x the third direction of the orthogonal set, which is approximately radial in this case.	159
7.13	Polar magnetic field, electric field and Poynting flux data in field-aligned coordinates for the interval 1830 to 1930 UT on the 7 th December 1999. Magnetic and electric field data are filtered between 1 and 10 mHz.	161
7.14	Spectral power for Polar B_x (top panel), B_y (second panel), E_x (third panel) and E_y (bottom panel) field data for the interval 1850 to 1910 UT on the 7 th December 1999. The original data were filtered between 1 and 15 mHz, and x and y components are the quasi-radial and azimuthal directions in a local field-aligned coordinate system.	162
7.15	Polar magnetic field (top three panels), electric field (middle three panels) and Poynting flux (bottom three panels) data for the interval 1858 to 1902 UT on the 7 th December 1999. Magnetic and Electric field data are filtered between 0.2 and 0.4 Hz, and all data are in a local field-aligned coordinate system.	164
7.16	Polar HYDRA data for the interval 1850 to 1905 UT on the 7 th December 1999. The top three panels represent electron fluxes in the Earthwards field-aligned, anti-Earthwards field-aligned and perpendicular directions respectively; lower plots represent 2-D velocity distributions for selected times during the interval with the upwards and downwards field-aligned directions corresponding to the negative and positive x -axis respectively. Plot produced by Reiner Friedel, Personal Communication, 2005.	165
7.17	Taken from Lysak (1998). Normalised magnetic fields (left panel) and parallel electric fields (right panel) for the kinetic Alfvén wave dispersion relation. Fields are plotted as a function of the perpendicular wavenumber, k_{\perp} , and the electron thermal speed, v_e , normalised by the electron inertial length, c/ω_p , and the Alfvén speed, V_A , respectively. Overplotted in red in the left panel is the locus constructed from observed values of v_e and $V_A B_y/E_x$, so that a constraint on k_{\perp} can be made. The right panel illustrates this locus and the constraints it implies for $k_{\perp} E_z/k_{\parallel} E_x$	167

7.18 Ratio of the spectral densities of E_{tot} and B_{\perp} plotted versus frequency for the intervals 1854 to 1906 UT (red line) and 1836 to 1848 UT (blue line) on the 7th December 1999. Also plotted are theoretical curves for the ration of $\delta E/\delta B$ derived from Equation 7.6 172

Chapter 1

The Sun-Earth Connection

The study of solar-terrestrial physics covers a wide area of research, including processes that occur in the solar atmosphere in close proximity to the Sun, through interplanetary space including the physics of the solar wind, to the Earth's local environment – including the magnetosphere, and even reaching the outer sections of the Earth's atmosphere, such as the ionosphere and thermosphere. This thesis is concerned with energy transport from the outer regions of the Earth's magnetosphere to its ionosphere via Alfvén waves in the ultra low frequency (ULF) band, and this Chapter aims to put this specialized area of research into a wider context by discussing the morphology of the Sun, the solar wind and the Earth's magnetosphere.

1.1 The Sun

The Sun is located at a distance of 1.5×10^{11} m from the Earth, and is a fairly typical type G2V star. The Sun's emitted radiation amounts to 1 kW/m^2 at the Earth, and provides the majority of the energy required for life to survive. Moving outwards from the center of the Sun (see Figure 1.1 for the internal structure of the Sun), the first region one encounters is the core. In this region nuclear fusion reactions convert hydrogen to helium, and it is this reaction that supplies most of the Sun's energy. The next layer is the radiative zone, so called because energy is transported through this region by the radiative motion of photons. The next region is the convective zone, where energy transport is performed by the thermal motion of the plasma. The photosphere, at the edge of the convective zone, is generally assumed to represent the visible "surface" of the Sun. Moving through the

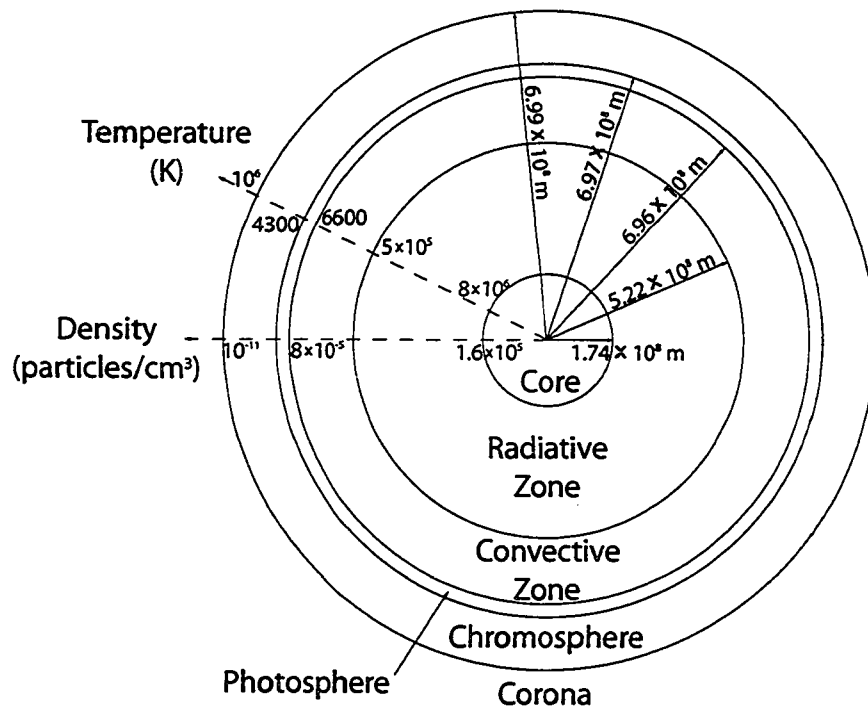


Figure 1.1: The structure of the Sun, showing approximate distances, temperatures and plasma densities. Adapted from Kivelson and Russell (1995)

solar atmosphere, above the photosphere which radiates the light that we observe from the Sun, one first encounters the chromosphere, which is a transparent layer of relatively low temperature and density, before reaching the outermost region of the solar corona. The corona is a tenuous plasma at a very high temperature (approximately 10^6 K), whose particles are of high enough energy to escape the gravitational attraction of the Sun, so that the corona expands into interplanetary space and forms the solar wind (see Section 1.2 for a full description of the solar wind). The energization mechanisms for the heating of the solar coronal plasma and the acceleration mechanism of the solar wind are still not fully understood.

The Sun possesses an internal magnetic field, with an average strength on the surface of the photosphere of approximately 10^{-4} T. This magnetic field, although often complex on small scale sizes (e.g., see the discussion of sunspots and coronal holes below), can usually be described macroscopically by a dipole or quadrupole.

The Sun exhibits an eleven year “Solar Cycle” in terms of its magnetic field configuration which consists of the internal magnetic dipole reversing its polarity (this is actually

a twenty-two year cycle, as the magnetic polarity switches in each hemisphere after every eleven year cycle). The number of sunspots on the surface of the Sun (sunspots are regions of cooler plasma associated with intense magnetic fields, and often occur in pairs) is directly related to the solar cycle. When the magnetic field lines protruding through the photosphere become twisted and sheared, magnetic reconnection can take place, which releases hot plasma that was trapped on the magnetic field lines into interplanetary space. This process is known as a coronal mass ejection (CME), and these events typically occur on timescales of a few hours.

Another category of solar atmospheric phenomena includes prominences or filaments. These are regions of high density plasma supported on loops of magnetic field lines. Prominences and filaments are essentially the same object, being called prominences when observed on the limb of the Sun, and filaments elsewhere. Prominences and filaments are thought to be related to some CMEs.

Helmet streamers typically occur above prominences, and generally overly a network of magnetic loops that connect sunspots in active regions of the Sun. These solar regions are believed to be the source of the low speed solar wind. The high speed solar wind is thought to originate from coronal holes, which are regions on the surface of the Sun that are associated with “open” magnetic field lines. During solar minimum coronal holes are confined to the polar regions of the Sun, whereas during the solar maximum they can occur at all solar latitudes.

1.2 The Solar Wind

The solar wind was first postulated by Parker (1958). He proposed that the pressure difference between interplanetary space and the solar corona would cause the hot plasma of the corona to stream away from the solar gravitational field. The large conductivity of the solar wind means that it transports the solar magnetic field with it (see Section 2.2), and Parker (1958) also proposed that this magnetic field would be of a spiral form. Although the solar wind propagates radially, the rotation of the sun causes the magnetic field to become distorted, producing the so-called “Parker Spiral” form of the interplanetary magnetic field (IMF) (see Figure 1.2). At the orbital distance of the Earth, the solar wind speed is

SOLAR WIND

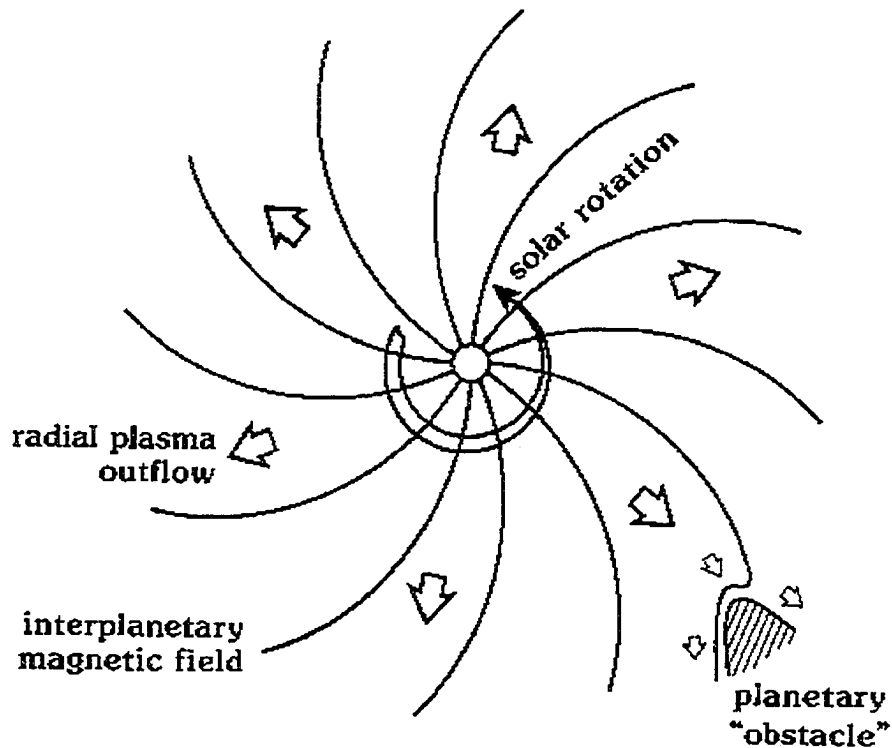


Figure 1.2: Spiral form of the solar wind showing the interplanetary magnetic field and solar wind flow. Taken from Allan and Poulter (1992).

typically of the order of 450 km/s, the electron and proton number densities are around 7 particles/cm³ and the magnetic field strength is approximately 7×10^{-9} T.

The solar wind plasma density and speed vary according to which region of the surface of the Sun the plasma originates from. The solar wind that originates from coronal holes is of high speed and low density, whereas the solar wind that originates from helmet streamers is of lower speed and higher density. These differing properties of the solar wind flow can cause the Parker spiral to become compressed and rarefacted in interplanetary space (see Figure 1.3).

The Sun possesses magnetic topologies which can be associated with essentially open and closed magnetic field lines, the open field lines being directed towards or away from the Sun in the northern or southern hemispheres. Thus, a current sheet exists in the heliosphere between the oppositely directed field lines, and due to the inclination angle of the Sun's

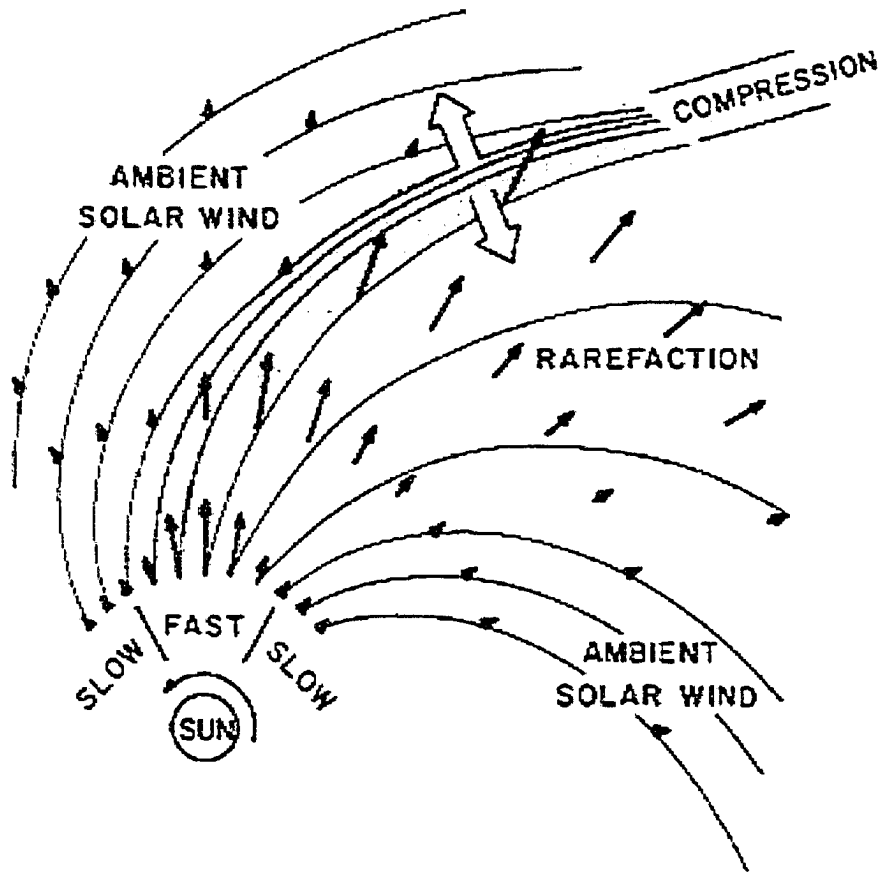


Figure 1.3: Compression and rarefaction of solar wind magnetic field lines by the fast and slow solar wind. Taken from Kivelson and Russell (1995).

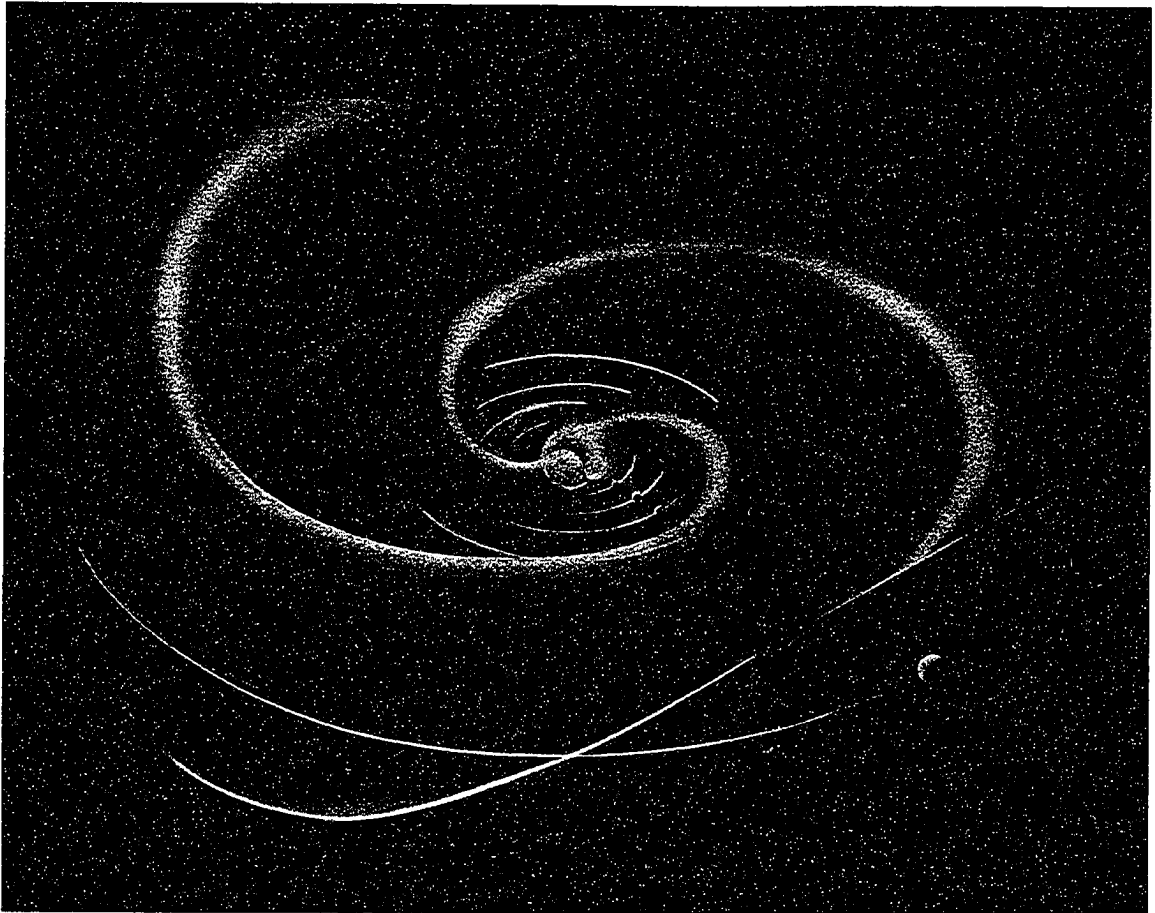


Figure 1.4: “Ballerina’s skirt” model of the heliospheric current sheet, with the orbits of the solar system planets out to Jupiter shown. Taken from the website at <http://pluto.space.swri.edu/IMAGE/glossary/IMF.html>.

magnetic dipole and rotational axis with respect to the Earth’s orbit, the Earth typically experiences either a sunward or an antisunward directed solar magnetic field. In fact, due to the wave like structure of the current sheet, the magnetic field of the Sun in the ecliptic plane of the heliosphere can usually be described by a four sector geometry with adjacent sectors having oppositely directed solar magnetic field lines. This geometry is often described as being analogous to a ballerina’s skirt, and is illustrated in Figure 1.4.

1.3 The Bow Shock

As the plasma of the solar wind streams away from the Sun, it encounters the magnetic field of the Earth. The solar wind particles cannot, in general, cross the magnetic field

lines of the Earth (as both the geomagnetic field and the solar wind magnetic field are “frozen in” to their respective plasmas, see Section 2.2.4), and the solar wind compresses the dipolar geomagnetic field. The geometry of the magnetospheric cavity caused by the solar wind interacting with the Earth’s magnetic field will be discussed in Section 1.4. Here we concentrate on the Bow Shock, the region where the solar wind plasma is slowed by the interaction with the Earth’s magnetic field.

The solar wind propagates at super-sonic and super-Alfvénic speeds, so that as it impinges on the geomagnetic field a shock front forms. Beyond this shock front (the bow shock) the plasma is slowed to subsonic speeds, becomes turbulent, and is deflected around the magnetospheric cavity. This region between the bow shock and the boundary of the magnetospheric cavity (the magnetopause) is known as the magnetosheath. The exact location of the magnetospheric bow shock depends on the solar wind Mach number (the ratio of the solar wind flow speed to the solar wind plasma sound speed) and the plasma beta of the solar wind (the ratio of the plasma thermal pressure to the magnetic pressure). For a fuller discussion of the bow shock, see e.g., Kivelson and Russell (1995).

1.4 The Magnetosphere

The magnetosphere is formed when solar wind plasma is slowed and deflected by the Earth’s magnetic field (see Figure 1.5). This braking of the solar wind causes the Earth’s dipolar magnetic field to become compressed on the dayside, and extended in the antisunward direction on the nightside. A pressure balance at the location of the magnetopause between the force of the impinging, turbulent, predominantly thermal pressure dominated magnetosheath plasma and the predominantly magnetic pressure dominated plasma on the geomagnetic field inside the magnetosphere determines the magnetopause stand off distance. Due to fluctuations in the solar wind speed and density, the magnetopause standoff distance can vary, although it is typically at around 10 Earth radii (R_E).

The magnetosphere extends beyond $1000 R_E$ in the antisunward direction, as the solar wind sweeps the geomagnetic field lines downstream into the magnetotail. The magnetotail is approximately circular in cross section, with a radius of approximately $30 R_E$, and, as we will see in Section 1.5, the magnetotail can act as a reservoir for plasma inside the mag-

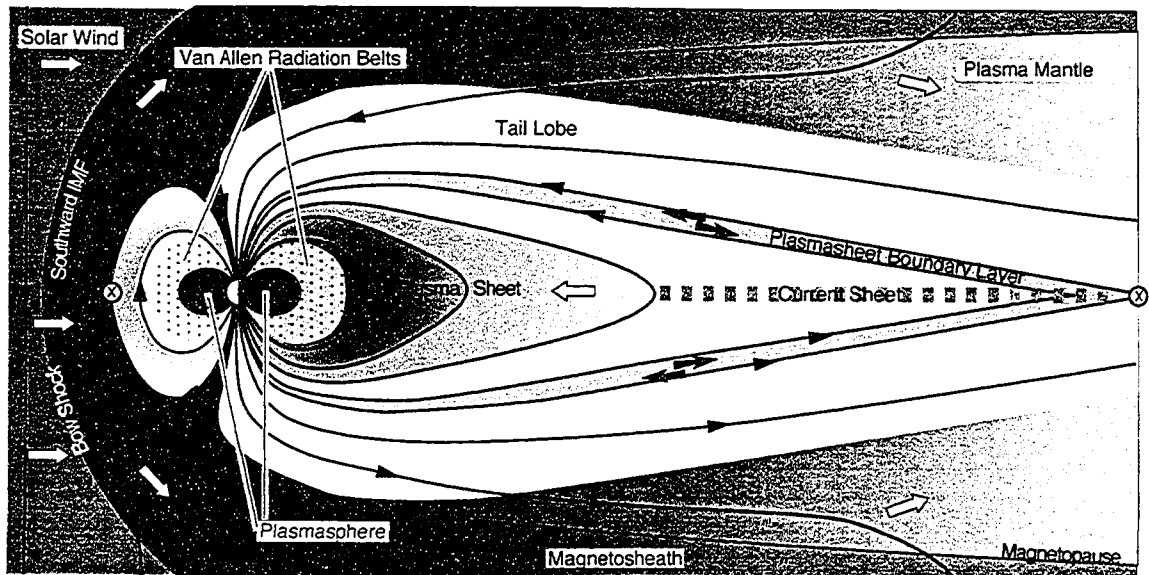


Figure 1.5: Diagrammatic representation of the Earth's magnetosphere with major regions labeled. Taken from the IMAGE website at Rice University, located at <http://space.rice.edu/IMAGE/livefrom/sunearth.html>.

netosphere. Inside the magnetotail, the geomagnetic field lines are stretched, and as a result are anti-parallel across the Earth's equatorial plane. Between these two oppositely directed magnetic fields lies a current sheet, which is embedded in a region of hot plasma known as the plasmasheet, which separates the northern and southern magnetospheric lobes.

Particle populations in the magnetosphere are either of ionospheric or solar wind origin. Ionospheric origin plasma is typically initially cold (energy ~ 1 eV) and comprised of protons, electrons and O^+ ions. The solar wind plasma is hotter (typical energies of ~ 1 keV) and comprises electrons, protons and a small number of He^{++} ions (approximately 5% by number). The plasma contained in the plasmasheet is predominantly of solar wind origin, this plasma being injected into the magnetosphere via either nose or tail reconnection (see Section 1.5 for a description of these processes), or entering along open field lines via the magnetospheric cusp. The ionospheric footprints of plasmasheet magnetic field lines lie in the northern and southern nightside auroral ovals, and plasmasheet particles account for the continuous nightside auroral emission as they are scattered to low altitudes and collide with the Earth's atmosphere. For a discussion of auroral production and auroral particle acceleration processes see Section 2.8.

The solar wind flow also produces the so-called convection (or dawn-dusk) electric field. This electric field drives the convection of geomagnetic field lines in the Earth's magnetosphere, and this is discussed further below. This electric field also dominates the overall drift motion of plasmasheet particles, causing them to drift Earthwards from the magnetotail. As these particles move inwards, their motion becomes dominated by gradient-curvature drifts (see Section 2.1.3), so that electrons drift eastwards around the Earth and ions drift westwards. This opposite motion of positive and negative charges produces a net current, known as the ring current, and the magnetic field that this current loop induces acts to oppose the geomagnetic field (i.e., in the equatorial plane inside the ring current, the ring current induced magnetic field is directed southwards, whereas the geomagnetic field is directed northwards). Depending on the energy of the ring current particles, they may either drift around the Earth on closed paths, or lie on open trajectories and be lost through the dayside magnetopause. For a discussion of the properties of ring current particles and the modeling of their trajectories, see e.g., Ozeke (2002) or Ozeke and Mann (2001) and references therein.

Close to the Earth, the motion of cold plasma is dominated by the force of the co-rotation electric field, which is caused by the rotation of closed geomagnetic field lines due to the rotation of the Earth. On these field lines, the cold plasma is trapped, and the equatorial density of the plasma is high (around 10^3 particles/cm³). This region of co-rotating plasma is known as the plasmasphere, and extends out to approximately $4 R_E$ in the equatorial plane, to a boundary known as the plasmapause. This boundary between the cold, high density co-rotating plasmaspheric plasma and the rest of the magnetosphere occurs over a short distance, typically around $0.5 R_E$. The exact location of the plasmapause depends on the strength of the convection electric field, which in turn is dependent upon geomagnetic activity. See e.g., Dent (2003) and references therein for a description of the plasmasphere region.

The radiation (or Van Allen) belts are regions of high energy particles that are trapped by the geomagnetic field (see Chapter 2.1 for a discussion of how magnetic fields may trap particles) between altitudes of around 1000 km above the Earth's surface and approximately $6 R_E$. The radiation belts are extremely hostile plasma regimes for manned and unmanned space flight, the ionizing particles can damage human tissue, and cause instruments to

malfunction (e.g., via single event upsets). The energization mechanism for the radiation belts is not fully understood, although recent work has shown that energetic particle fluxes correlate well with solar wind speed and ultra-low frequency (ULF) magnetic wave power in the magnetosphere [Mathie and Mann, 2001], suggesting that ULF waves may have a role to play in Van Allen belt particle acceleration.

The ionosphere represents the lower boundary of the Earth's magnetosphere, and occurs when either energetic photons or particles collide with, and ionize, the neutral particles in the terrestrial atmosphere. The major production mechanism for ionospheric ions on the dayside of the Earth is ionization from the solar photon flux in the extreme ultraviolet and ultraviolet wavelength ranges, whereas on the nightside energetic particle collisions with the atmosphere produce the majority of ionized particles. Energetic particle sources include cosmic rays, solar energetic particles, particles accelerated within the magnetosphere, and even ionospheric particles that undergo a local acceleration process. Figure 1.6 shows the structure of the neutral atmosphere and the ionosphere, with the ionospheric D, E, and F regions highlighted.

1.5 Geomagnetic Activity

Large magnitude geomagnetic activity can be generally divided into two separate categories, geomagnetic storms and substorms. Storms occur when an increase in the dynamic pressure of the solar wind (caused by e.g., a CME) forces the magnetopause (and hence the magnetopause current) closer to the Earth, followed by an increase in the intensity of the ring current. The signature of the start of a storm (the initial phase) can be identified at mid latitudes by an increase in the Dst index generated by magnetopause compression (Dst is defined in terms of the instantaneous worldwide average of the equatorial magnetic field disturbance in the north-south direction, as measured by ground-based magnetometers), and at higher latitudes by MHD waves propagating into the magnetosphere. The initial phase of a storm can last from minutes up to tens of hours. The main phase of the storm occurs when the Dst index decreases rapidly, to negative values of possibly hundreds of nT, as the ring current is built up. During this period the enhanced dawn-dusk electric field forces the plasmapause closer to the Earth, and removes the outer layers of the pre-existing

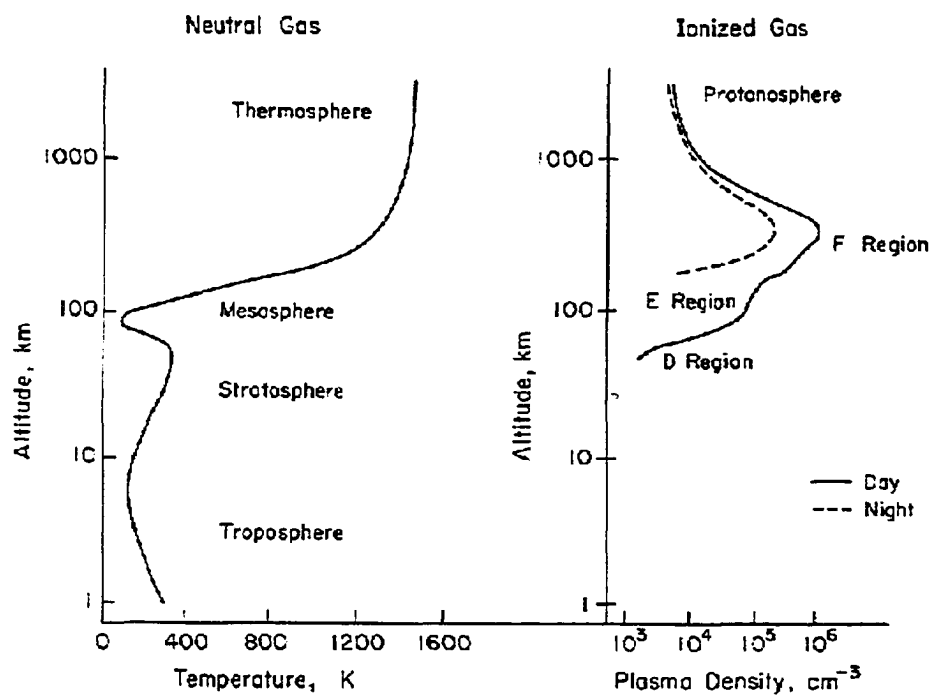


Figure 1.6: The vertical structure of the Earth's neutral atmosphere and ionosphere. Image courtesy Center for Space Sciences, University of Texas.

plasmasphere. The main phases of geomagnetic storms tend to last for around one day. The recovery phase of the storm usually lasts for several to many days, and is characterized by the slow return of Dst to normal values. During the recovery phase the ring current decreases with ions being lost, mostly either to the solar wind or by charge exchange with cold neutral hydrogen.

Magnetospheric substorms are a direct result of dayside and tail magnetic reconnection. Magnetic reconnection occurs when anti-parallel magnetic field lines are forced together due to plasma motion (see Figure 1.7). Initially, a current sheet separates the two oppositely directed fields (in this example the magnetopause current sheet lies between the oppositely directed magnetic fields of the magnetosheath and the Earth's magnetosphere). As the solar wind compresses the flux tubes outside the magnetopause, the current sheet becomes compressed and the magnetic Reynolds number approaches unity (the magnetic Reynolds number is given by $R_m \simeq \mu_0 \sigma u L$, where u is the plasma velocity, σ is the plasma conductivity and L is the length scale over which the transition between the two plasma regimes occurs). As the scale size of the boundary between the two regimes decreases, a diffusion region is created wherein the "frozen-in theorem" (see Section 2.2.4) does not apply. The oppositely directed field lines may then be cut and re-connected in the diffusion region, and magnetic tension forces pull these newly connected field lines away from the diffusion region (indicated by the large arrows in Figure 1.7). The process of reconnection allows the transport of energy across a boundary that under ideal MHD conditions would be impenetrable.

The traditional view of dayside reconnection states that for a purely southward IMF, reconnection occurs at the nose of the magnetopause at one point only. The component merging hypothesis of reconnection states that if the geomagnetic field and the solar wind magnetic field merely have components that are anti-parallel, then reconnection may occur (see e.g., Crooker (1979) for a full discussion of reconnection hypotheses). For an IMF with a negative GSM (see Appendix A) z-component, and non-zero x- and y-components, the reconnection region may be shifted to either the dawn or dusk flank, and field line merging can occur along a locus of points that lie on the magnetopause current sheet. During the process of dayside reconnection, solar wind field lines connect to geomagnetic field lines, producing field lines that have one end connected to the Earth, and one end connected to

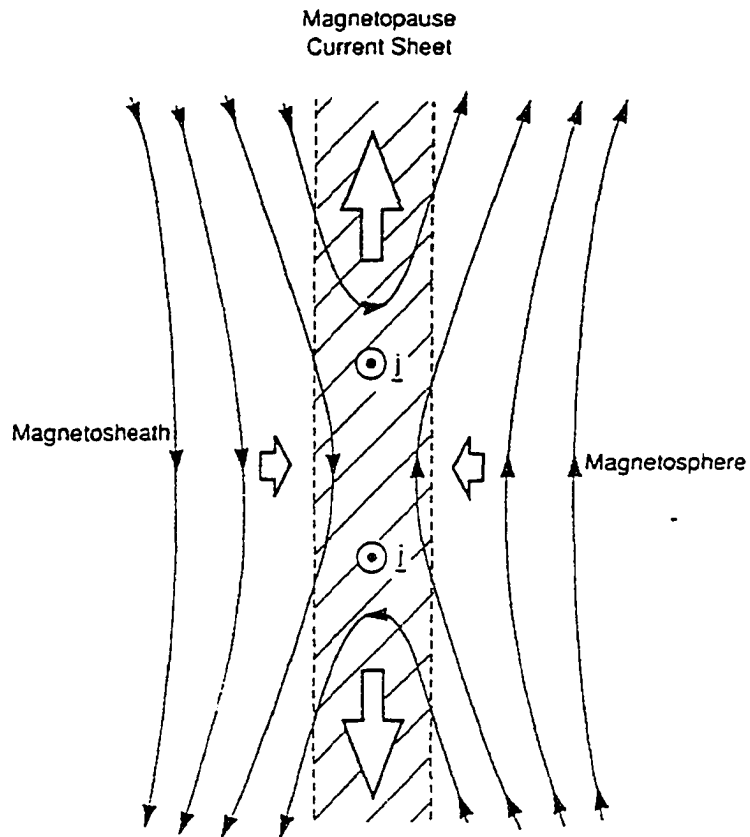


Figure 1.7: Illustration of magnetic connection of solar wind field lines to geomagnetic field lines at the Earth's magnetopause. From Cowley (1999).

the IMF. These “open” field lines are dragged polewards and tailwards by magnetic tension forces, increasing the flux of open magnetic field lines in the polar cap. As this process repeatedly occurs, the flux in the polar cap further increases, which can cause another reconnection site in the tail to become active (see Figure 1.8). At this new reconnection site, two open magnetospheric field lines connect to form one solar wind type field line and one closed geomagnetic field line. Due to magnetic tension forces, the solar wind field line propagates downtail, and the geomagnetic field line moves Earthward. Finally, the newly created geomagnetic field line convects to the dayside of the magnetosphere to end the cycle. This process of magnetic field lines connecting to solar wind field lines, propagating tailwards, reconnecting in the magnetotail and convecting to the dayside of the magnetosphere was first proposed by Dungey (1961), and is named the Dungey Cycle. In reality, the instantaneous reconnection rates at the magnetopause and in the tail are rarely in balance, so that the cycle continues in a bursty fashion. However, on average the Dungey Cycle is an accurate representation of magnetospheric convection and represents a major mechanism for energy transport from the solar wind into the magnetosphere.

Magnetic reconnection at the dayside magnetopause can also drive magnetic substorms, these substorms forming a non-steady component of magnetospheric convection. The substorm cycle begins with the growth phase, which lasts for around one hour and is characterized by dayside reconnection increasing the magnetic flux in the northern and southern lobes, and the dawn-dusk electric field increasing in magnitude. The next stage of substorm activity is the onset, the cause of which is a subject of much debate. The Near-Earth Neutral Line (NENL) model asserts that an instability in the mid-magnetotail creates fast flows, and causes other onset signatures (see e.g., Baker *et al.*, 1996). The current disruption model proposes that a thin current sheet forms just tailwards of dipolar geomagnetic field lines (between 6 and 15 R_E downtail) and that reconnection occurs only after a rarefaction wave from the instability region reaches the mid-tail (see e.g., Lui, 1996). The expansion phase occurs after the substorm onset and can range between 10 minutes and two hours in duration. Fast, Earthward propagating plasma flows are observed in the near Earth plasmasheet, and tailwards moving plasmoids are observed in the far tail. The dawn-dusk cross-tail current is disrupted, so that field aligned currents are produced, and the dawn-dusk cross tail current closes through the Earth’s ionosphere (see Figure 1.9). This

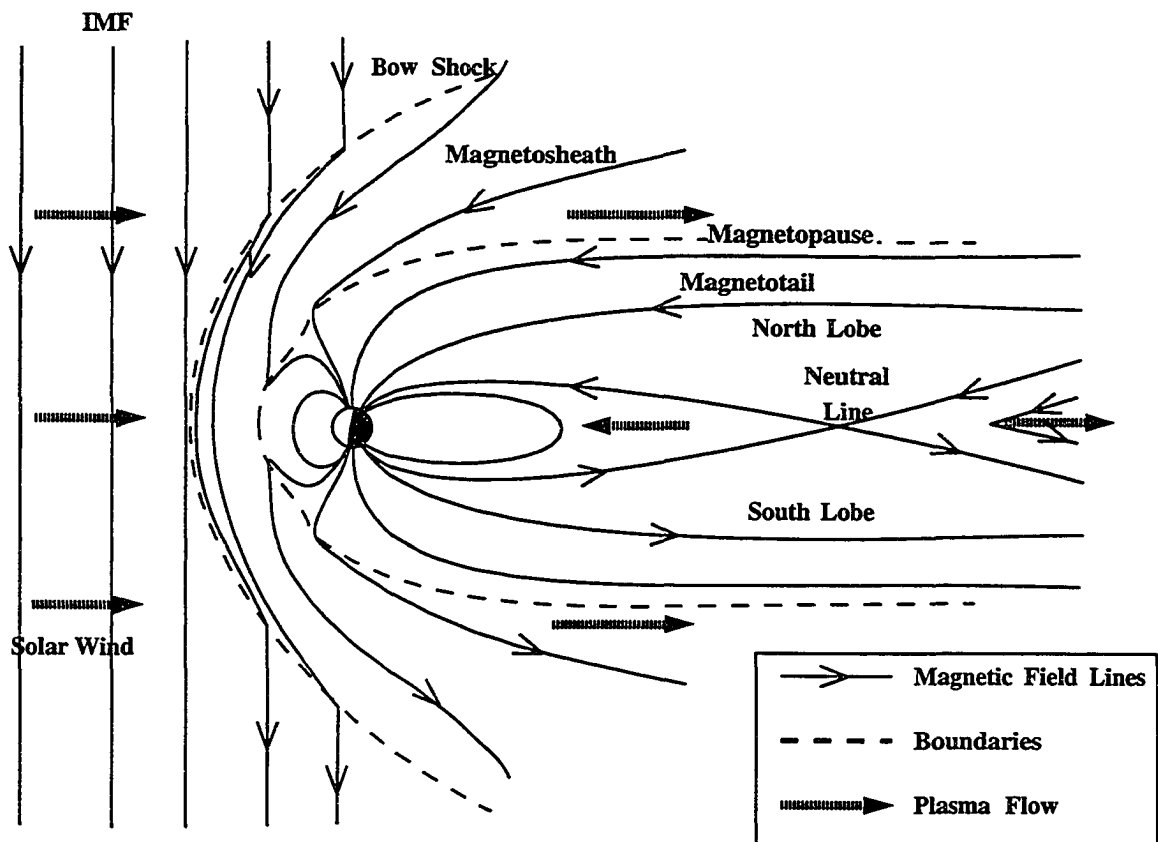


Figure 1.8: The magnetospheric cycle first proposed by Dungey (1961) for a purely southward IMF. From Ozeke (2002).

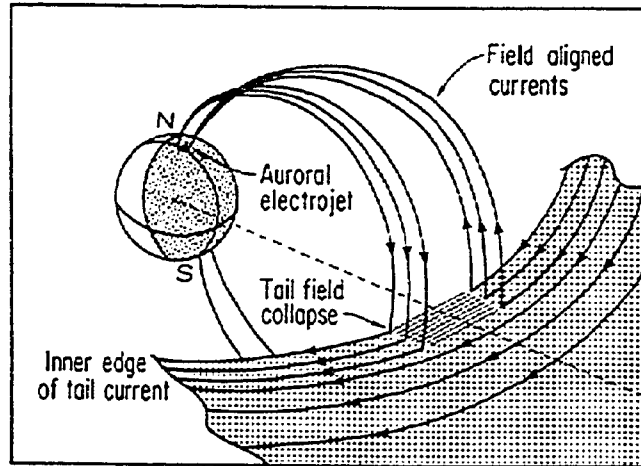


Figure 1.9: Diagram illustrating the form of the substorm current wedge. Taken from Russell (1974).

current system is known as the substorm current wedge. It is during the expansion phase that large auroral displays are observed on the ground. Finally, in the recovery phase, the magnetospheric current systems, magnetic field lines and the plasmasheet all revert to their normal state. The recovery phase typically lasts for 90 minutes.

1.6 Geomagnetic Indices

In this section we describe two magnetic indices, K_p and Dst that are used to characterise geomagnetic activity.

1.6.1 The Planetary K_p Index

The K_p index is an indication of the planetary magnetic activity, measured at magnetometer stations that lie between 44° and 60° geomagnetic latitude in either hemisphere. Magnetic activity is measured at each station using the deviation in the H- or D-component magnetic timeseries as compared to an assumed quiet time curve. The level of activity at each station is indicated by a number, K , ranging from 0 (for the most quiescent intervals) to 9 (for the most active intervals) on a logarithmic scale, for concurrent 3 hour windows.

The 3 hour K_p index is defined as the mean standardised K index from 13 magnetic observatories, and is converted from the 0 through 9 scale to third of a unit degradations

(e.g., 4 1/3, 4 2/3 etc which we represent as 4+, 5- etc). The K_p index is an indication of the magnetic field variation due to irregular currents in the magnetosphere, which are influenced by varying solar wind conditions, the magnetospheric configuration and ionospheric effects. For a full description of the K_p index see, e.g., Kivelson and Russell (1995).

1.6.2 The Dst Index

The disturbance storm time (Dst) index is typically used to characterise the strength of the ring current (see earlier in this chapter for a discussion of the ring current). During a geomagnetic storm, particles are injected into the ring current, and as these particles drift round the Earth a current loop results. The direction of the magnetic field of this current loop acts so as to oppose the geomagnetic field. Magnetic observatories observe the enhancement of the ring current as a negative deflection in the H-component of the geomagnetic field, and these deflections are compared to a typical quiet time reference field to compute the magnitude of the ring current enhancement. Data from 4 magnetometer stations located between 20° and 40° geomagnetic latitude are utilised to compute a planetary Dst index, with the stations located approximately evenly distributed in local time.

Errors in the Dst index typically arise from sources of H-component geomagnetic activity not related to storm activity, such as the magnetopause current and the substorm current wedge. At noon, the typical error in Dst can reach around 50%, with the error in the midnight being somewhat lower at typically 10%. For a full discussion of the Dst index see, e.g., Kivelson and Russell (1995).

1.7 Magnetospheric ULF Waves

Magnetospheric ultra-low frequency (ULF) waves occur in the approximate frequency range of 1 mHz to 1 Hz, corresponding to the lowest magnetospheric cavity modes to higher frequency ion-cyclotron modes. One of the first observations of magnetospheric ULF waves was by Stewart (1861) at Kew observatory in London. They observed waves with a periodicity of a few minutes that were coincident with auroral brightenings. The current classification of ULF waves was first proposed by Jacobs *et al.* (1964) and is shown in Table 1.1.

Category	Period range (s)
Pc1	0.2 - 5
Pc2	5 - 10
Pc3	10 - 45
Pc4	45 - 100
Pc5	100 - 600
Pi1	1 - 40
Pi2	40-150

Table 1.1: Classification of ULF waves first proposed by Jacobs *et al.* (1964). Adapted from Kivelson and Russell (1995).

The two broad classes of Pc and Pi pulsations correspond to differing signatures of ULF waves observed on the ground. The Pc band are generally continuous and regular, whereas the Pi band is characterised by a more irregular morphology. The sub-divisions within the Pc and Pi bands are not arbitrary, they correspond to physical and morphological properties of magnetospheric waves (see e.g., Jacobs *et al.*, 1964 or Kivelson and Russell, 1995 for a fuller discussion of ULF wave categorisation).

Chapter 2

Plasma Theory and ULF Waves

In this section two potential methods for understanding plasma behaviour in the magnetosphere will be discussed. Firstly we consider the motion of single particles moving in electric and magnetic fields, and secondly we follow the fluid approach of magnetohydrodynamics for describing plasma behaviour. Both of these approaches can be useful for understanding ULF wave energy transport in the magnetosphere.

2.1 Single Particle Motion

In general, the analytic solutions for single particle trajectories in generalized electric and magnetic fields are hard to obtain. We restrict ourselves to magnetic and electric field geometries similar to the near-Earth dipolar magnetic field, and show how a large number of plasma properties can be predicted with these simple yet powerful tools.

2.1.1 Motion of Charged Particles in a Constant, Uniform Magnetic Field - Gyromotion

In order to describe the motion of charged particles in electric and magnetic fields we need to consider the Lorentz force, F_L , which describes the force on a particle due to magnetic (\mathbf{B}) and electric (\mathbf{E}) fields

$$\mathbf{F}_L = q(\mathbf{E} + \mathbf{v} \times \mathbf{B}) \quad (2.1)$$

where q is the charge of the particle and \mathbf{v} is its velocity. For a non-relativistic particle moving in a uniform magnetic field where $\mathbf{E} = 0$, we may write

$$m \frac{d\mathbf{v}}{dt} = q(\mathbf{v} \times \mathbf{B}) \quad (2.2)$$

where m is the mass of the particle. If we take the dot product of Equation 2.2 with \mathbf{v} , and note that $\mathbf{v} \cdot (\mathbf{v} \times \mathbf{B}) = 0$, we obtain

$$m \frac{d\mathbf{v}}{dt} \cdot \mathbf{v} = \frac{d}{dt} \left(\frac{mv^2}{2} \right) = 0 \quad (2.3)$$

which shows that the particle's kinetic energy (and hence the magnitude of its velocity) is constant. Hence the magnetic field does no work on the particle. The solution to Equation 2.2 in a uniform straight magnetic field \mathbf{B} is periodic circular gyromotion around the background magnetic field with frequency ω_g , and constant velocity along the direction of the magnetic field, producing a helical particle trajectory. Here ω_g is the gyrofrequency of the particle and is defined as

$$\omega_g = \frac{qB}{m} \quad (2.4)$$

and has opposite signs for positive and negative charges. The radius of gyration is simply given by $r_g = v_{\perp}/\omega_g$ (where v_{\perp} is the velocity in the direction perpendicular to the magnetic field), therefore

$$r_g = \frac{mv_{\perp}}{qB}. \quad (2.5)$$

2.1.2 Mirroring of Charged Particles in Magnetic Fields

We now consider the case where a charged particle follows a magnetic field line that is inhomogeneous in nature. We begin by defining the particle's pitch angle, given by

$$\alpha = \sin^{-1} \left(\frac{v_{\perp}}{v_{\parallel}} \right) \quad (2.6)$$

where v_{\perp} and v_{\parallel} are the velocity components in the directions perpendicular and parallel to the magnetic field, respectively. We also introduce the magnetic moment, μ , which is given by

$$\mu = \frac{mv_{\perp}^2}{2B}. \quad (2.7)$$

μ is also known as the first adiabatic invariant. This quantity is conserved as long as the magnetic field changes encountered by a particle occur on timescales that are much larger than the gyroperiod of the particle.

We know that $v^2 = v_{\perp}^2 + v_{\parallel}^2$, and that the kinetic energy of a given particle remains constant if there are no external forces (i.e., $\frac{1}{2}mv^2 = K$). Hence we may write

$$v_{\parallel} = \left(\frac{2}{m} [K - \mu B] \right)^{1/2}, \quad (2.8)$$

so a particle traveling along a magnetic field line with increasing field strength will reverse direction (mirror) at the point where $B = K/\mu$.

If we now consider a dipolar magnetic field geometry similar to that of the Earth, charged particles can remain trapped on geomagnetic field lines as they bounce between mirror points in the northern and southern hemispheres. Hamlin *et al.* (1961) were able to show that the bounce frequency of this motion, ω_b , in a dipole field, is given by

$$\omega_b = \frac{\pi V}{2R_E L T(\alpha_{eq})} \quad (2.9)$$

where $T(\alpha_{eq}) \simeq 1.3 - 0.56 \sin \alpha_{eq}$ and α_{eq} is the equatorial pitch angle of the mirroring particles. The location of the mirror point for particles on a given geomagnetic field line is determined by their pitch angle in the equatorial plane. Particles with large pitch angles will mirror a short distance away from the equatorial plane, whereas smaller pitch angle particles mirror closer to the ionosphere in each hemisphere. In fact, particles with small pitch angles may never mirror at all, and may be lost to the Earth's atmosphere. This collision of low pitch angle particles with the Earth's atmosphere causes some types of aurora.

If there are no electric fields directed along the magnetic field, the kinetic energy of the particle remains constant, and

$$W = \frac{m}{2}(v_{\parallel}^2 + v_{\perp}^2) = \frac{m}{2}v_{\parallel}^2 + \mu B = \text{constant}. \quad (2.10)$$

Thus we may define the second adiabatic invariant as

$$J = 2 \int v_{\parallel} ds \quad (2.11)$$

where v_{\parallel} is the particle velocity in the direction of the background magnetic field and ds is a line segment along the magnetic field line. The second adiabatic invariant is conserved if changes in the magnetic field occur on timescales larger than the bounce period of the particle in consideration.

2.1.3 Drifting of Particles in a Dipolar Magnetic Field

Charged particles moving in geomagnetic fields also experience motion that occurs on longer timescales: drifting due to the distortion of gyromotion by the convection and co-rotation electric fields and by the non-uniform and curved magnetic field. Hamlin *et al.* (1961) also showed that for particles in a dipolar magnetic field, the bounce averaged gradient-curvature drift is given by

$$\dot{\phi}_{gc} = \frac{-6WLP(\alpha_{eq})}{qB_s R_E^2} \quad (2.12)$$

where W is the energy of the particle in Joules, $P(\alpha_{eq}) \simeq 0.35 + 0.15 \sin \alpha_{eq}$, B_s is the equatorial magnetic field strength at the surface of the Earth, R_E is the radius of the Earth, and L is a dimensionless quantity used to represent the position of geomagnetic field lines. In a dipole field, L is constant with azimuth and is given by

$$L = \frac{r}{R_E \sin^2 \theta} \quad (2.13)$$

in spherical polar coordinates, and is often called the McIlwain parameter (e.g., McIlwain, 1961).

As previously mentioned, charged particles on geomagnetic field lines will also experience a force, and hence a drift motion, due to the convection and co-rotation electric fields. However, for particles of energy > 30 keV these effects can be generally considered to be negligible [e.g., Ozeke, 2002].

It is also possible to define an adiabatic invariant relating to the drift motion of charged particles (the first adiabatic invariant is concerned with gyromotion, the second with bounce motion). If the magnetic field that a drifting particle experiences varies over timescales much longer than the drift period of that particle, then the magnetic flux enclosed by the drift shell remains constant. This constant magnetic flux is defined as the third adiabatic invariant (see e.g., Kivelson and Russell, 1995).

2.2 Magnetohydrodynamics

In theory we know how to numerically compute the trajectory of any charged particle in any prescribed magnetic and electric field combination exactly. However, for very large numbers of particles this feat becomes impossible, due to restrictions imposed by the length of time required to solve for every individual particle. Furthermore, feedback between charged particle motion and electric and magnetic fields (e.g., a moving charge generates a current, which in turn generates a magnetic field) means that the single particle approach is not totally self consistent. We must therefore express the behavior of plasmas in a more statistical manner, and here we discuss a fluid approach known as magnetohydrodynamics (MHD).

2.2.1 Properties of MHD Plasmas

Prior to a full magnetohydrodynamical (MHD) treatment of space plasmas, we must first understand under which conditions MHD is valid. The first assumption about the plasma we wish to investigate is that it is quasi-neutral, i.e., that macroscopically the number of positive and negative charges must equal one another. This assumption must obviously break down when one investigates very small scale phenomena, and as such we must quantify what the requirement of quasi-neutrality means. We consider a localized positive charge in a plasma which is neutral overall which will locally attract the more mobile electrons towards it. At some length scale the electric fields from these net charge distributions will be totally screened by the presence of other nearby charges, and the electrostatic potential it causes will be reduced to zero. We may therefore define a sphere, outside of which the net charge and electric field are screened from the remaining plasma. On these macroscopic scales the plasma feels no effects from the microscale net charge distributions.

We assume that the plasma is composed of protons and electrons, and so a single positive charge will produce an electric potential ϕ which must satisfy Poisson's equation for an electron-proton plasma

$$\nabla^2 \phi = -\frac{e}{\epsilon_0} (n_i - n_e) \quad (2.14)$$

where n_i and n_e are the ion and electron number densities respectively and e is the charge

of an electron. The ion density, n_i , can be assumed to be equal to the density of the ambient plasma, n_0 , since we assume that the ions are stationary at the electron timescales of interest, as $m_i \gg m_e$. The electron density, n_e , must then take into account the density disturbances due to the isolated ion. We require the electron thermal motion to be in equilibrium with the electric force, so that the energy distribution of the electrons is Maxwellian, and their density obeys Boltzmann's law

$$n_e(r) = n_0 \exp \left[\frac{e\phi(r)}{k_B T_e} \right] \quad (2.15)$$

where r is the radial distance from the ion, k_B is the Boltzmann constant and T_e is the electron thermal temperature. For an isolated ion, the potential will be small, and we may expand the exponential function into a Taylor series and substitute the new expression for $n_e(r)$ into Poisson's equation, giving

$$\nabla^2 \phi = \frac{e^2 n_0 \phi}{\epsilon_0 k_B T_e}. \quad (2.16)$$

The solution to this problem will be spherically symmetric with radius r , centered on the position of the ion. Classical electrostatics tells us that as $r \rightarrow 0$, $\phi(r)$ must converge to zero in a manner that is proportional to $1/r$. By dimensional inspection, may rewrite Equation 2.16 as

$$\nabla^2 \phi = \frac{\phi}{\lambda_D^2} \quad (2.17)$$

where we define λ_D as the Debye length. The solution of this equation is of the form $\phi = \phi(r) \exp(-r/\lambda_D)$, implying that when $r > \lambda_D (= \sqrt{\frac{\epsilon_0 k_B T_e}{n_0 e^2}})$ the plasma effectively screens the potential from the isolated ion and the effect of the lone charge on the plasma can be essentially ignored.

We may now define the limits under which the regime of magnetohydrodynamics is valid:

- The plasma is quasi-neutral
- Disturbances occur on length scales larger than the ion gyroradius and Debye length
- Disturbances occur on timescales longer than the ion gyroperiod

Following on from the assumptions regarding the applicability of MHD, we may formulate the equations that govern the collective motion of plasma fluid elements in such a system.

2.2.2 Maxwells Equations

We begin by explicitly stating Maxwells equations

$$\begin{aligned}
\nabla \cdot \mathbf{B} &= 0 \\
\nabla \cdot \mathbf{E} &= \rho^* / \epsilon_0 \\
\nabla \times \mathbf{B} &= \mu_0 \mathbf{j} + \epsilon_0 \mu_0 \frac{\partial \mathbf{E}}{\partial t} \\
\nabla \times \mathbf{E} &= -\frac{\partial \mathbf{B}}{\partial t}
\end{aligned} \tag{2.18}$$

where \mathbf{E} and \mathbf{B} are the electric and magnetic field vectors respectively, ρ^* is the charge density, defined as $\rho^* = e(n_i - n_e)$, where n_i and n_e are the ion and electron number densities respectively, \mathbf{j} is the current density, and ϵ_0 and μ_0 are the permittivity and permeability of free space, respectively. On MHD length scales, it can be shown that $\rho^* \simeq 0$, as the plasma is overall neutrally charged, and for $v^2 \ll c^2$, $\frac{\partial \mathbf{E}}{\partial t} \ll |\nabla \times \mathbf{B}|$ and $|\mu_0 \mathbf{j}|$ (e.g., Allan and Poulter, 1992). So for MHD plasmas, Maxwells equations become

$$\begin{aligned}
\nabla \cdot \mathbf{B} &= 0 \\
\nabla \cdot \mathbf{E} &= 0 \\
\nabla \times \mathbf{B} &= \mu_0 \mathbf{j} \\
\nabla \times \mathbf{E} &= -\frac{\partial \mathbf{B}}{\partial t}.
\end{aligned} \tag{2.19}$$

2.2.3 Continuity of Mass and Momentum

For any plasma, the change in mass of a given fluid element of volume V must be equal to the surface integral of the mass flux flowing through its outer boundary S :

$$\frac{\partial}{\partial t} \int_V \rho d\tau = - \int_S \rho \mathbf{v} \cdot d\mathbf{s} = - \int_V \nabla \cdot \rho \mathbf{v} d\tau \tag{2.20}$$

where ρ is the plasma mass density and \mathbf{v} is the velocity of a MHD fluid element, and where we have applied the divergence theorem to the middle term. It therefore follows that the continuity equation for MHD plasmas is

$$\frac{\partial \rho}{\partial t} + \nabla \cdot (\rho \mathbf{v}) = 0. \tag{2.21}$$

Similarly, it can be shown (e.g., Kivelson and Russell, 1995) that conservation of momentum implies that

$$\rho \frac{d\mathbf{v}}{dt} = \mathbf{j} \times \mathbf{B} - \nabla p \quad (2.22)$$

where p is the thermal pressure. Importantly, the Lorentz $\mathbf{j} \times \mathbf{B}$ force can be rewritten as consisting of two forces: magnetic tension and magnetic pressure. Since $\mu_0 \mathbf{j} = \nabla \times \mathbf{B}$,

$$\mathbf{j} \times \mathbf{B} = \frac{(\nabla \times \mathbf{B}) \times \mathbf{B}}{\mu_0} = (\mathbf{B} \cdot \nabla) \mathbf{B} - \nabla \left(\frac{B^2}{2\mu_0} \right). \quad (2.23)$$

Here, $B^2/2\mu_0$ acts as a magnetic pressure perpendicular to \mathbf{B} , whilst $(\mathbf{B} \cdot \nabla) \mathbf{B}$ acts like tension in a stretched string to straighten any curved field lines.

2.2.4 Equation of State and Ohms Law

To close the set of MHD equations we need to consider an equation of state and the generalized Ohms law. The equation of state is given by

$$p/\rho^\gamma = \text{constant} \quad (2.24)$$

where p is the thermal plasma pressure, ρ is the plasma density and γ is a constant. For adiabatic cases, γ can be taken as 5/3.

The generalized Ohms law states that

$$\mathbf{E} + \mathbf{v} \times \mathbf{B} = \eta \mathbf{j} + \frac{\mathbf{j} \times \mathbf{B}}{n_e} - \frac{\nabla \cdot \mathbf{P}_e}{n_e} + \frac{m_e}{n_e e^2} \frac{\partial \mathbf{j}}{\partial t} \quad (2.25)$$

where $\eta = 1/\sigma$ is the plasma resistivity (σ is the plasma conductivity), m_e is the electron mass, n_e is the electron number density, and \mathbf{P}_e is the electron pressure, and is derived from the two-fluid momentum equations for a plasma. The first term on the right hand side of equation 2.25 describes the resistivity of the plasma, the second term is the Hall term, the third term represents the anisotropic electron pressure and the final term represents the time variation of the current, which may be interpreted as the effect of electron inertia on the current flow.

If we assume that the plasma is infinitely conducting, the electron pressure gradients are small and that the currents vary slowly with time, we may neglect the first, third and

last terms on the right hand side of equation 2.25. It can also be shown that for typical space plasmas, the Hall term is small enough to be neglected (see e.g., Baumjohann and Treumann, 1997), and we may write the ideal Ohms Law as

$$\mathbf{E} + \mathbf{v} \times \mathbf{B} = 0. \quad (2.26)$$

This is related to the frozen flux theorem, as it can be used to show how traveling plasma volume elements can effectively ‘transport’ magnetic field lines, and is generally a good approximation in highly conducting MHD space plasmas.

This set of MHD equations yields a wealth of features, and we now concentrate on examining the properties of MHD waves.

2.3 Waves in Cold Magnetized Plasmas

The geometry of the magnetic field in the Earth’s magnetosphere is complex, and the plasma parameters can vary in three dimensions. To illustrate the wave modes that may exist in MHD plasmas we first restrict ourselves to the simplest model of a uniform straight background magnetic field (\mathbf{B}_0) embedded in a uniform, cold, fully ionized plasma (cold implies that the fluid kinetic pressure is small compared to the magnetic pressure). We may linearize the Maxwell equations by assuming that

$$\begin{aligned} \mathbf{B} &= \mathbf{B}_0 + \mathbf{b} \\ \mathbf{E} &= \mathbf{E}_0 + \mathbf{E} \\ \mathbf{j} &= \mathbf{j}_0 + \mathbf{j} \\ \mathbf{v} &= \mathbf{v}_0 + \mathbf{v} \\ \rho &= \rho_0 + \rho \end{aligned} \quad (2.27)$$

where the subscript 0 indicates a background time independent and unperturbed quantity. For simplicity we assume that $\mathbf{E}_0 = \mathbf{v}_0 = 0$, and this linearization can be performed independent of the geometry of the plasma. The relevant Maxwell equations in this model reduce to

$$\nabla \times \mathbf{E} = -\frac{\partial \mathbf{b}}{\partial t} \quad (2.28)$$

$$\nabla \times \mathbf{b} = \mu_0 \mathbf{j} \quad (2.29)$$

where we are considering small perturbations, and \mathbf{E} , \mathbf{b} and \mathbf{j} are small perturbations in the electric field, magnetic field and current density respectively. Also, we have implicitly assumed that $\mathbf{E} = \mathbf{E}_\perp$ since $\mathbf{E}_\parallel \simeq 0$ for ideal MHD. The equation of motion in the cold plasma limit (i.e., neglecting the $-\nabla P$ term in Equation 2.22) may be written as

$$\rho_0 \frac{\partial \mathbf{v}}{\partial t} = \mathbf{j} \times \mathbf{B}_0 \quad (2.30)$$

where \mathbf{v} is a small perturbation in the velocity, \mathbf{B}_0 is the ambient magnetic field, and ρ_0 is the ambient plasma mass density.

We may now substitute Equation 2.29 into Equation 2.30 to obtain

$$\frac{\partial \mathbf{v}}{\partial t} = \frac{(\nabla \times \mathbf{b}) \times \mathbf{B}_0}{\rho_0}. \quad (2.31)$$

And now substituting Equation 2.26 into the above equation yields

$$\frac{\partial \mathbf{E}}{\partial t} = \frac{(\nabla \times \mathbf{b}) B_0^2}{\mu_0 \rho_0}. \quad (2.32)$$

Taking the derivative with respect to time on both sides gives

$$\frac{\partial^2 \mathbf{E}}{\partial t^2} = \left(\nabla \times \frac{\partial \mathbf{b}}{\partial t} \right) \frac{B_0^2}{\mu_0 \rho_0}. \quad (2.33)$$

And finally, substituting Equation 2.28 yields the wave equation

$$\frac{\partial^2 \mathbf{E}}{\partial t^2} + v_A^2 \nabla \times (\nabla \times \mathbf{E}) = 0 \quad (2.34)$$

where $v_A = B_0/(\mu_0 \rho_0)^{1/2}$ and is known as the Alfvén speed. If we specify Cartesian coordinates with the magnetic field \mathbf{B}_0 directed along the z direction (i.e., $\mathbf{B}_0 = B_0 \hat{\mathbf{z}}$), Equation 2.34 may be split into two coupled equations for the perpendicular components of \mathbf{E} , E_x and E_y (after Allan and Poulter, 1992)

$$\left(\frac{1}{v_A^2} \frac{\partial^2}{\partial t^2} - \frac{\partial^2}{\partial y^2} - \frac{\partial^2}{\partial z^2} \right) E_x = -\frac{\partial^2 E_y}{\partial x \partial y} \quad (2.35)$$

$$\left(\frac{1}{v_A^2} \frac{\partial^2}{\partial t^2} - \frac{\partial^2}{\partial x^2} - \frac{\partial^2}{\partial z^2} \right) E_y = -\frac{\partial^2 E_x}{\partial x \partial y}. \quad (2.36)$$

Examining 1-D solutions where the perturbed quantities vary in plane-wave form (i.e., $\exp[i(k_y y + k_z z - \omega t)]$), and limiting ourselves to the y and z directions due to the fact that there is no preferred perpendicular direction to \mathbf{B}_0 (so we can specify $\partial/\partial x = 0$ without a loss of generality), Equations 2.35 and 2.36 reduce to (after Allan and Poulter, 1992)

$$\omega^2/k^2 = v_A^2 \quad (2.37)$$

$$\omega^2/k_z^2 = v_A^2 \quad (2.38)$$

where $k^2 = k_y^2 + k_z^2$. Thus we have derived two dispersion relations for two separate wave modes in our simple model.

Equation 2.37 represents a wave with a phase speed of v_A and a group velocity of $\pm v_A \hat{\mathbf{k}}$, known as the fast magnetoacoustic mode ($\hat{\mathbf{k}}$ is the unit vector in the direction of the wave vector \mathbf{k}). This implies energy flow parallel to \mathbf{k} which is independent of the direction of \mathbf{k} with respect to \mathbf{B}_0 . This fast magnetoacoustic mode is compressional, and it propagates across the magnetic field by compression of that field, see e.g., Allan and Poulter (1992).

We now consider the dispersion relation in Equation 2.38. The wave described here has a phase speed of $\omega/k_z = v_A$, and propagates with a group velocity $d\omega/dk = \pm v_A \hat{\mathbf{z}}$. This wave exhibits no compression of the magnetic field (i.e., a shear wave), with energy flow along \mathbf{B}_0 only. The velocity v_A is known as the Alfvén speed, and the wave is known as the Alfvén wave, after Alfvén (1942). The wave vector, \mathbf{k} , may be at any angle to the background field, so that wavefronts are oblique to \mathbf{B}_0 , but they still propagate energy only along \mathbf{B}_0 . It can be shown that \mathbf{j} is perpendicular to \mathbf{k} , implying that an oblique Alfvén wave generates field aligned currents, which will be important in later chapters. In the current model of an infinite, uniformly magnetized cold plasma the Alfvén mode and the fast magnetoacoustic modes are uncoupled.

2.4 Waves in Warm Magnetized Plasmas

We now relax our assumption that the plasma of interest is cold, and introduce a finite equilibrium pressure, p_0 . The dispersion relation of the Alfvén mode (Equation 2.38) is unchanged, and the Alfvén mode propagates along the ambient magnetic field as before.

However, there are now two solutions to Equation 2.37, the so-called fast and slow magnetosonic modes

$$\frac{\omega^2}{k^2} = \frac{c_s^2 + v_A^2}{2} \left(1 \pm \sqrt{1 - \frac{4c_s^2 v_A^2 \cos^2 \theta}{(c_s^2 + v_A^2)^2}} \right) \quad (2.39)$$

where θ is the angle between the wave vector, \mathbf{k} , and the ambient field, \mathbf{B}_0 , so that $k_y = \sin \theta$ and $k_z = \cos \theta$. If we first look at propagation along the magnetic field, i.e., $\theta = 0$, then the two solutions to Equation 2.39 become

$$\omega^2/k^2 = v_A^2 \quad (2.40)$$

and

$$\omega^2/k^2 = c_s^2 \quad (2.41)$$

Hence in a warm magnetized plasma we may expect fast mode and slow mode propagation in the field-aligned direction with phase speeds of v_A and c_s , respectively. However, if we examine the case where $\theta \simeq 90^\circ$ (i.e., $\cos^2 \theta \simeq 0$), which is the case for propagation perpendicular to the magnetic field, Equations 2.40 and 2.41 become, respectively,

$$\omega^2/k^2 \simeq c_s^2 + v_A^2 \quad (2.42)$$

and

$$\frac{\omega^2}{k_z^2} \simeq \frac{c_s^2 v_A^2}{c_s^2 + v_A^2}. \quad (2.43)$$

Hence for near perpendicular propagation, the fast mode has a phase and group speed $\simeq \sqrt{(v_A^2 + c_s^2)}$, whilst the slow mode has very small group speed perpendicular to \mathbf{B}_0 , the group speed being the so-called cusp speed. The slow magnetosonic mode is similar to the Alfvén mode in that the energy flow is predominantly directed along the magnetic field. The fast magnetosonic mode is similar to the fast mode in the cold plasma case, except that the phase speed of this mode is slightly greater than v_A for $\theta \neq 0$. The fast mode can propagate in the direction perpendicular to the magnetic field, and it is also important to note that in the uniform plasma model considered so far, the two magnetosonic modes are decoupled from the Alfvén mode.

2.5 Mode Conversion and Field Line Resonance

Thus far we have considered cold and warm homogeneous plasmas. In reality, a plasma will have a finite extent, so that boundary conditions become important, and it may also contain plasma density or magnetic field variations, so that the Alfvén speed varies across the plasma.

We now consider a simple model of the closed dipolar magnetic field close to the Earth where the curvature of magnetic field lines is neglected. In this case we may reduce the problem to that of a ‘box model magnetosphere’, first developed by Southwood (1974) (see Figure 2.1). The upper and lower boundaries of the box correspond to the northern and southern ionospheric footprints of magnetic field lines, respectively, and the boundaries at the left and right of the box correspond to the magnetopause and the low-latitude ionosphere, respectively. The magnetic field strength in the box is assumed to be constant, B_0 , and the field lines have constant length so that the variation of field line eigenfrequency is dictated purely by the plasma density. We then impose that the Alfvén speed, v_A , varies monotonically with x .

If we assume that the ionospheric conductivity is high, the electric field and wave displacement of any driven Alfvén wave must disappear there (i.e., the wave is reflected), and resonance may occur. However, this reflection condition may only be satisfied for quantized field-aligned wavelengths, in analogy to standing waves on a stretched string. If the length of a magnetic field line is given by l , the Alfvén speed is constant along the field line and the wavelength in the field-aligned direction is λ_{\parallel} , the allowed wavelengths are given by

$$\lambda_{\parallel} = 2l/n \quad (2.44)$$

where n is an integer. For a shear Alfvén wave, we recall that the parallel wavenumber is given by $k_{\parallel} = k \cos \theta = 2\pi/\lambda_{\parallel}$ which yields

$$\omega = v_A k_{\parallel} = \frac{v_A 2\pi}{\lambda_{\parallel}} \quad (2.45)$$

and so we can now express the allowed frequencies of a given field line as

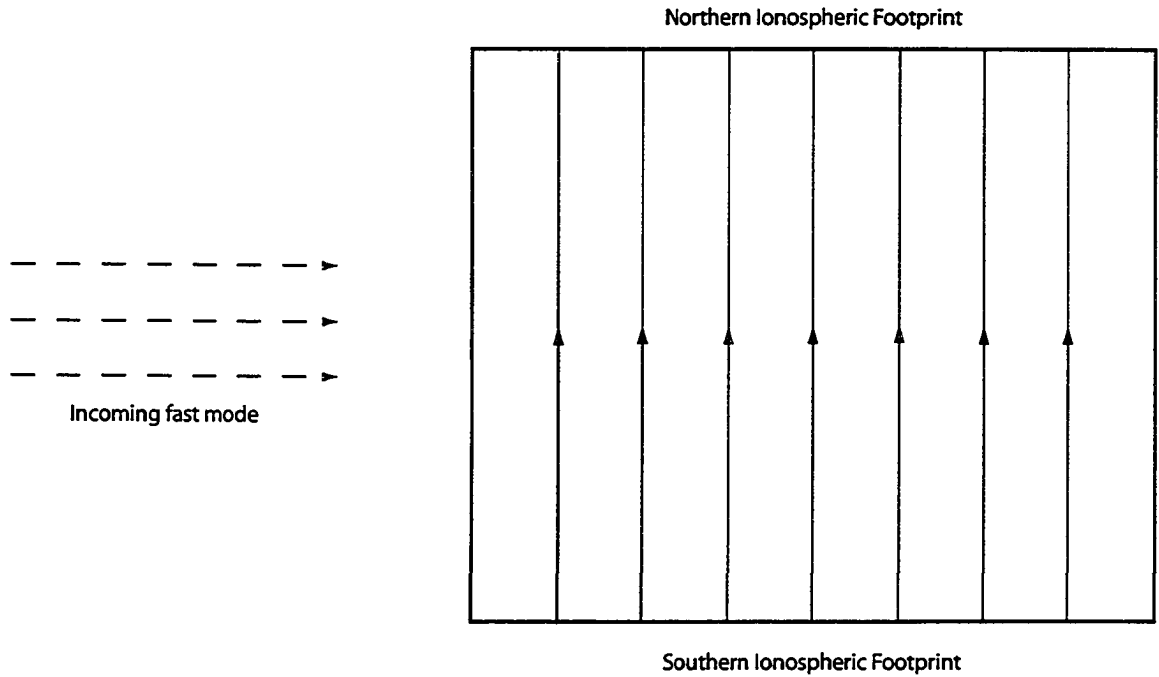


Figure 2.1: Schematic of box model for dipolar field lines. Solid arrows represent magnetic field, B_0 , which is uniform across the box, and dashed lines represent the incident fast mode wave.

$$f = \frac{nv_A}{2l} = \frac{nB_0}{2l\sqrt{\mu_0\rho_0}}. \quad (2.46)$$

Standing resonant Alfvén waves may be excited on magnetic field lines where a driving fast mode frequency equals one of these allowed frequencies (standing Alfvén wave eigenfrequencies), and the field line may be said to be in driven field line resonance (FLR).

We now approach this phenomenon from the standpoint of the wave equation and follow the treatment of Allan and Poulter (1992). We now assume that the wave electric field varies as

$$E_x(x, y, z, t) = E_x(x) \exp[i(k_y y + k_z z - \omega t)] \quad (2.47)$$

and

$$E_y(x, y, z, t) = E_y(x) \exp[i(k_y y + k_z z - \omega t)], \quad (2.48)$$

and hence the two wave equations (2.35 & 2.36) then become

$$(K^2 - k_y^2 - k_z^2)E_x = ik_y \frac{dE_y}{dx} \quad (2.49)$$

and

$$(K^2 - k_z^2) E_y = ik_y \frac{dE_x}{dx} - \frac{d^2 E_y}{dx^2} \quad (2.50)$$

where E_x and E_y are functions of x and $K^2 = \omega^2/v_A(x)$, which varies monotonically with respect to the x -direction.

If we now assume that $k_y = 0$, then Equations 2.49 and 2.50 decouple, and Equation 2.50 reduces to

$$(K^2 - k_z^2) E_y = -\frac{d^2 E_y}{dx^2}. \quad (2.51)$$

Now, since k_z is constant, then E_y must have a turning point when $K^2 = k_z^2$, i.e., at $x = x_r$ where x_r is some critical value of x . At $x = x_r$, the solutions to the equation change from oscillatory to evanescent in space. So physically, we may expect fast mode waves characterised by E_y and propagating Earthwards to reflect at some point x_r , with an evanescent component of the wave being transmitted beyond x_r . If the wave reflects from an outer boundary of x , say at the magnetopause, then fast mode waves with radially standing structure between the outer boundary and x_r may be created. Standing Alfvén wave modes derived from Equation 2.49 and polarised with E_x will be excited where $K^2 - k_z^2 = 0$. However, in this $k_y = 0$ case both modes are decoupled.

We now look at the more general case where $k_y \neq 0$. We may combine Equations 2.49 and 2.50 to obtain

$$\frac{d^2 E_y}{dx^2} - C \frac{dE_y}{dx} + (K^2 - k_y^2 - k_z^2) E_y = 0 \quad (2.52)$$

where

$$C = \frac{k_y^2}{(K^2 - k_z^2)(K^2 - k_y^2 - k_z^2)} \frac{dK^2}{dx}. \quad (2.53)$$

Equation 2.52 also has a turning point, this time the turning point x_r being approximately located where $K^2 - k_y^2 - k_z^2 = 0$. There is also a resonance at the position $x = x_c$, defined by $K^2 = k_z^2$. It can be shown that x_c represents the position where the fast mode phase

velocity in the field aligned direction equals the Alfvén phase velocity, so that the fast mode drives field line resonant Alfvén waves with frequencies defined by $K^2 = k_z^2$ at this point.

This mechanism, known as field line resonance (FLR), represents a major form of energy transport in the magnetosphere. Fast mode waves excited at the magnetopause can propagate across the background magnetic field, and produce field line resonant Alfvén waves in the region where the fast mode waves become evanescent. Since field line resonant Alfvén waves carry field aligned currents then they can transfer energy into the ionosphere via Joule heating, or electron precipitation (see Section 2.8). Figure 2.2 shows two fast mode waves with different values of k_y coupling to Alfvén waves in a dipole box model magnetosphere. Fast mode 1 has a smaller value of k_y , and so penetrates deeper into the magnetosphere. This in turn leads to the mode conversion point x_{c1} being close to the reflection point x_{r1} , so that the fast mode wave still contains an appreciable amount of energy to drive standing Alfvén waves. However, fast mode 2 has a larger value of k_y , so that the coupling point x_{c2} is far from the reflection point x_{r2} and the driven Alfvén waves are of a much lower amplitude. The above treatment of waves in cold and warm magnetized plasmas is a summary of work presented by Allan and Poulter (1992).

As one may expect, the obvious ground signature of field line resonance predicted by this model would be periodic oscillations in the magnetic field at the frequency of the fast mode driver. The resonant field line would exhibit the maximum amplitude of oscillation, with the amplitude decreasing as one moves away (northward or southward) from the resonance. A full discussion of the characteristics of field line resonance can be found in e.g., Allan and Poulter (1992). Mode conversion in this geometry always produces Alfvén wave FLRs that oscillate predominantly in the toroidal sense.

Following on from the box model of closed dipolar magnetic field lines, Allan and Wright (1998) and Wright *et al.* (1999) investigated the properties of a box model geometry that approximated the magnetotail. Figure 2.3 displays the morphology of the magnetotail waveguide; the northern and southern boundaries correspond to the northern and southern magnetopause, and the model assumes a source of fast mode waves in the tail. The area of interest is the coupling between fast modes and Alfvén modes, and how a plasma density gradient that realistically models the plasmashield, plasmashield boundary layer (PSBL) and lobes affects Alfvén mode production and propagation.

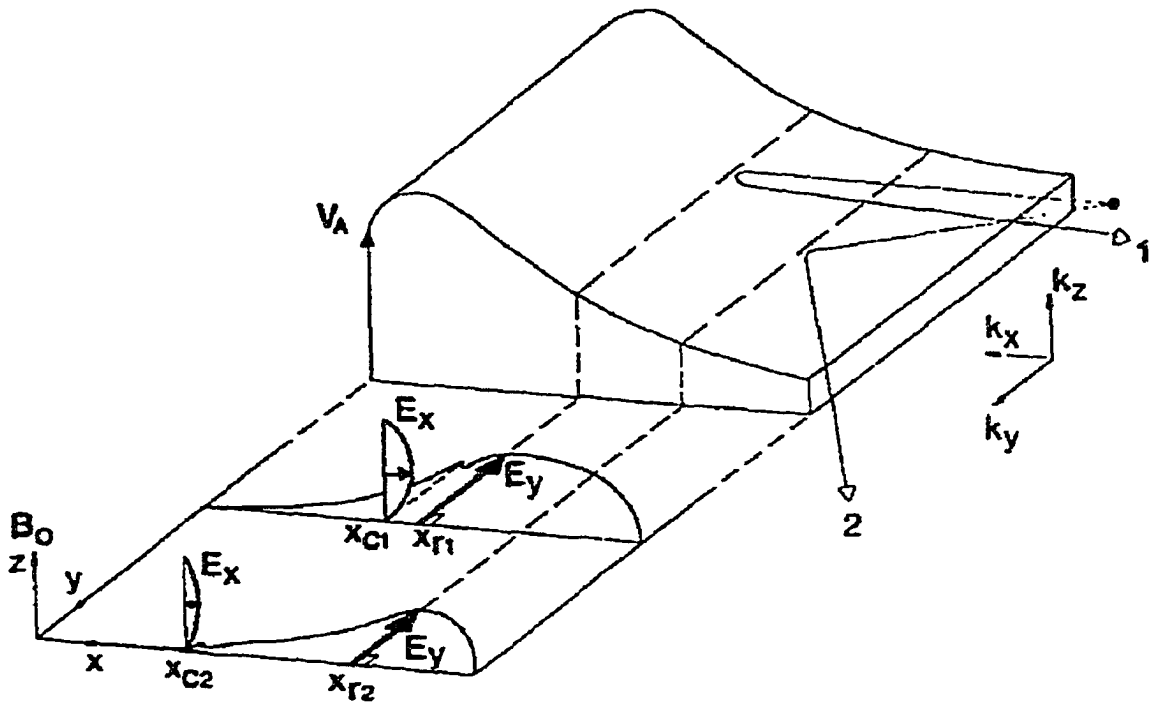


Figure 2.2: Taken from Allan and Poulter (1992). Schematic showing two fast mode waves (numbered 1 and 2) with differing values of k_y and different discrete frequencies propagating into the magnetosphere and reflecting at points x_{r1} and x_{r2} . The two fast mode waves drive field line resonant standing Alfvén waves at points x_{c1} and x_{c2} .

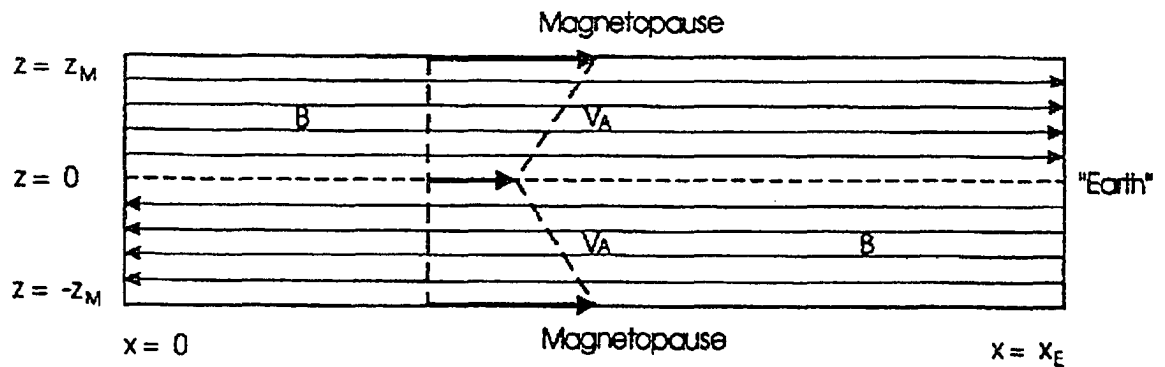


Figure 2.3: Schematic of box model for magnetotail, after Wright *et al.* (1999).

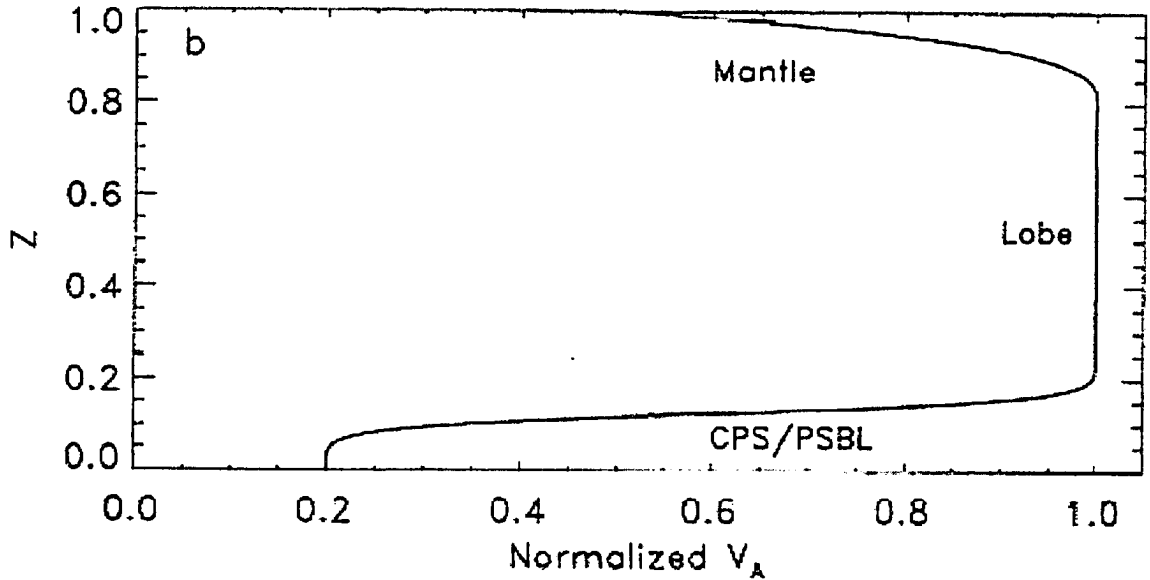


Figure 2.4: Alfvén speed profile in the z direction used by Wright *et al.* (1999). Preferentially, traveling Alfvén waves are excited in the region of large Alfvén speed gradient in the region that represents the PSBL.

Wright *et al.* (1999) found that in this geometry, fast mode waves can develop discrete frequencies by standing between turning points separated vertically across the tail. These fast modes which propagate Earthwards in the magnetotail with group velocities much less than the local Alfvén speed can mode convert and resonantly drive Alfvén waves on field lines in the PSBL. The Alfvén speed gradient (see Figure 2.4) dictates that Alfvén waves on the most northern auroral field lines have a shorter propagation time to the ionosphere than those on the southern field lines, so that any FAC structure at the ionosphere that is produced by the Alfvén waves will be evident at higher latitudes first, and then subsequent lower latitudes. This mechanism is believed to be responsible for some equatorward propagating auroral features.

2.6 Driving Mechanisms For Field Line Resonances

There are two different oscillatory modes for Alfvénic field line resonance and these are believed to be driven via two distinct mechanisms: i) Toroidal mode oscillations are believed to be driven by external energy sources in the solar wind and via mode conversion from

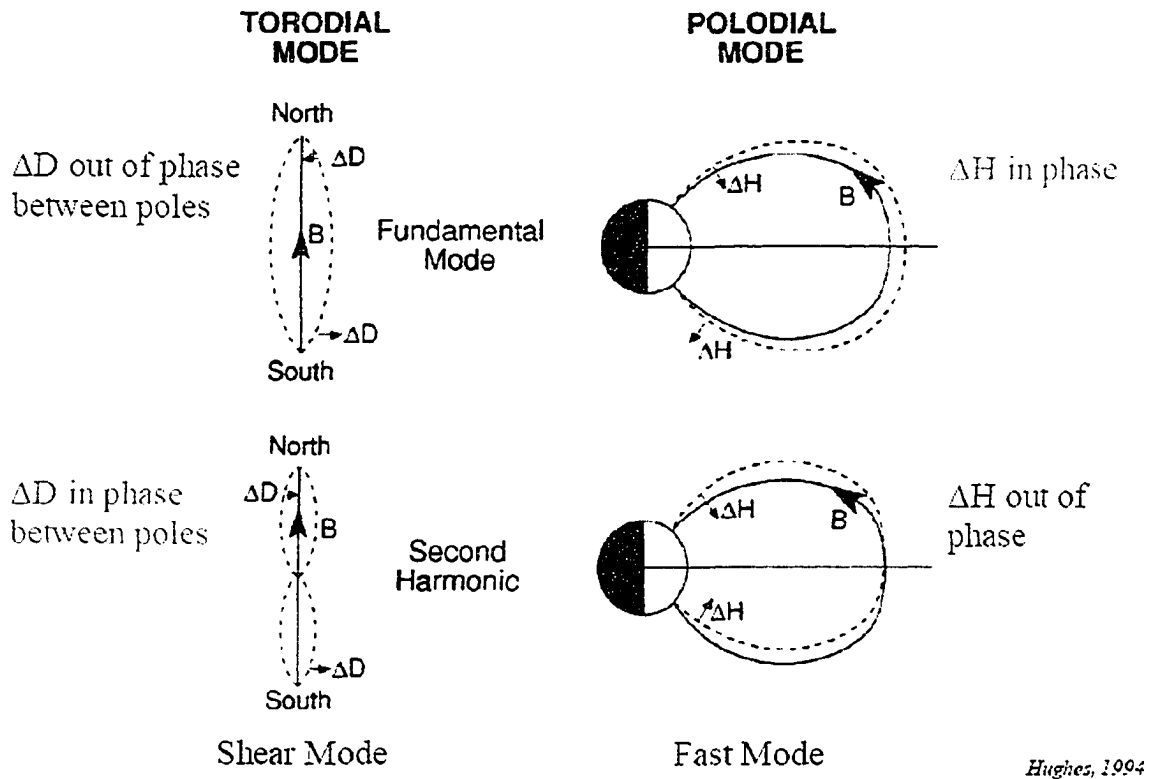


Figure 2.5: Representations of fundamental and second harmonic toroidal and poloidal field line resonance perturbations. ΔH and ΔD represent magnetic oscillations in the radial and azimuthal directions in the magnetosphere respectively. Taken from Hughes (1994).

fast mode waves to Alfvén waves, ii) Poloidal oscillations are believed to be driven by the free energy in ion distribution functions by wave-particle interactions. Physically, toroidal mode velocity and magnetic field oscillations are orientated azimuthally in a dipole field, with perturbations confined to shells of the dipole. Poloidal velocity oscillations are radial in a dipole field, so that these oscillations are often referred to as a “breathing mode”. Figure 2.5 displays a diagrammatic representation of the toroidal and poloidal modes of field line resonance

2.6.1 Poloidal Mode Field Line Resonance

The suggestion that energetic particles in the Earth's magnetosphere could transfer energy into field line resonances was first made by Southwood *et al.* (1969). They showed how ring current particles have to satisfy two criteria for poloidal FLRs to be produced, namely that

the resonance condition had to be satisfied, and that the particles that satisfy the resonance condition have to exhibit a positive gradient in their energy distribution.

The general resonance condition [Southwood *et al.*, 1969] is given by

$$\omega - m\omega_d = N\omega_b \quad (2.54)$$

where ω is the frequency of the FLR being driven, ω_d and ω_b are the drift and bounce frequencies of the particles, respectively, m is the azimuthal wavenumber of the wave, and N is an integer that represents the harmonic of the bounce resonance. For energy transfer to occur, the particles satisfying the above resonance condition must be in an unstable part of the overall particle energy distribution.

We have previously shown how particles in dipolar magnetic fields exhibit gyromotion, mirror motion and gradient-curvature and $\mathbf{E} \times \mathbf{B}$ drifts. Figure 2.6 schematically represents a particle drifting and mirroring in the magnetosphere in the rest frame of a standing Alfvén wave. Plus and minus signs represent the sign of the wave electric field, and the density of the symbols represents the magnitude of the electric field (from Ozeke, 2002).

A drifting and mirroring proton moving in the rest frame of a standing Alfvén wave may be accelerated or decelerated by the wave. The top panel of Figure 2.6 represents an ion drifting with respect to a second harmonic field line resonance, with the solid line representing an ion in $N=1$ resonance with the wave, and the dashed line representing an ion still in $N=1$ resonance, but 180° out of phase with the first particle. The ion on the solid line trajectory experiences a large positive and no negative electric field as it propagates through the wave field. Thus the ion is slowed, and some of its energy is transferred to the wave (usually increasing the wave amplitude). Conversely, the dashed line trajectory ion is accelerated by the wave, as it experiences predominantly large negative electric fields. Thus the wave does work on the particle and the wave is damped.

For a drift ($N=0$) resonance (middle panel of Figure 2.6), the particle drifts azimuthally with the same phase speed as the fundamental field-aligned harmonic wave, so that the azimuthal electric field it encounters is always of the same sign. Along the particle's trajectory it is accelerated (or decelerated) as it encounters the poloidal wave's azimuthal electric field, removing energy from (or giving energy to) the FLR through interaction with the particle's drift motion.

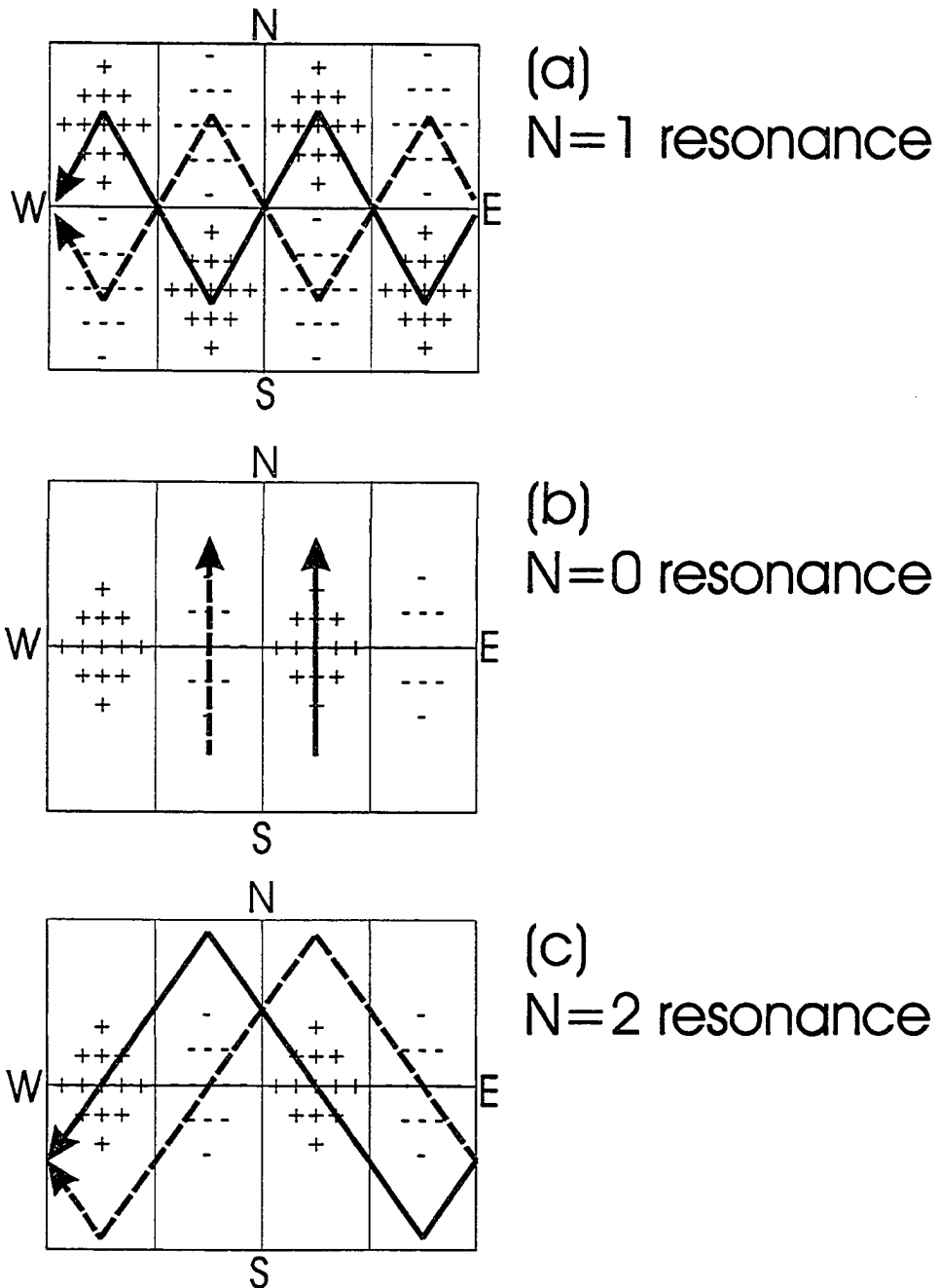


Figure 2.6: Schematic representation of three trajectories of drift-bounce motion of protons in the rest frame of a FLR. The schematic shows a box model geometry where the magnetic field lines are directed vertically from the southern to northern hemisphere. The electric field perturbations of a standing Alfvén wave are represented by plus and minus signs, the density of the symbols reflecting the magnitude of the electric field. Solid and dashed arrowed lines represent the trajectories of the guiding centers of mirroring and drifting protons in the rest frame of the wave. Taken from Ozeke (2002).

The bottom panel of Figure 2.6 displays an N=2 resonance with a fundamental mode field line resonance, with the solid line representing an ion that would amplify the wave oscillation, and the dashed line representing an ion that would damp the wave. The ion represented by the solid line experiences large positive and small negative electric fields, so that it transfers energy to the wave. Conversely, the ion represented by the dashed line experiences large negative and small positive electric fields, so that it damps the wave.

Southwood and Hughes (1982) showed that the rate of energy change of a charged particle moving through a small amplitude hydromagnetic wave is given by

$$\dot{W} = \mu \frac{\partial b_{\parallel}}{\partial t} + q\mathbf{E} \cdot \mathbf{v}_d + qE_{\parallel}v_{\parallel} \quad (2.55)$$

where μ is the magnetic dipole moment, \mathbf{v}_d is the drift velocity of a particle and the subscript \parallel represents variations in the direction parallel to the background magnetic field.

Poloidal Alfvénic oscillations have no compressional component and exhibit electric field perturbations in the particle drift direction. Hence poloidal mode oscillations can be excited only by azimuthally drifting particles in a dipolar background magnetic field geometry in an MHD ($E_{\parallel} = 0$) plasma. The rate of energy transferred in that case is

$$\dot{W} = qE_{\phi}v_d. \quad (2.56)$$

2.6.2 Toroidal Mode Field Line Resonance

At least three mechanisms have been identified as driving mechanisms for toroidal mode field line resonance, including impulses from the solar wind [e.g., Allan *et al.*, 1986; Wright, 1994], Kelvin-Helmholtz instabilities on the magnetopause at the flanks of the magnetosphere [Southwood, 1974; Chen and Hasegawa, 1974; Kivelson and Pu, 1984; Kivelson and Southwood, 1985; Kivelson and Southwood, 1986; Mann *et al.*, 2002] and direct driving from the solar wind [Allan and Poulter, 1992]. Large density and/or velocity steps in the solar wind (caused by e.g., interplanetary coronal mass ejections) may impart a shock onto the magnetosphere, and cause global fast mode waves to propagate earthwards. Due to the shape of the magnetosphere, the waves behave as if they were in a cavity and discrete frequency global fast mode harmonics may be established [e.g., Kivelson and Pu,

1984]. These may then couple to Alfvén waves on closed field lines where the fast mode frequency equals the local Alfvén eigenfrequency, and field line resonance can occur.

The solar wind may also cause a surface mode Kelvin-Helmholtz instability on the magnetopause on the flanks of the magnetosphere, analogous to wind causing ripples on a lake, which can cause fast mode waves to propagate through the magnetosphere. These fast mode waves will have a turning point close to the Earth; outside of this point the fast modes are reflected and inside they are evanescent. In the simple box model, FLRs are driven at points where the fast mode waves are evanescent.

Directly driven FLRs are believed to be caused by upstream waves in the solar wind. These waves can cause the magnetosphere to oscillate at the frequency of the solar wind driver, which in turn can drive fast mode waves Earthwards. This mechanism allows the excitation of fast mode frequencies that are not the same as the cavity eigenfrequencies which are usually observed in the discontinuity/waveguide process.

Figure 2.7 pictorially displays the sources of MHD waves in the magnetosphere.

2.7 Effects of the Ionosphere on the Observation of Geomagnetic Pulsations

Thus far we have assumed that the ionosphere is an infinitely thin and perfectly conducting medium, so that magnetic field lines are ‘rooted’ into the ionospheric plasma. If we relax this assumption and assume a finite ionospheric conductivity, and consider standing Alfvén waves with phase fronts that are oblique to the ionosphere, we may investigate the transmitted magnetic signal that we expect to observe with ground-based magnetometers. Such a standing wave will support a finite field aligned current, j_z , that will close with an oppositely directed field aligned current via a Pedersen current in the ionosphere (see Figure 2.8). This Pedersen current will have an associated electric field, which will in turn generate an ionospheric Hall current. In the absence of conductivity gradients in the ionosphere, the system of the two field aligned currents and the Pedersen current is approximately solenoidal, so that little magnetic signature of the system is observed on the ground. However, the Hall current will generate an associated magnetic field, and it is this magnetic field that is routinely observed by ground-based magnetometers. Thus the effect

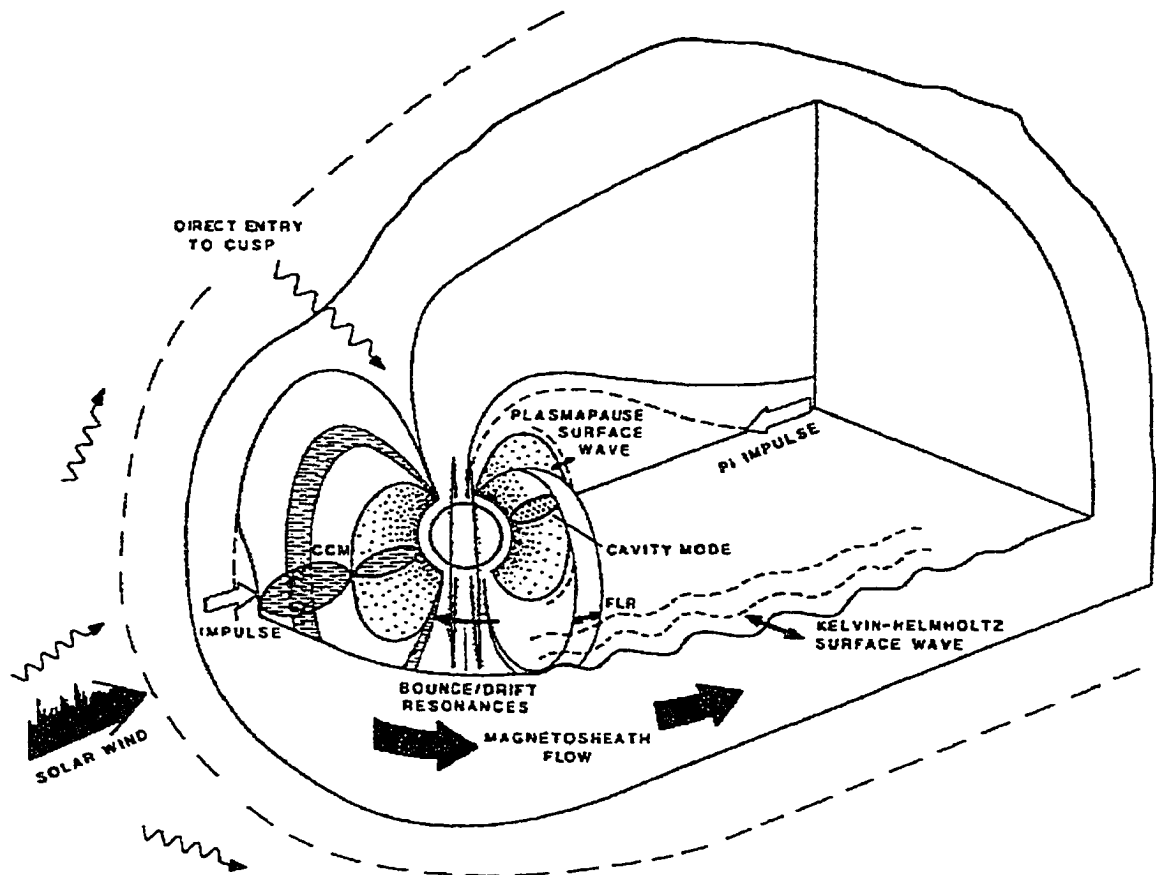


Figure 2.7: Diagram of the magnetosphere illustrating sources of waves in the magnetosphere. From Allan and Poulter (1992).

structure of oppositely directed small scale Hall currents generates a ground magnetic field of very small amplitude. Waves in the magnetosphere with large spatial sizes induce large scale Hall currents in the ionosphere, and ground-based magnetometers are able to resolve the induced magnetic fields due to these waves. For a full discussion of the screening of small scale geomagnetic pulsations by the ionosphere see, e.g., Hughes and Southwood (1976b).

2.8 Electron Acceleration by Alfvén Waves

So far we have assumed that the MHD approximations hold when discussing standing Alfvén waves. However, to explain some auroral phenomena that have been observationally linked to FLR (see e.g., Samson *et al.*, 1991; Samson *et al.*, 1996; Milan *et al.*, 2001) we need to consider the form of the Alfvén mode at heights that correspond to the auroral acceleration region. It can be shown [see e.g., Lysak and Lotko, 2002 and Appendix A of this thesis] that by considering Faradays law and the generalized Ohms law the time derivative of the parallel electric field in a plasma with a magnetic field orientated along the z direction can be written as

$$\frac{\partial E_z}{\partial t} = \frac{m_e}{ne^2} \frac{\partial^2 j_z}{\partial t^2} - \frac{T_e}{ne^2} \frac{\partial^2 j_z}{\partial z^2}. \quad (2.57)$$

where we have assumed an isotropic electron pressure in the plasma and that electrons carry any currents in the direction parallel to the local magnetic field. The smaller inertia of the electrons in the plasma means that they will respond more quickly to any small scale wave driven parallel electric fields, whereas the larger gyroradius of the ions in the plasma means that they will carry any perpendicular currents due to the Alfvén waves. Under these assumptions it can be shown [see e.g., Lysak and Lotko, 2002 and Appendix A of this thesis] that the wave equation in the limit where the wave scale size is of the same order of magnitude as the electron skin depth (defined by $\lambda_e = c/\omega_{pe}$) and/or the ion acoustic gyroradius (defined by $\rho_s = c\lambda_D/v_A$) can be written as

$$\frac{\partial^2 \mathbf{b}}{\partial t^2} = v_A^2 \frac{\partial^2 \mathbf{b}}{\partial z^2} + \frac{c^2}{\omega_{pe}^2} \frac{\partial^2}{\partial t^2} (\nabla_{\perp}^2 \mathbf{b}) - c^2 \lambda_D^2 \frac{\partial^2}{\partial z^2} (\nabla_{\perp}^2 \mathbf{b}) \quad (2.58)$$

where ω_{pe} is the electron plasma frequency and λ_D is the Debye length. The corresponding

dispersion relation can be shown to be [e.g., Lysak and Lotko, 2002 and Appendix A of this thesis]

$$\omega^2 = v_A^2 k_{\parallel}^2 \left(\frac{1 + \frac{c^2 \lambda_D^2}{v_A^2} k_{\perp}^2}{1 + \frac{c^2}{\omega_{pe}^2} k_{\perp}^2} \right). \quad (2.59)$$

By considering the equation of motion of the plasma it can be shown that the relationships between the wave velocity, \mathbf{v} , the wave magnetic field, \mathbf{b} , and the wave electric field, \mathbf{E}_{\perp} , can be written as

$$\mathbf{v} = \mp \sqrt{\frac{1 + k_{\perp}^2 \lambda_e^2}{1 + k_{\perp}^2 \rho_s^2}} \frac{\mathbf{b}}{\sqrt{\mu_0 \rho}} \quad (2.60)$$

and

$$\mathbf{E}_{\perp} = \pm v_A \sqrt{\frac{1 + k_{\perp}^2 \lambda_e^2}{1 + k_{\perp}^2 \rho_s^2}} \mathbf{b} \times \hat{\mathbf{b}} \quad (2.61)$$

where $\lambda_e = c/\omega_{pe}$ is the electron inertial length and $\rho_s = c\lambda_D/v_A$ is the ion acoustic gyroradius. We may now rearrange Equation 2.61 and substitute \mathbf{b} into Amperes law. The relationship between the wave magnetic and electric field may be written as

$$\mathbf{b} = \pm \frac{\mathbf{E}_{\perp} \times \hat{\mathbf{b}}}{v_A \sqrt{\frac{1 + k_{\perp}^2 \lambda_e^2}{1 + k_{\perp}^2 \rho_s^2}}} \quad (2.62)$$

which then yields

$$j_z = \mp \frac{\nabla_{\perp} \cdot \mathbf{E}_{\perp}}{\mu_0 v_A \sqrt{\frac{1 + k_{\perp}^2 \lambda_e^2}{1 + k_{\perp}^2 \rho_s^2}}}. \quad (2.63)$$

Finally we may Fourier analyze Equation 2.57 and substitute in the expression for j_z above to give the parallel electric field in this regime

$$E_z = \pm \left(\rho_s^2 - \lambda_e^2 \frac{1 + k_{\perp}^2 \lambda_e^2}{1 + k_{\perp}^2 \rho_s^2} \right) \frac{\partial}{\partial z} (\nabla_{\perp} \cdot \mathbf{E}_{\perp}). \quad (2.64)$$

For a full derivation of the equations governing the properties of kinetic Alfvén waves, see Appendix B.

Equation 2.64 states that in the limit where ρ_s and λ_e are small compared to the Alfvén wave perpendicular scale size, the parallel electric field of the wave becomes small. Equation 2.64 also shows that there are two competing effects that produce a parallel electric field, due to the two terms of opposite sign on the right hand side of the equation. The direction of the parallel electric field is determined by which term in Equation 2.64 dominates, the two limits being known as the electron inertial limit (when λ_e dominates) and the electron pressure limit (when ρ_s dominates). Lysak and Carlson (1981) showed that on auroral field lines the electron inertial limit is valid for altitudes of below 4-5 R_E , and that above these altitudes the effects of finite electron pressure dominate. Thus, in either regime, we expect Alfvén waves with small perpendicular scale sizes to have an associated parallel electric field. This implies that any source mechanism that produces small scale Alfvén waves on auroral field lines could be responsible for the acceleration of charged particles, and thus the production of discrete auroral features. In this way, Alfvén waves can be a significant mechanism of energy transport between the distant magnetospheric plasma and near-Earth space [e.g., Wygant *et al.*, 2000; Keiling *et al.*, 2001; Wygant *et al.*, 2002].

Thus far we have not discussed the possible production mechanisms for kinetic Alfvén waves. Hasegawa (1976) showed that the wave equation for MHD surface waves includes a term that describes mode conversion from the surface wave to Alfvén waves; the scale size of which is determined by the density gradient at the surface layer. Wygant *et al.* (2002) suggest that traveling Alfvén waves in the PSBL can act as surface waves, and may be responsible for small scale Alfvén wave structure in the PS/PSBL. The signature of such coupled waves would be a large scale Alfvénic ULF-type oscillation with superimposed small scale structure. This mechanism would allow for energy transfer from the deep magnetotail to auroral arc structures in the ionosphere. Lysak and Song (2003) argue that density gradients in the perpendicular direction in the PSBL can cause linear phase mixing, which in turn produces small perpendicular scale sizes. The resulting wave scale size is dependent on the scale of the density structures in the PSBL region, which can be of the same order as λ_e or ρ_s , and so this process is also able to produce kinetic Alfvén waves with appreciable parallel electric fields and hence mediate parallel particle energization.

2.9 Auroral Emissions

Auroral emissions are caused by energetic particles or photons colliding with particles in the Earth's ionosphere. These collisions give rise to excited atomic states that decay to their unexcited state via the emission of light. It is this emitted light that we observe on the ground and in space that is known as the aurora. Figure 2.9 shows three 'forbidden' transitions of the oxygen atom that produce the auroral red, green and UV lines. The lifetime of the auroral red line is an order of magnitude larger than the lifetime of the green line, so that red line auroras tend to be more diffuse, as the excited oxygen atoms have more time to move away from the collision region in the atmosphere. The emission heights for these transitions are approximately 110 km for the auroral green line and 250 km for the red line [e.g., Kivelson and Russell, 1995]. This is due to the fact that below these cut-off heights the excited oxygen atoms are quenched via collisional de-excitation due to the larger atmospheric number density [e.g., Kivelson and Russell, 1995].

The auroral red line is caused by particles of energy $\lesssim 1$ keV colliding and exciting oxygen, whereas the green line is caused by more energetic particles (energy > 1 keV). So we may expect the auroral red line emission to be nearly always present, as low energy particles from the plasmashet continuously get scattered into the loss cone and collide with the Earth's atmosphere, which in turn leads to a more diffuse aurora. Indeed, it is believed that the poleward boundary of the auroral red line emission is a proxy for the location of the open-close field line boundary, as this polewards edge maps to the edge of the plasmashet in the magnetosphere (see, e.g., de la Beaujardiere *et al.*, 1994). The more energetic particles that cause the green line, however, must have some discrete production mechanism in the magnetosphere (e.g., substorm processes, particle acceleration by Alfvén waves or other mechanisms) as particles must, in general, be accelerated by some mechanism in order to reach energies of greater than 1 keV.

Other auroral emission lines of major importance are the hydrogen emissions, H_α and H_β [e.g., Kivelson and Russell, 1995]. These emission lines occur when a proton from the magnetosphere collides with the Earth's atmosphere and captures an electron to form an excited hydrogen atom. This atom then returns to its ground state via the emission of a photon. By measuring the Doppler shift of the H_α and H_β lines one can infer the velocity

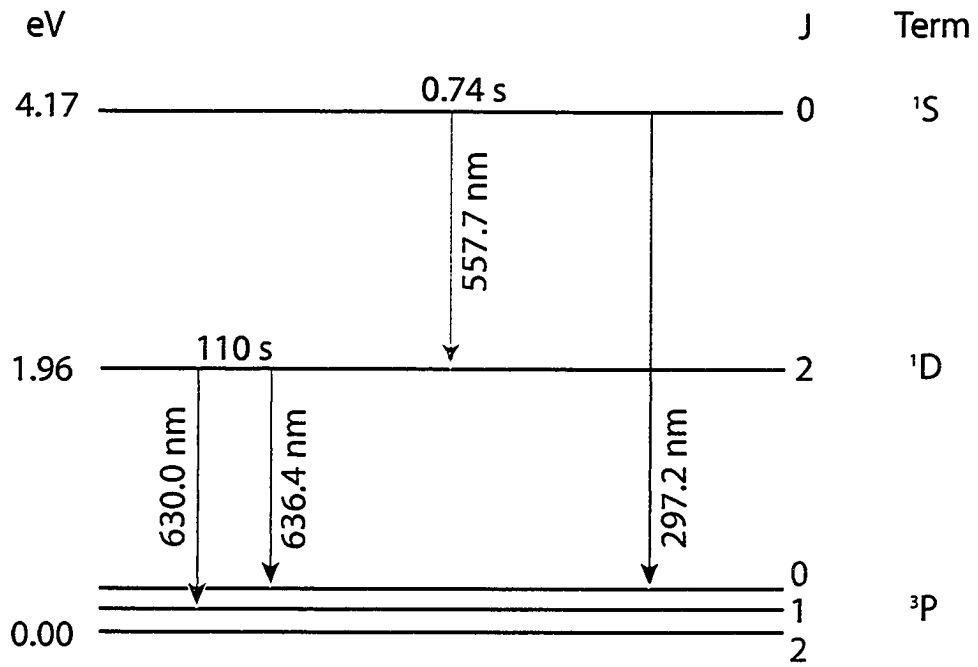


Figure 2.9: Excited oxygen states that give rise to auroral emissions. Included are the green line (557.7 nm), red line (630.0 nm) and UV line (297.2 nm), with the energies of the transitions and their respective lifetimes.

and hence energy of the initial proton, and hence determine from which particle population it originated.

Chapter 3

Instrumentation and Analysis Techniques

In this chapter we aim to put the wealth of ground-based and satellite instrumentation into the context of the research in the later chapters of this thesis. We present brief descriptions of ground-based magnetometers, coherent scatter radars, incoherent scatter radars and optical instrumentation as well as an overview of the Polar and ACE satellites.

3.1 Ground-Based Magnetometers

When trying to measure magnetospheric D.C. magnetic fields, the most commonly used ground-based instrument is the fluxgate magnetometer, which was invented by Aschenbrenner and Goubau in 1936. Fluxgates consist of two high permeability ring shaped cores aligned along a common axis with a driver current winding per ring and a single secondary coil used to detect the output. The high frequency (~ 5 kHz) alternating current of the driver windings are chosen to be equal and opposite, and the permeability of the core is chosen as to drive the cores into saturation every half A.C. cycle. For zero external field, the two coils produce equal and opposite effects in the secondary coil, producing zero output. For a non-zero external field, the secondary coil detects even harmonics of the input frequency, with odd harmonics still canceling. The second harmonic is usually amplified, and the resultant voltage is proportional to the field along the axis through the center of the rings. In ground-based fluxgates, three mutually orthogonal sensors are used to collect information about the vector geomagnetic field, usually in the geographic north-south (X) and east-west (Y) directions, and the vertical (Z) direction.

The International Monitor for Auroral Geomagnetic Effects (IMAGE) magnetometer network [Viljanen and Hakkinen, 1997] ranges from 75° to 55° in magnetic latitude ($L \sim 3.3$ to 15.5) and from 90° to 115° in magnetic longitude. It comprises 27 fluxgate magnetometers (as of November 2003), located in Norway, Sweden, Finland, Russia and Estonia (see Figure 3.1 and Table 3.1). The magnetometers are maintained by ten institutes from Estonia, Finland, Germany, Norway, Poland, Russia and Sweden. Each magnetometer measures magnetic field strength at a temporal resolution of ten seconds with an accuracy of 1 nT (0.1 nT at permanent stations), and the baselines of the instruments are continually checked for any obvious errors. The data are collected in X, Y, Z geographic coordinates and for the analysis in this thesis are then rotated into a magnetic H, D, Z coordinate system, where H and D point in the local magnetic north-south and east-west directions respectively, with Z remaining in the direction of the local vertical.

Latitudinal arrays of magnetometers allow the latitudinal power and phase profiles of field line resonances to be investigated. The magnitude of spectral peaks produced when a fast Fourier transform (FFT) of a wavepacket is performed allow us to determine the L-shell on which the resonance occurred (the station which has the largest amplitude of oscillation), and Fourier phase allows us to investigate the predicted 180° phase change that should occur as one moves across a resonance in latitude. Longitudinally spaced magnetometers that lie on a similar latitude allow us to calculate the azimuthal wavenumber, m , of an FLR, although ionospheric screening makes this process difficult for large- m waves (i.e., waves with small spatial sizes) [e.g., Hughes and Southwood, 1976b].

Magnetometer data often exhibit long-period variations, which can mask any pulsation activity that may be superimposed. For this reason, the time series are often filtered, and the technique employed here is to use a bandpass filter to remove high and low frequency components that lie outside a specified frequency range. This is performed by convolving each point in the raw timeseries with a filter kernel. The kernel contains a number of terms, and a weighting for each term. As it is applied to each data point, the shape of the kernel controls which frequencies are removed from the timeseries, so that the resulting array of data contains the bandpass filtered timeseries.

In order to accurately determine the dominant frequency components in a given function or timeseries, a Fourier transform is used. For a one dimensional function, $f(x)$, that

Station Code	Name	Geographic Latitude	Geographic Longitude	Magnetic Latitude (CGM)	Magnetic Longitude (CGM)
NAL	Ny Ålesund	78.92°	11.95°	75.25°	112.08°
LYR	Longyearbyen	78.20°	15.82°	75.12°	113.00°
HOR	Hornsund	77.00°	15.60°	74.13°	109.59°
HOP	Hopen Island	76.51°	25.01°	73.06°	115.10°
BJN	Bear Island	74.50°	19.20°	71.45°	108.07°
SOR	Sørøya	70.54°	22.22°	67.34°	106.17°
KEV	Kevo	69.76°	27.01°	66.32°	109.24°
TRO	Tromsø	69.66°	18.94°	66.64°	102.90°
MAS	Masi	69.46°	23.70°	66.18°	106.42°
AND	Andenes	69.30°	16.03°	66.45°	100.37°
KIL	Kilpisjärvi	69.02°	20.79°	65.88°	103.79°
IVA	Ivalo	68.56°	27.29°	65.10°	108.57°
ABK	Abisko	68.35°	18.82°	65.30°	101.75°
LEK	Leknes	68.13°	13.54°	65.40°	97.50°
MUO	Muonio	68.02°	23.53°	64.72°	105.22°
LOZ	Lovozero	67.97°	35.08°	64.23°	114.49°
KIR	Kiruna	67.84°	20.42°	64.69°	102.64°
SOD	Sodankylä	67.37°	26.63°	63.92°	107.26°
PEL	Pello	66.90°	24.08°	63.55°	104.92°
RVK	Rørvik	64.94°	10.98°	62.23°	93.31°
LYC	Lycksele	64.61°	18.75°	61.44°	99.29°
OUJ	Oulujärvi	64.52°	27.23°	60.99°	106.14°
HAN	Hankasalmi	62.30°	26.65°	58.71°	104.61°
DOB	Dombås	62.07°	9.11°	59.29°	90.20°
NUR	Nurmijärvi	60.50°	24.65°	56.89°	102.18°
UPS	Uppsala	59.90°	17.35°	56.51°	95.84°
TAR	Tartu	58.26°	26.46°	54.47°	102.89°

Table 3.1: IMAGE magnetometer stations with their geographic and corrected geomagnetic (CGM) coordinates (for full details see the IMAGE website at <http://www.ava.fmi.fi/image/stations.html>). Magnetic coordinate transformations are calculated for an altitude of 120 km for the 1 January 2003 epoch via the online tool at <http://nssdc.gsfc.nasa.gov/space/cgm/cgm.html>.

MIRACLE

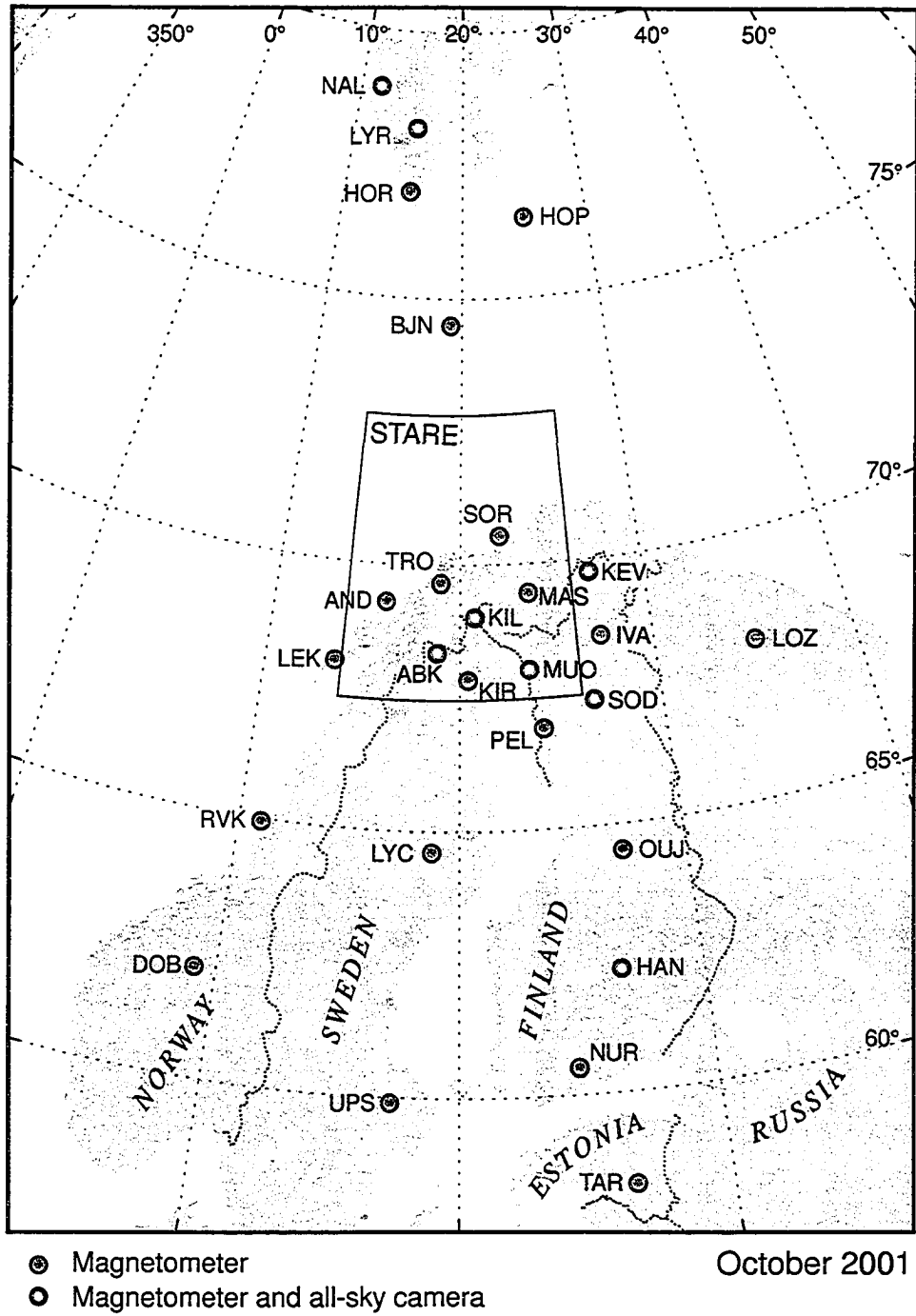


Figure 3.1: Locations of IMAGE magnetometer stations from the IMAGE website at <http://www.geo.fmi.fi/image/stations.html>. Magnetometers are marked by red dots, all sky cameras by white dots and the STARE radars common field of view is also shown. Dashed lines represent lines of geographic latitude and longitude.

contains N elements, the discrete Fourier transform (DFT), $F(u)$, is defined as

$$F(u) = \frac{1}{N} \sum_{x=0}^{N-1} f(x) \exp\left[\frac{-i2\pi ux}{N}\right]. \quad (3.1)$$

In general, the function $F(u)$ will be complex, with magnitude and phase given by

$$\begin{aligned} \text{magnitude} &= \sqrt{F_{real}^2 + F_{imag}^2}, \\ \text{phase} &= \tan^{-1}\left(\frac{F_{imag}}{F_{real}}\right). \end{aligned} \quad (3.2)$$

Therefore the function $F(u)$ supplies information about the dominant spectral peaks and the phase variation of any given discrete timeseries. This technique allows us to compute power and phase estimates for the timeseries from each magnetometer station, and thus we are able to investigate the latitudinal and longitudinal variations of the power and phase of geomagnetic pulsations.

Fourier analysis of timeseries only yields accurate variations in signal amplitude and phase at a specific discrete frequency for stationary timeseries, i.e., signals that exhibit no systematic change in mean, have no trend in variance and have an autocorrelation that is dependent on the time between data points and not on the periodicity of the signal [e.g., Banks, 1975]. In general, geomagnetic timeseries do not satisfy these criteria, however we can use a technique known as complex demodulation to investigate more accurately their power and phase properties. The method of complex demodulation is composed of two separate mathematical operations that can be applied to a timeseries [Banks, 1975], and to explain the methods involved we follow the treatment of Banks (1975).

For a given timeseries $x(t)$, the first operation is to shift the frequency band of interest to zero frequency by multiplying by the function $\exp(-i\omega't)$, where ω' is the central frequency of the shifted band. A new timeseries, $X(\omega', t)$, is produced that is given by

$$X(\omega', t) = x(t) \exp(-i\omega't). \quad (3.3)$$

The frequency shifted timeseries, $X(\omega', t)$, is then band-pass filtered using a set of weights (e.g., a cosine bell function), a_k (k varies from $-m$ to $+m$, where m is an individual data point in the timeseries). The complex demodulated timeseries can then be written as

$$X_d(\omega', t) = \sum_{k=-m}^{k=+m} a_k X(\omega', t + k\Delta t) \quad (3.4)$$

where Δt is the time interval between successive data points. The demodulates can be expressed more conveniently in terms of their modulus and phase, ϕ , as

$$X_d(\omega', t) = |X_d(\omega', t)| \exp(i\phi(\omega', t)). \quad (3.5)$$

If we consider a timeseries with a periodic component of frequency ω_0 given by

$$x(t) = A \cos(\omega_0 t + \gamma) \quad (3.6)$$

then the complex demodulate centered on the frequency $\omega' = \omega_0 + \delta\omega$ is

$$\begin{aligned} X(\omega', t) &= (A/2) \exp(-i(\omega_0 + \delta\omega)t) [\exp i(\omega_0 t + \gamma) + \exp -i(\omega_0 t + \gamma)] \\ &= \frac{A}{2} [\exp -i(\delta\omega t - \gamma) + \exp -i((2\omega_0 + \delta\omega)t + \gamma)]. \end{aligned} \quad (3.7)$$

If we low-pass filter the timeseries for $X(\omega', t)$ to obtain $X_d(\omega', t)$, then the term involving $2\omega_0 + \delta\omega$ disappears, and if we set $\omega' = \omega_0$ (i.e., $\delta\omega = 0$) then we may write

$$X_d(\omega_0, t) = (A/2) \exp i\gamma. \quad (3.8)$$

Thus the modulus of the demodulate is equal to $A/2$ and its phase is equal to the phase of the periodic variation at ω_0 . If the amplitude and phase of the signal change with time, the demodulate will reflect this, so that for a non-stationary timeseries we may obtain instantaneous values of amplitude and relative phase for any data point in the signal, so that for a finite timeseries we may obtain values of amplitude and phase at any point along that timeseries. Complex demodulation offers a more robust technique for the analysis of geomagnetic timeseries, as we can investigate latitudinal and longitudinal power and phase properties of ULF waves that vary in time. For a discussion of complex demodulation and its use in analyzing geomagnetic timeseries data see e.g., Banks (1975) or Myers and Orr (1990).

3.2 Coherent HF Radars

High frequency (HF) radars are a very useful tool for investigating irregularities and flows in the D- and E-region ionosphere. This type of instrument functions by emitting pulsed radio waves, and receiving the reflected pulse, which yields one dimensional information (i.e., either towards or away from the radar) about the motion of irregularities in the Earth's ionosphere. We utilize data from two radar arrays: the Scandinavian Twin Auroral Radar Experiment (STARE) and the Super Dual Auroral Radar Network (SuperDARN).

STARE [Greenwald *et al.*, 1978] consists of two pulsed bi-static radars located at Malvik, Norway, and Hankasalmi, Finland, that transmit radio waves at 140.0 and 143.8 MHz, respectively. They measure irregularities in the E-region of the ionosphere along eight beams, with 50 range gates per beam at a time resolution of 20 seconds (although resolution of up to 1s is possible when using a special mode). The common viewing area of the two radars lies over northern Scandinavia (see Figure 3.1), and at any point within this area (backscatter permitting) it is possible to construct vector diagrams of E-region electron drift velocities and hence derive ionospheric electric currents from the two Doppler velocity measurements (if an ionospheric conductivity is assumed). The electric field can also be determined from calculations assuming the following relationships

$$V = -|\mathbf{V}_0| \cos \alpha \quad (3.9)$$

and

$$\mathbf{V}_0 \simeq \mathbf{E} \times \mathbf{B} / B^2 \quad (3.10)$$

where V is the observed Doppler velocity, \mathbf{V}_0 is the mean irregularity drift velocity, and α is the angle between \mathbf{V}_0 and the radar wave vector. Hence the electric field vectors, \mathbf{E} , can be found from measurements of the observed Doppler velocities, V , along the line of sight of the two radar beams scattered from a common volume.

The Super Dual Auroral Radar Network (SuperDARN) is an international chain of HF radars located in the northern and southern hemispheres [e.g., Greenwald *et al.*, 1995]. Each radar operates in the frequency range 8-20 MHz to allow the signal to propagate to the area of interest during different ionospheric conditions. The radars emit pulses at either



Figure 3.2: Location and field of view of the nine northern hemisphere SuperDARN radars.

300 μ s or 100 μ s which allow a range resolution of 45 km and 15 km, respectively, and the transmitters are phased to allow 1 of a possible 16 beam pointing directions. Each beam is 3.6 degrees in width, yielding an azimuthal coverage of approximately 50 degrees and ranges are sampled from 180 to 3500 km. Each radar routinely measures the line-of-sight (l-o-s) Doppler velocity, the spectral width, and the backscattered power, of ionospheric plasma irregularities at a temporal resolution of up to 1 second. Common volume data from two radars can be combined to provide convection velocities in the ionosphere, and multiple radar pairs facilitate the investigation of ionospheric convection across large areas of the northern and southern hemispheres. The locations of the northern hemisphere SuperDARN radars are displayed in Figure 3.2.

The SuperDARN radars scatter off meter-scale irregularities in the ionosphere, caused

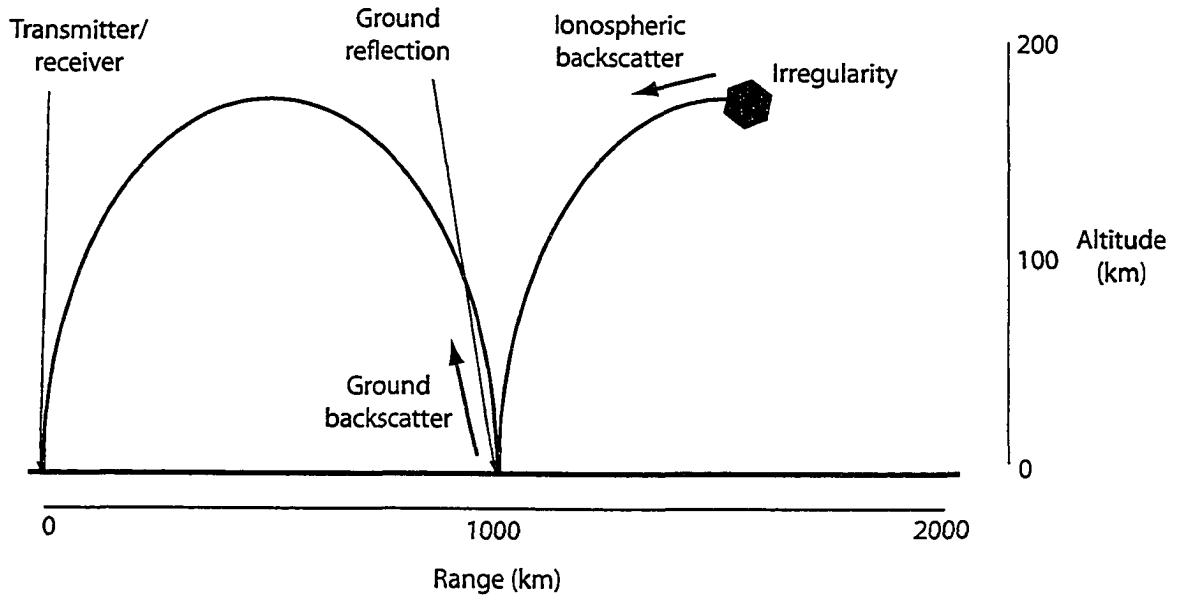


Figure 3.3: Diagram representing the pulse transmission and reflection paths for a SuperDARN radar. A pulse is emitted from the transmitter, transmitted from the ground to reflect off an ionospheric irregularity, transmitted back to the ground on its return path and received by the radar (known as $1\frac{1}{2}$ hop scattering). Scattering can also occur at closer distances to the radar, before the ray is transmitted by the ground, and this is known as $1/2$ hop scattering. All ranges and altitudes are approximate and depend on ionospheric conditions.

by e.g., ULF waves, magnetospheric substorms, travelling ionospheric disturbances, artificially stimulated irregularities etc. Figure 3.3 displays the $\frac{1}{2}$ hop and more standard $1\frac{1}{2}$ hop scattering method, with approximate ranges and altitudes of scattering.

Due to the differing frequencies of the STARE and SuperDARN radars, STARE backscatter occurs from the E-region of the ionosphere and SuperDARN backscatter occurs in the F-region.

3.3 Incoherent Scatter Radars

The theory behind incoherent scatter (IS) radars is simple to understand, yet difficult to implement. Classical physics tells us that an electron scatters electromagnetic radiation with a cross section of $\sigma_e = 1.0 \times 10^{-28}$ m. We may use this result to directly and indirectly measure a number of ionospheric parameters by analyzing the scattered spectrum of an electromagnetic wave emitted into the atmosphere. Table 3.2 lists the parameters that

Directly Measured Parameters	Inferred Parameters
Electron Density, N_e	Neutral particle density, ρ
Electron temperature, T_e	Neutral gas temperature, T
Ion Temperature, T_i	Neutral air velocity, U
Ion composition	Pedersen conductivity, Σ_P
Ion drift velocity, V_i	Hall conductivity, Σ_H
Ion-neutral collision frequency, ν_{in}	Electric current
Photoelectron flux	Heat flux

Table 3.2: Parameters measured by IS radars. After Risbeth and Williams (1985)

Station	Location	L-value	Antenna
Tromsø UHF	70°N, 19°E	6.5	32m parabolic trans/rec
Kiruna UHF	68°N, 20°E	5.6	32m parabolic receiver
Sodankylä UHF	67°N, 27°E	5.3	32m parabolic receiver
Tromsø VHF	70°N, 19°E	6.5	120×40m parabolic cylinder trans/rec
ESR ¹	78°N, 16°E	15.2	32m parabolic trans/rec
ESR ²	78°N, 16°E	15.2	32m field aligned parabolic trans/rec

Table 3.3: Locations of EISCAT radars. Superscripts 1 and 2 refer to the EISCAT Svalbard radar (ESR) steerable and field aligned dishes, respectively. Adapted from <http://www.eiscat.com/instrumentation.html>.

can be directly measured by IS radars, and those that may be inferred (after Risbeth and Williams (1985)).

These types of radars are expensive to construct and run; taking a typical scattering volume of 100 km^3 , containing 10^{23} particles (a reasonable estimate for the F_2 layer of the ionosphere), the total scattering cross section is of order 10 mm^2 , which means that for megawatts of power emitted in a pulse, microwatts will be scattered by the ionosphere, and only femtowatts will be received by the ground-based antennas. IS radars therefore need to incorporate powerful transmitters, sensitive receivers and sophisticated signal processing techniques.

A mono-static IS radar consists of a transmitter and receiver that are co-located. A pulse is emitted from the transmitter, and the power of the reflected signal tells us the electron density (as the scattering cross section of a given volume of ionospheric plasma is directly determined by the local electron number density). If the pulse emitted has some inherent coding, i.e., a burst of duration two seconds is emitted, then a burst of duration

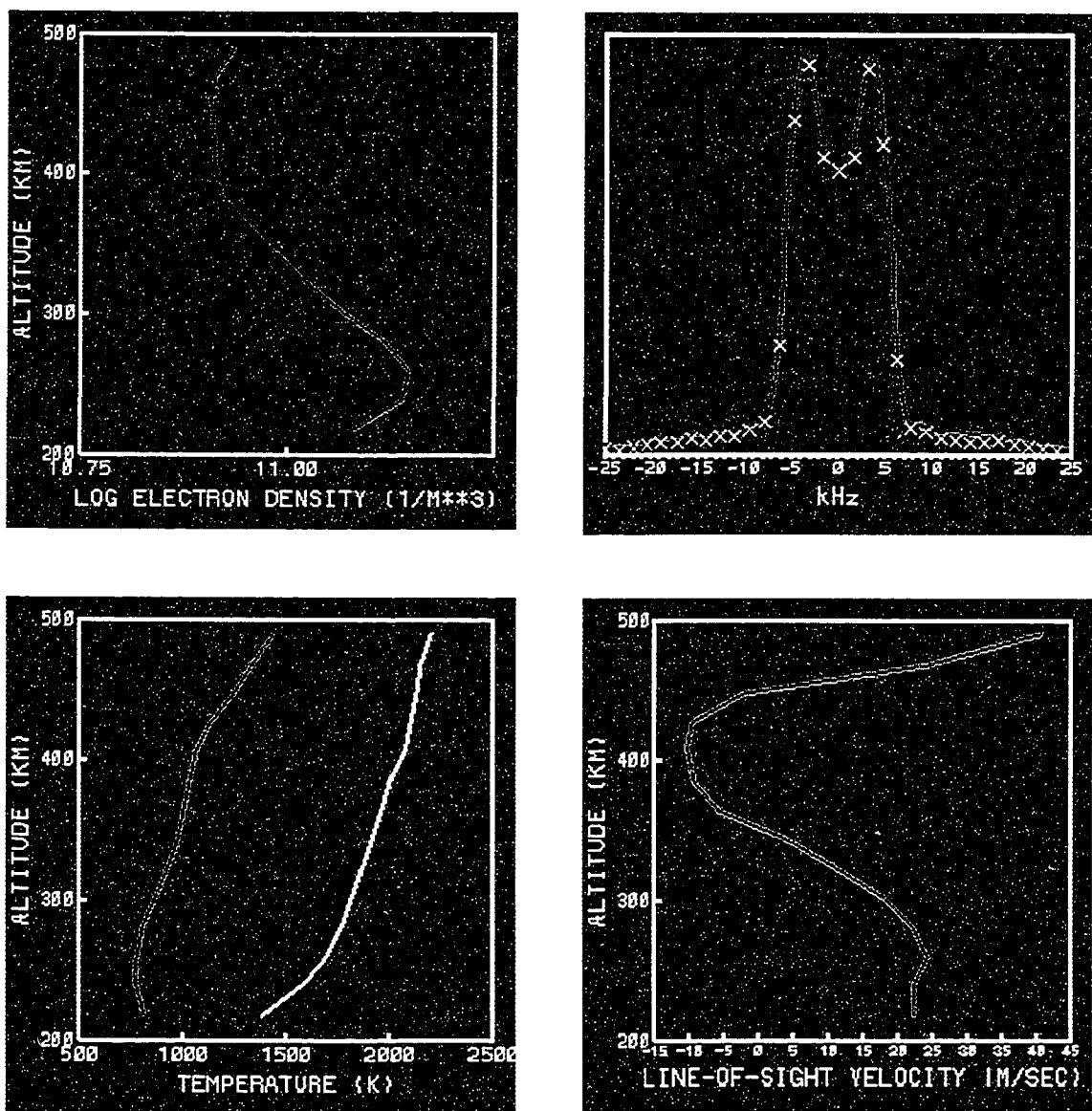


Figure 3.4: Sample ionospheric properties measured by IS radars. Shown are electron density (top left), the shape of the received spectrum (top right), ion and electron temperature profiles (bottom left, red and yellow respectively) and the line-of-sight ion drift (bottom right). Taken from the Millstone Hill IS website at <http://hyperion.haystack.edu/midas/inscal.html>.

CUTLASS viewing areas

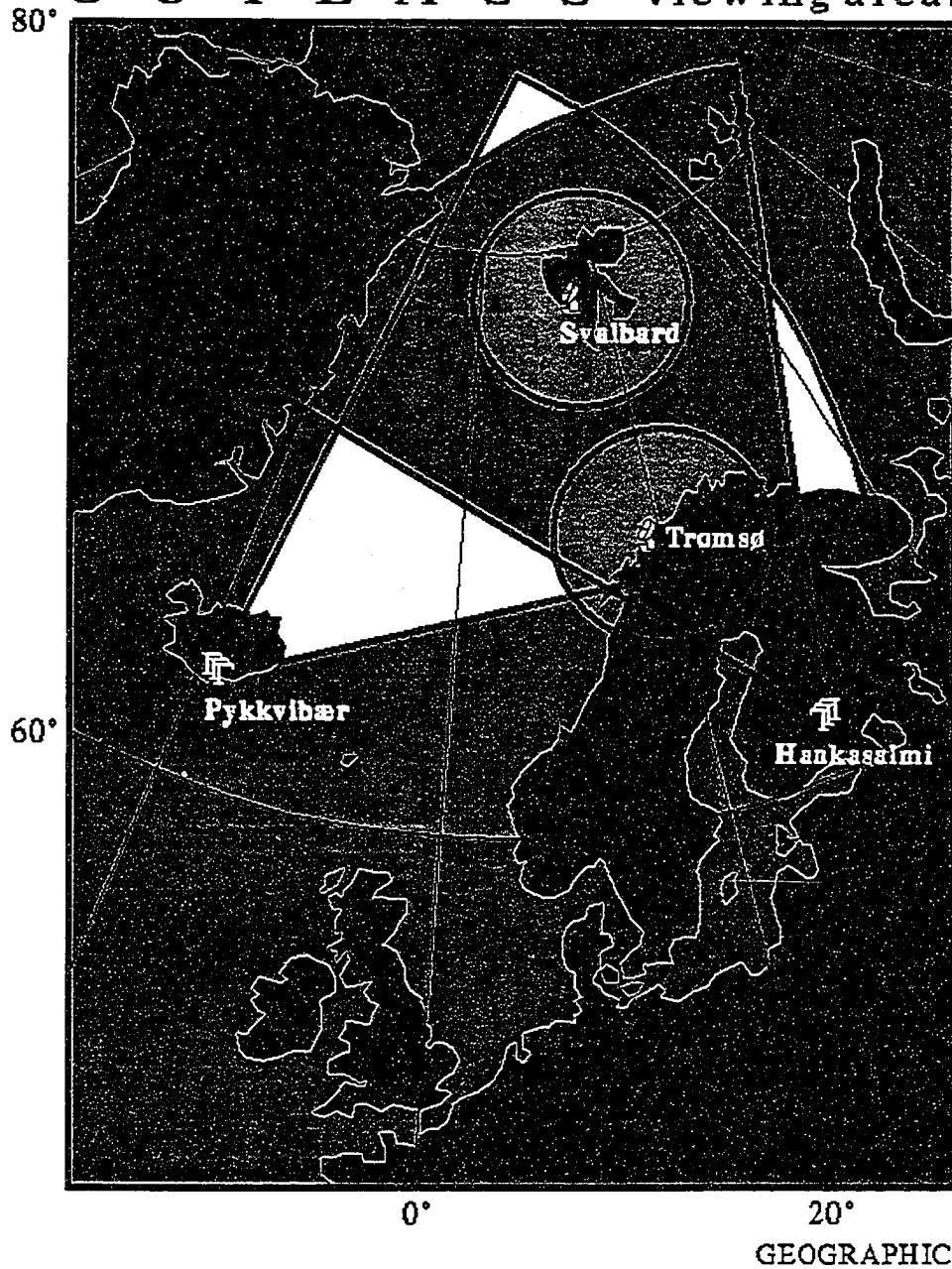


Figure 3.5: Field of view of the CUTLASS HF radars (fans) and the EISCAT Svalbard radar (ESR) and EISCAT Tromsø UHF IS radar (circles) projected to an altitude of 110 km. Taken from the University of Leicester CUTLASS website at <http://www.ion.le.ac.uk/cutlass/pictures/cutlassmap.gif>.

three seconds, etc., we may identify at what altitude the received signal was scattered. In general, pulse schemes need to be of a longer duration than the time taken for the pulse to pass through all of the scattering volume. In practice, the longest pulse required is $\sim 300 \mu\text{s}$, for sampling of the ionospheric F-region. This technique allows us to directly measure the electron number density, n_e , but if we want to investigate other ionospheric properties we need to investigate the spectral shape of the returned signal and the Doppler shift. If the velocity of an ion-acoustic wave (we are trying to measure the random plasma wave fluctuations in the ionosphere) is given by $v_+ = \sqrt{\frac{2kT_i}{m_i}}$ then the Doppler shift is simply $\Delta f_+ = \frac{2f_0}{c} \sqrt{\frac{2kT_i}{m_i}}$ where f_0 is the frequency of the transmitted pulse. The Doppler shift observed by the receiver must have an associated spectral width (see Figure 3.4 for typical IS radar observations) due to the random thermal motion of the plasma, and theoretical work (e.g., Fejer (1960); Hagfors (1961)) has shown that the spectral width is an indication of the ion temperature. However, the spectrum received on the ground is usually double peaked, and it is from the nature of these peaks that the electron temperature is found.

The European Incoherent Scatter (EISCAT) radar system consists of four incoherent scatter radars, with two remote sites [e.g., Risbeth and Williams, 1985]. The locations of the EISCAT radars and other associated parameters are listed in Table 3.3, and Figure 3.5 indicates the EISCAT radar fields of view in relation to the CUTLASS SuperDARN radars.

3.4 Ground-Based Optical Instruments

The two main types of optical instrument used in this thesis are Meridian Scanning Photometers (MSPs) and All Sky Cameras (ASCs). The location of the MSP at Longyearbyen and the ASC at Ny Ålesund and their fields of view projected to an emission altitude of 110 km are displayed in Figure 3.6. Both instruments use a range of filters of different wavelengths to investigate auroral emission lines. These emission lines and the energy of the particle precipitation associated source mechanisms are listed in Table 3.4.

MSPs allow us to look at the latitudinal structure of the aurora at high time resolution (the Longyearbyen MSP scans meridionally every 16 seconds) and they can also allow the diagnosis of various magnetospheric boundaries. For example the 630.0 nm filter allows us to specify the location of the open-closed field line boundary (OCFLB) [de la Beaujardiere

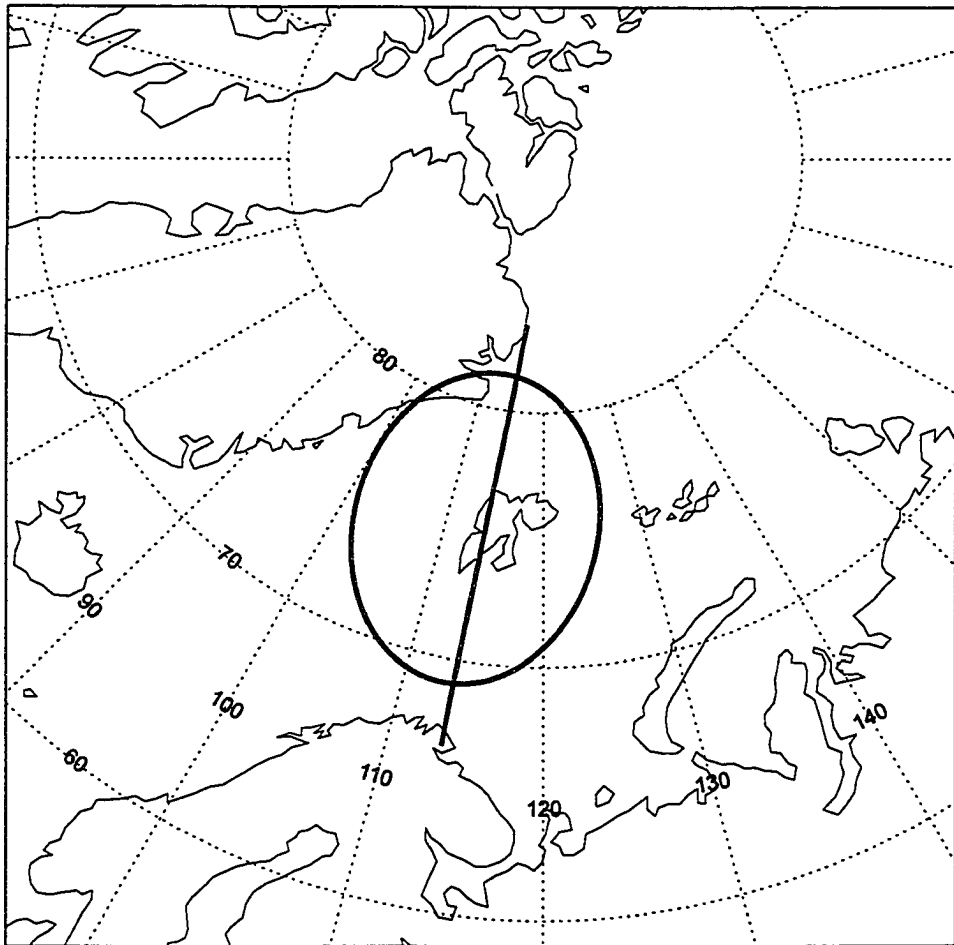


Figure 3.6: Location and field of view of the Longyearbyen MSP (line) and Ny Ålesund ASC (oval). Fields of view are projected to an emission altitude of 110 km.

Atomic Transition	Wavelength of Emission (nm)	Source Mechanism	Peak Emission Altitude
$O(^1S) \rightarrow O(^1D) + h\nu$	557.7	$e > 1 \text{ keV}$	$\sim 110 \text{ km}$
$O(^1D) \rightarrow O(^3P_2) + h\nu$	630.0	$e \ll 1 \text{ keV}$	$\sim 250 \text{ km}$
$(N_2^+)^* \rightarrow N_2^+ + h\nu$	427.8	$0.5 \text{ keV} \lesssim e \lesssim 20 \text{ keV}$	
$H^+ + e \rightarrow H + h\nu$	486.0	Protons	

Table 3.4: The four major auroral transitions measured by optical instrumentation. The superscript * represents an excited rotational energy state. Adapted from Kivelson and Russell (1995).

et al., 1994]. Precipitation producing this emission line is somewhat continuous and is believed to occur when low energy particles from the plasmashet undergo pitch angle scattering and impinge upon the Earth's atmosphere. The 557.7 nm filter is used to identify energetic precipitation events caused by electrons of energy greater than 1 keV, which are generally associated with a discrete auroral acceleration mechanism in the magnetosphere.

ASCs utilize a fish-eye lens to take images of the aurora, usually through the same filters as MSPs. They facilitate the analysis of the two-dimensional structure of auroral emissions, although the time to build up an image is much longer than that for MSPs, typically being between 30 and 60 seconds.

In this thesis we use data from the Longyearbyen MSP and Ny Ålesund ASC, located as shown in Figure 3.6. The Longyearbyen MSP builds up a meridional scan every 16 seconds. The incident light passes through a slit to produce a beam, and this beam is then split into four, with the four subsequent beams passing through a filter corresponding to one of the wavelengths highlighted in Table 3.4. The Ny Ålesund ASC builds up an image of the auroral activity overhead every 30 seconds, although only one filter may be used at any one time. Thus the final dataset for e.g., the 557.7 nm emission may have data gaps at the times when a different filter was being used.

3.5 Satellites

Satellites allow us to make direct in-situ measurements of plasma characteristics in the Earth's magnetosphere or solar wind, which can be coupled with ground-based measurements to trace solar wind and magnetospheric events down to the Earth's ionosphere.

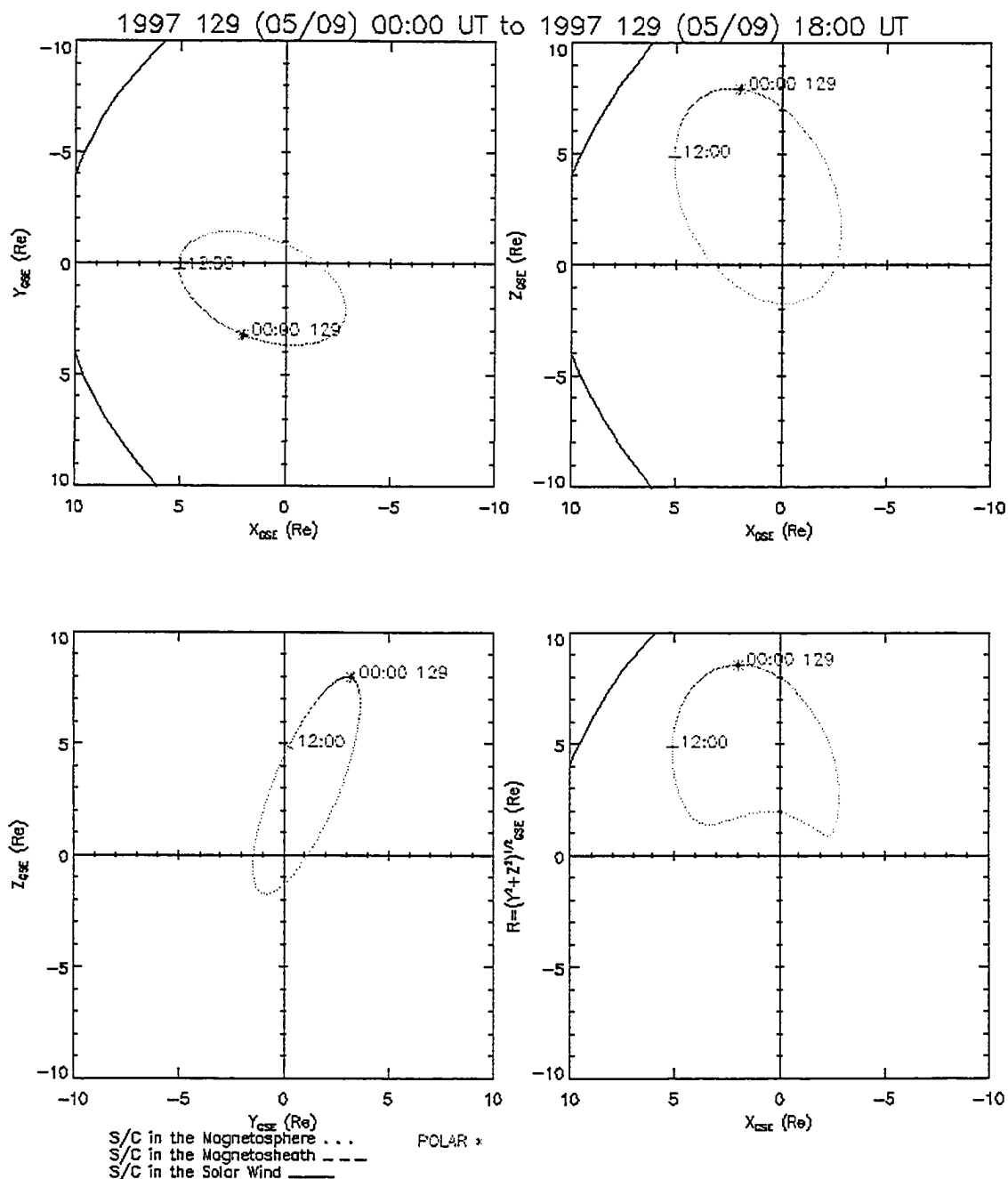
3.5.1 Polar

The orbit of the Polar satellite [Harten and Clark, 1995] is highly elliptical, with an apogee at an altitude of 9 Earth radii (R_E), a perigee at an altitude of 1.8 R_E and with an initial inclination of 86° (see Figure 3.7 for a typical Polar orbit). The orbital period is approximately 18 hours, and the apogee has been moving from over the north pole towards the equator at a rate of $\sim 16^\circ$ per year since its launch in February 1996.

The first instrument of interest to us on-board Polar is the Magnetospheric Ion Composition Sensor (MICS) [Wilken *et al.*, 1992], part of the Charge And Mass Magnetospheric Ion Composition Experiment (CAMMICE). MICS detects ions in the energy range 1-240 MeV/ q , and utilizes energy spectroscopy in combination with an electrostatic entrance filter to measure the mass, energy and charge of incident ions. The resulting data, in counts, can then be converted to Ion Distribution Functions (IDFs) using instrument specific parameters, such as the efficiency at a given energy and the field of view of the instrument.

Polar may also be used to make direct magnetic and electric field observations in near-Earth space. The instruments of particular interest are the UCLA three dimensional flux-gate magnetometer [Russell *et al.*, 1995], which samples the Earth's magnetic field at 8.3 samples/s in spacecraft coordinates, and the U. C. Berkeley Electric Field instrument (EFI) [Harvey *et al.*, 1995], with a sampling rate of 20 samples/s. The EFI utilizes current-biased spherical sensors located on the ends three orthogonal pairs of booms (which have tip to tip separations of 100 m and 130 m in the spin plane and 13.8 m in the spin axis), and the electric field is determined by the electric potential between these sensors. Electric and magnetic field vectors are recorded in the x-y (spin) plane and z (axis of rotation) direction, and require transformation into inertial and sometimes subsequently into field-aligned coordinates before they can be fully explored. The transformation between an orthogonal inertial coordinate system (e.g., geocentric solar magnetic, GSM) and local field aligned coordinates will be discussed in Chapter 7.

The final instrument on Polar used in this thesis is HYDRA [Scudder *et al.*, 1995]. HYDRA is a collection of electrostatic analyzers that are designed for high temporal and spatial resolution observations of electron and ion velocity distributions in the magnetosphere. HYDRA produces measurements of the local electron density, electron average energy, and electron and ion 2-D velocity distributions every six seconds, although the data



Generated by SSCweb on: Thu Nov 27 19:11:29 2003

Solar Wind Pressure=2.1nP IMF BZ=0.0nT

Figure 3.7: Typical orbit of the Polar satellite for the 9th May 1997, projected into the GSE X-Y, X-Z and Y-Z planes. Also included is the spacecrafts radial distance from the Sun-Earth line. Calculations were made by the online tool at SSC web (<http://sscweb.gsfc.nasa.gov/>).

in this thesis are averaged over three instrument integrations to increase statistical validity.

3.5.2 The Advanced Composition Explorer (ACE)

The ACE satellite [Stone, 1989] orbits the L1 Libration point between the Sun and the Earth (the point at which the Sun's and the Earth's gravitational forces are equal) at a distance of 1.5 million km from the Earth. Orbits around the L1 point are not stable, and the ACE satellite has enough fuel on-board to maintain its orbit until around 2019.

The main use of ACE is to characterize the solar wind velocity, density and magnetic field. The Solar Wind Electron Proton Alpha Monitor (SWEPAM) [McComas *et al.*, 1998] on ACE measures electron and ion fluxes in the solar wind, in the energy range 0.26-36 keV for ions and 1-1350 eV for electrons. The instrument samples the E/Q distribution of the solar wind, and the full distribution may be reconstructed from these moments. Magnetic field measurements by ACE are taken by the MAG instrument [Smith *et al.*, 1998], which consists of twin, triaxial fluxgate magnetometers that can sample at a rate of 3, 4 or 6 samples/s. For analysis of events in the magnetosphere, ACE data are usually time lagged to take into account the delay time as the solar wind propagates from the ACE satellite to the Earth, and this delay is typically of the order of one hour.

Chapter 4

Multi-Instrument Observations of Particle Driven Field Line Resonance

4.1 Introduction

In their seminal paper, Southwood *et al.* (1969) investigated the possibility that particles in the Earth's magnetosphere may become resonant with standing poloidally polarised ULF waves on closed magnetic field lines, and postulated that in specific circumstances energy transfer between the waves and the particles could take place. Southwood *et al.* (1969) showed that the condition for particles to be resonant with a wave is

$$\omega - m\omega_d = N\omega_b \quad (4.1)$$

where ω is the frequency of the wave in the magnetosphere, m is the azimuthal wavenumber, ω_d is the drift frequency of the particles around the Earth, N is an integer determined by which field-aligned harmonic is being excited and ω_b is the frequency of the bounce motion of the particles as they mirror in either hemisphere. Equation 4.1 states that for any integer value of N , particles may excite poloidal mode FLRs in the Earth's magnetosphere [see, e.g., Southwood *et al.*, 1969 or Chapter 2 of this thesis].

The $N=1$ resonance is believed to excite poloidal mode Pc4 [see e.g., Section 1.7] waves, and previous statistical studies of the spatial locations of waves in the Pc3, Pc4 and Pc5 bands have shown that poloidal Pc4 waves peak in amplitude in the afternoon magnetic local time sector [e.g., Anderson *et al.*, 1990; Cao *et al.*, 1994]. Satellite observations of such poloidal Pc4 waves have shown them to have high m -values (sometimes between 50 and 100 [e.g., Engebretson *et al.*, 1992]), thus making observations of such

waves using ground-based magnetometers sometimes difficult due to ionospheric screening [Hughes and Southwood, 1976b]. One specific type of Pc4 wave observed in the morning sector in the auroral zone is known as a Giant Pulsation or Pg. These waves are extremely monochromatic and occur during geomagnetically quiet times [e.g., Brekke *et al.*, 1987]. The harmonic mode of Pgs is currently under dispute, with different authors proposing different field-aligned harmonic numbers for the waves. Chisham and Orr (1991) argue that Pgs are a second harmonic rather than a fundamental mode standing wave, whereas Takahashi *et al.* (1992) and Glassmeier *et al.* (1999) found evidence that Pgs exhibit an odd-mode standing wave structure.

The $N=0$ resonance is observed in the afternoon sector, often during storm times [e.g., Walker and Nielsen, 1984]. It is believed that wave growth during storm times is primarily due to the enhanced ring current that occurs when solar wind ions enter the magnetosphere at storm onset.

One method of investigating high- m waves in the magnetosphere is to use coherent scatter radar. Pulses from the radar reflect off irregularities in the ionosphere, which can be advected by periodic ULF waves. The ionosphere is effectively the end point of magnetic field line oscillations (due to its high conductivity), and so oscillations therein can be related to oscillations in the magnetosphere. Wright *et al.* (2001) used the IMAGE magnetometer chain and the Doppler Pulsation Experiment (DOPE) to investigate the ionospheric response to a Pg, and used instruments on the Polar satellite to study the energy distribution of particles in the ring current. The satellite data that they presented showed a positive gradient in the energy distribution, but as the satellite was three hours away in magnetic local time, no causal relationship could be produced. They concluded that further work is required to determine whether Pgs are an odd or even mode oscillation.

Yeoman and Wright (2001) used the Tromsø heater to produce density striations in the ionosphere, which acted as targets for HF backscatter. These artificial irregularities accurately track the ionospheric convection patterns, and the backscatter produced was of high power and low spectral width. This allowed short integration times on the radar to be used, providing an extremely high spatial and temporal resolution for wave observations. They concluded that their observations were of a large scale fundamental toroidal FLR (not discussed here), a fundamental poloidal drift ($N=0$) resonance, and a second harmonic

drift-bounce ($N=\pm 1$) resonance.

In a recent paper, Ozeke and Mann (2001) introduced a new model of drift-bounce resonance interactions which can account for many of the features exhibited by wave particle interactions. Their model trajectories of protons in a dipolar magnetosphere showed why Pgs are only observed in the morning sector, why they are so monochromatic, why they are only produced in the auroral zone, and why they are so highly localized in latitude. Furthermore, their model is in excellent agreement with the statistically observed distribution of poloidal mode, presumably particle driven ULF waves, in both the morning and afternoon sectors. For a given L-shell (or FLR frequency), magnetic local time, and m number, the model can predict what energy particles are required to amplify background wave fluctuations to produce FLR.

The first observations of oscillations on magnetic field lines with associated satellite observations of a bump on tail distribution were presented by Hughes *et al.* (1978). They used satellite data to show that Alfvén waves were present on field lines at geostationary orbit, and argued that these waves were caused by particles of between 1 and 10 keV; the region at which the particle energy distribution was observed to have a positive gradient. No trace of the poloidal waves was observed on the ground, and it was concluded that the event was of the high- m type, and thus were screened from the ground (see e.g., Hughes and Southwood (1976b) or Chapter 2 of this thesis).

Currently, no observations exist in the literature of afternoon sector particle driven Pc5 poloidal FLRs with corresponding satellite data that clearly shows an unstable energy distribution of particles in the ring current that are of the correct energy to excite the wave. This Chapter aims to highlight one such event that is characterised on the ground by magnetometer and radar observations of a poloidal mode Pc5 FLR with associated satellite measurements from the ring current that show an unstable energy distribution that may provide the energy source for the wave.

We present multi-instrument observations of a poloidal mode Pc5 wave in the afternoon local time sector. The wave is similar to Pgs in that it is extremely monochromatic and is characterised by a moderate m -value, however it occurs in the afternoon sector and is in the Pc5 band, not the Pc4 band. The wave shows excellent coherence in both ground-based magnetometer and radar datasets which is highly unusual as the ionosphere often screens

such waves from the ground (e.g., Hughes and Southwood, 1976b), and the resonant latitude of the resonance lies within the field of view of the STARE radar. Thus we have the opportunity to characterise the ionospheric flows and the magnetic perturbations of this highly monochromatic event and investigate the hypothesis that it is excited by an $N=0$ resonance and compare the results to theory. Further, the Polar satellite passed through the ring current before and after the time of the ULF wave, allowing us to investigate the particle distribution functions in the ring current, which allows a characterisation of the potential production mechanism of the wave to be constructed.

4.2 Observations

4.2.1 Magnetospheric Configuration

Figure 4.1 shows solar wind data from the ACE spacecraft for the 26th August 1999. The solar wind speed remained fairly constant at around 500 km/s until 1530 UT, whereupon a slower solar wind stream was observed to last for approximately three hours (top panel of Figure 4.1). Between 1900 and 2400 UT the solar wind speed steadily increased from 540 to 640 km/s, with brief periods of high speed solar wind flow. The solar wind H^+ number density varied between 1 and 6 particles/cm³ over the 24 hour interval, with a major drop in the solar wind density beginning at 1730 UT (second panel of Figure 4.1). The GSM z-component of the solar wind varied between -5 and 5 nT throughout the day, with a period of $B_z \simeq 0$ occurring between 1500 and 1800 UT (bottom panel of Figure 4.1).

Figure 4.2 displays hourly averages of the Dst index for the 26th August 1999, with no signatures of magnetic storm activity observed. Between 1500 and 1800 UT the planetary K index, K_P , was 2, and the average K_P for the entire day was 3. Overall, the magnetospheric conditions were generally quiet to moderate, with no large density perturbations or speed discontinuities in the solar wind and no storm activity.

Figures 4.3 and 4.4 display data from the IMAGE magnetometer network for the 26th August 1999. Two substorms are observed, one at around 1200 UT and one at around 2100 UT, with no other evidence of large scale magnetospheric activity. In Figure 4.4 a magnetic pulsation is clearly visible beginning at around 1530 UT, and it is this oscillation and its associated production mechanism upon which we focus in this Chapter.

ACE MGF and SWEPAM Data for 26/08/1999

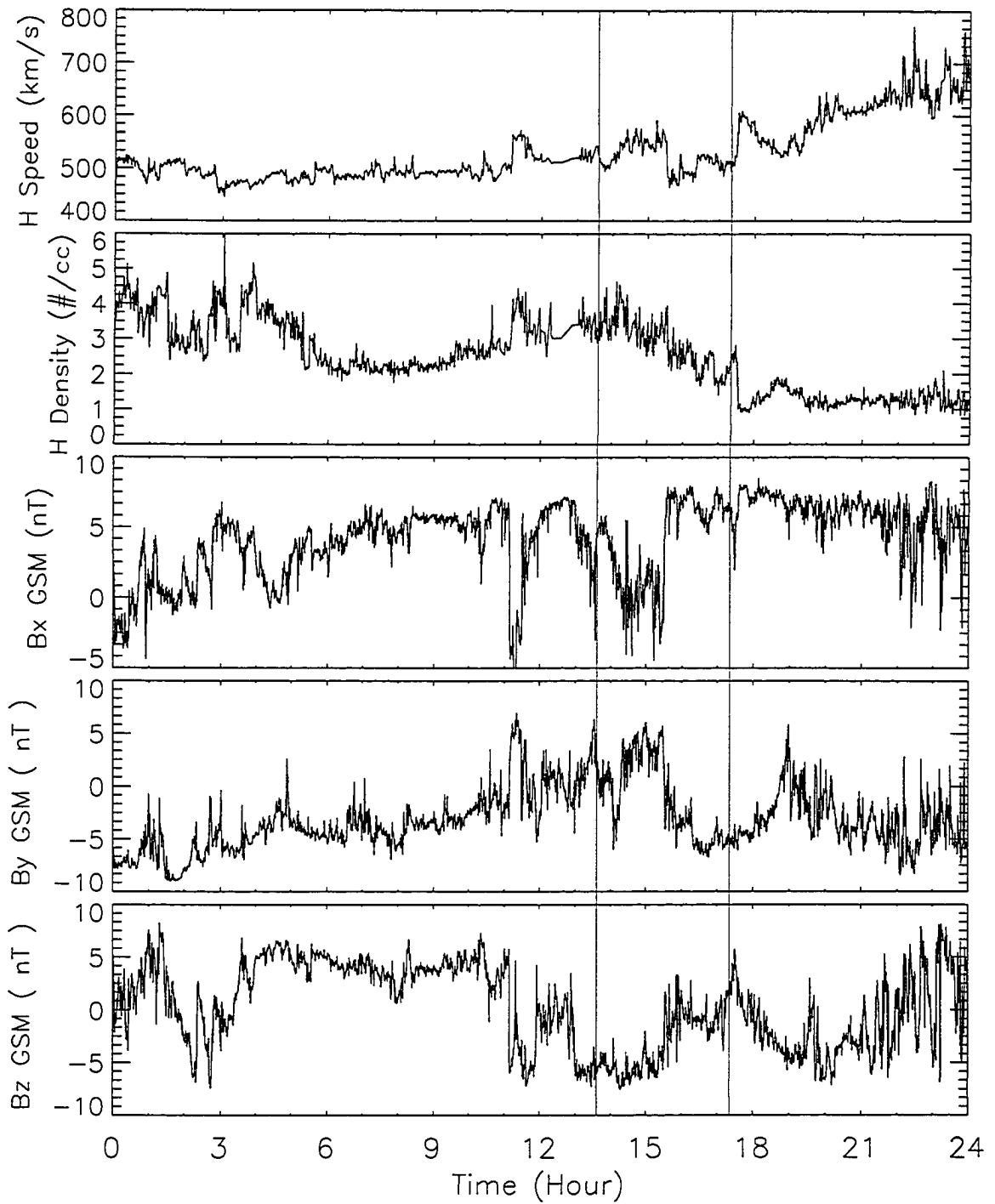


Figure 4.1: ACE SWEPAM [McComas *et al.* (1998)] H^+ speed and density and MGF [Smith *et al.* (1998)] B_x , B_y and B_z magnetic field data for the 26th August 1999. Red vertical lines indicate the solar wind conditions during the period of ULF wave activity on the ground. ACE MGF data provided courtesy of N. Ness at Bartol Research Institute, SWEPAM data provided courtesy of D. J. McComas at SWRI.

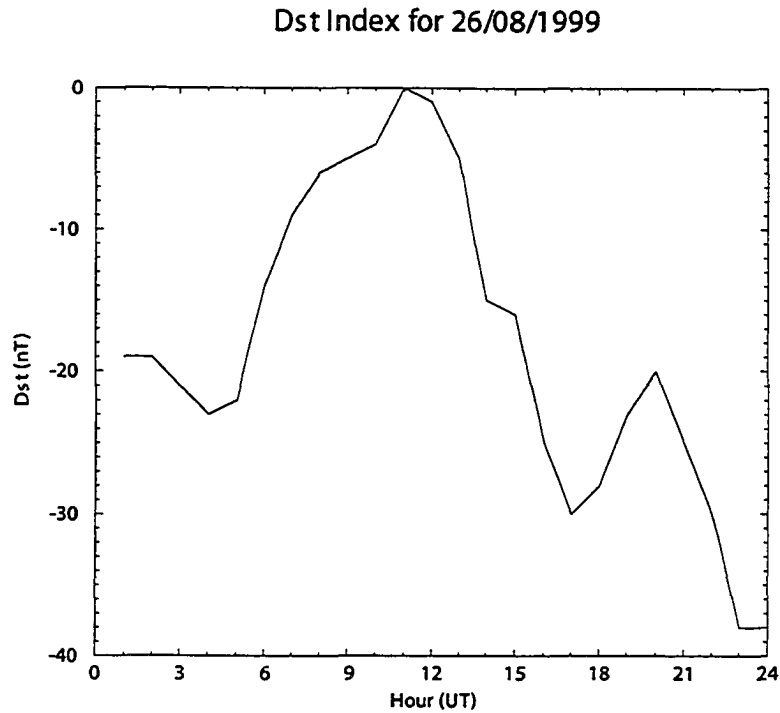


Figure 4.2: Hourly averages of the Dst index for the 26th August 1999.

4.2.2 IMAGE Magnetometer Data

Figures 4.5 and 4.6 display unfiltered IMAGE H- and D-component magnetometer time-series for the interval 1430 to 1630 UT respectively. The largest amplitude oscillations were observed in the magnetic D-component, and the latitudinal extent of the wave was approximately 8° (i.e., between Bear Island and Pello, labelled BJN and PEL in Figure 4.6 respectively).

Figure 4.7 displays H- and D-component power spectra for the timeseries in Figures 4.5 and 4.6 filtered between 750 and 100 seconds (1.3 to 10 mHz). The discrete frequency pulsation is visible between the stations at Sørøya and Pello (labelled SOR and PEL) as a peak at 3.3 mHz in both components, indicating that the wave is not polarised purely in the poloidal sense, but as the magnitude of oscillation in the D-component is larger by a factor of five we may conclude that the wave is predominantly polarised in the poloidal sense in the magnetosphere. The lack of any power at highest and lowest latitude magnetometer stations indicates that the wave is localized in latitude, and is probably a field line resonance.

IMAGE H component plot: Day26 Month: 8 Year: 1999 Unfiltered

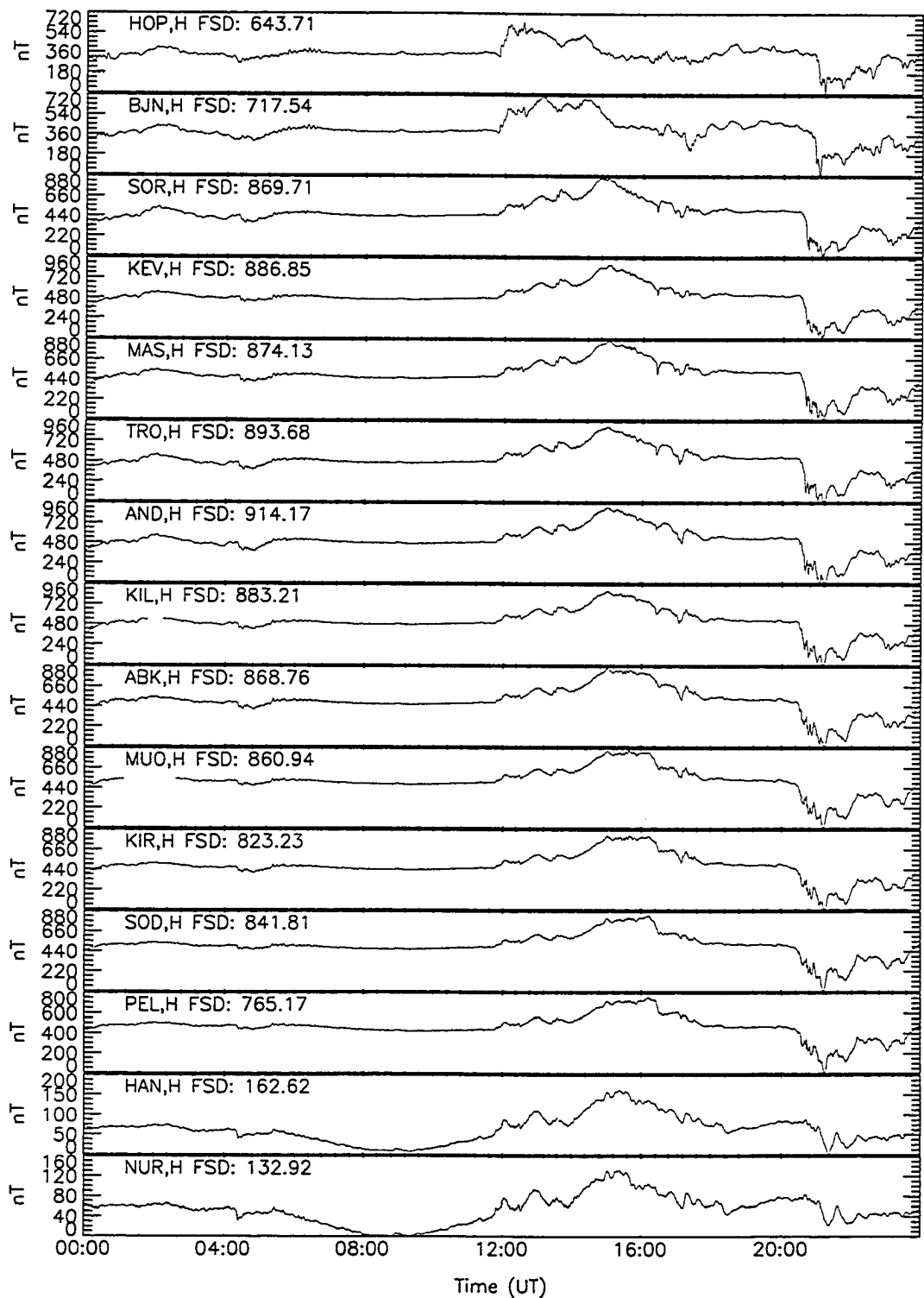


Figure 4.3: Unfiltered H-component magnetometer data from selected stations from the IMAGE array for the 26th August 1999.

IMAGE D component plot: Day26 Month: 8 Year: 1999 Unfiltered

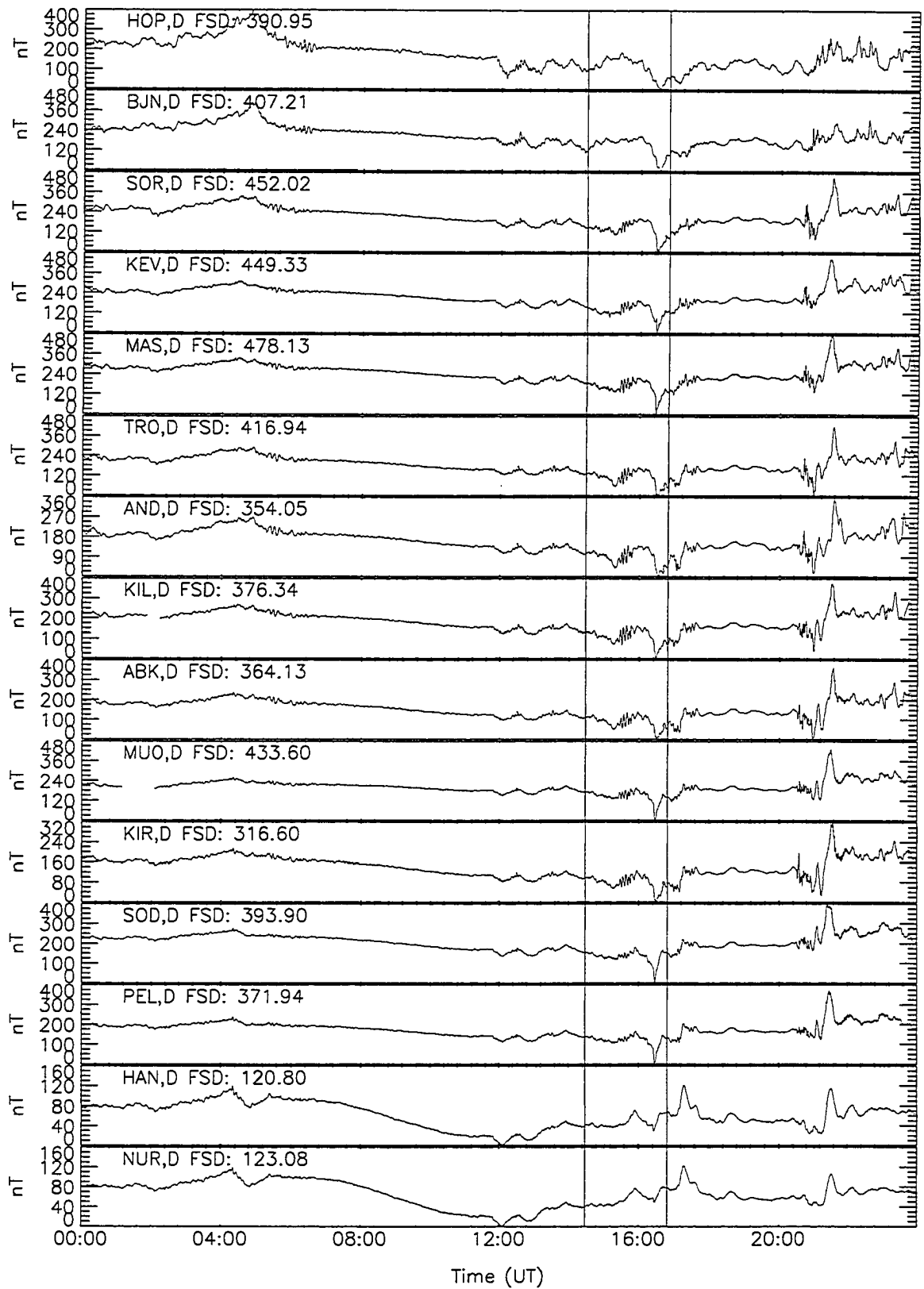


Figure 4.4: Unfiltered D-component magnetometer data from selected stations from the IMAGE array for the 26th August 1999. Red vertical lines represent the interval of ULF wave activity.

IMAGE H component plot: Day26 Month: 8 Year: 1999 Unfiltered

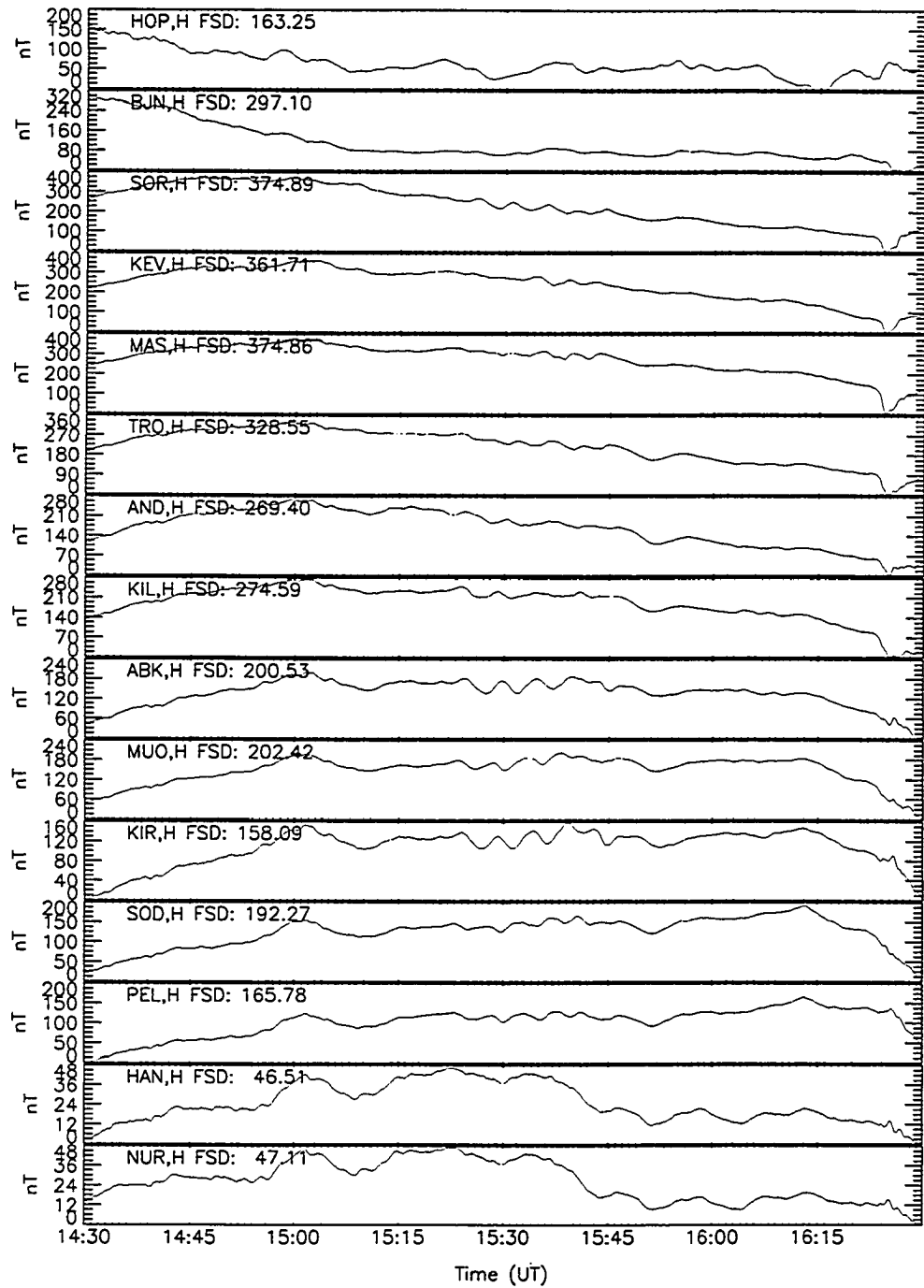


Figure 4.5: Unfiltered H-component magnetograms from selected IMAGE magnetometer stations for the interval 1430 to 1630 UT on the 26th August 1999. Note that the scales for the stations are independently scaled, full scale deflection being indicated on each time-series as FSD.

IMAGE D component plot: Day26 Month: 8 Year: 1999 Unfiltered

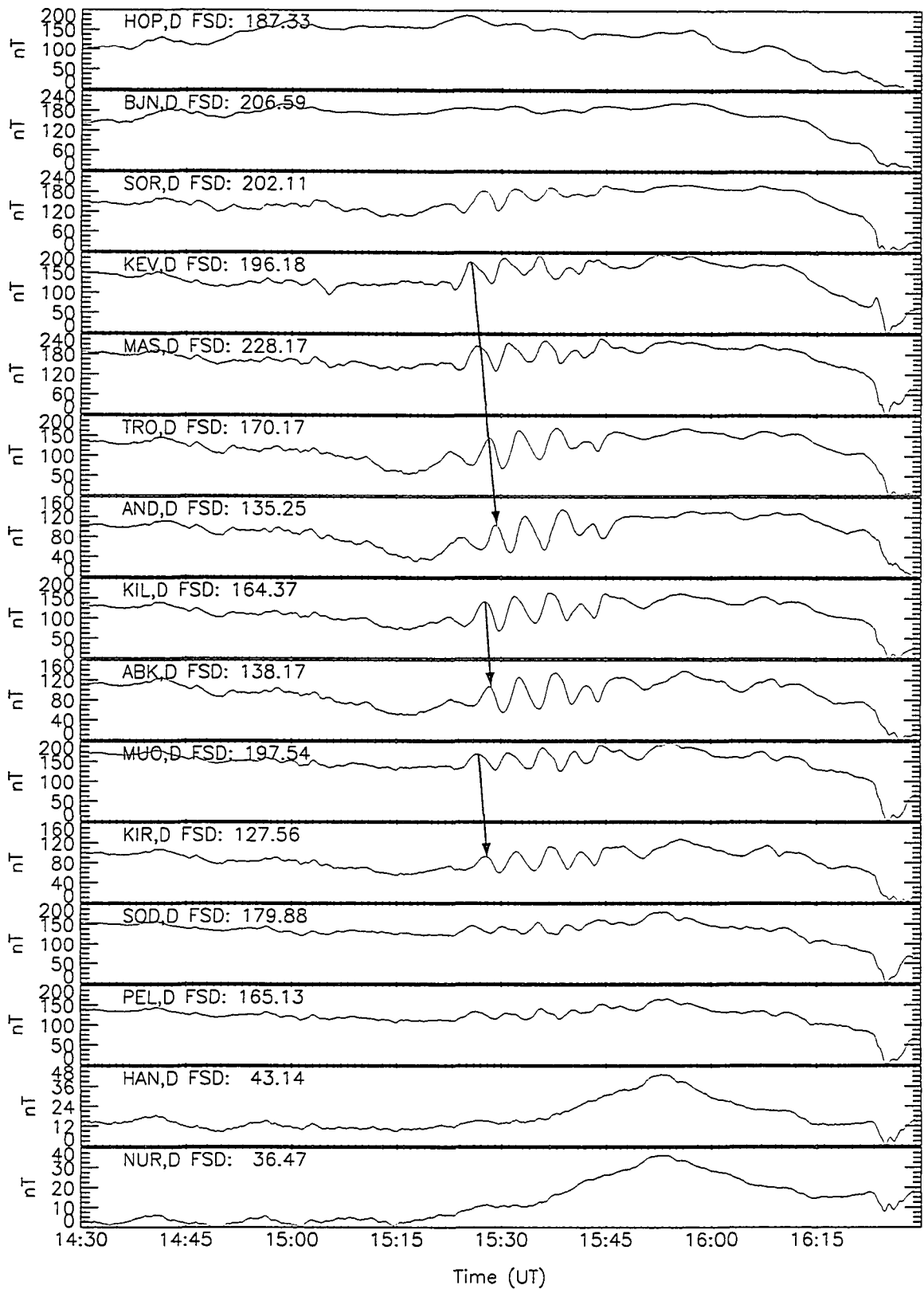


Figure 4.6: Unfiltered D-component data for the same interval and in the same format as Figure 4.5. Red arrows illustrate the westwards phase motion of the pulsation.

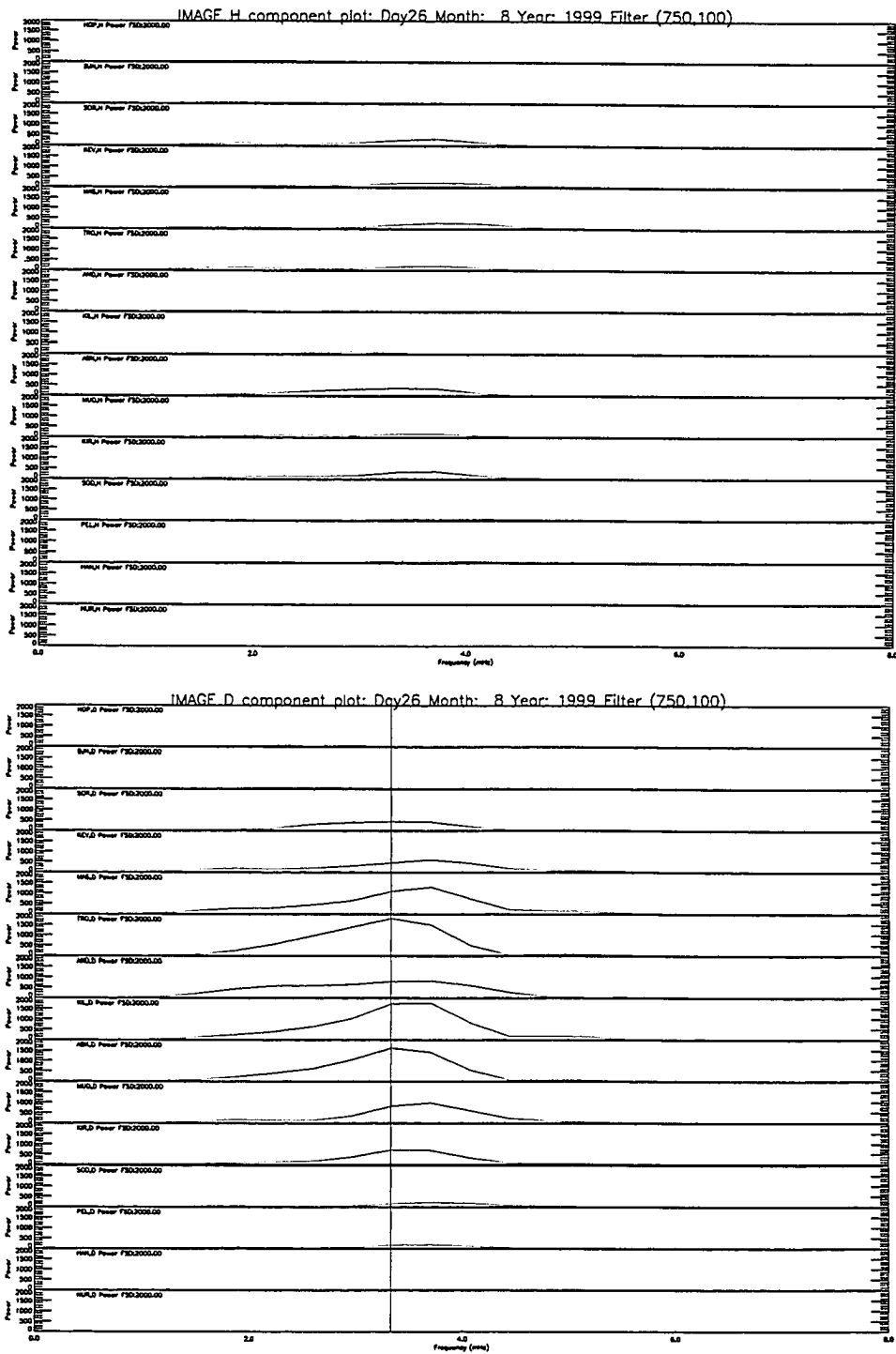


Figure 4.7: H- (upper panel) and D -(lower panel) component power spectra for IMAGE magnetometer stations for the interval 1515 to 1600 UT. The spectra in each panel are plotted on the same scale so that the relative spectral power at differing stations may be easily compared. The red line on the D component spectra corresponds to the frequency at which the largest amplitude was observed at the station with the highest power (TRO).

We may investigate the latitudinal power and phase of the wave by using the technique of complex demodulation (see e.g., Banks, 1975 and Chapter 3 of this thesis). A central frequency of 3.3 mHz was selected from the FFT analysis, and the instantaneous amplitude of oscillation at this frequency for the time period 1520 to 1550 UT was computed. Again the timeseries were filtered between 750 and 100 seconds to remove any high or low frequency oscillations not of interest here. Figure 4.8 displays the instantaneous amplitude of oscillation for each magnetometer station plotted versus the latitude of the station, with the H-component represented with a dotted line and the D-component with a solid line.

The error bars in Figure 4.8 are due to the maximum amplitude of the wave lasting for a finite interval, rather than the wave envelope maximising at one specific data point then decreasing again. Due to this range of maximal amplitudes, two demodulates were selected to compute the power and phase profiles of the wave, so that the error bars represent the deviation of these two instantaneous values from the mean of the two.

In Figure 4.8 the D-component is clearly confined between 61° and 71° magnetic latitude, with a peak amplitude of 62 nT at a magnetic latitude of 67° ($L=8.3$). The H-component is similarly confined in latitude, however the peak amplitude is half that of the D-component, and the H-component also exhibits a double peaked nature, with minimal amplitude in the H-component at the same location in latitude as the maximum in the D-component. For a poloidally polarised Pg, Chisham *et al.* (1997) attributed this double peaked H-component signature to be a required characteristic for these perturbations to keep $\nabla \cdot \mathbf{b} = 0$, and we discuss this later in this Chapter. Following the rotation of approximately 90° of Alfvénic waves by the ionosphere (e.g., Hughes and Southwood, 1976b) the D-component would represent a poloidal magnetic disturbance in the magnetosphere, with the H-component representing a toroidal oscillation.

The technique of complex demodulation was also used to compute the phase profile of the wave versus latitude, and these profiles are displayed in Figure 4.9. The upper panel represents the H-component phase, with the lower panel displaying the D-component phase profile. The blue lines in Figure 4.9 are the results of the complex demodulation analysis, with the red lines representing the phase profile corrected for the m number of the wave (see later in this Chapter for a discussion of the technique used to correct for m). The D-component phase profile displays a general trend of a 180° phase change across the resonant

Power versus latitude plot for H and D components

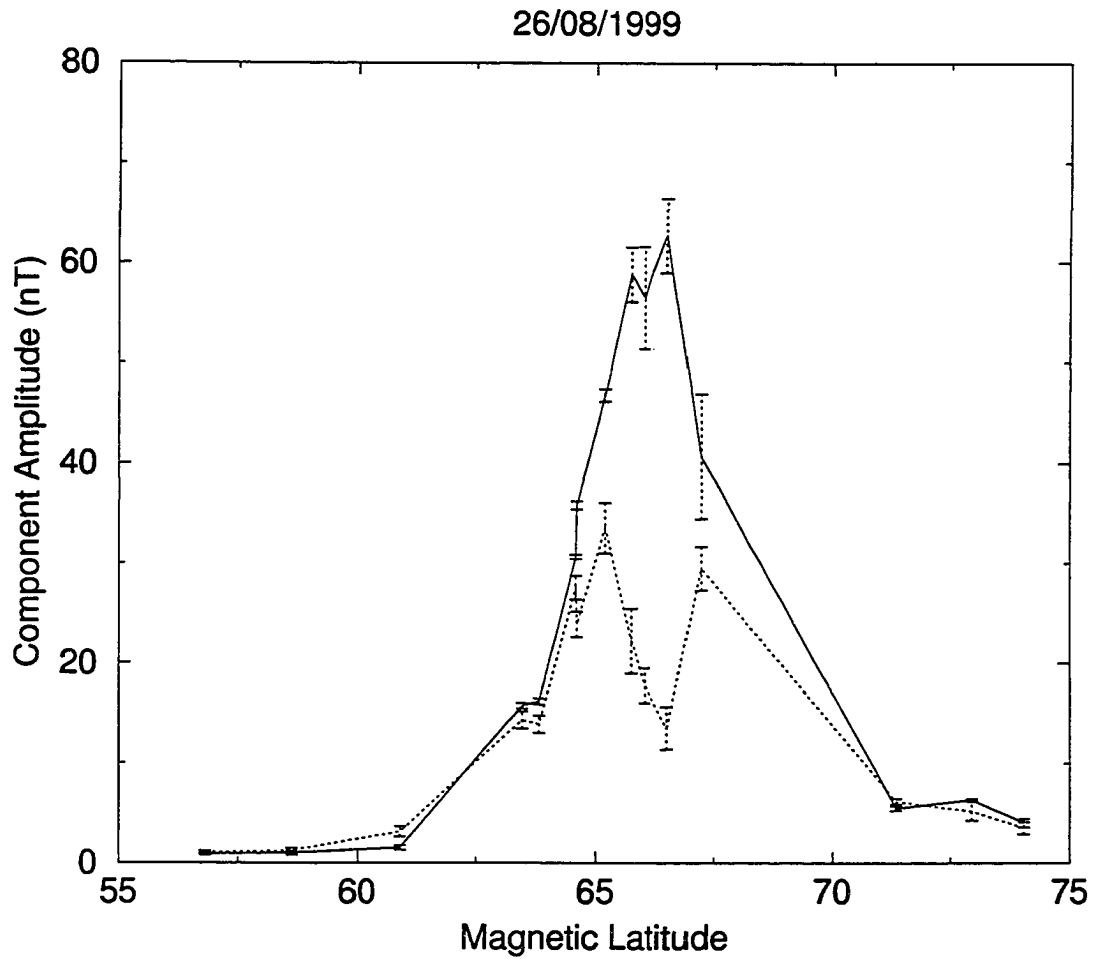


Figure 4.8: Latitudinal power profiles for the H- and D-components of the wave (dotted and solid lines, respectively).

latitude of 67° , although the points themselves are somewhat scattered. This 180° phase change across the latitude of peak oscillation is typical of field line resonance (see e.g., Southwood, 1974). The H-component phase profile exhibits a phase change of more than 180° across the resonant latitude, and this will be discussed in detail later in this Chapter.

The station chain KEV-MAS-TRO-AND are aligned (to a good approximation) along the same magnetic latitude, and Figure 4.6 clearly shows the propagation of the first wavefront from the easternmost station, Kevo, to the westernmost, Andenes. This effect is also evident in other station chains (notably between Kilpisjärvi and Abisko, KIL and ABK, respectively, and Muonio and Kiruna, MUO and KIR, respectively). We expect to observe a 180° phase change across the resonant latitude of the oscillation, see e.g., Samson *et al.* (1971), and so care must be taken to differentiate between longitudinal effects (due to the propagation of the wave) and latitudinal effects (due to the FLR). These large longitudinal phase effects inevitably mask the classical latitudinal phase change associated with field line resonance. Using phase differences between eight pairs of longitudinally spaced magnetometer stations (namely the stations in the chains of KEV-MAS-TRO-AND, KIL-ABK and MUO-KIR) the azimuthal wavenumber of the wave was found to be -25 ± 3 , where the error is taken as being two standard deviations from the mean value. This indicates that the phase propagation of the wave was westwards, i.e., in the same direction as the gradient-curvature drifts of protons in the ring current.

Due to the small error in the calculation of m , we may attempt to correct the latitudinal phase profiles (the blue lines in Figure 4.9) to remove any longitudinal phase effects. The complex demodulation analysis yielded instantaneous values of the phase of the wave during its period of maximum oscillation (i.e., at exactly the same UT), so that these phase measurements are all relative to each other. Thus, if we know the longitudinal separation between two stations, we may compute the phase difference due to the azimuthal wavenumber between these two stations, and thus remove any phase variations due to the azimuthal structure of the wave. It was decided to compute the phase difference due to the azimuthal phase variation (i.e., m) between every station and the station at Tromsø, and correct each phase measurement from the complex demodulation analysis to effectively map each station to a constant longitude, that of the Tromsø station. These corrected phase measurements are plotted as the two red lines in Figure 4.9, and are due to the latitudinal

H and D phase versus latitude

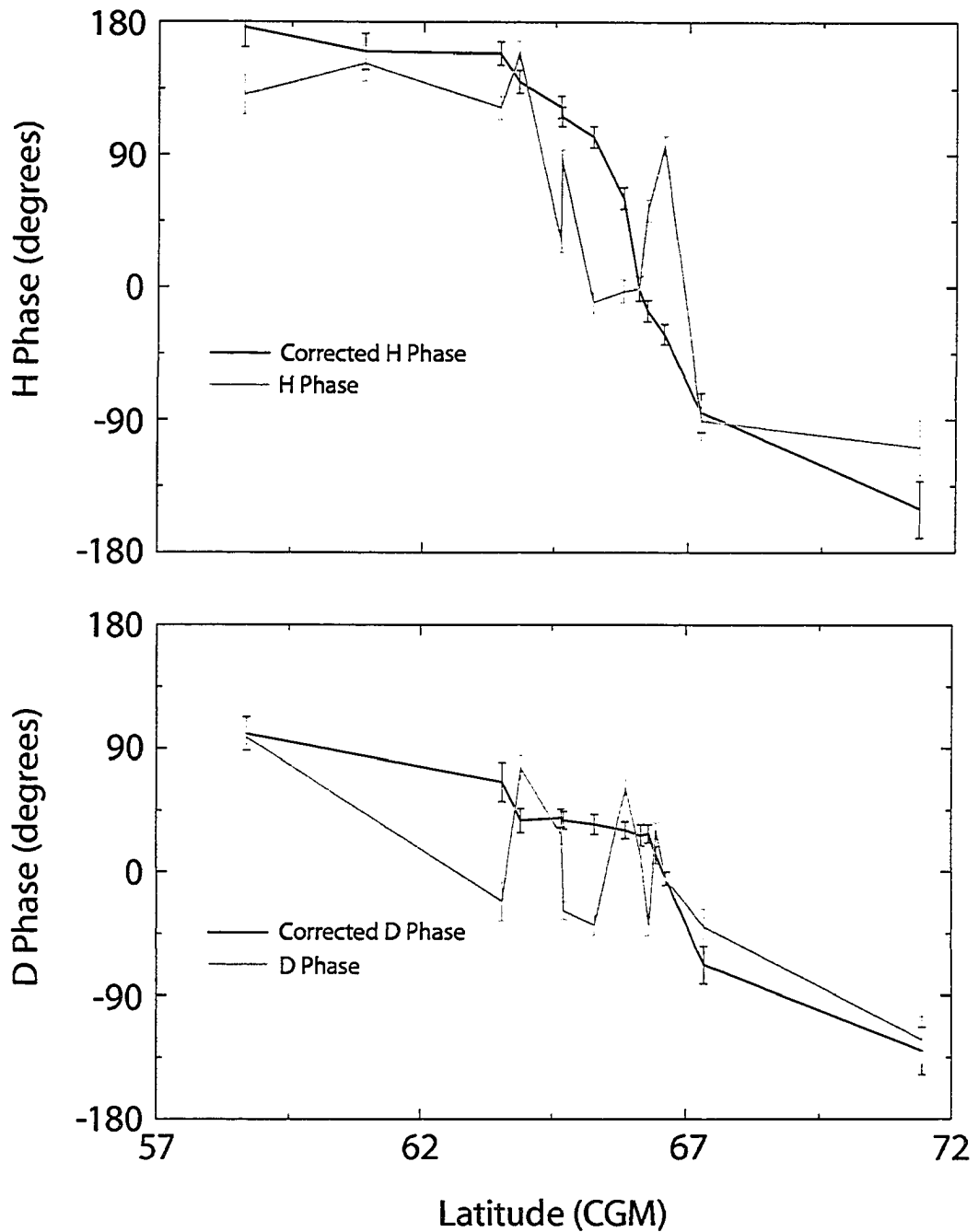


Figure 4.9: Latitudinal phase profile for the H- and D-components of the wave. Blue lines indicate uncorrected measurements, red lines represent phase measurements corrected for m value.

structure of the field line resonance only.

In Figure 4.9 it is clear that the wave phase has become extremely well-behaved with monotonic phase variation after the application of a phase correction due to a single m number. This implies that as well as being extremely localised in latitude, the wave is very coherent in azimuth and probably has a very narrow m -value spectrum. Thus the wave is very monochromatic and coherent in both ω and m .

Although the wave exhibits a clear, well defined peak in amplitude at the resonant latitude, and an expected 180° phase change across this latitude in the D-component, the H-component exhibits a double peaked amplitude profile, with an associated phase change of approximately 270° . One explanation for this is if $\nabla \cdot \mathbf{b} = 0$ in the magnetosphere and $b_z = 0$, as is appropriate for an Alfvénic wave in a box model magnetosphere (c.f. Southwood, 1974), then

$$\frac{\partial b_x}{\partial x} + imb_y = 0 \quad (4.2)$$

thus

$$b_y(x) \sim -\frac{\partial b_x}{\partial x} \quad (4.3)$$

i.e., $H \sim -\partial D/\partial \lambda$ (see the discussion by Chisham *et al.*, 1997). This implies that for an amplitude profile in the D-component that may be approximated via a Gaussian, the corresponding H-component amplitude profile will be double peaked in nature. This relation will be expanded upon in Section 4.3 of this Chapter to explain the ionospheric response to a poloidal FLR that has an m number of around 25.

4.2.3 STARE Radar Data

Between 1500UT and 1600UT oscillations in the E region of the ionosphere were detected by the Scandinavian Twin Auroral Radar Experiment (STARE). Figure 4.10 shows time-series plots for the STARE Hankasalmi and Trondheim radars. The plots are in units of backscatter power, which is believed to be a proxy for the line of sight velocity [Yeoman and Wright, 2001], as the line of sight velocity data had more data gaps. Power spectra produced from the timeseries of the STARE backscatter power data (Figure 4.11) indicate that

the frequency spectra of the wave observed by STARE peaked at 3.3 mHz, which agrees extremely well with the magnetometer observations. Further, the Fourier phase produced from an FFT of a timeseries from an individual range gate of the STARE radar may be compared to a phase measurement from an adjacent range gate in longitude, to compute the azimuthal wavenumber, m . The Fourier phase from range gates that map to between 65° and 68° magnetic latitude was computed for both STARE radars, so that the m -value for the observed wave could be calculated by comparing the longitudinal phase difference between range gates of known longitudinal position. These measurements indicated that for the wave observed by the STARE radars, m was equal to -28 ± 7 , with the error representing one standard deviations from the mean value. This is clearly in excellent agreement with the m -value calculated from the magnetometer dataset.

The STARE radar also facilitates the production of merged vector fields, displaying 2D vector electron velocities and electric fields in the E-region ionosphere. These data allow us to further investigate the ionospheric response to the ULF wave. Figure 4.12 shows STARE merged velocities at 1545:00 UT as derived from the line of sight velocities of each radar. A running mean of duration 600 seconds has been removed from the data, and the timeseries for each range gate have been filtered between 200 and 500 seconds. A clear discontinuity exists between 69 and 70 degrees geographic latitude, which corresponds to the resonant latitude of approximately 67° CGM of the driven FLR determined from the magnetometer data. This discontinuity clearly exhibits the typical 180 degree phase change across the resonant latitude. Due to the differing directions of geographic and geomagnetic north, the discontinuity at the resonant latitude is observed to occur at differing latitudes geographically as one moves in longitude.

Figure 4.13 is of the same format as Figure 4.12 but for 1537:20 UT, and clearly shows vortex-like flow patterns of the ionospheric plasma between 18.5 and 27.0 degrees longitude and 68.5 and 71.0 degrees latitude (geographic). Previous and subsequent convection maps (not shown) show that the vortical structure propagates westwards through the STARE field of view, in the same direction as the azimuthal wavenumber, m , and the gradient-curvature drift of ions in the ring current. Interestingly, an m value of -26 implies a westwards propagating wave with a wavelength scale size of 14.4 degrees in azimuth. Figure 4.13 shows that half an azimuthal cycle covers approximately $(25^\circ - 18^\circ) = 7^\circ$ in

STARE Parameter Plot

Hankasalmi (top) and Trondheim (bottom) Backscatter Power

26 Aug 1999⁽²³⁸⁾

to

27 Aug 1999⁽²³⁹⁾

unknown scan mode (0)

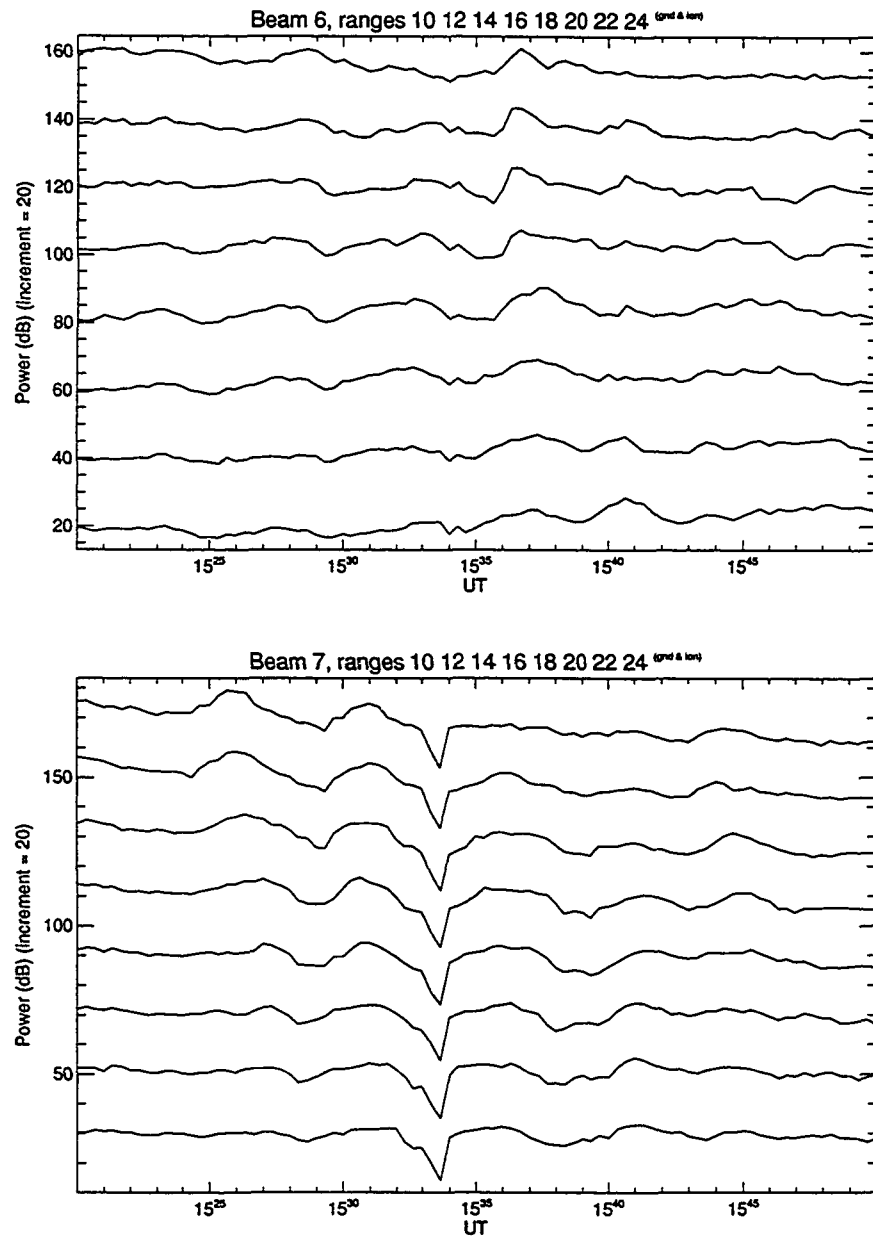


Figure 4.10: Stacked timeseries for the two STARE radars. The plotted parameter is backscatter power for alternate range gates between 10 to 24 for beam 6 of the Hankasalmi radar (upper panel), and beam 7 of the Trondheim radar (lower panel). Latitudinal coverage is 65° to 68° for the upper panel, and longitudinal range is 101° to 104° for the lower panel.

Hankasalmi (left) and Trondheim (right) Power Spectra

Range Gates 10 (top) to 20 (bottom)

26 Aug 1999 ⁽²³⁸⁾
10
27 Aug 1999 ⁽²³⁹⁾
unknown scan mode (0)

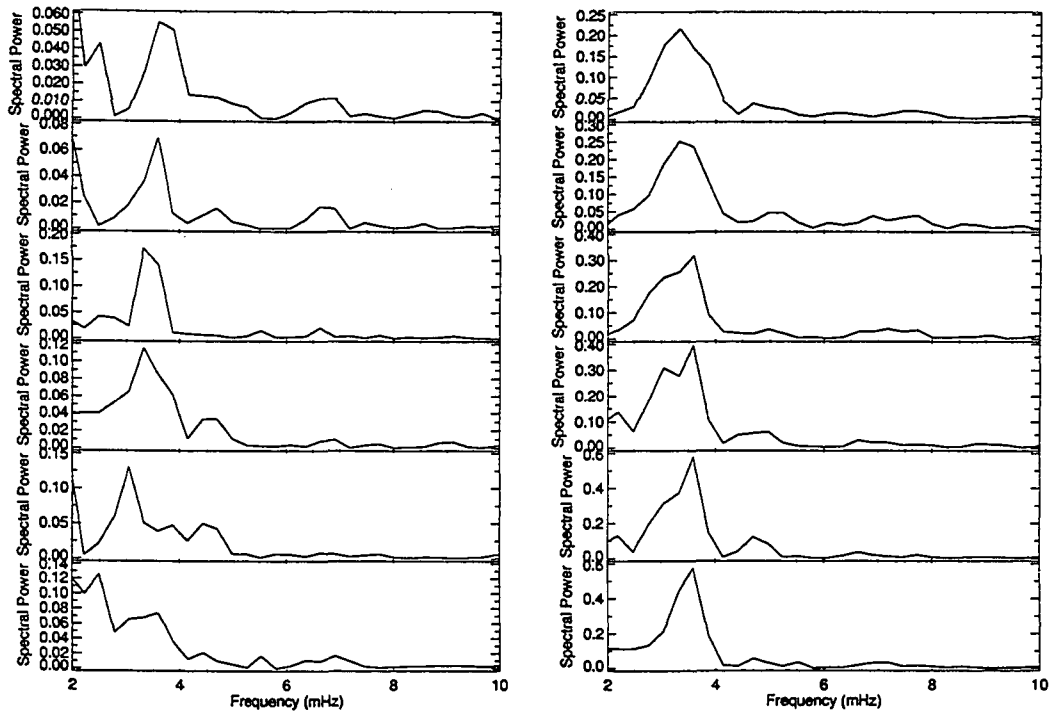


Figure 4.11: Power spectra for beam 6 of the Hankasalmi STARE radar (left column) and beam 7 of the Trondheim STARE radar (right column). Spectra are stacked for range gates 10 through 20, even numbered gates only, with the nearest range gates at the top and farthest at the bottom.

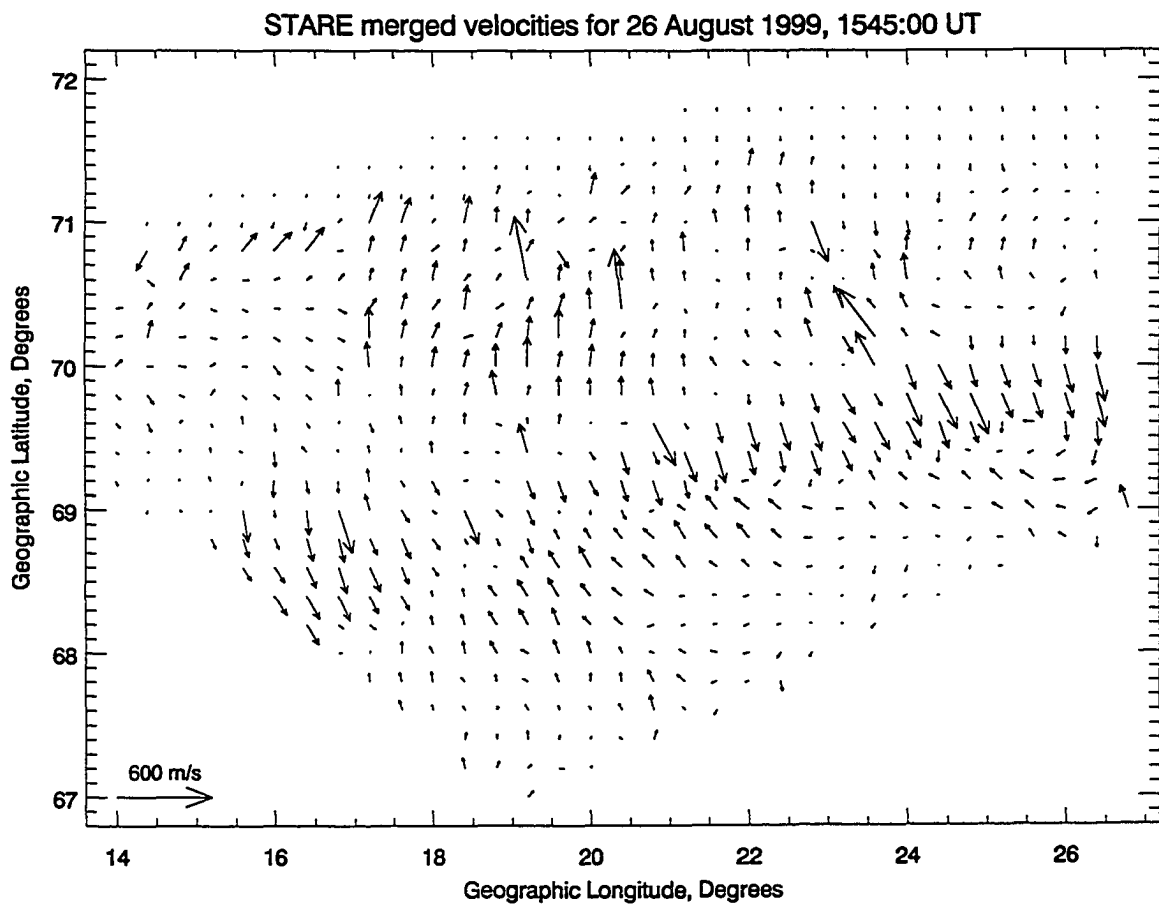


Figure 4.12: STARE merged velocities for 1545:00 UT on the 26 August 1999.

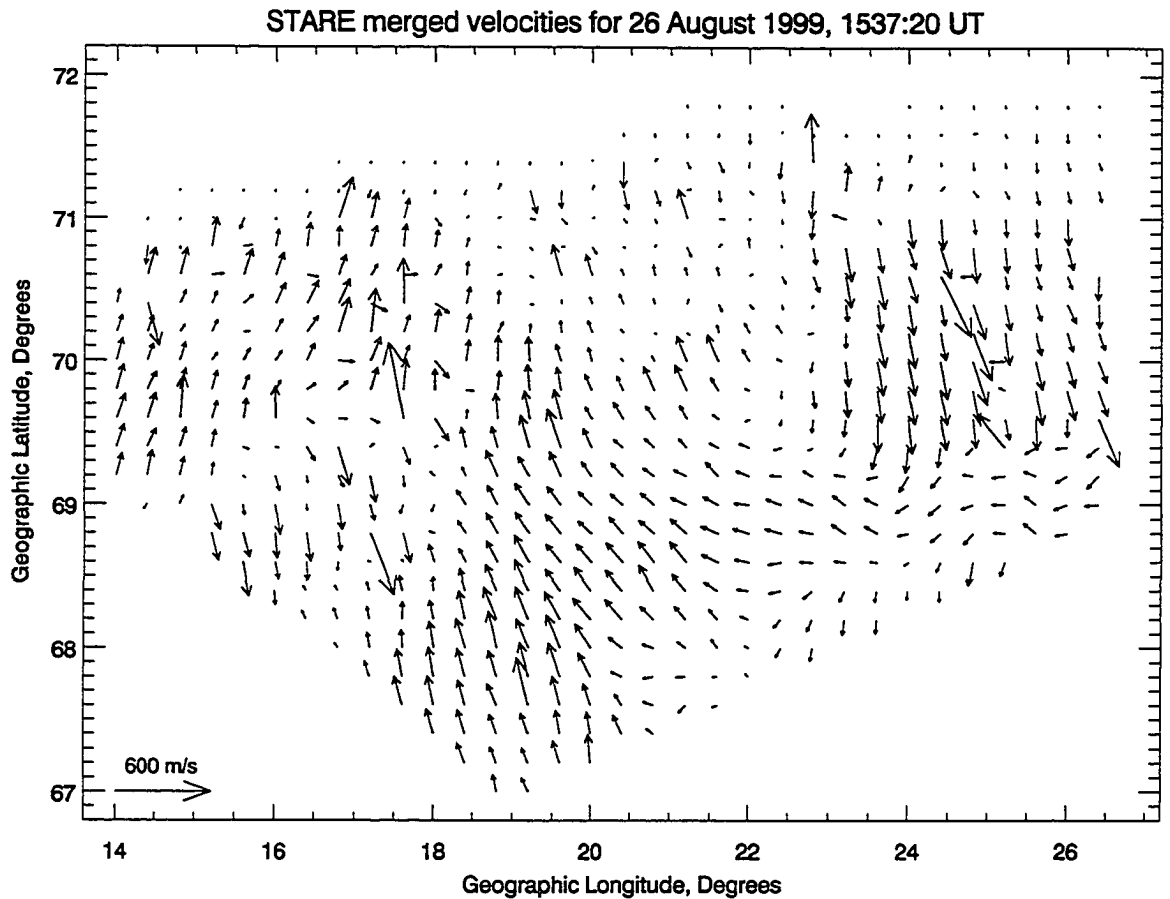


Figure 4.13: STARE merged velocities for 1537:20 UT on the 26 August 1999.

geographic longitude, which is in excellent agreement with the magnetometer derived m -value.

If we assume that the electric field of the wave is related to the velocity perturbation and the background magnetic field by

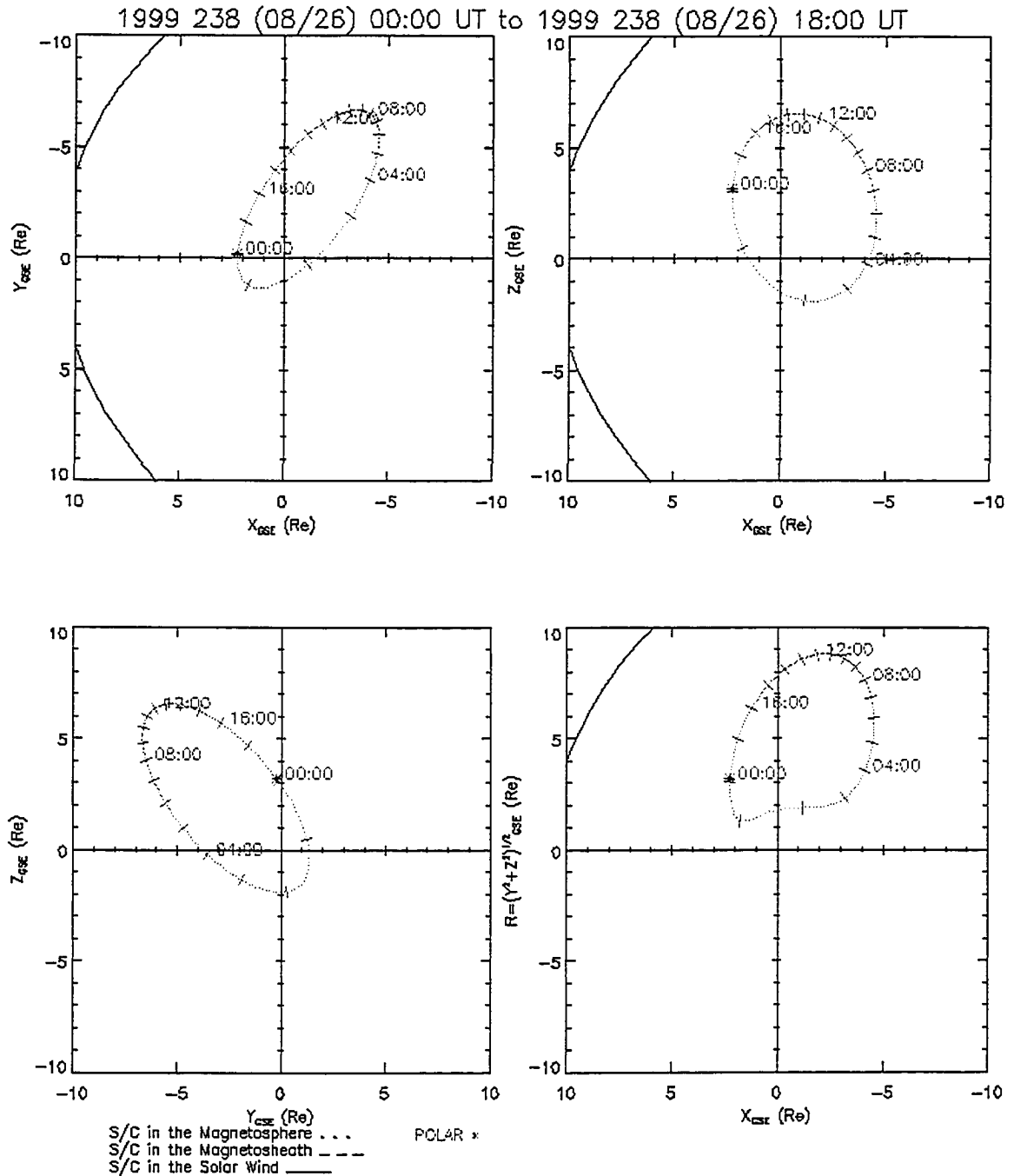
$$\mathbf{E} = -\mathbf{v} \times \mathbf{B}_0 \quad (4.4)$$

then the dominant north-south flows observed in Figure 4.12 correspond to an electric field that is east-west polarised in the ionosphere and magnetosphere. This can be attributed to a poloidal mode oscillation where $\delta\mathbf{B}$ is radial in the magnetosphere and is contained within the D-component on the ground. The predicted ionospheric flow of a purely poloidal oscillation will be discussed in detail in Section 4.3 of this Chapter and compared to the observed ionospheric signatures.

4.2.4 Polar CAMMICE Data

To investigate whether the field line resonance observed in Sections 4.2.2 and 4.2.3 was driven by an interaction with energetic particles in the ring current, we need in-situ plasma measurements at the correct magnetic L-shell before and after the FLR. Between the intervals 0330-0430 and 2100-2300 UT on the 26th August 1999 the Polar satellite crossed the ring current in the equatorial plane on L-shells of between 4.8 and 6.6, as determined from a dipolar magnetic field model. The orbital configuration of Polar for two orbits, starting at 0000 UT on the 26th August 1999 are displayed as projections into the GSE x-y, x-z and y-z planes in Figures 4.14 and 4.15. Also shown is the radial distance from the Sun-Earth line. At 0330 UT on the 26th August 1999 Polar passed through the ring current at a distance of $L=4.8$ at a magnetic local time of approximately 0300. As it moved northwards through the ring current, it also moved in L, leaving the ring current at 0430 UT at $L=6.6$ (as determined by the plasma ion number density) and still at approximately 0300 MLT. On the next orbit, Polar crossed through the ring current at the same L-shell and magnetic local time, however due to the 18 hour period of the Polar orbit the crossing occurred between 2100 and 2300 UT. The observations of the FLR described in Sections 4.2.2 and 4.2.3 occurred between 1520 and 1550 UT on the same day, at an MLT of between 1320 to 1350. Thus any ring current observations from Polar from the correct L-shell will either be around 12 hours before or 6 hours after the FLR. However, we may expect some ring current particles drifting around the Earth to be on closed orbits, i.e., they don't become lost to the solar wind at the magnetopause. Hence if ring current ions drive the wave it may be possible to observe an unstable energy distribution in ring current ions before the FLR, with no unstable energy distribution afterwards (if indeed the FLR is being driven by an unstable energy distribution in ring current ions).

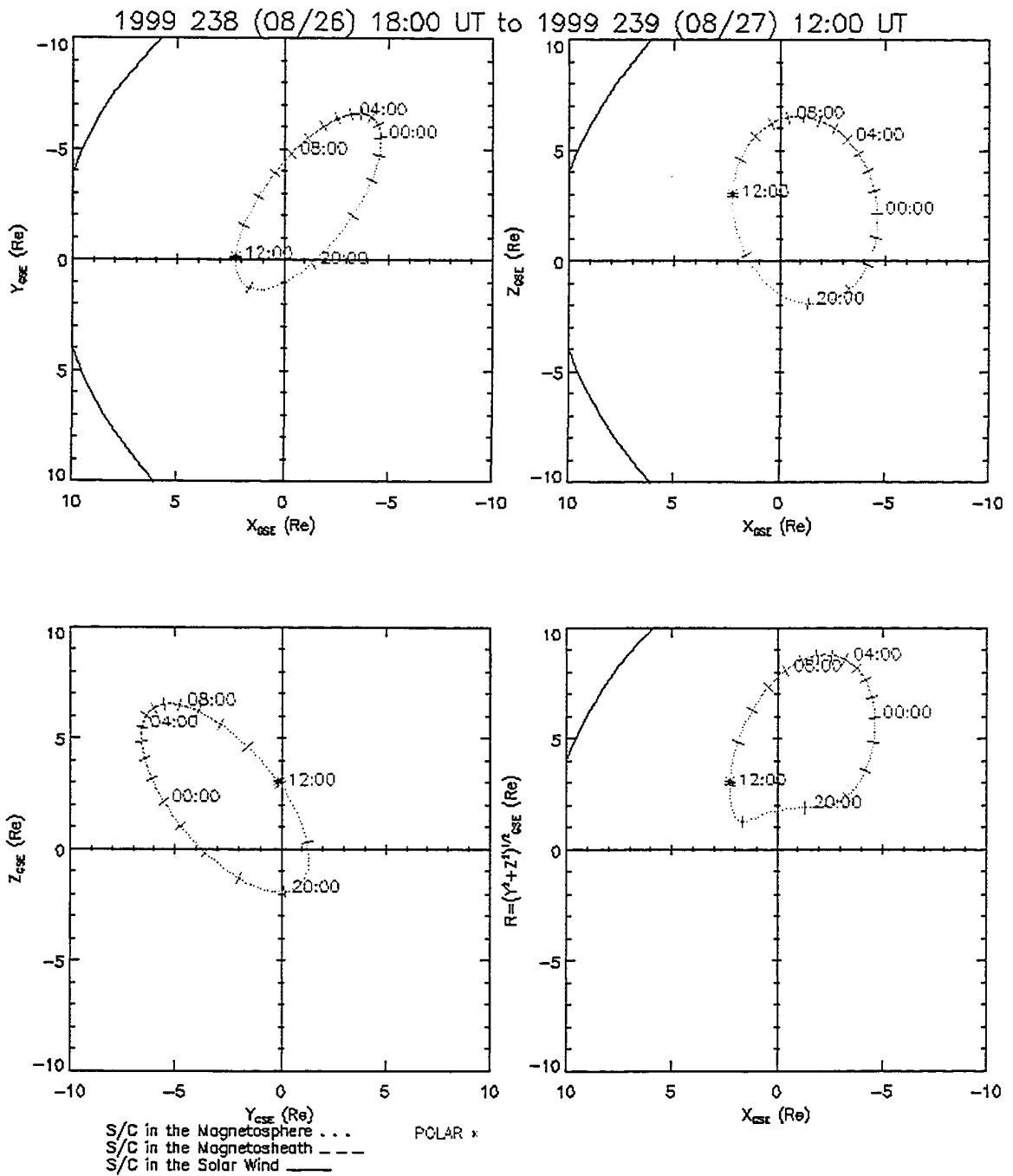
The plots in the left panel of Figure 4.16 display Polar ion distribution functions (IDFs) from the CAMMICE instrument for 0330 to 0430 UT on the 26th of August 1999. The measured flux is based on the dual coincidence rate (DCR) which is a measure of the total flux of singly charged ions. The measured flux is then converted into phase space density, f . These two conversions are performed by first applying a correction to each of the 25 energy channels, which is instrument specific and dependent upon the energy of the channel, the field of view of the instrument, and the efficiency of the detector at the particular energy



Generated by SSCweb on: Tue Jun 21 09:44:54 2005

Solar Wind Pressure=2.1nP IMF BZ=0.0nT

Figure 4.14: Orbital configuration of the Polar satellite for one orbit starting at 0000 UT on the 26th August 1999. Upper left panel is the projection into the GSE x-y plane, the upper right panel is the projection into the GSE x-z plane, the lower left panel is the projection into the GSE y-z plane and the lower right panel is the radial distance of the satellite from the center of the Earth. Plot provided by SSCWEB at <http://sscweb.gsfc.nasa.gov>.



Generated by SSCweb on: Tue Jun 21 09:46:14 2005

Solar Wind Pressure=2.1nP IMF BZ=0.0nT

Figure 4.15: Orbital configuration of the Polar satellite for the orbit immediately after that in, and in the same format as, Figure 4.14. Figure provided by SSCWEB at <http://sscweb.gsfc.nasa.gov>.

of the channel. The resultant flux is then combined with a magnetic field model, which is used to determine f . The CAMMICE instrument can construct an IDF over a period of 204 seconds, and each trace in Figure 4.16 is built up over this period of time. The IDFs in Figure 4.16 are incremented in increasing powers of ten, i.e., the second trace is offset from the first by 10^1 , the second by 10^2 etc. and the lowest L-shell is at the bottom of the panel. A positive gradient in the energy distribution is observed between approximately 20 and 40 keV in all of the plots in the left hand panel. The right hand panel of Figure 4.16 displays data from the orbit after that in the left panel, in the same format. It is clear that the bump in the energy distribution between 20 and 40 keV is reduced in the later interval, which also displays a lower flux of particles at all energies.

4.3 Discussion

A ULF wave was observed in the IMAGE magnetometer network between 1525 and 1550 UT on the 26th of August 1999. The largest amplitude oscillations were observed in the magnetic D-component, and the latitudinal extent of the wave was approximately 8° (i.e., between Bear Island and Pello). The azimuthal wavenumber of the wave, as determined by longitudinally separated magnetometer stations was -25 ± 3 , which indicates that the phase propagation of the wave was westwards, i.e., in the same direction as the gradient curvature drifts of protons in the ring current. The frequency of the oscillation was found to be 3.3 mHz, i.e., in the Pc5 band. The data further show that the resonant latitude of the wave was 67° (magnetic), with a double peak in the H component centered at the same point. This double peaked nature of the H component has previously been observed in a statistical study of Pgs by Chisham *et al.* (1997). The explanation for the dip in the H-component amplitude at the latitude of the maxima of the D-component amplitude is explained via the MHD wave equation for the poloidal and toroidal mode. For a box-model magnetosphere with $\nabla \cdot \mathbf{b} = 0$ and $b_z = 0$ the poloidal mode amplitude envelope may be assumed to be described via a Gaussian. The toroidal mode is then simply described by the derivative of this Gaussian (c.f. Equation 4.5), which must have a trough at the Gaussian maxima. The ionospheric response to such a wave will be discussed and modelled later in this Section.

The wave was also observed in the field of view of the two STARE radars, as an os-

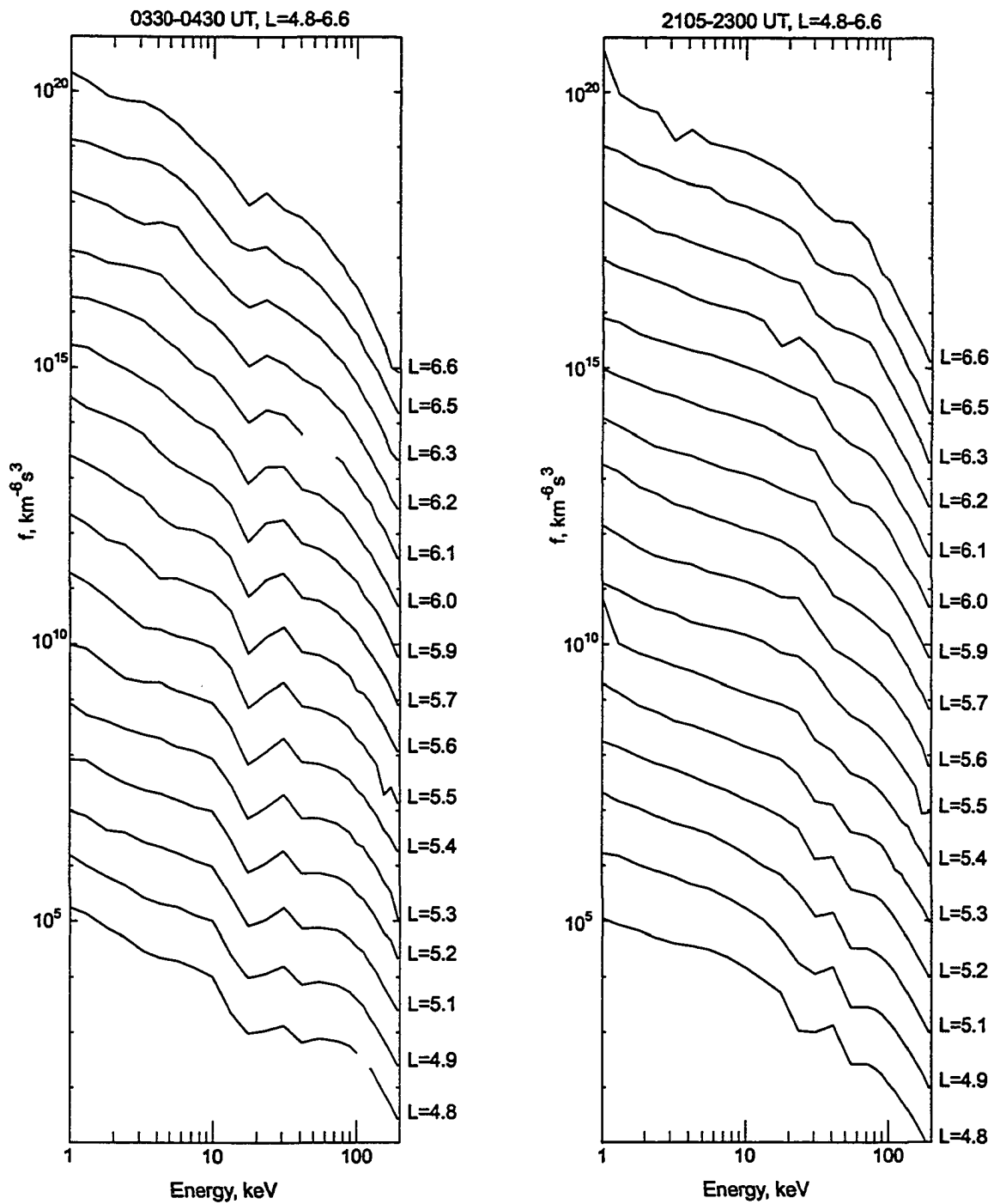


Figure 4.16: Polar CAMMICE ion distribution functions (IDFs) from two consecutive orbits on the 26 August 1999. Timeseries are offset by increasing powers of 10, and the lowest trace in each panel corresponds to the lowest L-shell, as determined by the Tsyganenko 96 model (Tsyganenko and Stern, 1996a).

cillating signature in the backscattered power (believed to be a proxy for the line of sight velocity). The timeseries of the backscattered power was passed through a fast Fourier transform routine, which confirmed the frequency of the oscillation at just over 3 mHz. The coordinates of the range cells of STARE are known accurately, which allows the calculation of an average m value, for magnetically adjacent cells (via phase information derived from the FFT of the raw timeseries). The m value derived from the STARE data was -28 ± 7 , i.e., the two different methods of m value analysis agree well with each other. This leads us to the conclusion that on certain occasions (i.e., when the azimuthal wavenumber is moderate) it is possible to use magnetometers to analyze relatively high- m particle driven field line resonance.

Merged velocities from STARE further illustrate the nature of the FLR, with a clear phase change across the resonant latitude, and transient, westwards propagating vortex-like flows with scale sizes of around eight degrees in longitude observed. Assuming that the azimuthal wavenumber of the FLR is around 25, we may expect a single azimuthal wavelength to subtend an angle of fifteen degrees in longitude, so that the observed scale size of the travelling vortices is around a half of the azimuthal wavelength of the FLR. Further, we may expect the vortices to occur in pairs [e.g., Zesta *et al.*, 2002a], so that the scale size of the pair of vortices is consistent with the scale size of the FLR in azimuth. Due to the limited field of view of STARE and the transient nature of the vortex events, it is unsurprising that the pair of vortices is not observed in the dataset together. However, the half azimuthal wavelength resolved within the STARE field of view is in excellent agreement with the magnetometer derived m -value.

As mentioned earlier, it is possible to use an MHD description of a poloidal mode field line resonance to investigate the ionospheric response to such a process. We begin by letting the north-south flow in the ionosphere due to a poloidal FLR be given by

$$v_{NS} = A(x) \exp(i\Phi(x)) \exp(im\phi) \quad (4.5)$$

where $A(x)$ is the amplitude profile of the poloidal mode in terms of the poloidal coordinate, x , $\Phi(x)$ is the phase profile of the poloidal mode, m is the azimuthal wavenumber and ϕ is the distance in longitude from the central latitude of the resonance. We assume a box-model magnetosphere with $\nabla \cdot \mathbf{b} = 0$ and $\mathbf{b}_z = 0$ so that

$$\frac{\partial \mathbf{b}}{\partial t} = -\nabla \times \mathbf{E} = \nabla \times (\mathbf{v} \times \mathbf{B}_0) \quad (4.6)$$

as $\mathbf{E} = -\mathbf{v} \times \mathbf{B}_0$. Now,

$$\mathbf{v} \times \mathbf{B}_0 = \begin{pmatrix} v_x \\ v_y \\ 0 \end{pmatrix} \begin{pmatrix} 0 \\ 0 \\ B_0 \end{pmatrix} = \begin{pmatrix} v_y B_0 \\ -v_x B_0 \\ 0 \end{pmatrix} \quad (4.7)$$

so we may finally write

$$\begin{aligned} \frac{\partial \mathbf{b}}{\partial t} &= \begin{vmatrix} \hat{i} & \hat{j} & \hat{k} \\ \partial/\partial x & \partial/\partial y & \partial/\partial z \\ v_y B_0 & -v_x B_0 & 0 \end{vmatrix} \\ &= \hat{i} \frac{\partial v_x B_0}{\partial z} + \hat{j} \frac{\partial v_y B_0}{\partial z} + \hat{k} \left(-\frac{\partial v_x B_0}{\partial x} - \frac{\partial v_y B_0}{\partial y} \right). \end{aligned} \quad (4.8)$$

If $b_z = 0$ then $\partial v_x / \partial x = -\partial v_y / \partial y$ for a box model, with $B_0 = \text{constant}$. So we may write

$$v_y = \frac{-1}{im} \frac{dv_x}{dx} = \frac{i}{m} \frac{dv_x}{dx}. \quad (4.9)$$

Using the above Equation we may substitute in the differentiated form of the velocity perturbation described in Equation 4.5 to yield the velocity perturbation in the y -direction

$$v_y = \frac{i}{m} (A' + A\Phi') \exp(i\Phi(x)) \exp(im\phi). \quad (4.10)$$

Finally we take the real parts of Equations 4.5 and 4.10 to give

$$v_x = A(x) \cos(m\phi + \Phi(x)) \quad (4.11)$$

$$v_y = \frac{-1}{m} \{A' + A\Phi'(x)\} \sin(m\phi + \Phi(x)) \quad (4.12)$$

Thus with a prescribed form of $A(x)$ and $\Phi(x)$ we can produce a model of the expected 2D vector flow in the ionosphere due to a poloidal field line resonance. We assume that the amplitude and phase profiles are given by

$$A(x) = \exp - \frac{(x - x_0)^2}{\Delta x_1} \quad (4.13)$$

$$\Phi(x) = \tanh \frac{x - x_0}{\Delta x_2} \quad (4.14)$$

respectively, where x_0 is the location of the maxima of the Gaussian function in x , and Δx_1 and Δx_2 are the $1/e$ width of the Gaussian and the width of the tanh function respectively. In order to directly compare the model results with the observed STARE 2D velocity flows, we take a Gaussian and a tanh function centered on the middle row of a 26×33 matrix (the same size as the STARE velocity matrix), with a $1/e$ Gaussian width of 13 and a tanh width of 5, as shown in Figure 4.17. The corresponding derivatives of these two functions are required to compute the ionospheric velocity flows, and these are displayed in Figure 4.18.

The ionospheric flows produced by these amplitude and phase profiles are displayed in Figure 4.19. The scale size in longitude of the vortex-like structures in Figure 4.19 is determined purely by the m -value of the wave, with the model being normalised so as to represent the same field of view as the STARE merged vector plots in Figures 4.12 and 4.13. It should also be noted that the STARE merged velocity vectors in Figures 4.12 and 4.13 are presented in a geographic coordinate system (i.e., with the northwards direction towards the north geographic pole), whereas the model flows in Figure 4.19 are in a magnetic coordinate system (i.e., with the northwards direction towards the north magnetic pole). It is clear that the model results are in excellent agreement with the vortex structure observed in Figure 4.13.

The Polar CAMMICE data clearly show a positive energy gradient in the energy range 20 to 40 keV between 0330 and 0430 UT. By using the measured characteristics of the ULF wave, we can estimate the energy of particles required to produce such a wave, and compare this theoretical value to the data. Chisham (1996) expressed the angular frequency of drifting protons in the Earth's magnetosphere in terms of the gradient-curvature drift and the $\mathbf{E} \times \mathbf{B}$ drift of particles, and the angular frequency of the Earth's rotation. We utilize this equation to approximate the particle energy required to produce the observed FLR. After

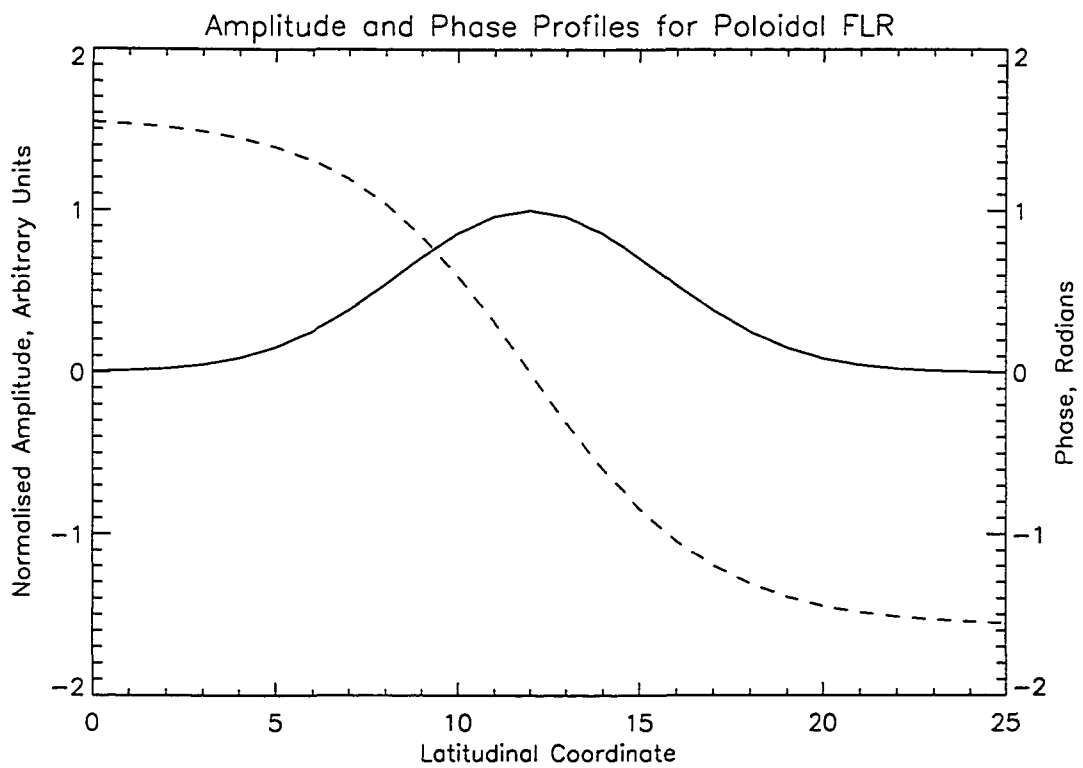


Figure 4.17: Amplitude (solid line) and phase (dashed line) profiles used to calculate model flows for a poloidal field line resonance.

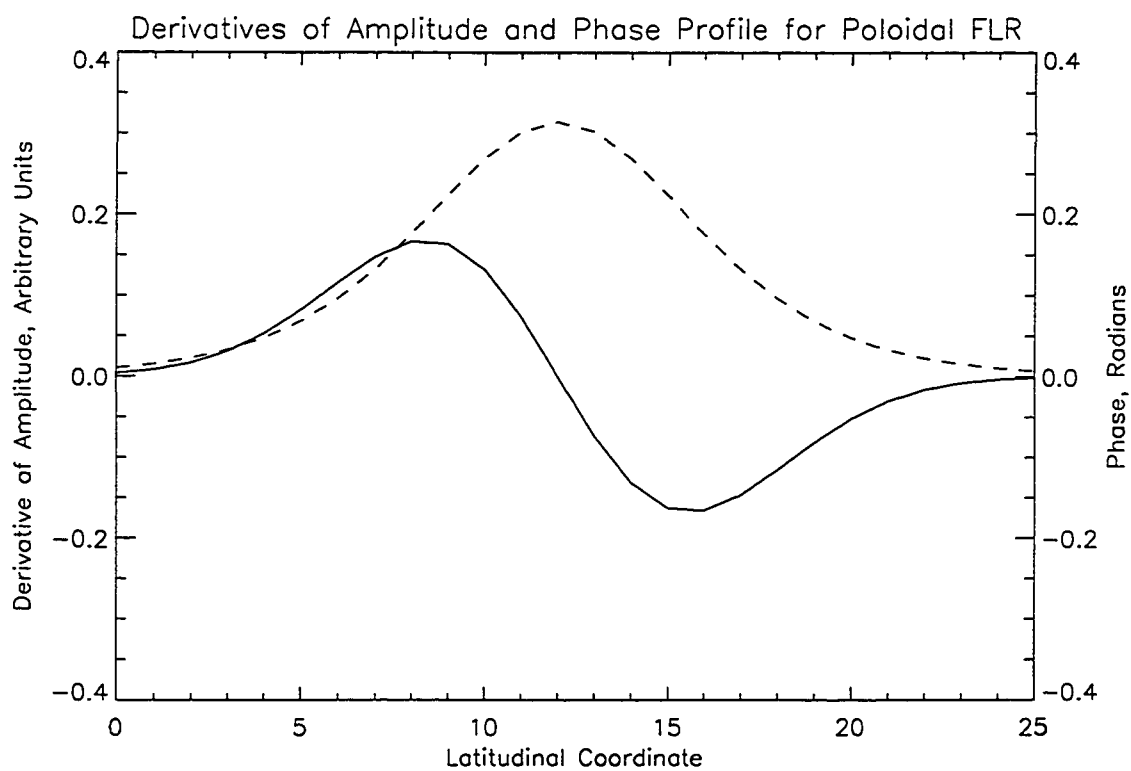


Figure 4.18: Derivatives of amplitude (solid line) and phase (dashed line) profiles used in computing ionospheric velocity flows due to a poloidal FLR.

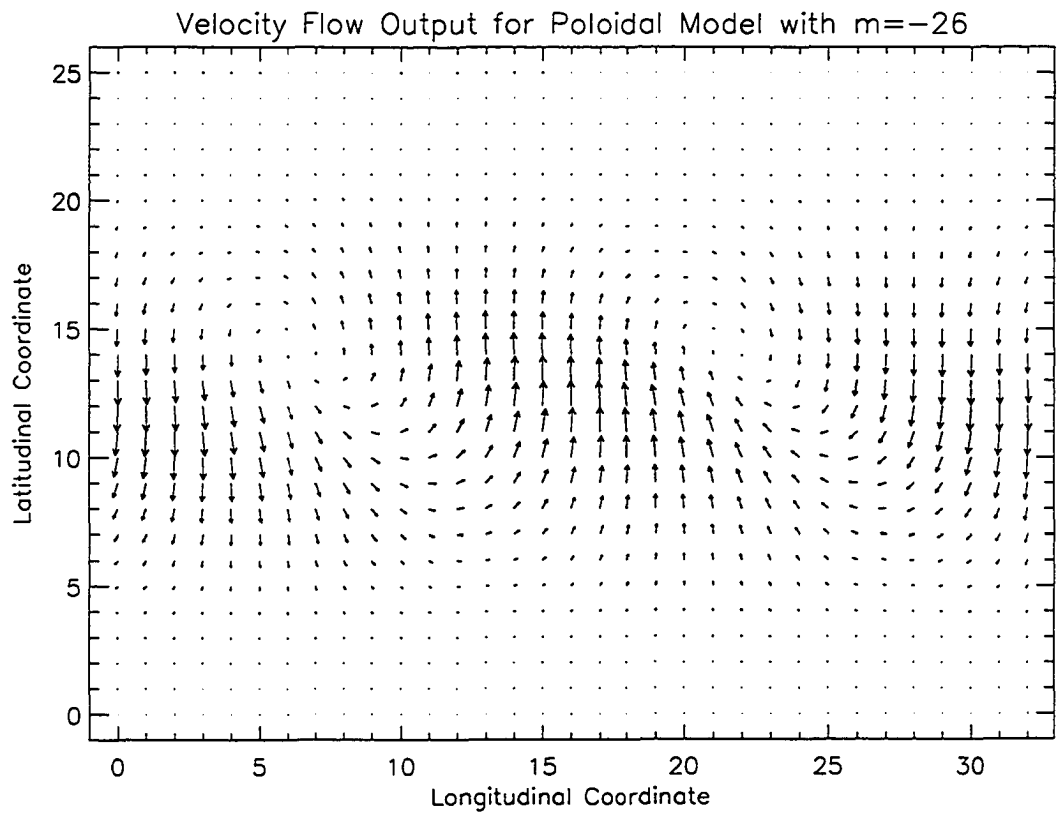


Figure 4.19: Model results for the 2D velocity flow structure in the ionosphere produced by a poloidal field line resonance.

Chisham (1996),

$$\omega_{drift} = -\frac{6WL(0.35 + 0.15 \sin \alpha)}{B_s R_E^2} + \frac{90(1 - 0.159K_p + 0.0093K_p^2)^{-3} L^3 \sin \phi}{B_s R_E^2} + \Omega_E \quad (4.15)$$

where W is the particle energy in eV, L is the particles L-shell, B_s is the equatorial surface magnetic field strength, R_E is the radius of the Earth, α is the particle equatorial pitch angle, ϕ the azimuth of the particle measured anticlockwise from local midnight, K_p the planetary magnetic index and Ω_E is the angular frequency of the Earth's rotation. By rearranging this equation, and substituting in $L = 8.3$, $B_s = 3.12 \times 10^{-5}$, $R_E = 6.371 \times 10^6$ m, $\alpha = 90^\circ$, $\phi = 225^\circ$, $K_p = 2$ and $\omega_{drift} = (\omega - N\omega_{bounce})/m = \omega/m$ (assuming $N=0$) with $\omega = 3.3 \times 10^{-3}$ mHz and $m = -26$, the particle energy, W , was calculated to be 38.2 keV for the $N=0$ resonance. Similarly, the high and low energy solutions to the $N=1$ resonance can be calculated (see Ozeke and Mann (2001)). It was found that protons of either 48.4 eV or 1.04 MeV could produce an $N=\pm 1$ resonance for this local time and K_p , so these two branches were ignored as a mechanism of wave production.

Recent work by Ozeke and Mann (2001) traced the trajectories of ions in the magnetosphere, with a view to investigating their relationship to drift and drift-bounce resonance excitation of ULF waves. Their technique involved solving for the guiding center motion of ions in a dipolar, time stationary magnetosphere and included the effects of the convection and radial co-rotation electric fields. This technique facilitates the production of open-closed orbit plots for protons, thus allowing the determination of whether a proton of a given energy at a specific local time and during a specific interval of K_p will be lost to the solar wind. Further, Ozeke and Mann (2001) solved the resonance equation for drift and drift-bounce resonance (Equations 4.1 and 4.15) using a model for the field line eigenfrequencies, ω , as a function of L -shell. Thus the combination of these two techniques allows one to predict the resonant energy of a particle-driven FLR on a given dipole L -shell, and whether the particles that may drive this FLR lie on closed or open trajectories. Using their techniques, we can use the universal time of the event and the planetary magnetic index, K_p , to produce a plot of all closed trajectories for protons. Furthermore, we superimpose a plot of all of the points that satisfy the $N=0$ drift resonance equation to ascertain whether the particles thought to produce the observed ULF wave are on open or closed trajectories

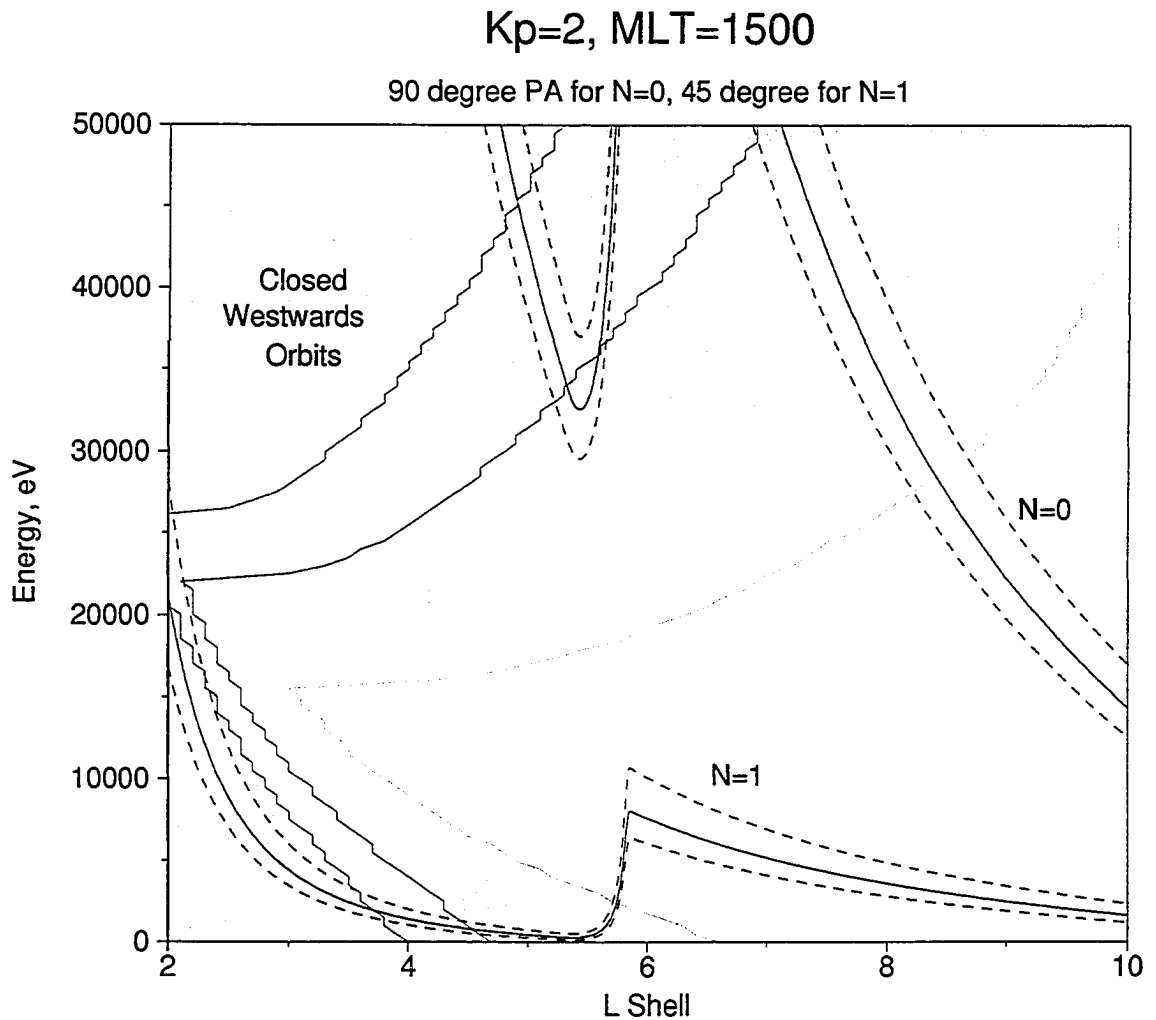


Figure 4.20: Plot of N=0 and N=1 resonance curves as a function of energy, W , and L -shell, superimposed onto open-closed orbit plot for $K_p=2$ and where shaded regions indicate closed orbits (see main text and Ozeke and Mann (2001) for more details). Dashed lines represent N=0 and N=1 resonance curves with a 25 percent difference on the equatorial plasma density. For reference, the open-closed orbit boundaries for K_p values of 1, 3 and 4 are plotted as green, red and blue lines respectively.

(Figure 4.20).

Figure 4.20 displays the N=0 and N=1 resonance curves calculated with the Ozeke and Mann (2001) model for a dipole magnetic field that has a density variation of r^{-6} along the field line, and that varies equatorially as L^{-3} inside the plasmasphere and L^{-4} outside of the plasmasphere. Figure 4.20 shows that for L=8, the predicted energy for protons to resonantly interact with an FLR is around 38 keV, and furthermore that these protons are on closed orbits, albeit very close to the open-closed orbit boundary (shaded areas in Figure 4.20 correspond to closed proton trajectories). We infer from these results that the drift time of these ring current particles is long – the closer the particle is to the open-closed orbit boundary the longer its orbit [Ozeke and Mann, 2001]. Indeed, by integrating the equation of motion, it is possible to compute the time taken for a particle of energy 38.2 keV to drift once around the Earth under the constraints of L and K_p , we observe for the FLR, and this was found to be 4.5 hours. Thus the particles in the “bump on tail” region of the energy distribution observed by Polar between 0330 and 0430 UT at a magnetic local time of 0300 return to the same MLT 4.5 hours later, after one complete orbit of the Earth, at 0800 to 0900 UT. This may occur again, so that the particles observed by Polar return to 0300 MLT between 1230 and 1330 UT, and finally take 2.25 hours to move round 12 hours of magnetic local time, so that between 1445 and 1545 UT the particles observed by Polar between 0330 and 0430 UT that exist in the unstable region of the energy distribution would have drifted to the around the same MLT location of the ULF wave, at the same time that the wave occurred. Furthermore, we can use the model of Ozeke and Mann (2001) to calculate the energy change of the particles as they drift around the Earth. Calculations show that ring current particles with an energy of 38.2 keV at L=8.3 at 1500 MLT will have an energy of around 28 keV at 0400 MLT (the magnetic local time of the Polar observations). However, it must be noted that the value of K_p strongly affects the location of the open-closed orbit boundary (as shown by the green, red and blue lines in Figure 4.20) as well as the resonance equation, so that the planetary average of $K_p=2$ may introduce large uncertainty in any energy calculation for drifting ions (see Figure 4.21).

Multiple particle orbits allow the loss of open orbit particles to the solar wind, so that a bump-on-tail distribution may be created at the open-closed orbit boundary. This is a likely explanation for the formation of the bump observed in Figure 4.16, which occurs at the

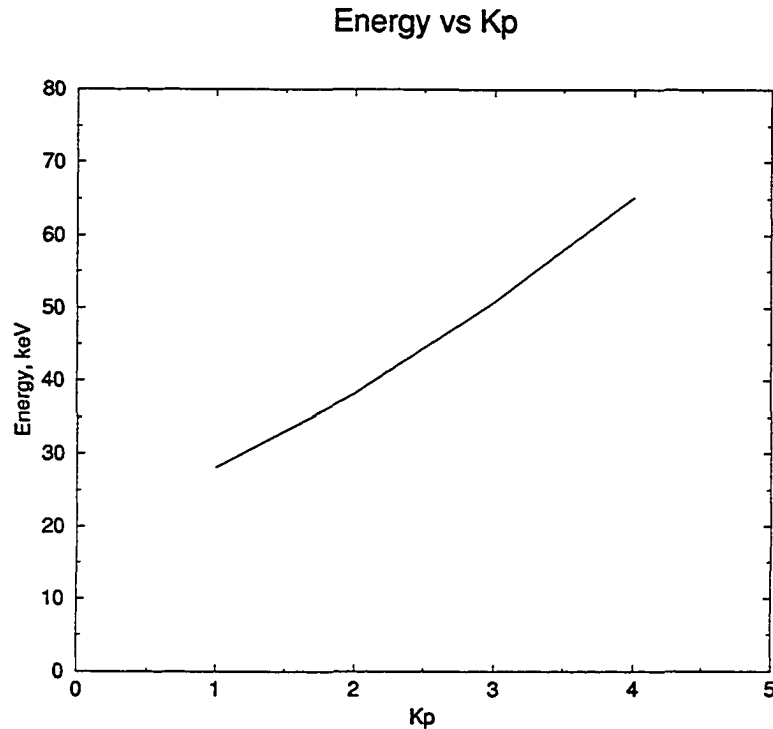


Figure 4.21: Variation of resonant proton energy with Kp for L=8.3 and MLT=1500 using the model of Ozeke and Mann (2001).

predicted open-closed trajectory boundary (see figure 4.20).

4.4 Conclusions

We have presented ground-based magnetometer and radar measurements of a drift resonance in the afternoon sector. Magnetometers were first used to investigate the resonant latitude of the field line resonance, and also the power and phase versus latitude characteristics of the wave. Longitudinally-separated magnetometers were used to calculate the azimuthal wavenumber of the wave, and a new technique to differentiate between latitudinal and longitudinal phase variation implemented. This technique was applied to the power and phase versus latitude data for the FLR, and these data matched theoretical predictions once the azimuthal phase variation was accounted for, i.e., the D-component variation showed a 180° phase change across the resonant latitude, and the H-component exhibited a double peaked nature previously reported in the literature [e.g., Chisham *et al.*, 1997]. The technique of de-convolving the two phase properties of the FLR (due to the azimuthal spatial

scale of the FLR and the typical FLR latitudinal phase change), and the remarkable coherence of the latitudinal phase after the correction was applied, implies that the FLR observed here was extremely coherent in m across the ground-based instrument array.

The STARE radars were used to investigate the azimuthal wavenumber of the FLR, and it was found that the m -value obtained from the magnetometers and the radars was in excellent agreement, again illustrating the waves coherence in azimuth. The radars also allowed the two dimensional velocity flow in the ionosphere to be investigated, and it was found that this flow exhibited a vortical nature, with a phase discontinuity across the resonant latitude of the FLR. We report the first comparison of such observations to a simple model of poloidal field line resonance, and found that the observed vortical nature was reproduced theoretically for a wave with a moderate m value, similar to that observed here. Although observations of high- m ULF waves using backscatter in a single look direction from ground-based HF radars exist in the literature [e.g., Yeoman and Wright, 2001], including some events with conjugate satellite observations from the ring current [e.g., Baddeley *et al.*, 2002], no measurements of the magnetometer signals of such a particle driven FLR with 2-D radar velocity flow observations from the ionosphere and satellite observations from the ring current have been completed.

Using Polar satellite data we concluded that prior to the FLR, there existed an unstable energy distribution in ring current ions at an energy consistent with particles that could excite the observed FLR, using the technique of Chisham *et al.* (1997) to calculate the expected resonant energy of ions in the ring current. After the FLR was excited, the unstable energy distribution was much reduced, with a lower flux at all energies. We used the model of Ozeke and Mann (2001) to show that the resonant ions were on closed trajectories in the magnetosphere, so that although the particle's drift time was small, they could have remained in the ring current and drifted to the correct MLT to excite the FLR. Indeed, calculations of the drift time of such ions showed that the drift time is consistent with the ions orbiting the Earth twice and arriving at the correct MLT to excite the wave at the UT of the observed FLR. Previous observations of such "bump-on-tail" energy distributions have either been statistical in nature and un-correlated with ground based measurements [e.g., Baddeley *et al.*, 2002], or have been correlated with pulsations in the Pc4 band [e.g., Hughes *et al.*, 1978; Glassmeier *et al.*, 1999; Wright *et al.*, 2001], so that these are the

first observations of FLR in the Pc5 band with in-situ measurements of an unstable particle energy distribution in the ring current.

This study is the first to observe an afternoon sector particle-driven Pc5 poloidal mode FLR in both magnetometer and radar data, and the first to implement a method for correcting for the azimuthal phase variation of FLR. Previous studies of so-called “giant pulsations” in the Pc4 band have shown that this type of wave coupling between the ring current and the ionosphere can be important energetically in the morning sector [e.g., Chisham *et al.*, 1997], but not typically for Pc5 waves in the afternoon sector. Although Pc5 wave activity in the afternoon sector associated with geomagnetic storms (so-called “storm-time Pc5 events”) has been characterised in STARE radar data before [e.g., Walker and Nielsen, 1984] the 2-dimensional flow characteristics of such events have not been studied and this type of event has thus far not been correlated with unstable energy distributions in the ring current. As such, these are the first afternoon sector Pc5 FLR observations using magnetometer data and 2-D ionospheric flow data with conjugate satellite measurements from the ring current.

These results clearly show that interactions between particles in the ring current and ULF waves represent a viable mechanism for wave growth in the afternoon sector, and represents a mechanism by which ions injected from e.g., substorm activity from the deep tail may transport energy to low altitudes in the ionosphere via the generation of ULF waves excited by drift resonance with ring current ions.

Chapter 5

Quiet Time Magnetospheric Flank FLR and Waveguide Study¹

5.1 Introduction

The phenomenon of field line resonance (FLR) discussed in Chapter 2 has been studied in detail, both observationally [Samson *et al.*, 1971; Allan *et al.*, 1986; Mann *et al.*, 2002] and theoretically [Southwood, 1974; Chen and Hasegawa, 1974; Wright and Allan, 1996]. FLRs have been linked with two distinct driving mechanisms: toroidal modes driven by coupling of fast mode waves to standing Alfvén waves, [e.g., Southwood, 1974 and Chen and Hasegawa, 1974] and poloidal modes driven internally by wave-particle interactions [e.g., Southwood *et al.*, 1969 and Hughes *et al.*, 1978]. Historically, the fast modes driving toroidal mode FLRs were assumed to be excited by the solar wind, either via cavity/waveguide modes excited by solar wind discontinuities [Allan *et al.*, 1986; Wright, 1994] or by Kelvin-Helmholtz instabilities on the flanks [Southwood, 1974; Chen and Hasegawa, 1974; Kivelson and Pu, 1984; Kivelson and Southwood, 1985; Kivelson and Southwood, 1986; Mann *et al.*, 2002]. The flank of the magnetosphere is thought to be able to act as a waveguide, with outer and inner boundaries corresponding to the magnetopause (or the bow shock) and an inner turning point. Discrete-frequency fast mode waves can propagate anti-sunwards in this waveguide between the magnetopause and the turning point when driven by either a magnetopause Kelvin-Helmholtz instability, or by a disconti-

¹The work presented in this Chapter has also been published in the paper “Multi-instrument observations of ULF wave-driven discrete auroral arcs propagating sunward and equatorward from the poleward boundary of the duskside auroral oval” by J. T. Mathews, I. R. Mann, I. J. Rae, I. J. and J. Moen, (2004) *Phys. Plasma.*, Vol. 11, No. 4 p 1250.

nuity in the solar wind. Optical observations of discrete field line resonances in association with discrete auroral arcs [Samson *et al.*, 1991; Samson *et al.*, 1996] have suggested that FLRs can stimulate auroral emissions, and hence these optical discrete arc features should exhibit the same polewards phase propagation as that observed in the magnetic perturbations of the FLR [Wright and Allan, 1996; Milan *et al.*, 2001]

Recent work by Wright *et al.* (1999) and Allan and Wright (2000) has shown that it is also possible for the nightside magnetotail between the central plasmashet and the plasmashet boundary layer (PSBL) to act as a waveguide, and support discrete frequency fast mode waves in the magnetotail or mantle. Fast mode waves that originate from a source in the nightside plasmashet propagating Earthward in such a waveguide will in general have some phase velocity component in the GSM \hat{Z} direction, and will experience reflection at the turning point of the waveguide. The exact point of reflection depends upon the wave frequency and the Alfvén velocity profile, i.e., the magnetic field and density profile in the \hat{Z} direction, but it is thought to lie in the plasmashet boundary layer. It is possible for such fast mode waves to drive Alfvén waves, which then propagate Earthwards along open field lines in the PSBL at a velocity greater than the Earthward group propagation speed of the fast mode waves in the magnetotail waveguide [Wright *et al.*, 1999]. As described by Wright *et al.* (1999), due to the fact that the Alfvén speed in the tail waveguide increases as one moves away from the central plasmashet (c.f. Figure 2.4), the driven Alfvén waves in the PSBL that map to higher latitudes at the ionosphere will reach the Earth first, followed by waves on lower latitude field lines. This leads to an equatorwards propagation direction in the observed magnetic (and possibly auroral) signatures of this type of nightside event in the PSBL [Wright *et al.*, 1999]. This mechanism may also explain the characteristics of some other auroral arcs such as some classes of poleward boundary intensifications (PBIs), such as those reported by Lyons *et al.* (1999).

In this Chapter we examine the possibility that fast mode waves excited in the magnetotail may also propagate sunwards into the flank waveguide and mode convert to Alfvén waves on closed but stretched field lines in the dusk sector. In this instance the archetypal closed field line poleward toroidal FLR phase propagation [Wright and Allan, 1996; Milan *et al.*, 2001] might be modified due to the stretched closed field line morphology. Our study considers the possibility that the flank waveguide can be excited from the magnetotail, and

that due to field line stretching the standard polewards FLR phase propagation may be reversed, manifesting itself in periodic auroral arc as well as magnetic field perturbations with equatorwards and sunwards propagation.

5.2 Ground-Based Instrumentation

Figure 5.1 shows the location of the ground-based instruments used in this study and their respective fields of view. Optical data were taken from two separate instruments, the Longyearbyen meridian scanning photometer (MSP) at Nordlysstasjonen (field of view shown by the solid line in Fig. 5.1) and the Ny Ålesund all sky camera (ASC) (field of view shown by the oval in Fig. 5.1). In Fig. 5.1 the fields of view of the MSP and ASC are projected to 110 km altitude (the assumed emission height for the 557.7 nm wavelength) with a cut-off at 80° from the zenith. A geographic map is overlaid for reference.

Ground-based magnetometer data were taken from the IMAGE magnetometer network [Viljanen and Hakkinen, 1997]. This study utilizes data from the six northernmost stations (see crosses in Fig. 5.1 and Table 3.1 in Chapter 3) which lie within the field of view of the MSP and ASC.

The Super Dual Auroral Radar Network (SuperDARN) [Greenwald *et al.*, 1995] was used to investigate the ionospheric flow velocities during our intervals of study, and the fields of view of the two CUTLASS SuperDARN radars are displayed in Fig. 5.1 as dashed fans. For reference, Fig. 3.2 in Chapter 3 shows the locations of all of the northern hemisphere SuperDARN radars.

For a full description of the instrumentation used in this study, see Chapter 3.

5.3 Events

In the subsections below we present observations of periodic dusk flank discrete auroral arcs which propagate equatorwards. Each of the events below displays very similar solar wind, local time and, most importantly, auroral morphology. Subsequently, in Section 5.4 we examine the morphology of the January 3rd 1998 event in detail, this event being characteristic of the other events which have almost identical auroral morphology.

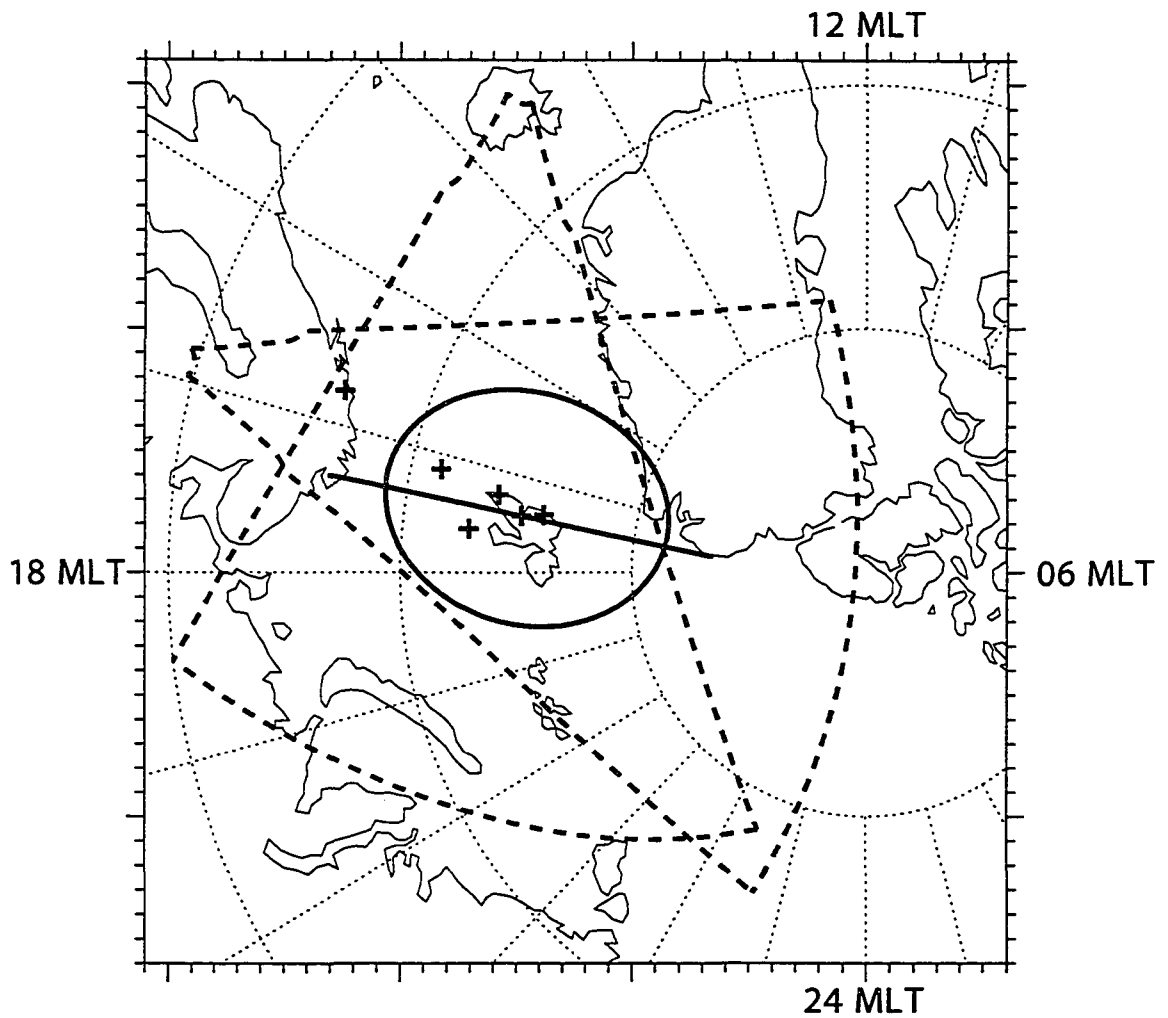


Figure 5.1: Location of ground-based instrumentation used in this study. Locations are shown at 1400 UT on 03 January 1998. Plotted are representations of the Longyearbyen MSP (thick line), Ny Ålesund ASC (oval) and SuperDARN CUTLASS radars (fans) fields of view. The locations of the IMAGE magnetometers used in this study (Table 3.1) are plotted with + symbols.

5.3.1 3rd January 1998

The Wind spacecraft provides high time resolution data of plasma flows and magnetic field variations in the solar wind. On the 3rd January 1998, the Wind spacecraft traveled from approximately [225.8, 20.1, 5.39] to [226.2, 20.4, 4.5] R_E (in X, Y, Z GSM coordinates), where R_E is the Earth's radius. Assuming planar propagation phase fronts [Lester *et al.*, 1993] and a constant solar wind velocity of 360 km/s, a time delay of 67 minutes is assumed throughout the interval, and the Wind data, which we show in Fig. 5.2 are time lagged by this amount. The data during the interval of study (1400 to 1500 UT in the magnetosphere) show that the flow velocity in the GSM \hat{X} direction and the dynamic pressure as observed by the solar wind experiment (SWE) [Ogilvie *et al.*, 1995] both remained approximately constant, at 360 km/s and 1.5 nPa, respectively (fourth and sixth panels of Fig. 5.2). Observations from the Wind magnetic fields investigation (MFI) [Lepping *et al.*, 1995] show that the time lagged IMF B_Z GSM component turned northward at 1300 UT (third panel of Fig. 5.2), returning to a southward direction at 1330 UT. Throughout the study interval (1400 to 1500 UT) the IMF remained southward (~ -4 nT), with B_Y positive ($\sim +2$ nT) and B_X approximately zero.

The top panel of Figure 5.3 displays 630.0 nm auroral emissions, as measured by the Longyearbyen MSP. The poleward cut-off of this emission is believed to be a proxy for the location of the open-closed field line boundary (OCFLB) [Blanchard *et al.*, 1997] and the keogram clearly shows that this boundary moved polewards from $\sim 74^\circ$ to $\sim 80^\circ$ magnetic latitude at around 1220 UT, which may be related to substorm activity observed in the Circum-pacific Magnetometer Network (CPMN) [Yumoto and The CPMN Group, 2001] at approximately 1200 UT (not shown). The OCFLB remained at this latitude until 1510 UT, when it moved equatorwards to $\sim 75^\circ$ magnetic latitude. The bottom panel of Figure 5.3 shows the 557.7 nm auroral emission, produced by electrons of energy ≥ 1 keV. Between 1400 and 1500 UT extremely clear, multiple, periodic auroral features were observed to propagate equatorwards from the poleward boundary of the 557.7 nm emission (so called Poleward Boundary Intensifications (PBIs) [Lyons *et al.*, 1999]). Intensifications at the polewards boundary which do not clearly propagate equatorwards can also be seen from 1235 to 1530 UT, with more sporadic equatorwards propagating auroral features being a general characteristic during this more extended time interval.

WIND MFE and SWE 980103

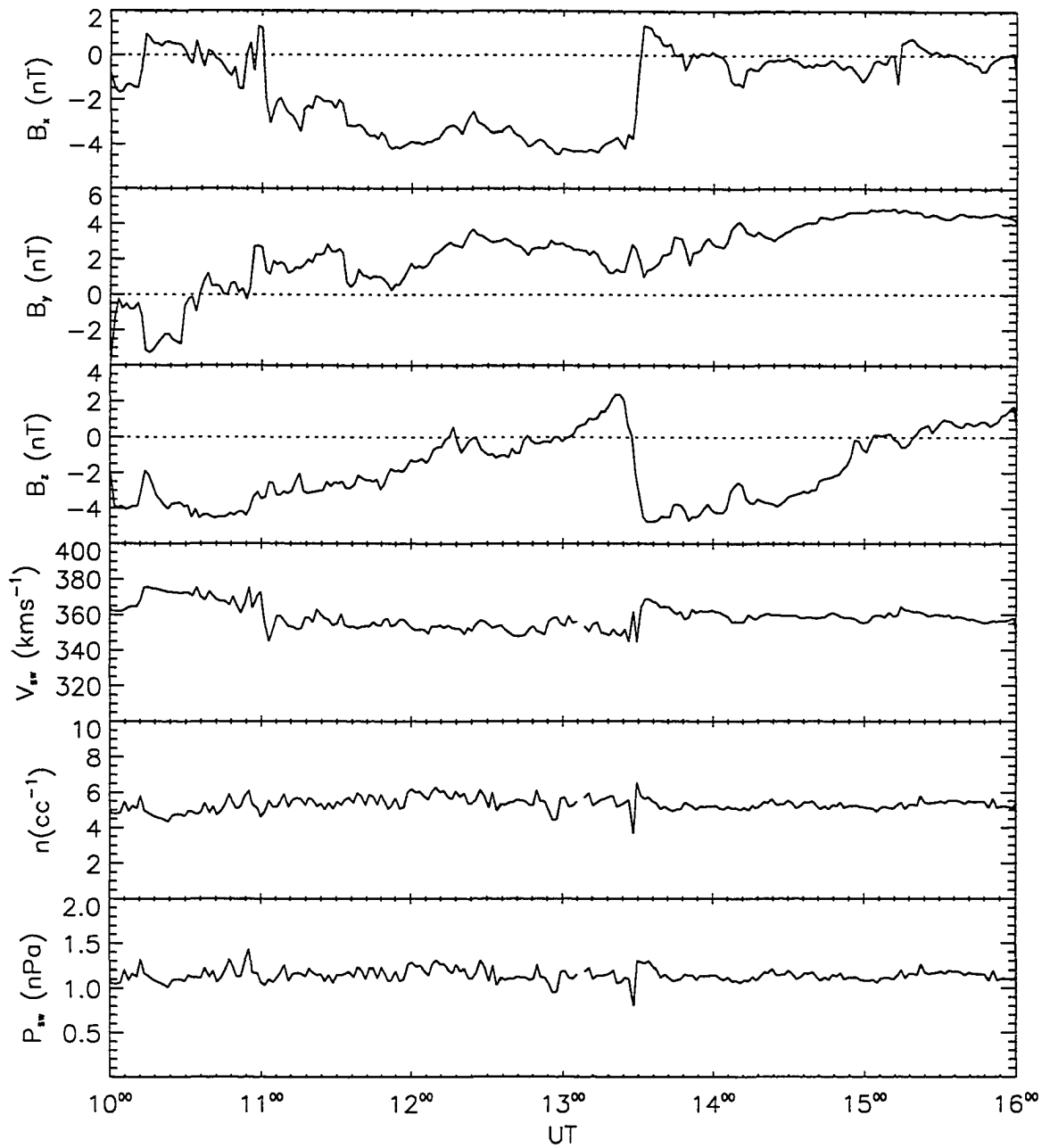


Figure 5.2: WIND MFI (B_X , B_Y and B_Z in GSM coordinates; top three panels) and SWE (v_x GSM, number density and dynamic pressure; bottom three panels) solar wind parameters for 3rd January 1998. The data are time lagged by 67 minutes (the assumed travel time from Wind to the Earth).

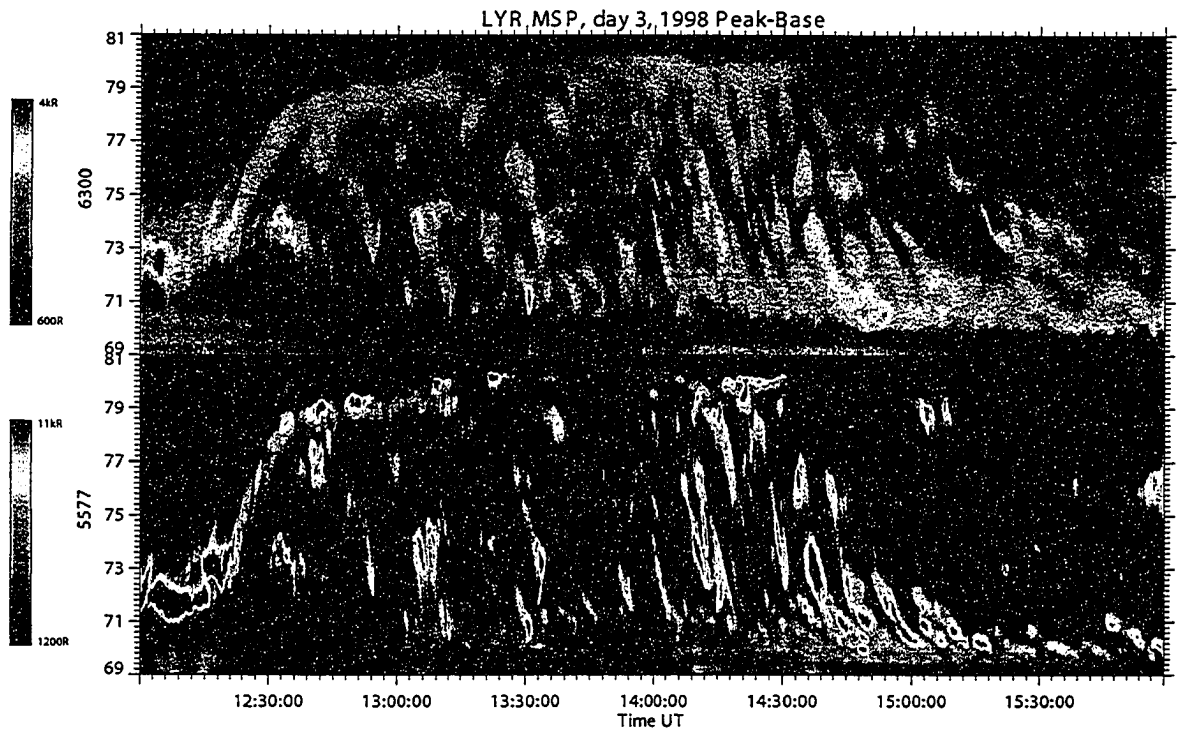


Figure 5.3: Longyearbyen MSP data for 1200 to 1700 UT on the 3rd January 1998; 630.0 and 557.7 nm filters are shown. The y axis runs from 81 to 69 degrees geomagnetic latitude. The 630.0 nm field of view has been cropped to coincide with the field of view of the 557.7 nm filter.

5.3.2 29th December 2000

On the 29th December 2000 the ACE satellite [Stone, 1989] was located upstream of the Earth in the solar wind at a location of [238, 29, 7] R_E in X , Y , Z GSM coordinates. Figure 5.4 displays ACE SWEPAM [McComas *et al.* (1998), 1998] solar wind velocity and number density (top two panels respectively) and MFI [Smith *et al.*, 1998] B_x , B_y and B_z (in GSM coordinates, bottom three panels respectively) data from the 29th December 2000. The solar wind speed was low throughout the interval, varying between 350 and 380 km/s, so that the delay time from ACE to the Earth was around 71 minutes. A step in the number density was observed at 1540 UT, which would have impinged upon the magnetosphere at around 1650 UT. The solar wind magnetic field was negative in B_x and positive in B_y throughout, with B_z varying between -2.5 and 5 nT.

Figure 5.5 displays data from the Longyearbyen MSP for the 29th December 2000. The instrument began collecting data at 1230 UT, and the polewards boundary of the auroral oval remained at approximately 80° CGM latitude until around 1800 UT, whereupon it moved equatorwards to around 70° CGM latitude. Auroral features were observed to repetitively propagate equatorwards from the poleward boundary of the auroral oval between 1400 and 1600 UT in the 844.6, 557.7 and 630.0 nm filters, similar to those observed in Figure 5.3.

5.3.3 18th January 2002

Similar to the 26th December 2000 event, on the 18th January 2002 the ACE spacecraft was located upstream of the Earth at a location of [241, -17, 22] R_E in X , Y , Z GSM coordinates. The upper panel of Figure 5.6 displays SWEPAM velocity data (top panel) and MFI magnetic field data (lower three panels) for the interval 1000 to 1800 UT on the 18th January 2002. The solar wind velocity was again low, varying between 300 and 325 km/s so that the delay time to the Earth was approximately 65 minutes. Unfortunately no solar wind number density data exist for this event. The lower three panels of Figure 5.6 display ACE MFI magnetic field data in GSM coordinates, with B_x varying between -5 and 5 nT and B_y staying at approximately 3 nT for the entire interval. B_y remained around zero nT until 1540 UT, when it increased to 5 nT.

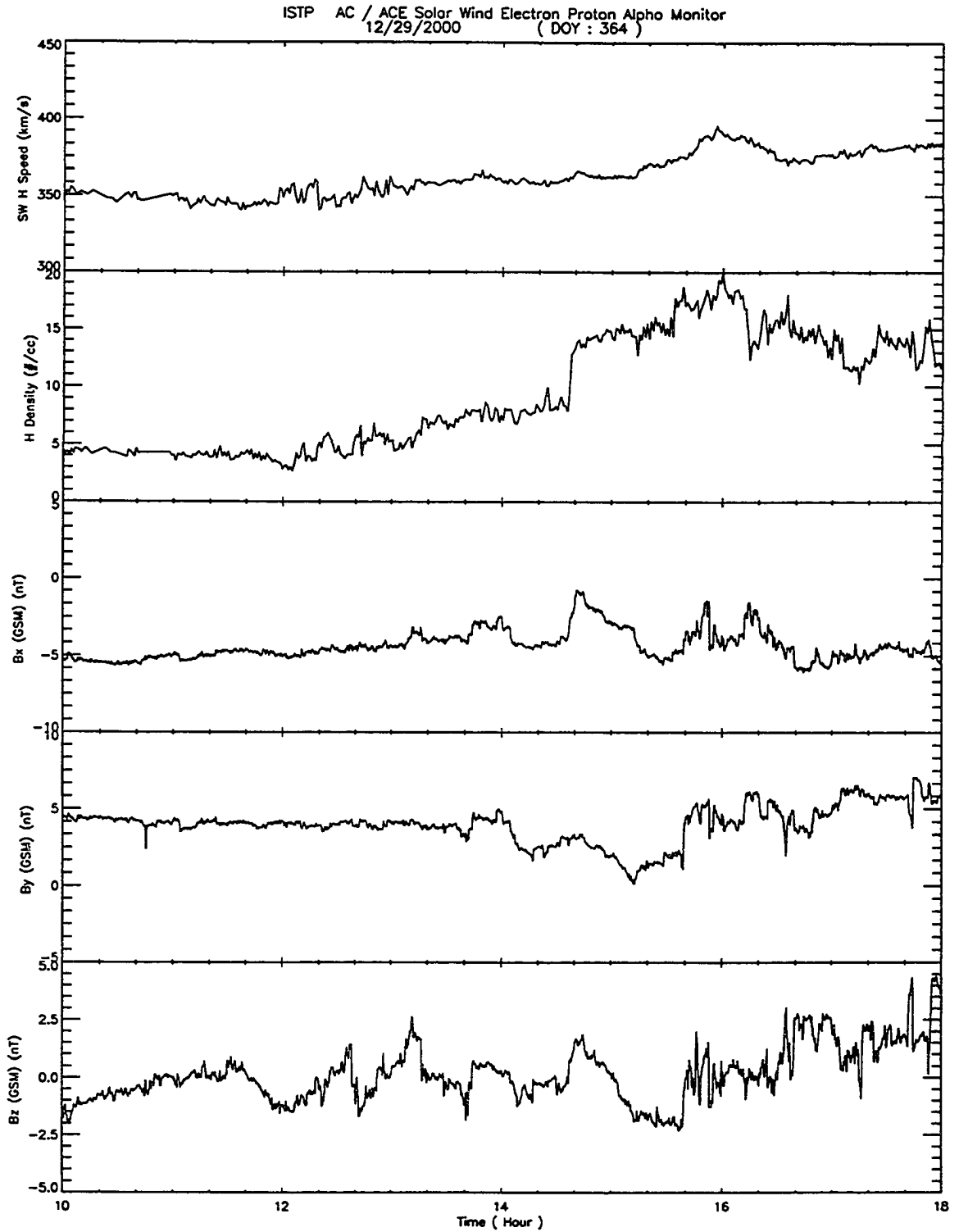


Figure 5.4: ACE SWEPAM (v_x GSM and number density; top two panels) and MFI (B_x , B_y and B_z in GSM coordinates; lower three panels) solar wind parameters for 29th December 2000.

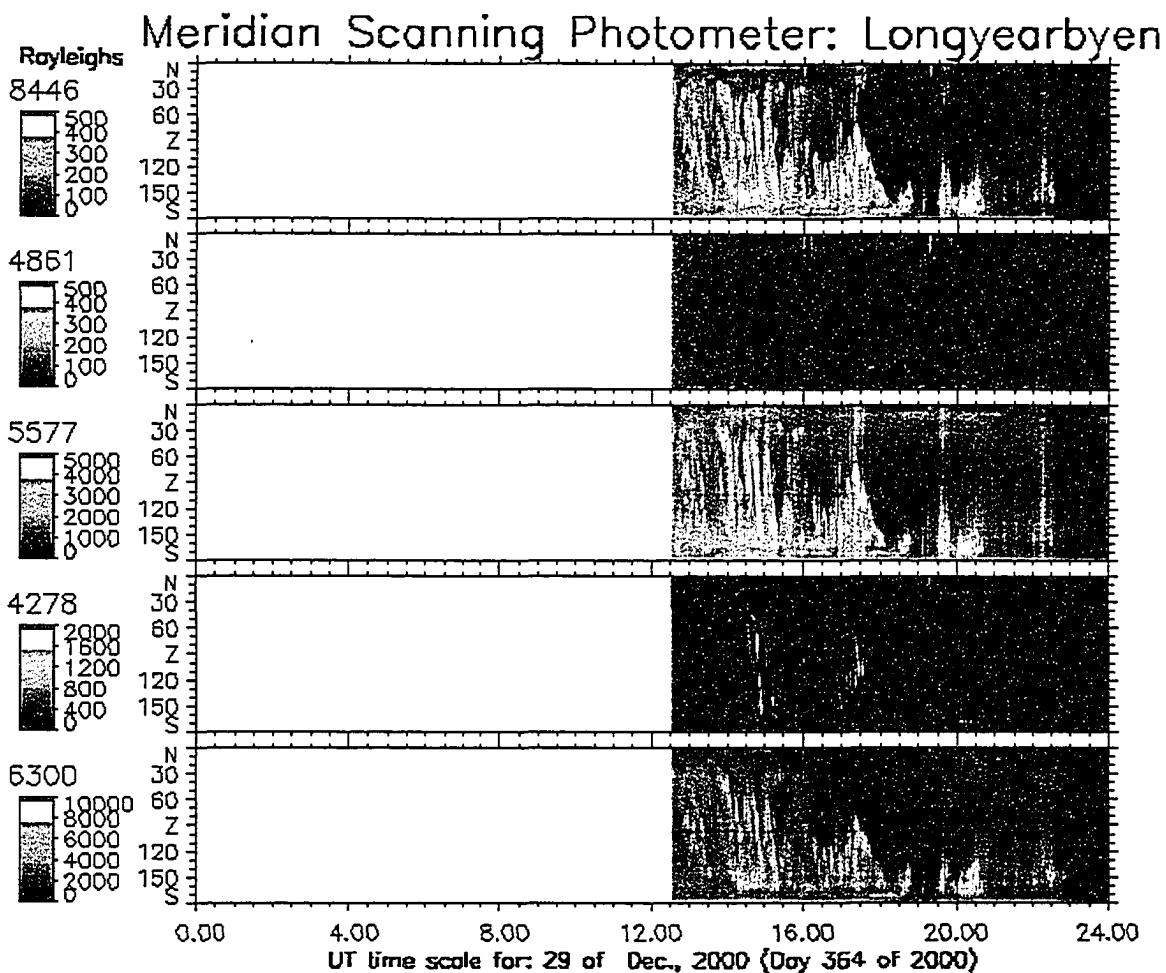


Figure 5.5: Longyearbyen MSP data for the 29th December 2000. The y axis runs from -170 to 170 degrees look angle, corresponding to 69 to 81 degrees geomagnetic latitude. All five filters from the MSP are shown. Periodic, equatorwards propagating auroral features are observed between 1400 and 1600 UT.

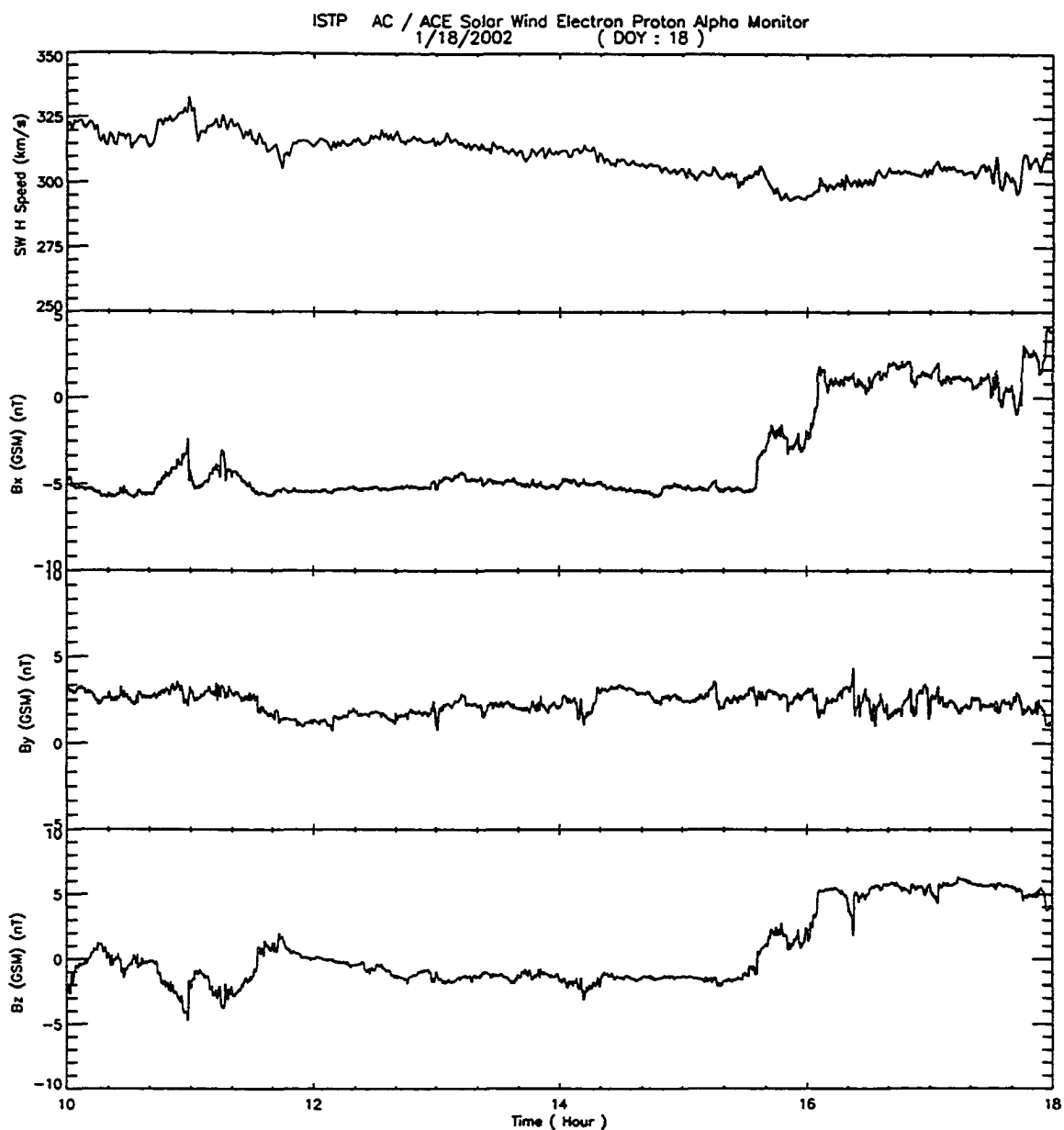


Figure 5.6: ACE SWEPAM (v_x GSM, top panel) and MFI (B_X , B_Y and B_Z in GSM coordinates; lower three panels) solar wind parameters for 18th January 2002. No number density data exists for this interval.

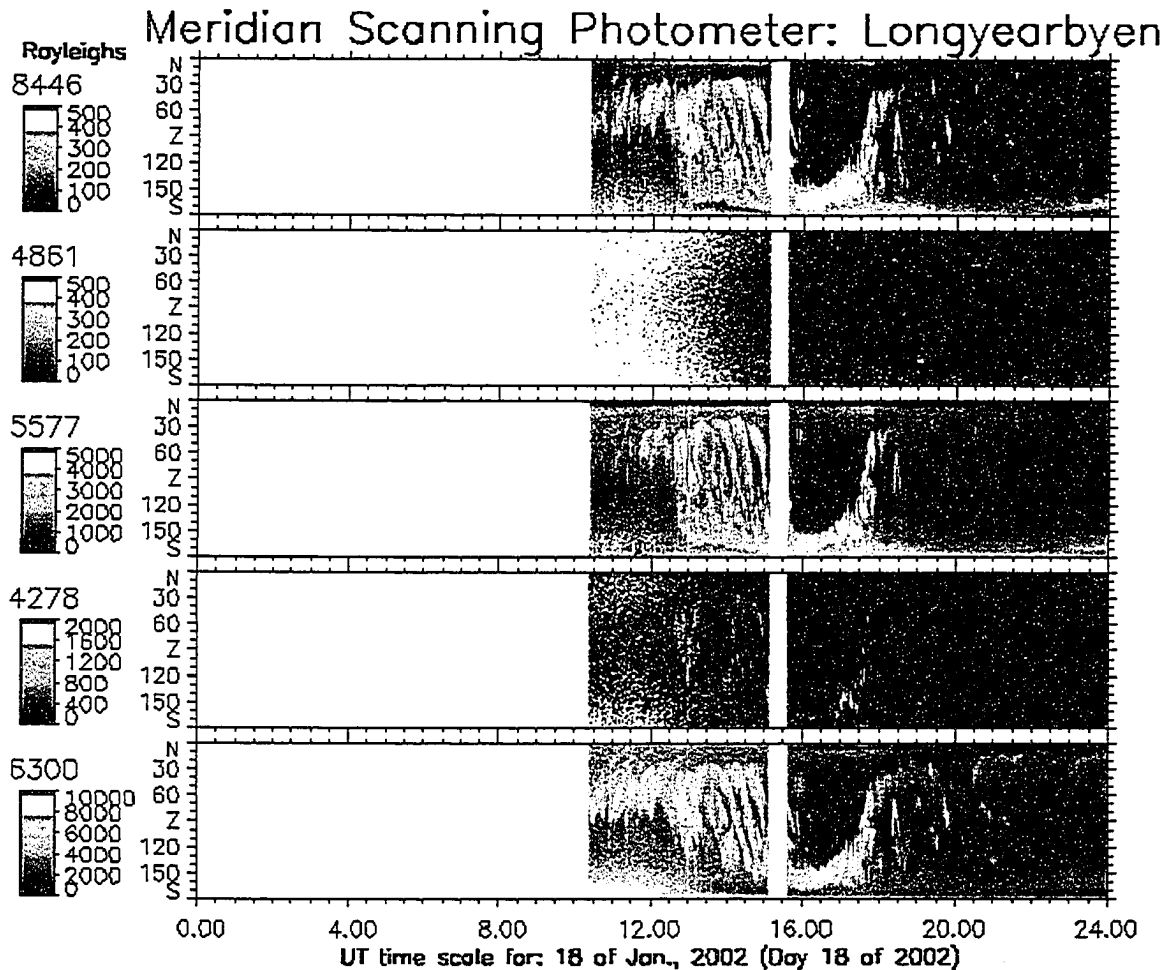


Figure 5.7: Longyearbyen MSP data for the 18th January 2002. The y axis runs from -170 to 170 degrees look angle, corresponding to 69 to 81 degrees geomagnetic latitude. All five filters from the MSP are shown. Clear, periodic equatorwards propagating auroral features are observed between 1300 and 1500 UT.

Figure 5.7 displays MSP data from Longyearbyen from the 18th January 2002. The instrument began taking measurements at 1030 UT, and repetitive, discrete auroral features were observed to propagate equatorwards from the polewards boundary of the auroral oval between 1230 and 1500 UT in the 844.6, 630.0 and 557.7 nm filters. Again, these auroral features are morphologically very similar to those observed in Figures 5.3 and 5.5.

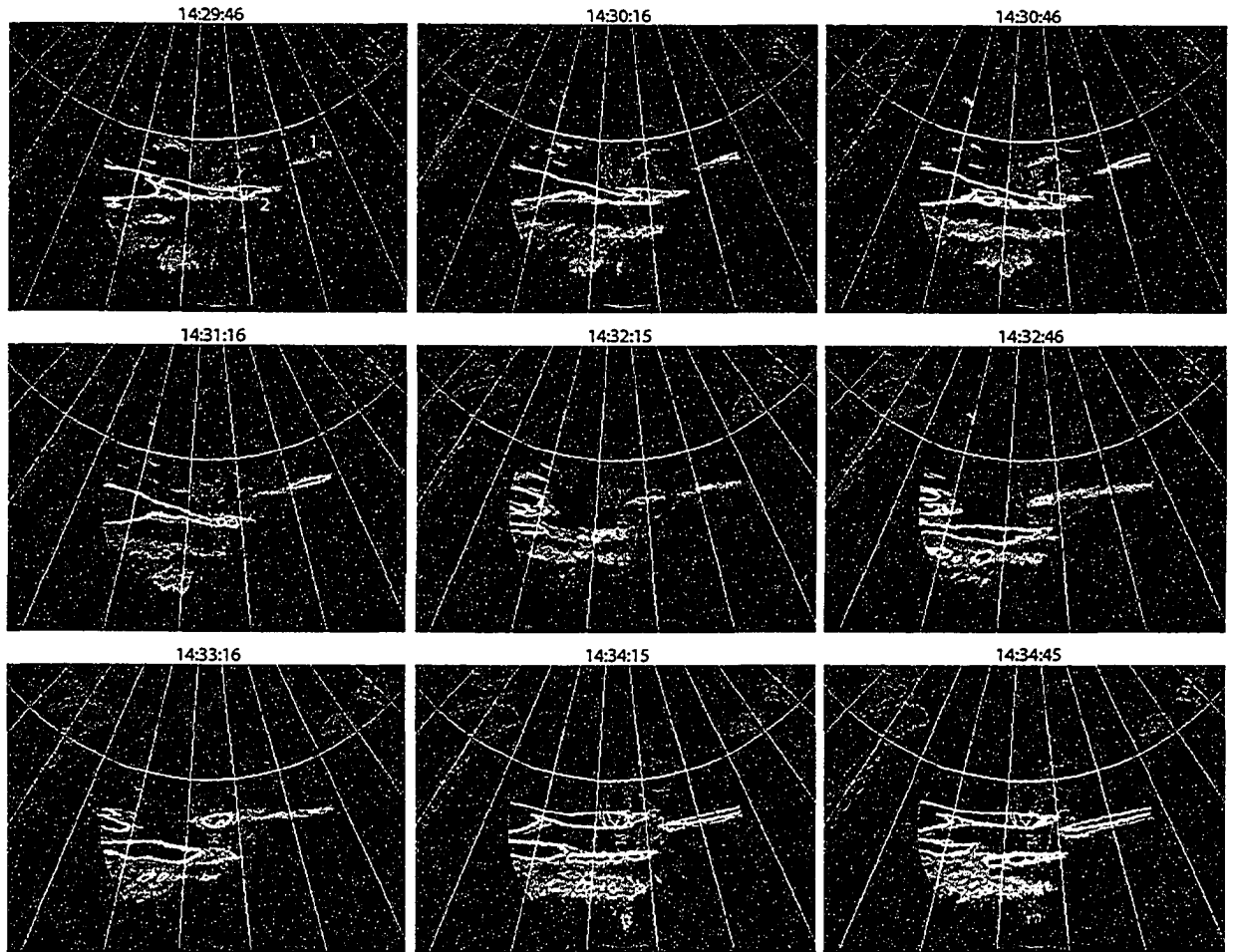


Figure 5.8: Ny Ålesund 557.7 nm ASC data for the interval 1429:46 to 1434:45 UT, projected to 110 km altitude with geographic overlay. The data are cut at 80° from the zenith.

5.4 Detailed Study of 3rd January 1998 Event

As shown in Sections 5.3.1, 5.3.2 and 5.3.3 above, a repeatable auroral morphology demonstrating periodic equatorwards moving discrete arc features can be observed in MSP data on the dusk flank during periods of relative geomagnetic quiet. These moving discrete auroral forms propagate equatorwards from near the open-closed field line boundary as determined by the 630.0 nm cutoff [Blanchard *et al.*, 1997], indicating that they are confined to closed field line regions of the magnetosphere. In this section we examine in more detail the characteristics of the event of 3rd January 1998 as a case study of this type of auroral feature.

The frames Fig. 5.8, taken by the Ny Ålesund ASC during the 1400 to 1500 UT interval,

clearly show multiple, east-west aligned auroral arcs in the 557.7 nm wavelength. In the first four frames, arc 1 is observed to extrude westwards through the field of view and brighten significantly. Between 1431:16 and 1434:15 arc 1 splits, with the westernmost section proceeding to propagate westwards (1433:16 to 1434:15). Meanwhile, arc 2 is observed to propagate westwards, out of the field of view of the ASC. Further analysis of the data shows that the mean sunwards phase propagation velocity of the arcs is ~ 2.2 km/s. 'Missing' frames (e.g., 1431:45) correspond to when the camera was imaging in the 630.0 nm wavelength.

Figure 5.9 displays a keogram constructed from the central slice of the Ny Ålesund ASC data, in the 557.7 nm filter for the interval 1400 to 1500 UT. As in the Longyearbyen MSP data, multiple auroral features that propagate equatorwards through the field of view are observed. These data clearly show that the MSP observations made at Longyearbyen correspond to the multiple, east-west aligned auroral arcs observed in the Ny Ålesund ASC images. The equatorwards propagation of the auroral arcs was measured to be approximately 1.3° per minute in both the Longyearbyen MSP and Ny Ålesund ASC datasets.

Figure 5.10 displays timeseries from look directions from the Longyearbyen MSP corresponding to the latitudes directly above the LYR and HOP IMAGE magnetometer stations (top panels of the left and right columns respectively), and IMAGE magnetometer data from these stations themselves in magnetic H, D, Z co-ordinates (lower panels) for the interval 1300 to 1600 UT on the 3 January 1998. The eight timeseries represent raw and unfiltered data. The Hopen Island dataset in particular show clear magnetic pulsations in the H, D and Z component magnetograms corresponding to the intervals of the strongest periodic auroral brightenings (1425 to 1510 UT). However, despite the existence of discrete frequency disturbances in both the MSP and magnetometer data it is clear that there is not an exact one-to-one correspondence between the magnetic pulsations observed by the magnetometers and the periodic emissions observed in a given look direction of the 557.7 nm MSP. Given that the magnetometers spatially integrate in a Biot-Savart sense over the magnetic perturbations produced by the Hall currents in the ionosphere (e.g., Poulter and Allan, 1985), this is, perhaps, not surprising. Indeed, the discrete 557.7 nm E-W aligned arcs shown in Figure 5.8 have widths ~ 40 km and the arc-related upward field aligned currents (FACs) are separated by ~ 150 km at an assumed emission altitude of 110 km. The

03 January 1998

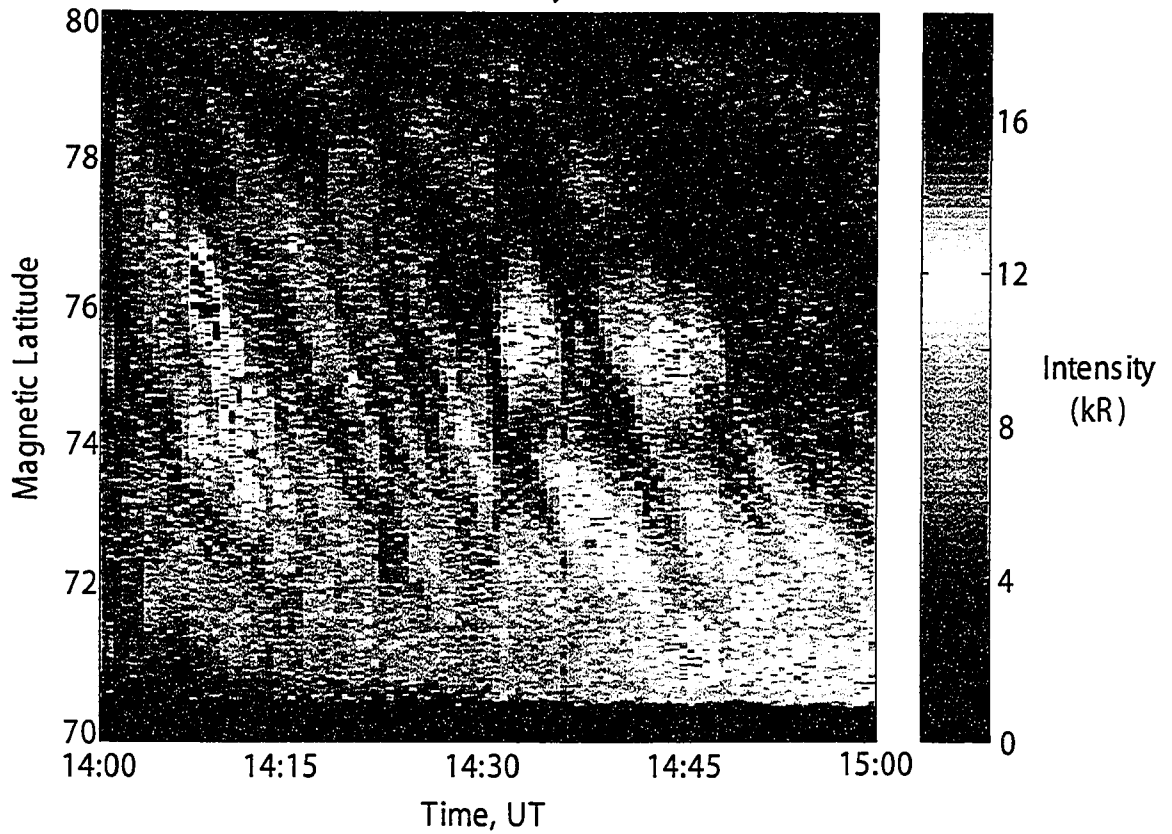


Figure 5.9: Keogram constructed from the 557.7 nm filter of the Ny Ålesund ASC for the interval 1400 to 1500 UT.

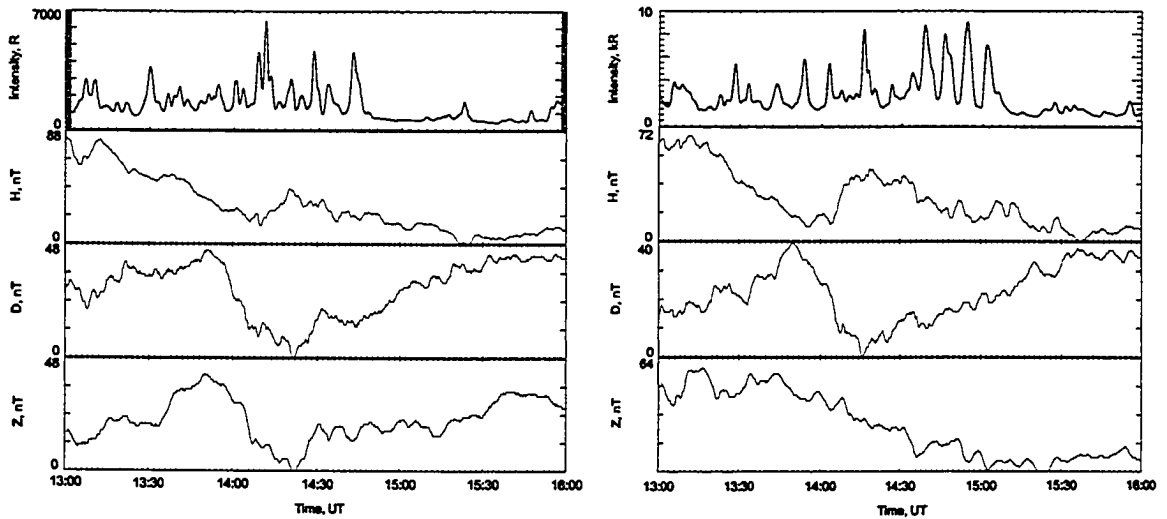


Figure 5.10: Longyearbyen MSP 557.7 nm emission (top row panels) and IMAGE magnetometer (bottom three row panels) data from 1300 to 1600 UT on the 3 January 1998. Left hand stack displays 557.7 nm MSP data from the zenith (top panel) and LYR H,D,Z magnetometer data (bottom three panels). Right hand stack displays 557.7 nm MSP data corresponding to the latitude of Hopen Island (zenith angle of 136° assuming a 110 km emission altitude) and HOP magnetometer data. All time-series are unfiltered.

amplitude and phase of the spatially integrated ground-magnetometer signal will likely be distorted, especially in the presence of oppositely directed small scale current features, by this spatial integration (e.g., Poulter and Allan, 1985). Hence it is unlikely that the magnetometer time-series will show a direct one-to-one correspondence with the MSP data in any given look direction, however, their power spectra might be expected to show the same dominant spectral peaks.

Figure 5.11 displays stacked power spectra taken from one hour of Longyearbyen MSP (16.2 second time resolution) and IMAGE magnetic north-south component (10 second time resolution) timeseries data, between 1400 to 1500 UT. Both datasets were bandpass filtered between 1000 and 100 seconds (1 to 10 mHz) and a Hanning window was applied before the fast Fourier transform (FFT). The left hand panels of Fig. 5.11 display power spectral intensity versus frequency for nine scan angles of the MSP (in degrees), from the zenith (top panel, 90 degrees) to the southern horizon (bottom panel, 170 degrees). A clear spectral peak is observed at ~ 1.7 mHz in the higher azimuthal scans, with a broader and more complex spectrum at lower scan angles as one approaches the horizon. The right hand panels of Fig. 5.11 display stacked power spectra from the H-component

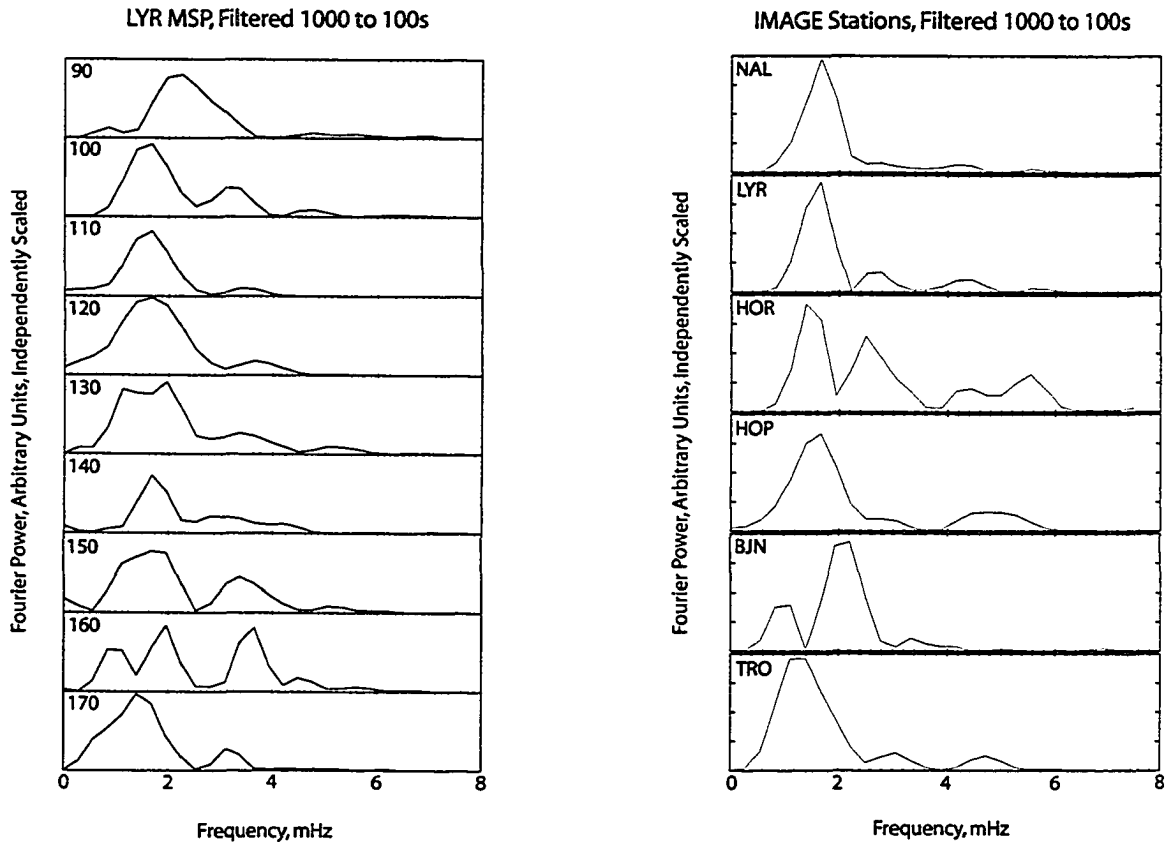


Figure 5.11: Power spectra from 557.7 nm MSP (left panel) and IMAGE magnetometer X-component (right panel) data, filtered between 1000 and 100 seconds. MSP scans were taken from the zenith southward (with 90° indicating the zenith), at intervals of ten degrees in look direction; panel labels indicate zenith angle and magnetometer stations in the left and right panels, respectively.

of six selected magnetometer stations from the IMAGE array (see Table 3.1 in Chapter 3), from Ny Ålesund (top panel) to Tromsø (bottom panel). The magnetometer spectra clearly mirror the MSP data, in that a distinct spectral peak is observed at ~ 1.7 mHz at the four northernmost stations, with the signatures at Bear Island and Tromsø being somewhat more complex. The clear correlation between the spectral peaks and structure of both the MSP and magnetometer measurements implies that the periodic auroral features have a significant and periodic magnetic signature. Therefore it is likely that the auroral production mechanism is related to the observed periodic magnetic perturbations.

Figure 5.12 shows two velocity plots obtained from the SuperDARN northern hemisphere radars, for the intervals 1442 to 1444 UT and 1444 to 1446 UT on the 3rd January

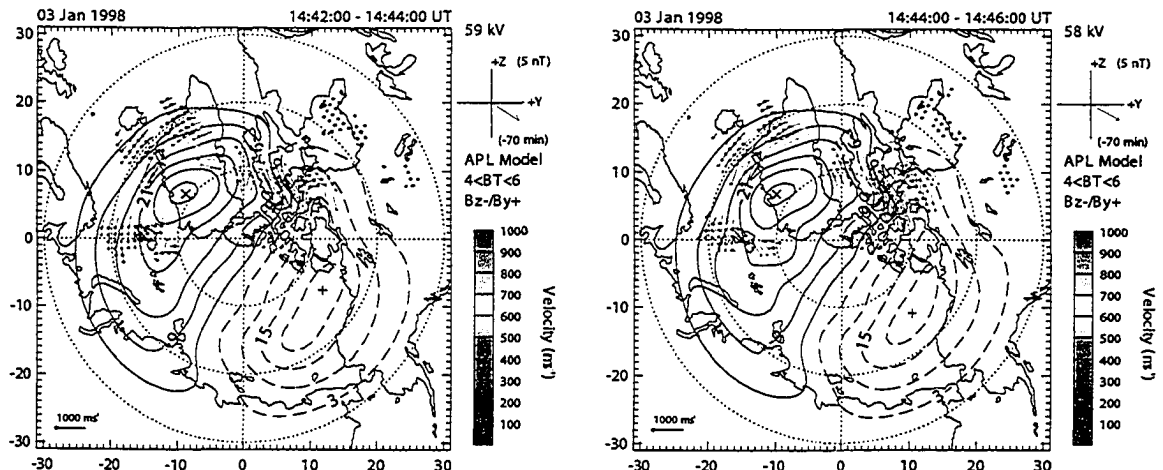


Figure 5.12: SuperDARN northern hemisphere merged velocity vectors for the intervals 1442 to 1444 UT (left panel) and 1444 to 1446 UT (right panel) on the 03 January 1998, projected onto a geographic overlay. Also plotted are the predicted location of convection cells from the APL map-potential model.

1998. Back-scatter was observed above Svalbard in the CUTLASS radars at the times shown, and the measurements show that the ionospheric convection at Svalbard latitudes was sunward, with a speed of approximately 200 m/s. The map potential model [Ruohoniemi and Baker, 1998] (represented by contours in Fig. 5.12) indicates that field lines with a footprint in the ASC field of view lie on the sunwards return flow of two-cell magnetospheric convection, where the dusk cell is enhanced as expected for B_Y positive. The convection maps in Fig. 5.12 and at other times (not shown) show enhanced convection flows near local noon which can be attributed to dayside reconnection. Consequently, we interpret that the field lines at Svalbard latitudes which lie equatorwards of the convection reversal within a standard 2-cell pattern can be inferred to be closed, consistent with the OCFLB inferred from the 630.0 nm optical observations shown in the top panel of Figure 5.3

5.5 Discussion

We have presented multi-instrument observations of multiple, east-west aligned discrete auroral arcs which propagate sunwards and equatorwards from the poleward boundary of the auroral oval in the dusk sector. A previous study [Moen *et al.*, 1994] reported observa-

tions of multiple, discrete east-west aligned arcs in the dusk sector from a fast solar wind speed interval ($v_X \sim 700$ km/s), during IMF conditions of B_Y positive and $B_Z \sim 0$, which are somewhat similar to our observations. The arcs observed by Moen *et al.* (1994) also lay equatorwards of the convection reversal boundary on closed field lines, however, they displayed no evidence of westwards propagation other than that related to the local ionospheric convection, and were characterized by a polewards rather than an equatorwards phase propagation (compare Fig. 2a of Moen *et al.* (1994) with our Fig. 5.3). Our observations differ extensively from those in Moen *et al.* (1994) in that firstly the arcs studied here demonstrated a sunwards phase propagation speed which was an order of magnitude larger than the local ionospheric convection velocity, and secondly that they propagated very clearly and periodically equatorwards from the poleward boundary of the auroral oval.

The periodicity of the optical auroral arcs was the same as that of the magnetic oscillations observed in IMAGE magnetometer data, implying that the driving mechanism for these auroral features may be wave-like, most likely due to Alfvén waves on auroral field lines. Since the arcs were observed to propagate sunwards at a velocity an order of magnitude larger than the local ionospheric convection speed, this further implies the action of a source which originates in the magnetotail and which propagates faster than the local convection speed.

Previous work by Lyons *et al.* (2002) has suggested that global ULF oscillations in the magnetotail may be the driving mechanism for certain types of PBI related auroral features. They observed flow oscillations in the plasmashet which were related to auroral brightenings that moved sunwards toward the dawn and dusk flanks with an azimuthal phase speed of between 500 and 2000 ms^{-1} . They also observed that the azimuthal phase speeds of these events in the ionosphere as observed by the SuperDARN radars was greater than typical ionospheric convection flow speeds, implying that the auroral arcs were not simply being carried by ionospheric sunward return flow. The Lyons *et al.* (2002) phenomena were observed in the midnight sector, but since Lyons *et al.* (2002) observed their auroral features to propagate down both flanks there are obvious parallels with the observations made in this paper regarding the phase velocity of the auroral features being related to a possible ULF wave source in the tail.

Work by Wild and Yeoman (2000) focusing on substorm related auroral brightenings

also showed how a source in the magnetotail can impart energy into the midnight sector ionosphere in the form of auroral intensifications, and how these aurora can propagate azimuthally from midnight around both flanks. They observed ionospheric velocity enhancements in the morning sector of up to 850 ms^{-1} in the sunwards direction, which were much higher than the ambient convective ionospheric flow. Although the Wild and Yeoman (2000) observations were made during more disturbed geomagnetic conditions, the auroral phase propagation velocities are of the same order of magnitude as those observed here, implying that tail phenomena can drive auroral features which propagate around both flanks at the fast phase velocities which we report here.

Figure 5.13 shows Tsyganenko 1996 [Tsyganenko and Stern, 1996a] magnetic field model mappings into the equatorial GSM plane for field lines whose ionospheric footprints correspond to the locations of the IMAGE magnetometers used in this study, at 1430 UT on the 3rd January 1998. Also shown in Fig. 5.13 is the equatorial location of the magnetopause as derived from the empirical model of Shue *et al.* (1997) with IMF $B_z = -4 \text{ nT}$ and a solar wind dynamic pressure of 1.0 nPa as appropriate to 1430 UT in this day. Clearly, significant field line stretching and distortion out of a meridional plane occurs at this local time, i.e., the most poleward field line (corresponding to the Ny Ålesund magnetometer station) maps deepest into the magnetotail, with subsequent equatorwards field lines experiencing less distortion. This distortion means that a fast mode wave propagating Earthwards from the magnetotail with its phase fronts aligned with the Y GSM axis would impinge upon the equatorial plane of the most poleward field line first. If mode conversion occurs, an Alfvén wave will be launched along this field line first, followed by Alfvén waves subsequently being launched along more equatorward field lines. Whether the Alfvén wave launched along a more poleward field line reaches the ionosphere before the wave launched along a more equatorward field line depends, in a time of flight sense, upon the difference between the propagation times along these two paths. Assuming that the fast mode wave propagates in the equatorial plane it is possible to calculate the phase difference between the two field lines by calculating the fast mode propagation time between the equatorial crossing points of the two field lines, as well as the Alfvén wave propagation time along the two field lines. The choice of an equatorial fast mode propagation path can be justified by assuming that the excitation source of the fast mode waves resides in the equatorial

Equatorial T96 mappings of IMAGE stations at 1430 UT

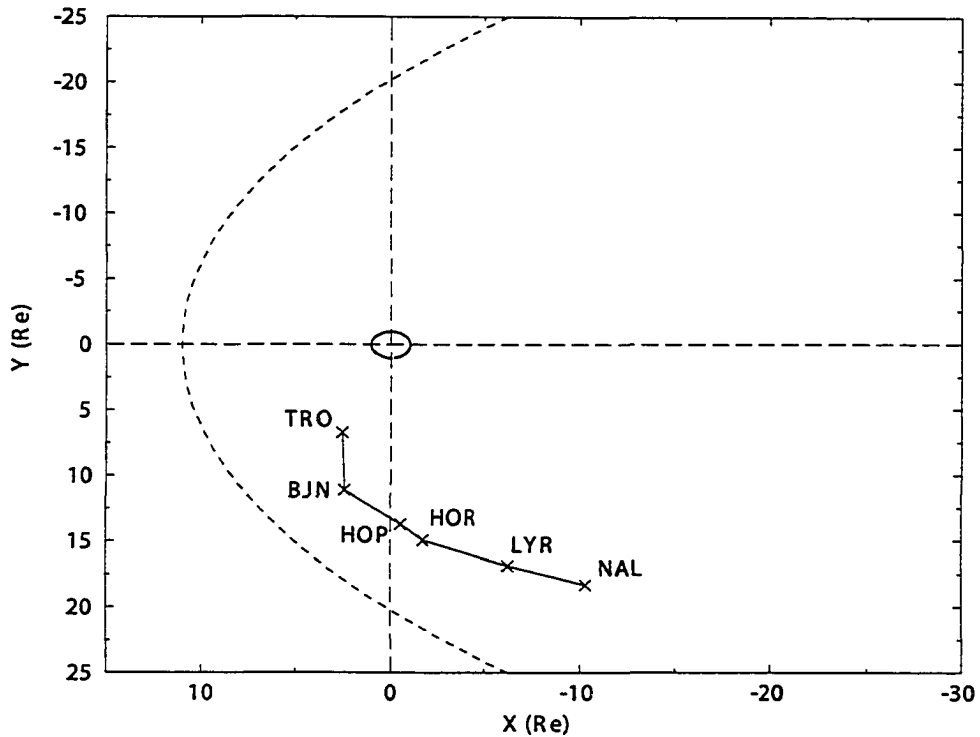


Figure 5.13: Tsyganenko 1996 model results for field lines corresponding to IMAGE magnetometer stations from Table 3.1, mapped into the equatorial GSM plane at 1430 UT on the 3rd January 1998. Also plotted as a dashed line is the magnetopause location from the Shue *et al.* (1997) model.

plane of the magnetotail. Since the distance from the source to the equatorial crossing point of the field line is the shortest fast mode path length to any point along the field line, and since the fast mode wave power will be reduced as it propagates and diverges isotropically from the source region, the wave power propagated along the equatorial path will be likely strongest (c.f. Chi *et al.*, 2001).

To investigate this phenomenon quantitatively we compare the latitudinal phase lags in a purely dipolar geometry with those in a more stretched geometry using the time of flight approximation. We first consider two dipolar magnetic field lines at L-shells of L_1 and L_2 in the same meridian and whose footpoints reach the ionosphere at latitudes λ_1 and λ_2 , respectively. We assume standing waves are formed on both field lines, and investigate the phase relation between the two (see Fig. 5.14). Assuming the fast mode wave driving the Alfvén waves propagates in the equatorial plane (c.f. Chi *et al.*, 2001) the time difference

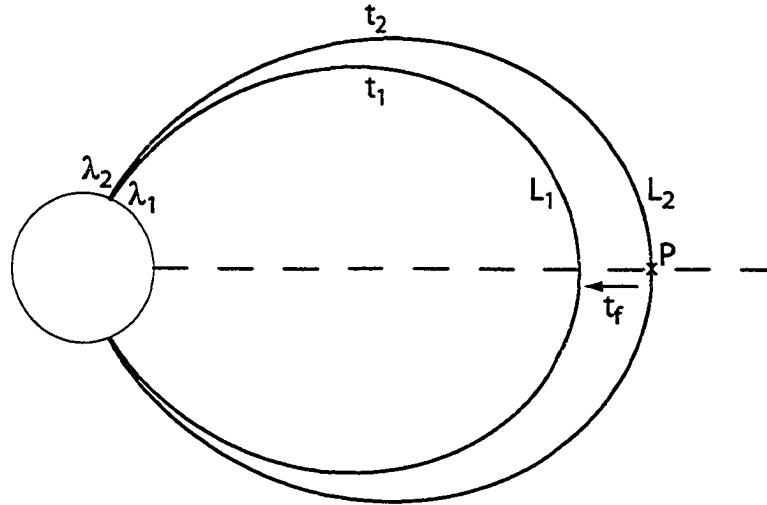


Figure 5.14: Schematic of the dipolar field line geometry. The propagation time for an Alfvén wave along field lines L_1 and L_2 from the equatorial plane to the Earth (at latitudes λ_1 and λ_2) is t_1 and t_2 .

between propagation from P to the ionosphere along field lines L_1 and L_2 is given by

$$\Delta t = t_2 - (t_1 + t_f) \quad (5.1)$$

where t_1 and t_2 are the Alfvén wave propagation times from the equatorial plane to the ionosphere along L_1 and L_2 and t_f is the fast mode propagation time in the equatorial plane from L_2 to L_1 . Hence the rate of latitudinal phase propagation due to this propagation time lag is

$$\frac{\Delta \lambda}{\Delta t} = \frac{4(\lambda_2 - \lambda_1)}{T_2 - (T_1 + 4t_f)} \quad (5.2)$$

where we have used the WKB time of flight approximation that $t_1 = T_1/4$ where T_1 is the standing Alfvén wave eigenperiod at L_1 (and similarly for T_2). Hence if $\Delta t > 0$ then the wave phase propagates polewards, and conversely if $\Delta t < 0$ equatorwards phase propagation occurs.

In general, the time t_f can be estimated based upon the fast waveguide mode equatorial group speed, v_{gf} , and the distance between the equatorial crossing points of the field lines, d . If we assume that the fast waveguide mode phase fronts are aligned with the Y GSM axis in the equatorial plane, the phase lag due to the fast mode propagation will be governed by

the X GSM separation of the equatorial crossing points of the two field lines, Δx . If we parameterize $v_{gf} = \alpha v_{Aeq}$, then $t_f = \Delta x / \alpha v_{Aeq}$, where v_{Aeq} is the equatorial Alfvén speed. Increased field line distortion will in general increase Δx , and hence t_f , and this acts to reduce Δt . Similarly, low azimuthal wavenumber flank waveguide modes in general have $v_{gf} < v_A$, and α may be ~ 0.1 and is in general < 1 (see e.g., the discussion section of Allan and Wright, 2000). Both of these act to favor more equatorwards phase propagation.

For a dipolar geometry, with no field line distortion out of the meridional plane, the maximum value of $\Delta x = \Delta L R_E$, where $\Delta L = L_2 - L_1$. The distance from the equatorial plane to the ionosphere (assumed to be at $1 R_E$) of a given field line is given approximately by

$$l \simeq (1.38L - 1)R_E. \quad (5.3)$$

Hence, assuming a constant Alfvén speed both along the field lines and in the equatorial plane for simplicity, in the dipolar case the minimum value of Δt is given by

$$\Delta t = \frac{R_E}{v_A} (0.38) \Delta L > 0. \quad (5.4)$$

Consequently the dipolar field line geometry is expected in general to support field line resonant Alfvén waves with polewards phase propagation. Indeed, in most studies of field line resonant Alfvén wave excitation, the fast mode phase difference generated by t_f is neglected (i.e., the phase difference introduced by fast mode propagation along the distance d between the equatorial crossings of the field lines is assumed to be much smaller than the phase difference resulting from the difference in field line eigenfrequencies). This leads to the phase propagation being defined entirely by the direction of the local Alfvén frequency gradient which, with the possible exception of the plasmopause region, generates polewards phase propagation (e.g., Wright and Allan, 1996; Allan and Wright, 2000; Mann *et al.*, 1995 and Mann, 1997).

We now consider a stretched field line case. We assume that the field line lengths are still given by the dipolar geometry expression (Eq. 5.3, with L defined by the dipolar latitude of the field line ionospheric footprint), but the field lines themselves are stretched out of meridional planes and into the magnetotail (in fact the assumption regarding field line lengths compares well with results from more advanced magnetic field models, e.g.,

the BATS-R-US global MHD model [K. Kabin, Personal Communication, 2003]). In this case we can rewrite Eq. 5.2 as:

$$\frac{\Delta\lambda}{\Delta t} = \frac{\lambda_2 - \lambda_1}{(1.38\Delta L - \Delta x/\alpha)\frac{R_E}{v_A}} \quad (5.5)$$

where Δx is in units of Earth radii. Calculating the predicted phase propagation for the two magnetometer stations NAL and LYR (see Tab. 3.1 and Fig. 5.13) using the T96 field stretching into the GSM equatorial plane gives $\Delta x = 4.06R_E$, so that

$$\frac{\Delta\lambda}{\Delta t} = \frac{76.11 - 75.16}{(1.38 \times 2.11 - 4.06/0.4) \times 6.38} = -0.021^\circ/s \quad (5.6)$$

where we have assumed a constant Alfvén speed of 1000 km/s along the field lines, and that $\alpha = 0.4$, $R_E \simeq 6380$ km.

This result clearly shows that the time of flight phase lag can overcome the typical poleward FLR phase propagation (i.e., $\Delta\lambda/\Delta t$ is negative). The equatorwards phase propagation of $-0.021^\circ/s$ corresponds to $1.2^\circ/\text{min}$, which is clearly similar to the observed equatorwards phase propagation of $1.3^\circ/\text{min}$ observed in the MSP and ASC keograms. The value of 0.4 for α was derived from the sunwards (azimuthal) phase motion of the arcs. The observed azimuthal velocity of 2.2 km/s was converted to an angular velocity, and the small angle approximation $s = r\theta$ was used to convert to an approximate azimuthal distance per second of 400 km/s at a radial distance of $21 R_E$ in the geomagnetic equatorial plane. More realistic modeling which takes account of realistic variations of magnetic field strength and density along the MHD wave paths should allow more accurate values for $\Delta\lambda/\Delta t$ to be estimated. However, our simple calculation shows that it is theoretically possible for the phase of field line resonant Alfvén waves to be reversed due to the fast mode propagation delay which can occur in distorted magnetic field geometries.

We can further illustrate how fast mode propagation lags can introduce equatorwards phase propagation by examining the driven Alfvén wave response of magnetic field lines. The characteristics of a toroidal field line resonant Alfvén wave, b_y , driven by fast mode waves with discrete frequency ω_d at latitude λ at the ionosphere can be described using the simple harmonic oscillator analogy where

$$\frac{d^2 b_y}{dt^2} + \gamma \frac{db_y}{dt} + \omega_o^2(\lambda) b_y = F_d \quad (5.7)$$

and $F_d = F \cos \omega_d t$ represents fast mode wave driving (c.f. Menk *et al.*, 1994) The driven solution to this equation is given by

$$b_y = \frac{F \cos[\omega_d t + \phi(\lambda)]}{([\omega_o^2(\lambda) - \omega_d^2]^2 + \gamma^2 \omega_d^2)^{1/2}} \quad (5.8)$$

where

$$\phi(\lambda) = \tan^{-1} \left[\frac{\omega_d \gamma}{\omega_o^2(\lambda) - \omega_d^2} \right] \quad (5.9)$$

and where $\omega_o^2(\lambda)$ represents the natural Alfvén wave frequency as a function of latitude, λ , and the resonant field line latitude λ_r is defined by the position where $\omega_d = \omega_o(\lambda)$ and the phase $\phi(\lambda = \lambda_r) = 0$.

If we assume that the fast mode wave which drives the Alfvén wave response at the ionosphere develops an additional phase lag $\phi_f(\lambda)$ due to equatorial fast mode wave propagation so that $F_d = F \cos[\omega_d t + \phi_f(\lambda)]$ then the solution becomes

$$b_y = \frac{F \cos[\omega_d t + \phi(\lambda) + \phi_f(\lambda)]}{([\omega_o^2(\lambda) - \omega_d^2]^2 + \gamma^2 \omega_d^2)^{1/2}}. \quad (5.10)$$

The phase of $\phi_f(\lambda)$ can be chosen with respect to an arbitrary latitude, and for simplicity we choose $\phi_f(\lambda = \lambda_r) = 0$. We can examine the direction of overall latitudinal wave phase propagation by examining the variation of the total phase $\phi_{total}(\lambda) = \phi(\lambda) + \phi_f(\lambda)$.

For the undistorted dipole field case, $\phi_f(\lambda)$ can be neglected in comparison to $\phi(\lambda)$, and for the case appropriate to the outer magnetosphere where $\omega_o(\lambda)$ is a monotonically decreasing function we obtain

$$\frac{d\phi_{total}}{d\lambda} < 0. \quad (5.11)$$

In this case the wave phase propagates polewards as expected. However, in the distorted flank field case for waves propagating sunwards from the tail, $d\phi_f/d\lambda > 0$. If the fast mode phase lag is sufficiently large this can reverse the sign of $d\phi_{total}/d\lambda$ which becomes positive, representing a phase reversal into equatorwards phase propagation at the ionosphere. This shows that field line distortion can theoretically generate equatorwards moving FLR

arcs on closed field lines, our observations suggesting that this is the explanation for the observed sunwards and equatorwards moving arcs which we reported in the dusk sector.

5.6 Conclusions

We have presented multi-instrument observations of a number of intervals, each characterised by periodic, multiple east-west aligned auroral arcs in the dusk sector. In each case the auroral features were observed to propagate sunwards and equatorwards from the poleward boundary of the auroral oval, and were located on closed field lines. Using IMAGE magnetometer data for the archetypal case study of 3rd January 1998, the periodicity of the arcs was shown to match the periodicity of fluctuations in the local magnetic field, indicating that the auroral driving mechanism was likely to be related to periodic Alfvén waves. SuperDARN merged velocity data were utilized in this case study to compare the sunwards arc motion with the ionospheric convection velocity, and it was found that the propagation phase speed of the arcs was an order of magnitude higher than the local convection speed, implying that the driving mechanism propagated in from the magnetotail faster than the local convection. We showed how a distorted magnetic field geometry can account for the observed phase propagation features if the arcs are excited by field line resonances driven by flank fast waveguide mode waves which propagate sunwards from the magnetotail and whose phase fronts impinge on more polewards field lines first. We hence propose that in addition to the usual anti-sunwards excitation by the solar wind, the magnetospheric flank waveguide can also be excited by disturbances propagating sunwards from the magnetotail. These sunwards propagating waveguide modes can then drive field line resonant Alfvén waves on auroral field lines, and these Alfvén waves produce the observed sunwards and equatorwards arc propagation characteristics as a result of field line stretching into the magnetotail. Consequently, our study presents the important result that equatorwards propagating discrete east-west aligned auroral arcs can be generated on closed field lines via FLR on stretched field lines in the duskside flank waveguide. This morphology is in addition to the polewards (standard) phase propagation of closed field line arcs [Wright and Allan, 1996; Milan *et al.*, 2001], as well as the equatorwards motion studied by Wright *et al.* (1999) on open field lines in the nightside plasmasheet boundary layer (PSBL) gen-

erated by tail waveguide modes coupling to Alfvén waves in the PSBL. Although previous measurements of periodic aurora in the night-time sector have been associated with ground-based magnetometer pulsations of the same frequency [e.g., Lyons *et al.*, 2002], these are the first observations of equatorwards and sunwards propagating auroral arcs in the dusk sector. We explain the occurrence of such auroral forms as fast mode waves propagating sunwards from the magnetotail in the flank waveguide coupling to Alfvén waves on closed, stretched auroral field lines, which then modulate auroral particle precipitation.

Chapter 6

Energy Deposition In Nightside Auroral Poleward Boundary Intensifications

6.1 Introduction

Quiet time auroral poleward boundary intensifications were first discussed in detail by de la Beaujardiere *et al.* (1994), these authors also being the first to relate these auroral poleward boundary intensifications to dynamics in the magnetotail. de la Beaujardiere *et al.* (1994) reported the occurrence of large intensifications during geomagnetically quiet periods with CANOPUS photometers, and noted that the particles precipitating into the ionosphere were of plasmashet boundary layer origin (as determined from their proximity to the open-closed field line boundary). Henderson *et al.* (1998) extended this work by showing that bursty bulk flows (BBFs) in the magnetotail appeared to be related to the production of these auroral poleward boundary intensifications, these intensifications often being related to north-south aligned auroral structures during intervals when a double auroral oval formed.

More recent multi-instrument studies of these auroral features, now named as polewards boundary intensifications (PBIs), have shown that PBIs are not only related to BBFs in the magnetotail, but are also related to large magnetic disturbances at geosynchronous orbit, to large magnetic fluctuations on ground, and to ionospheric features which propagate sunwards away from the midnight sector down both flanks [Lyons *et al.*, 1998; Lyons *et al.*, 1999, Lyons *et al.*, 2002]. Interestingly, although the optical features of the PBIs begin at the poleward edge, they also often propagate equatorwards reaching latitudes inside geosynchronous orbit.

Previous studies of PBIs tended to concentrate on their optical structure in the ionosphere, and have not shown the influence of PBIs on ionospheric structure. In this Chapter we use IS radar data to calculate in-situ energy deposition rates during PBI events, to our knowledge this being the first time that such a calculation has been completed for PBIs. Further, we compare the IS determined ionospheric response and periodicity of ionospheric heating with the magnetic as well as optical temporal variations observed during PBIs.

We present ground-based observations of a “typical” PBI event, using optical, magnetometer and incoherent scatter (IS) radar data. We use the IS radar data to show that the energy deposited into the ionosphere during PBI events is large, and that PBIs may represent the ionospheric signature of dynamic coupling between the distant magnetosphere and near Earth space via Alfvénic wave activity.

6.2 Observations

The observations in this study are taken exclusively from ground-based instrumentation, and include the Longyearbyen meridian scanning photometer (MSP), the Ny Ålesund all sky camera (ASC), the EISCAT Svalbard IS radar (ESR) and the IMAGE magnetometer chain (for a full description of these instruments see Chapter 3).

Figure 6.1 displays MSP data from Longyearbyen for the interval 0000 to 0700 UT on the 10th February 2000. The poleward boundary of the auroral oval was observed to move polewards between 70° and 76° corrected geomagnetic latitude between 0000 and 0230 UT, with PBI auroral features moving clearly equatorwards from the polewards boundary at 76° towards 71° between 0120 and 0150 UT. The polewards edge of the auroral oval abruptly moved equatorwards at 0240 UT to 71° magnetic latitude, and remained at low latitudes until 0420 UT, whereupon it swiftly moved polewards reaching magnetic latitudes of around 77°. Polewards boundary intensifications (PBIs) were also observed between 0430 and 0600 UT, although the extent of the equatorwards latitudinal motion of these auroral forms was not as significant as that of the previous PBIs at around 0130 UT.

We focus on the three extended equatorwards propagating auroral features that occurred between 0120 and 0150 UT. We may investigate the magnetic signature of these auroral forms using the northernmost stations of the IMAGE magnetometer network. Figure 6.2

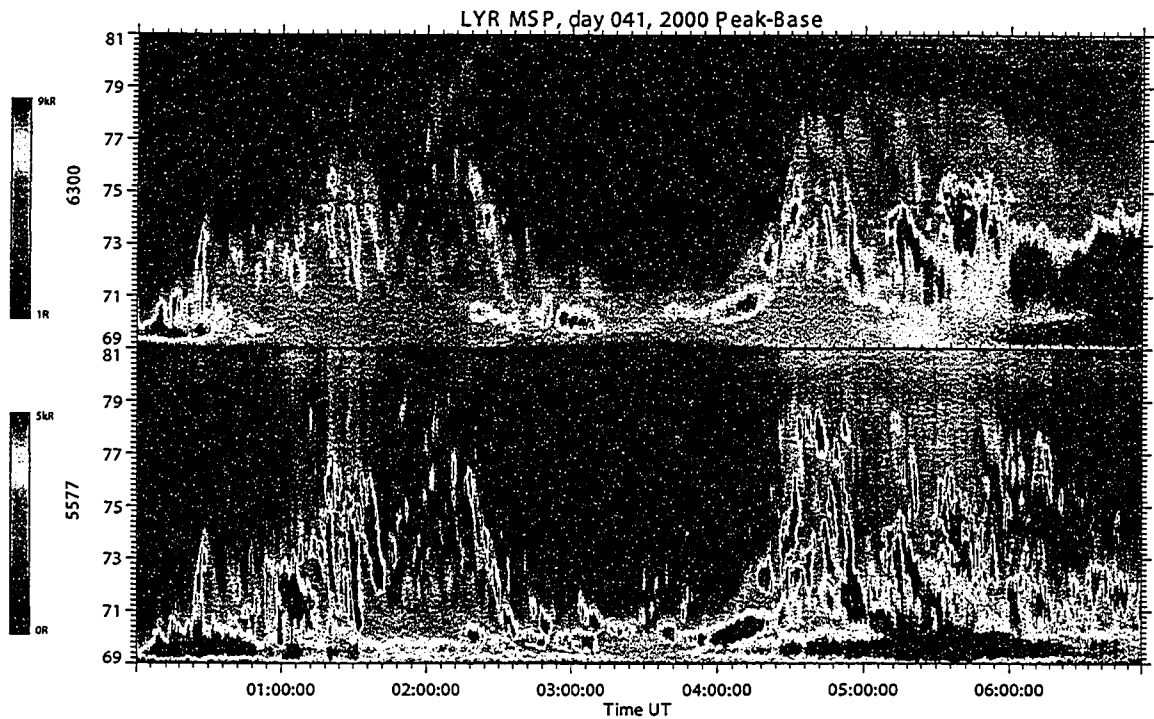


Figure 6.1: MSP data from Longyearbyen for the interval 0000 to 0700 UT on the 10th February 2000, plotted against magnetic latitude. The polewards edge of the auroral oval, as characterised by 630.0 nm emission is seen to move throughout the interval, and there is clear activity at the polewards edge in both the 630.0 nm and 557.7 nm bands throughout the interval. Clear, equatorwards propagating auroral features are observed between 0120 and 0150 UT and also between 0430 and 0500 UT.

displays IMAGE H- and D-component magnetometer data from the five northernmost stations. The southernmost two stations, Hopen Island and Bear Island (labelled HOP and BJN respectively) are located at latitudes of 73.1° and 71.5° magnetic, in the lower half of the field of view of the Longyearbyen MSP. These two stations clearly show wave-like signatures in both components between 0100 and 0150 UT, the interval during which the Longyearbyen MSP observed clear PBI activity.

We may quantitatively investigate the ionospheric heating rate associated with the observed PBIs by analysing data from the ESR (see Chapter 3 for a full description of incoherent scatter radars). Figure 6.3 displays electron density, ion temperature, electron temperature and ion velocity data for the interval 0000 to 0330 UT on the 10th February 2000. The electron density plot (top panel of Figure 6.3) clearly shows intensifications at low altitudes (between 200 and 100 km) at around 0130 UT that correspond to the PBIs observed in the MSP, although the individual PBI structures are not as clearly defined. Ion temperature intensifications are also observed (second panel of 6.3), although generally at higher altitudes. The third panel of Figure 6.3 illustrates that during the interval of PBI activity appreciable heating of the ionospheric plasma occurred, which reached a maximum at between 300 and 600 km altitude, where the electron temperature was periodically raised from 2000 to 3000 K. The velocity profile (fourth panel of Figure 6.3) show no clear intensifications during the period of PBI activity.

To further illustrate the properties of the observed PBI activity, we can overplot time-series of MSP data, magnetometer data and ESR data. Figure 6.4 shows a slice through the Longyearbyen MSP data taken at a look angle of 120° , which corresponds to a magnetic latitude of 73° . The second and third panels display unfiltered H- and D-component magnetic field data from the magnetometer at Bear Island. Evidence of magnetic pulsations that directly correspond to the three discrete auroral features observed in the MSP are clearly visible. The lower three panels of Figure 6.4 show ESR electron density, electron temperature and ion temperature timeseries taken from an altitude of 110 km - the presumed altitude of maximum auroral green line emission. Clear electron temperature peaks are coincident with the three auroral arcs, whereas the electron and ion temperature data show no real correlation with the MSP features. However, at higher altitudes the electron temperature data does show clear intensifications during the periods of PBI activity (see the

IMAGE H and D component plot: Day10 Month: 2 Year: 2000 Unfiltered

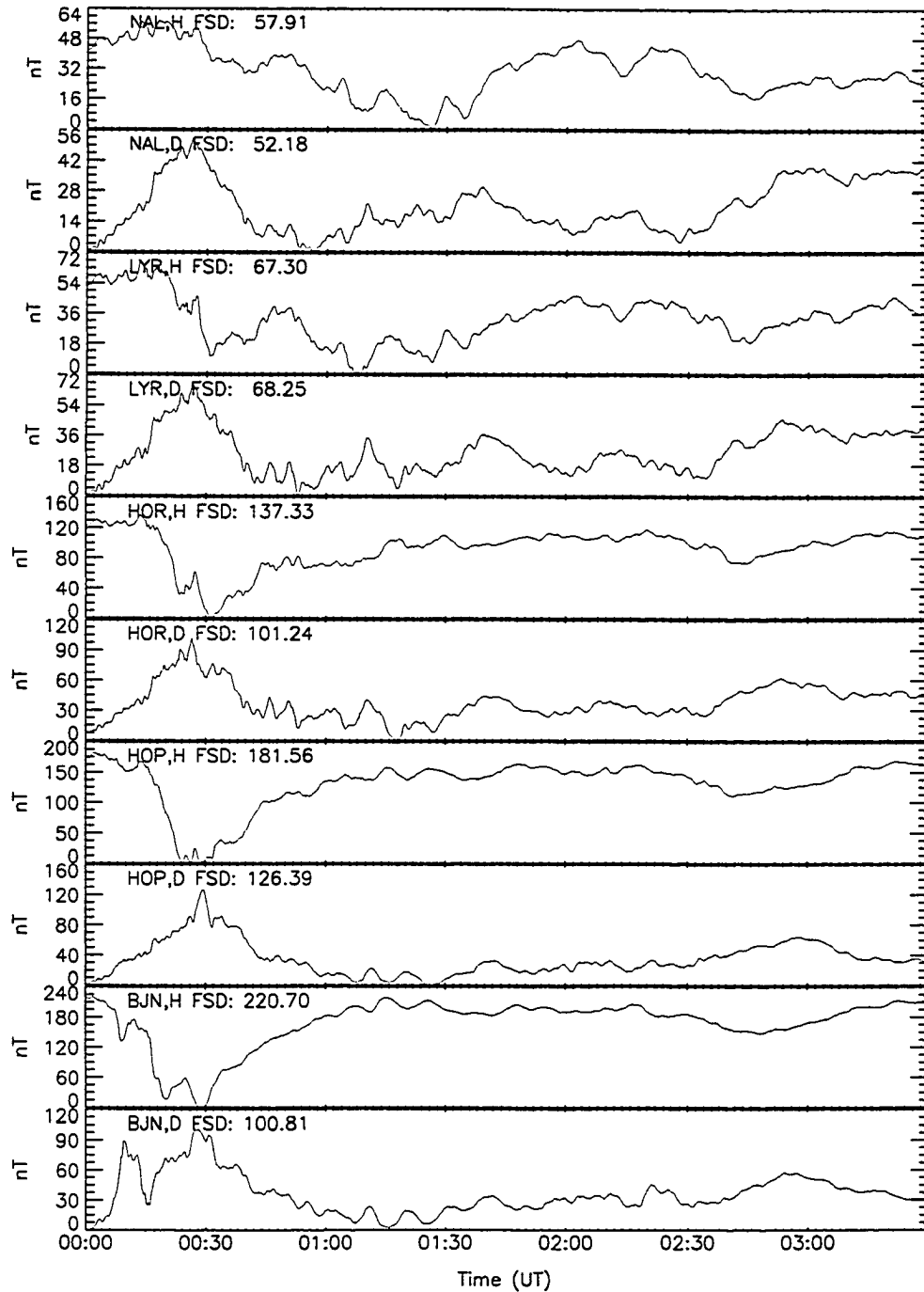


Figure 6.2: IMAGE H- and D-component magnetometer data for the interval 0000 to 0330 UT on the 10th February 2000. Each timeseries is independently scaled, FSD indicating the full scale deflection of the trace in each panel.

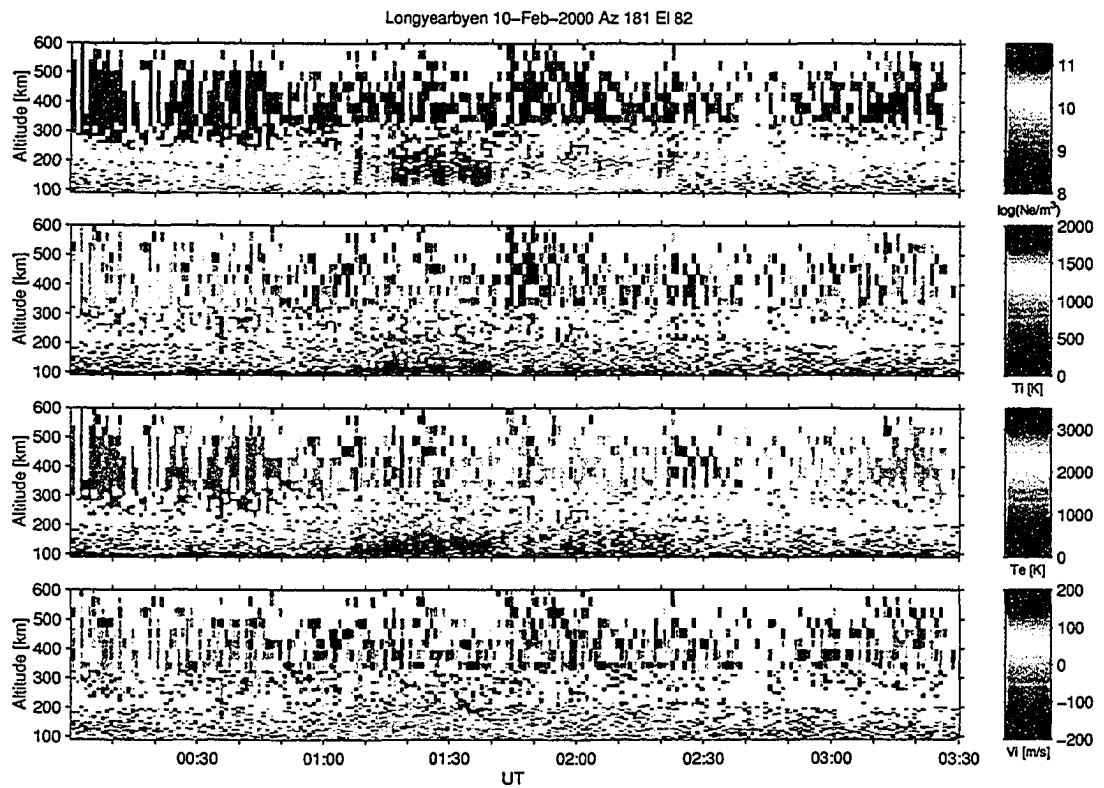


Figure 6.3: ESR data for the interval 0000 to 0330 UT on the 10th February 2000. Parameters plotted are electron number density (top panel), ion temperature (second panel), electron temperature (third panel) and ion velocity (lower panel).

third panel of Figure 6.3), implying that the majority of electron heating occurs at altitudes higher than the assumed green line auroral emission height of 110 km.

6.3 Discussion

Recent theoretical work has shown that when fast mode waves are excited in the magnetotail, they can propagate Earthwards in a magnetotail waveguide which consists of the plasmashet, the plasmashet boundary layer (PSBL), and the lobe [Wright *et al.*, 1999; Allan and Wright, 2000]. Here, fast mode waves propagate towards the Earth with a group speed much slower than the local Alfvén speed. These modes can couple to Alfvén waves in the PSBL, the Alfvén waves propagating Earthwards ahead of the fast modes. Since the Alfvén speed in the PSBL increases with altitude, the Alfvén waves at the poleward edge of the auroral oval, at the top of the PSBL, arrive at the Earth first. Only the Alfvén waves carry the field aligned current which may be necessary for the production of auroral arcs, the resulting dispersion across the PSBL creating signatures of equatorwards moving arcs with characteristics very similar to PBIs [Wright *et al.*, 1999] (for a full discussion of mode coupling in a tail-like environment, see Chapter 2).

Interestingly, in recent work with the Polar satellite, Wygant *et al.* (2000) have shown that at altitudes of around $6 R_E$ in the PSBL, very large amplitude Earthward propagating Alfvén waves can exist [see also Keiling *et al.*, 2001]. These Alfvén waves were shown, on a global scale, to map to the locations of large scale intense auroral features seen with the Polar VIS instrument [Wygant *et al.*, 2000], supporting the hypothesis that the Alfvén waves in the PSBL are related to, and possibly drive, the auroral features. Of great significance is the calculation by Wygant *et al.* (2000) which shows that the Earthward propagating PSBL Alfvén waves carry a Poynting flux which is of the same order or greater than the combined incident electron and ion particle fluxes, and 1-2 orders of magnitude greater than the steady-state Poynting flux from magnetospheric convection. Wygant *et al.* (2000) conclude that the PSBL Alfvén waves are one of the most energetically significant and hence potentially dominant components of magnetotail-auroral coupling in the night-side magnetosphere. Consequently the propagation of these Alfvén waves and the creation of PBIs can represent a major component of auroral zone activity. If PBIs are related to

Timeseries of LYR MSP, BJN magnetometer and ESR datasets

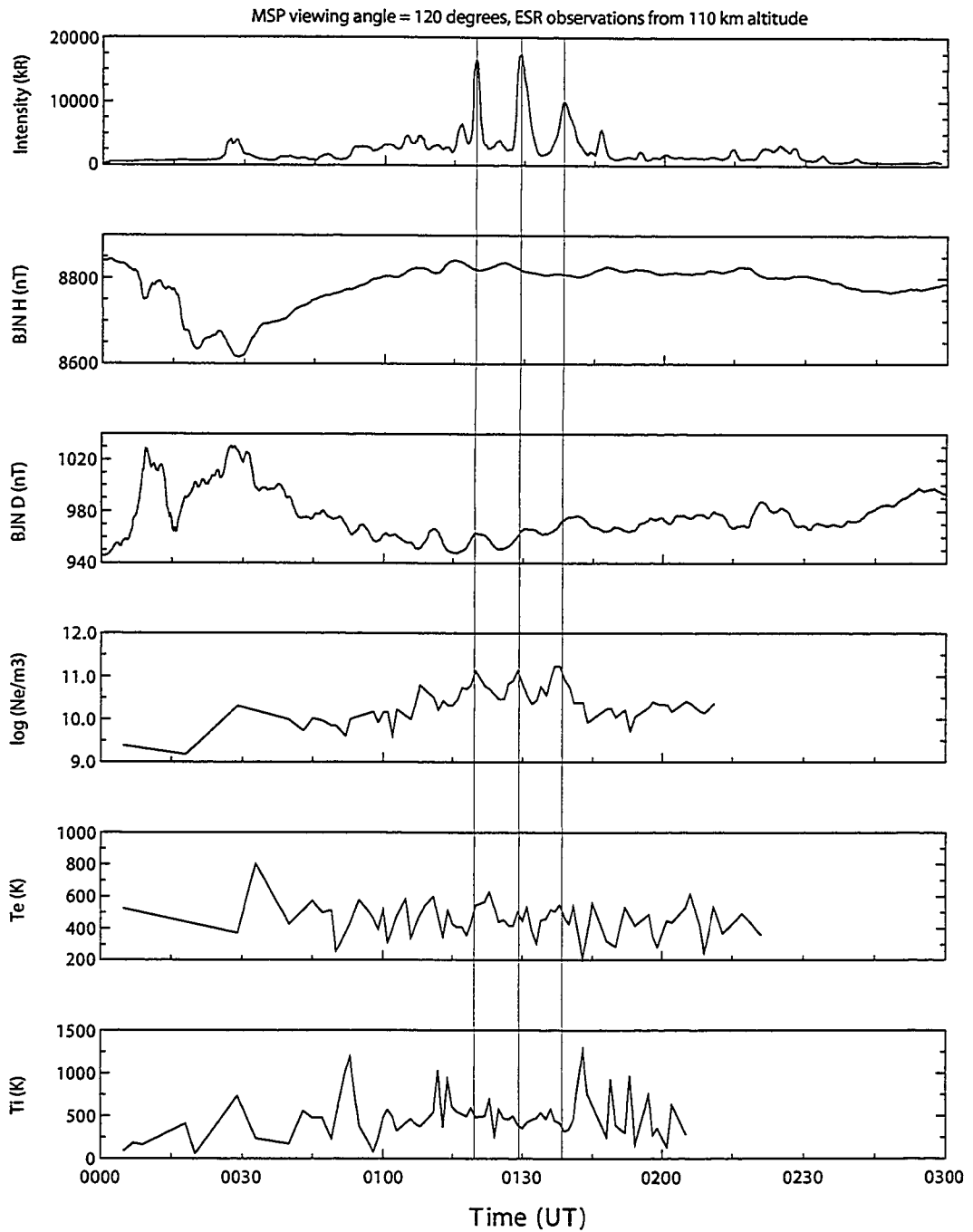


Figure 6.4: Stacked timeseries from the Longyearbyen MSP (top panel), unfiltered Bear Island magnetometer (second and third panels) and the EISCAT Svalbard radar (lower three panels). Red vertical lines correspond to the maximum intensity of the three quasi-periodic auroral features.

the propagation of ULF waves in the tail waveguide, then these waves may represent a major source of direct magnetotail-ionosphere coupling [Wygant *et al.*, 2000] which is of very considerable importance for energy transport from the tail to the auroral zone in the near-Earth magnetosphere.

In a recent paper, Lyons *et al.* (2002) show convincing evidence that auroral activations in the nightside polewards edge, as monitored by meridian scanning photometers (MSPs), are related to the propagation of ULF pulsations in the tail and nightside plasmashet. The Lyons *et al.* (2002) work shows that tail bursty bulk flows (BBFs), geosynchronous magnetic field fluctuations, large amplitude ULF waves on the ground, and arcs which propagate equatorwards from the polewards edge are all related. The top panel of Figure 6.5 (taken from Lyons *et al.*, 2002) displays MSP data from the Canadian sector and PBIs are clearly visible. Interestingly, the optical signatures are seen to propagate from the polewards edge and to reach inside geosynchronous orbit. The bottom half of Figure 6.5 displays Polar satellite low resolution VIS camera data during the interval when PBIs were occurring and when a double auroral oval is present. Most spectacularly, these global Polar auroral images show that the PBIs occurring on the polewards edge appear to have long azimuthal wavelength structure which can develop into vortices. However, the activity occurring at the polewards edge appears to be unrelated to the quiet and substorm free conditions of the equatorwards arc, and can hence occur during more geomagnetically quiet times [Lyons *et al.*, 2002].

The PBI structures observed by Lyons *et al.* (2002) are observed to propagate away from midnight towards both flanks (as observed by SuperDARN radars), and have a repetition frequency of around 10 minutes. The full details of how waves propagate in the global magnetotail waveguide have yet to be worked out, however it seems possible that they are related to some type of global eigenmodes of the entire tail [cf. Lyons *et al.*, 2002]. In follow up work, Zesta *et al.* (2002b) have shown that PBIs exhibit two distinct forms in the auroral oval; being either north-south structures or east-west arcs. These authors conclude that the north-south structures are manifestations of flow bursts in the tail, and that the east-west arcs may be the result of global ULF mode in the magnetotail.

Previous observations of particle heating in the auroral ionosphere during substorm activity [e.g., Banks, 1977] have shown that particle heating rates can be as high as 50

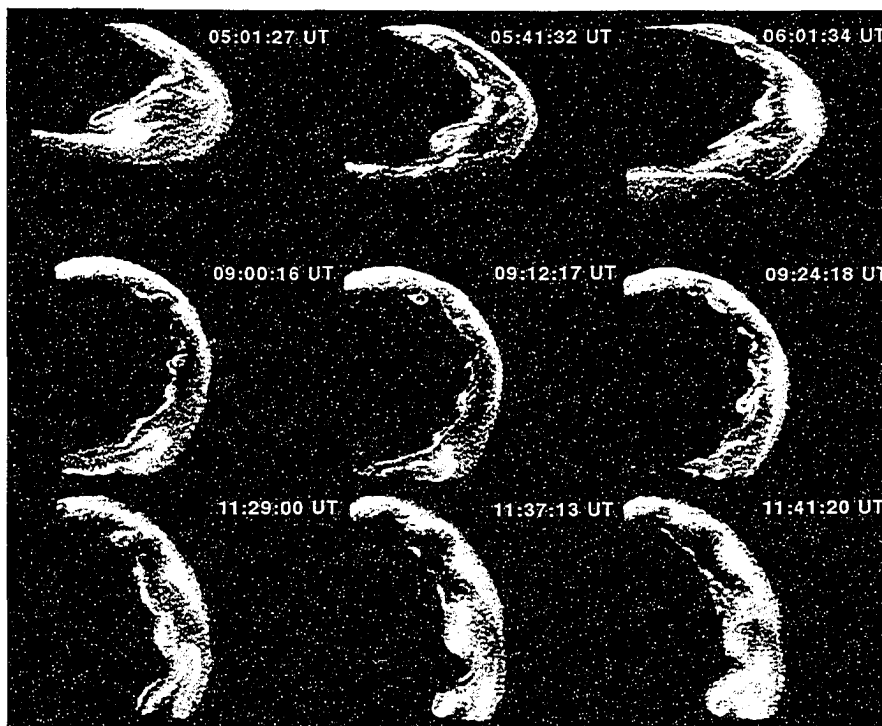
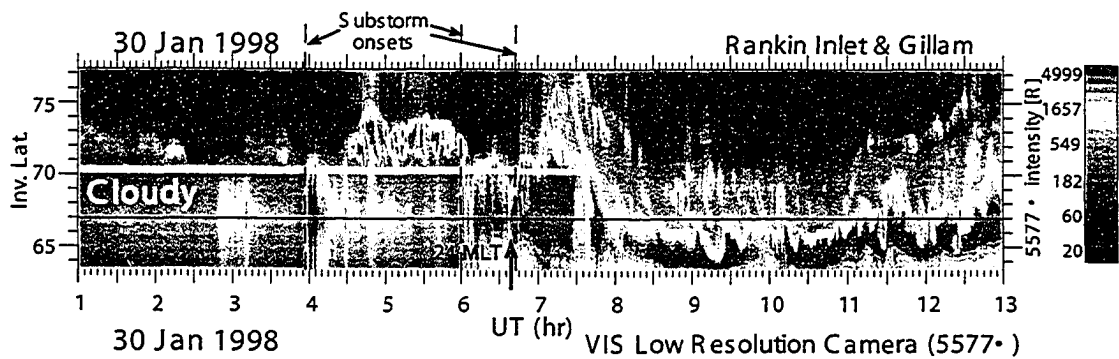


Plate 1

Figure 6.5: Taken from Lyons *et al.* (2002). Top panel shows MSP data from Canadian sector, with PBI events. The horizontal line at 67° latitude delineates data from Rankin Inlet (above 67° latitude) and Gillam (below 67° latitude). Bottom shows Polar data where the auroral zone shows evidence of wave-like structure.

mJ/m²s. We may compute the particle heating rate for an intensification during the interval of PBIs, using the method of Vickrey *et al.* (1982). They employed an empirical model dependent on the collision frequency at a given altitude and the electron density at that altitude to compute the ionospheric particle heating for a range of events with differing conditions. They investigated a relation of the form

$$\epsilon(z) = W_{ion}\alpha(z)N_e^2(z) \quad (6.1)$$

where ϵ is the particle heating rate at an altitude z , W_{ion} is the average energy deposited per ion-electron pair, α is a function of z that encompasses the plasma variation with altitude and the neutral temperature profile, and N_e is the electron density at altitude z . Vickrey *et al.* (1982) found that the best fit was produced for

$$\epsilon(z) = 2.5 \times 10^{-12}e^{(-z/51.2)}N_e^2(z) \quad (6.2)$$

and this is the equation we use to calculate ionospheric heating due to particle precipitation. This method yields a maximum particle heating rate of 20 mJ/m²s, i.e., the deposition of energy into the ionosphere during PBI events may be of the same order of magnitude per unit area as the energy deposition during substorms.

A statistical study by Keiling *et al.* (2002) showed that observations of in-situ Alfvén wave Poynting flux can be mapped to energy fluxes in the ionosphere. They found that in-situ Poynting fluxes in the PSBL of between 0.02 and 2 mJ/m²s corresponded to a heating rate of between 0.4 and 40 mJ/m²s at the ionosphere. The determination of the heating rate by Keiling *et al.* (2002) was done purely on the magnitude of the emission from visible aurora, whereas in this study we have directly measured the ionospheric heating using ionospheric parameters derived from IS radar measurements. However, our ground-based results are consistent with those of Keiling *et al.* (2002), the heating rate we observe on the ground corresponding to an Alfvénic Poynting flux of around 1 mJ/m²s in the PSBL. Furthermore, the correspondence between the ground magnetic field perturbations and the arc repetition rate as observed both optically and with the IS radar indicate that this particular PBI event may have been driven by Alfvén waves propagating from the PSBL region into the auroral ionosphere. We investigate this further in the next Chapter.

6.4 Conclusions

We have presented ground-based multi-instrument observations of a PBI event between 0100 and 0200 UT on the 10th February 2000. Meridian scanning photometer data from Longyearbyen showed multiple, discrete auroral forms propagating equatorwards from the poleward boundary of the auroral oval (defined by the cut-off in the 630.0 nm emission [Blanchard *et al.*, 1997]), and all sky camera data from Ny Alesund illustrated that these auroral forms were east-west aligned arcs. Data from the IMAGE magnetometer chain showed periodic pulsations that corresponded to the repetition rate of the PBIs, implying that the source mechanism for the aurora may have been wave activity in the magnetosphere. EISCAT Svalbard Radar data further illustrated the ionospheric electron temperature intensifications associated with the auroral forms, and allowed the computation of the particle heating rate. This heating rate was found to be maximally 20 mJ/m²s, consistent with the predicted heating rates due to Alfvén waves with large Poynting fluxes propagating earthwards from the magnetotail on auroral field lines [Keiling *et al.*, 2002]. Further, we may estimate the required Poynting flux in the magnetosphere to produce such auroral features, and find that the prediction of a magnetospheric Poynting flux of at least 0.2 mJ/m²s at an altitude of around 5 R_E is totally consistent with previous observations [e.g., Wygant *et al.*, 2000; Keiling *et al.*, 2002; Wygant *et al.*, 2002]. Our observations hence suggest that Alfvénic waves at high altitudes in the PSBL may produce some types of auroral PBIs, the ionospheric particle heating and energisation being provided by incoming Alfvén wave Poynting flux. Interestingly, this suggests, in agreement with Wygant *et al.* (2002), that the high altitude PSBL region may be an important energy source for auroral emissions in addition to the acceleration in the “acceleration region” at much lower altitudes. We discuss this possibility further in the next Chapter.

Chapter 7

Observations of Large Alfvén Wave Poynting Flux in the Plasmasheet Boundary Layer Associated with Auroral Arcs

7.1 Introduction

Recent theoretical work has indicated that the magnetotail may be capable of acting as a waveguide supporting discrete frequency fast mode MHD waves [Allan and Wright, 1998; Wright *et al.*, 1999; Allan and Wright, 2000]. Fast mode waves in such a geometry can mode convert to Alfvén waves on field lines in the plasmasheet boundary layer (PSBL), and thus propagate energy to near Earth space (see Section 2.5 for a full discussion of the magnetotail waveguide). Observations of poleward boundary intensifications (PBIs) [Lyons *et al.*, 1999; Lyons *et al.*, 2002; Zesta *et al.*, 2002b] have suggested that these types of auroral activity may be related to wave phenomena in the magnetosphere, specifically global ULF oscillations in the magnetotail. Direct observations from the high-altitude ($\sim 5-6 R_E$) PSBL [Wygant *et al.*, 2000; Keiling *et al.*, 2001; Wygant *et al.*, 2002] have shown that during periods of auroral activity Alfvén wave activity is observed on auroral field lines, with associated large amplitude earthward directed Poynting fluxes, and Wygant *et al.* (2000) argue that wave power in the PSBL contains enough energy to power the most intense auroral structures observed in their Polar UVI data. Wygant *et al.* (2002) suggest that small scale kinetic Alfvén waves in the PSBL produce electric fields parallel to the ambient magnetic field, and can accelerate electrons on auroral field lines to produce auroral activity. Thus far

no comparison between the time-dependence of Alfvén wave power in the PSBL and fine scale ground-based measurements of the aurora has been made. The work of Wygant *et al.* (2002) links PSBL Alfvén wave power to large regions of auroral emissions, but no studies have been made which show temporal coherence between high altitude PSBL Alfvénic waves and fine-scale auroral emissions. In this Chapter we examine these relationships and address the question of the degree to which high-altitude PSBL activity controls the features of PBI auroral emissions.

7.2 Observations

Figure 7.1 displays Longyearbyen meridian scanning photometer (MSP) data from 1730 to 1930 UT on the 7th December 1999. The top panel, corresponding to the 630.0 nm wavelength (and believed to be a proxy for the location of the open-closed field line boundary [Blanchard *et al.*, 1997]), indicates that a poleward expansion of the auroral oval occurred, beginning at approximately 1830 UT. The bottom panel, corresponding to the 557.7 nm wavelength, shows that for the period 1830 to 1910 UT discrete auroral features were observed at the polewards edge of the auroral oval, with evidence of equatorwards propagation between 1850 and 1910 UT.

Figure 7.2 displays solar wind magnetic field data from the ACE satellite for the interval 1700 to 2000 UT. The spacecraft was located at [223, 20, 5] R_E (in GSM x, y, z coordinates) and observed the solar wind to be traveling at a speed ~ 590 km/s. The delay time for the plasma at the satellite to impinge upon the Earth was therefore ~ 40 minutes (assuming planar propagation phase fronts [Lester *et al.*, 1993]). The vertical red line in Figure 7.2 corresponds to the time of the onset of the substorm, at 1825 UT on the ground, as determined from the SAMNET magnetometer array (see later in this section and Figure 7.5). The solar wind during the interval of auroral brightenings was characterised by steady $0 < B_y < 4$, with B_z ranging between positive and negative values.

Figures 7.3 and 7.4 display 557.7 nm data from the Ny Ålesund all sky camera, which is located around 100 km north of the Longyearbyen MSP. Clear westwards and equatorwards motion is observed in the auroral features, which seem to have neither purely east-west nor a purely north-south structure. The most polewards structures in these ASC images are

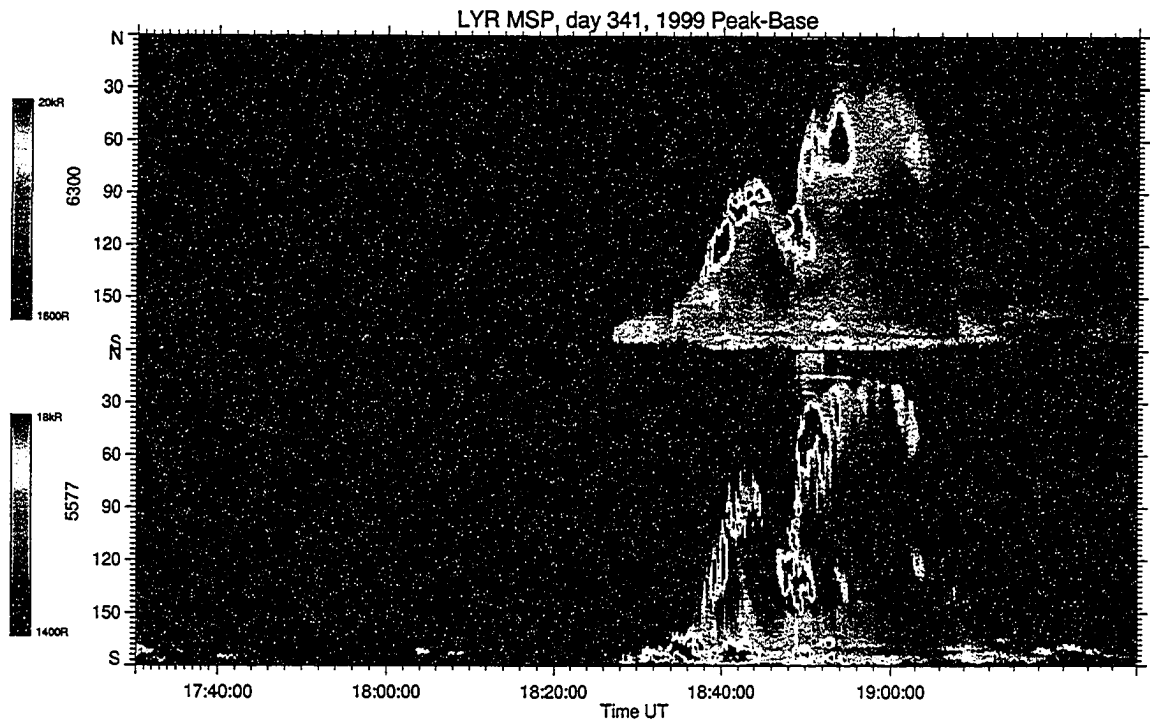


Figure 7.1: Data from the Longyearbyen MSP for the interval 1730 to 1930 UT on the 7th December 1999. The top panel corresponds to the 630.0 nm filter, the bottom to the 557.7 nm emission. The vertical scale represents the look angle of the MSP in the north-south direction, and ninety degrees corresponds to the zenith. PBIs are observed to propagate equatorward from the poleward boundary of the auroral oval 1854 and 1904.

ACE Magnetic Field Instrument, 07 December 1999

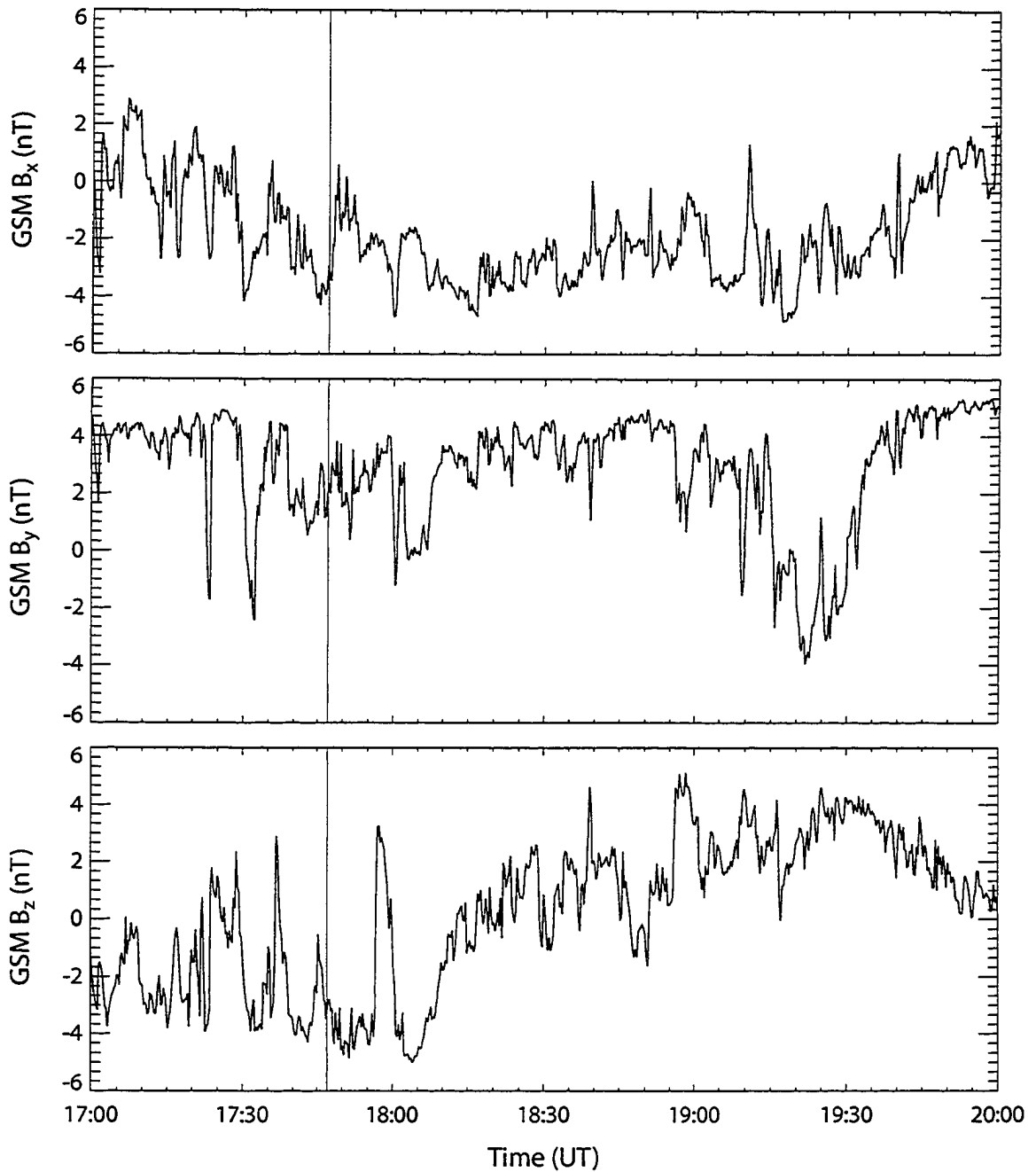


Figure 7.2: Solar wind magnetic field data from the ACE satellite in GSM coordinates for the interval 1700 to 2000 UT on the 7th December 1999. The travel time from ACE to the Earth is ~ 40 minutes, and the red vertical line is the time of the substorm onset observed by SAMNET (see text) lagged by this amount.

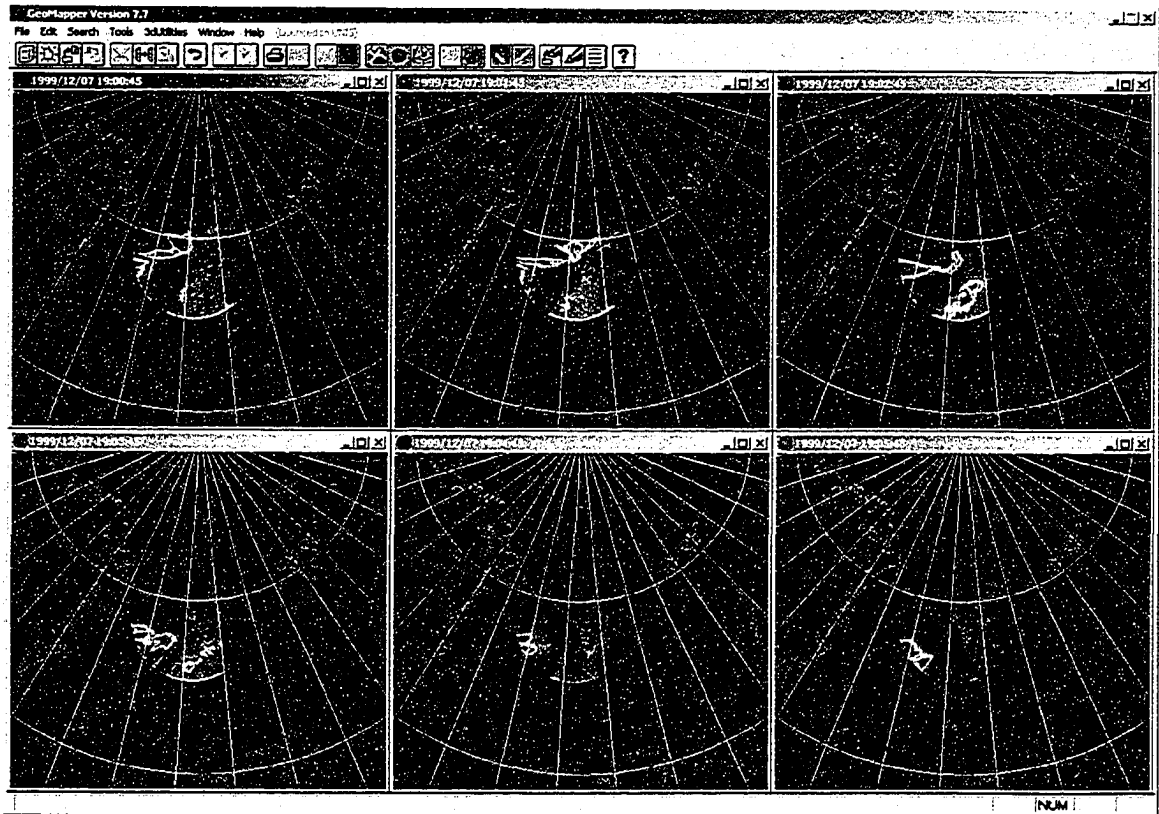


Figure 7.3: 557.7 nm Ny Ålesund all sky camera data for the interval 1900 to 1906 UT on the 7th December 1999 superimposed onto a geographic map. Data are cut off at 170° from the zenith. Magnetic north is approximately in the north-north east direction.

however different, showing an arc orientated in the east-north-east direction geographically, which corresponds to an approximately east-west alignment magnetically.

Figure 7.5 displays data from the SAMNET magnetometer array. The data have been filtered between 200 and 20 seconds, to highlight oscillations in the Pi2 band. The time-series clearly show Pi2 activity at around 1825 UT which is believed to be the signature of substorm onset [e.g., Saito *et al.*, 1976].

Data from the IMAGE [Viljanen and Hakkinen, 1997] magnetometer chain are presented in Figure 7.6. The data clearly show a large negative magnetic deflection in the H-component that is first apparent at the southernmost station, BJN, at 1825 UT and is subsequently observed at more polewards stations. For the interval 1800-1930 UT quasi-periodic perturbations are observed, most notably in the D-component data from LYR and HOR. These pulsations correspond to the period of PBI activity illustrated in Figure 7.1,

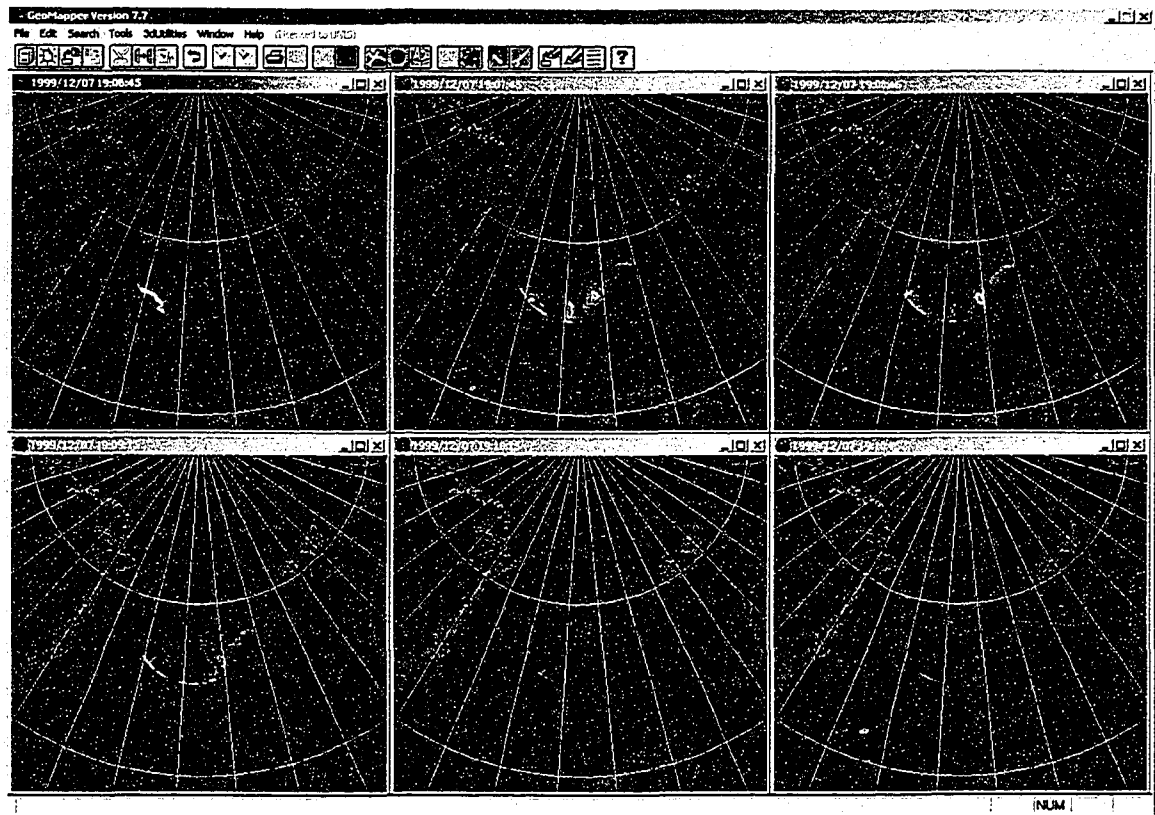


Figure 7.4: 557.7 nm Ny Ålesund all sky camera data for the interval 1906 to 1912 UT on the 7th December 1999 superimposed onto a geographic map. Data are cut off at 170° from the zenith.

SAMNET H and D component plot: Day 7 Month: 12 Year: 1999 Filter (200, 20)

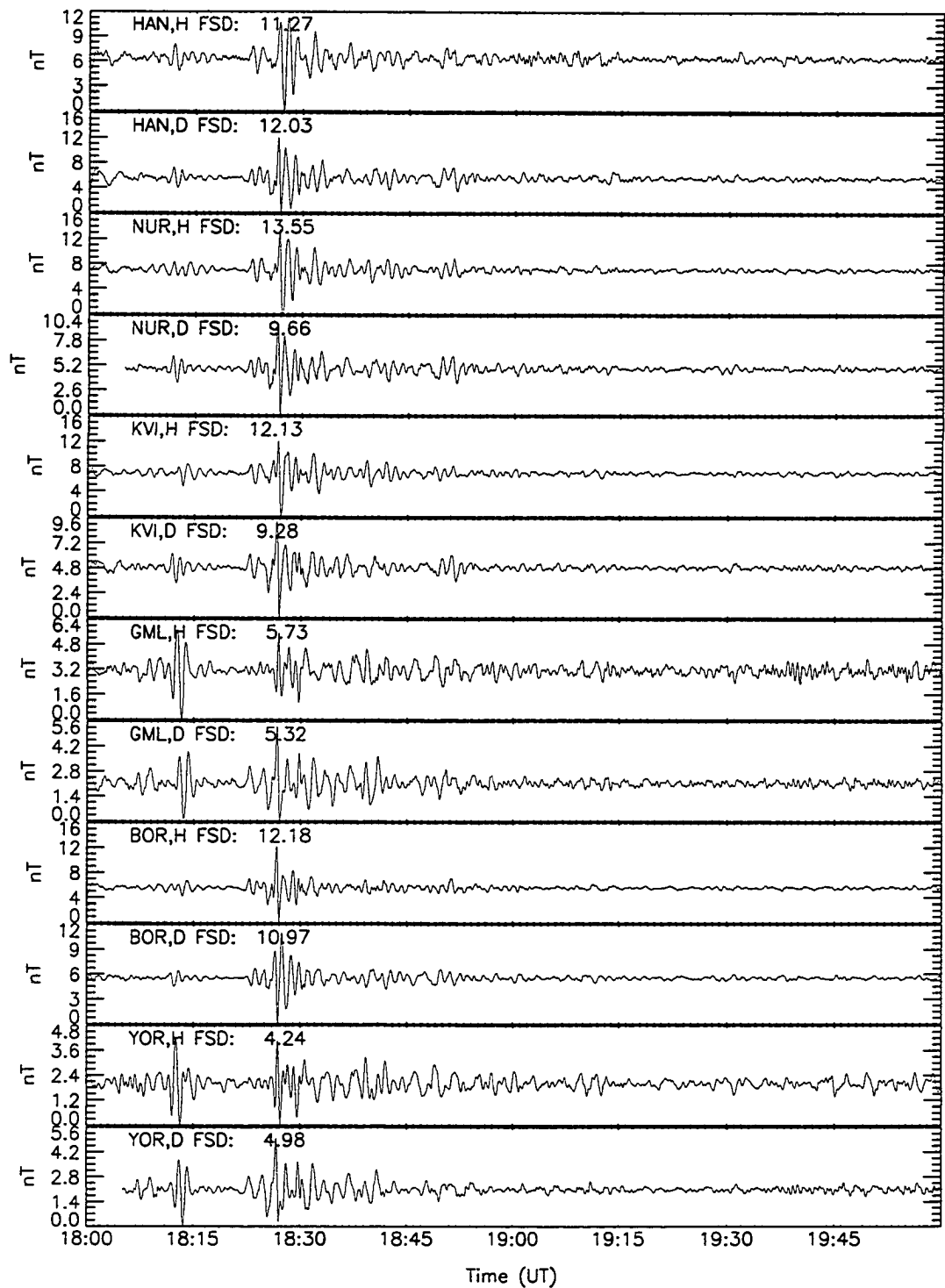


Figure 7.5: SAMNET magnetometer data for the interval 1800 to 2000 UT on the 7th December 1999. The timeseries have been filtered between 200 and 20 seconds to highlight Pi2 activity, believed to be indicative of substorm onset timing.

and Figure 7.7 displays the fast Fourier transform of the D-component of the IMAGE data. A clear spectral peak is observed at the three northernmost stations between 7.5 and 8 mHz, i.e. with a periodicity of between 125 and 133 seconds. This spectral peak highlights ULF wave power of the same frequency as the observed PBI repetition rate (see Figure 7.8).

Figure 7.8 displays a slice through the 557.7 nm MSP data at a look angle of 90° , i.e., the zenith at Longyearbyen (top panel) and unfiltered D-component Longyearbyen magnetometer data (bottom panel) for the interval 1835 to 1905 UT on the 7th December 1999. During this period of wave activity, the repetition rate of the auroral forms observed with the MSP clearly matched the wave periodicity (see red vertical lines in Figure 7.8), with both instruments observing a periodicity of around 150 seconds.

The EISCAT Svalbard Radar (ESR) field-aligned dish was operating in common mode for the duration of the substorm interval, and Figure 7.9 displays electron density (top panel), ion and electron temperature (second and third panels, respectively) and ion velocity (bottom panel) data for the interval 1730 to 1930 UT. Intensifications in the electron number density are clearly evident at low altitudes (around 100 km) during the period of optical brightenings observed in the Longyearbyen MSP data between 1840 and 1910 UT. Also, large ion and electron temperature enhancements are observed at all altitudes after the substorm onset, with the electron temperature seeing the largest increase. High altitude observations of the ion velocity (bottom panel of Figure 7.9, between 350 and 500 km) show that during the substorm interval large increases in the flux of anti-Earthward directed ions occurred, which may be related to the downward field-aligned current caused by the substorm.

Between 1730 and 1930 UT, the Polar satellite crossed field lines that were conjugate to the field of view of the MSP at Longyearbyen. Figure 7.10 shows the footprint of the satellite when traced along a Tsyganenko 1996 [Tsyganenko and Stern, 1996b] model magnetic field line from Polar to the ionosphere, and the field of view of the MSP at Longyearbyen.

To fully utilize the data from the Polar spacecraft, we first determine in which plasma regime of the magnetosphere the spacecraft was located. Figure 7.11 displays spectrograms from the HYDRA instrument on-board the Polar satellite, and it is clear that the spacecraft moved from a region of hot plasma into a region of cold plasma at approximately 1745 UT. At this time the spacecraft was moving northwards through the magnetosphere in the

IMAGE H and D component plot: Day 7 Month: 12 Year: 1999 Unfiltered

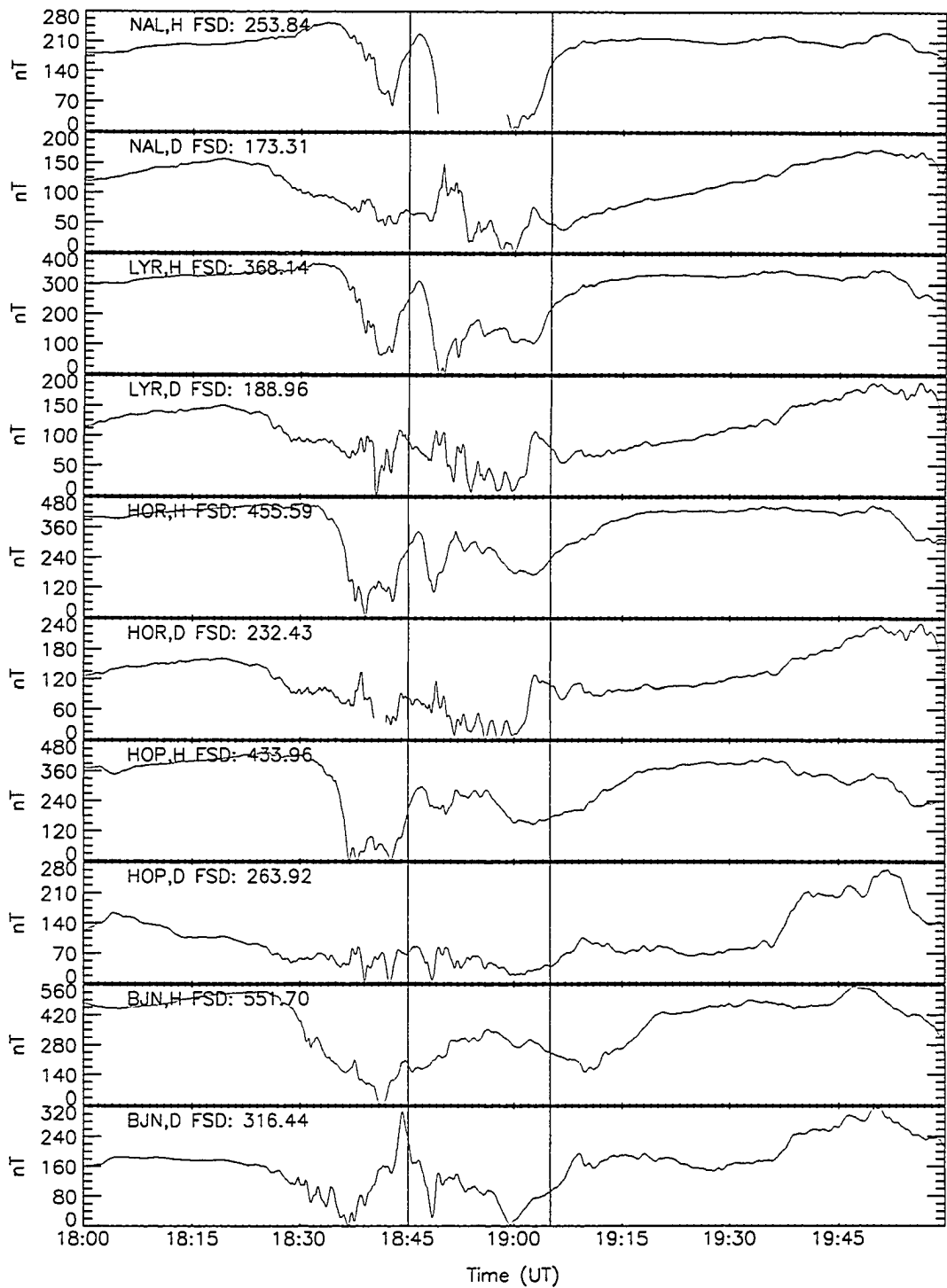


Figure 7.6: Unfiltered H- and D-component data from the five northernmost IMAGE magnetometer stations for the interval 1800 - 2000 UT on the 7th December 1999. Red vertical lines indicate the time interval for which Fourier analysis was performed.

IMAGE D component plot: Day 7 Month: 12 Year: 1999 Filter (350, 50)

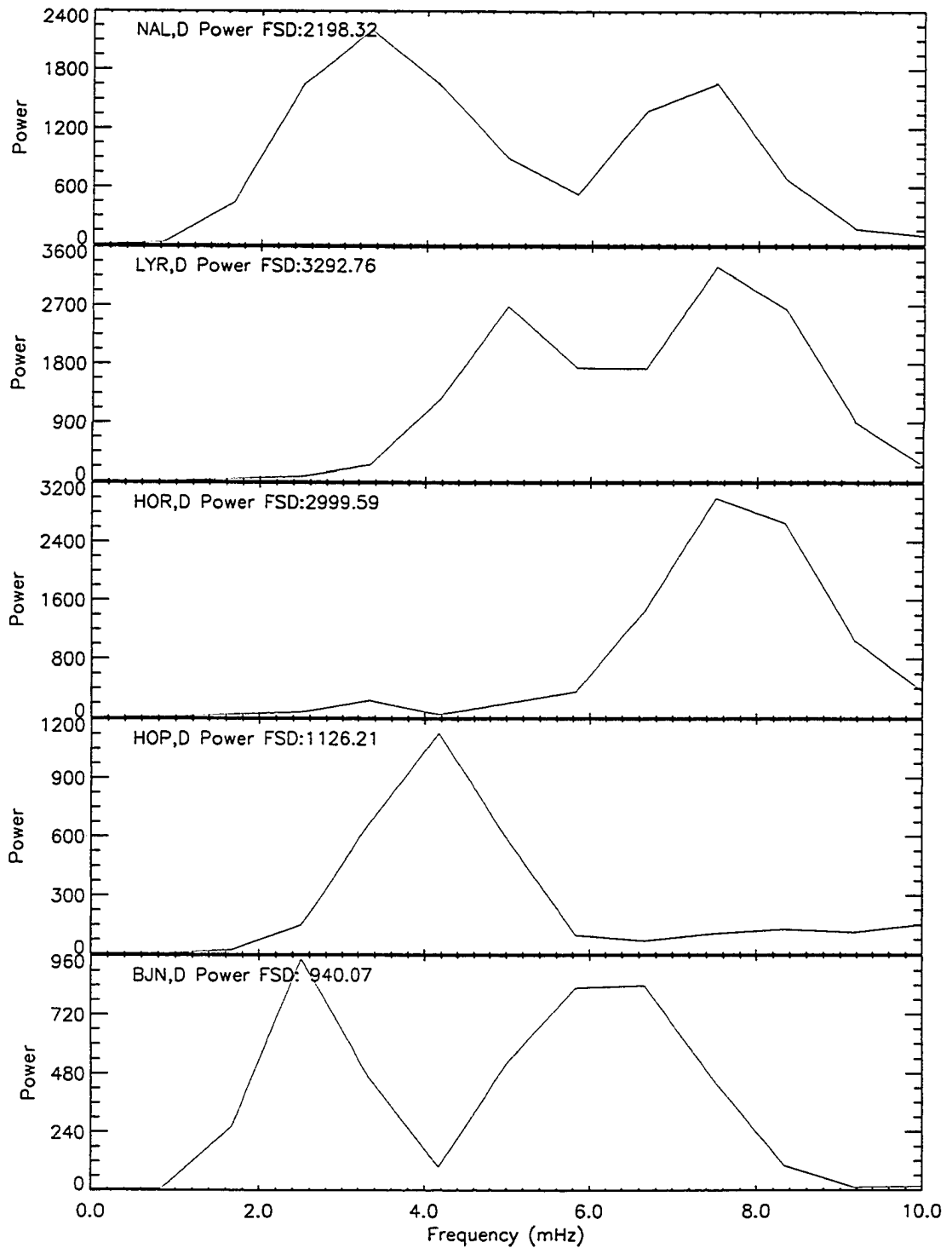


Figure 7.7: Fourier transforms of the D-component data from the five northernmost IMAGE magnetometer stations for the interval 1845 to 1905 UT on the 7th December 1999 (highlighted in Figure 7.6). Timeseries are filtered between 50 and 350s, i.e., 2.6 to 20 mHz.

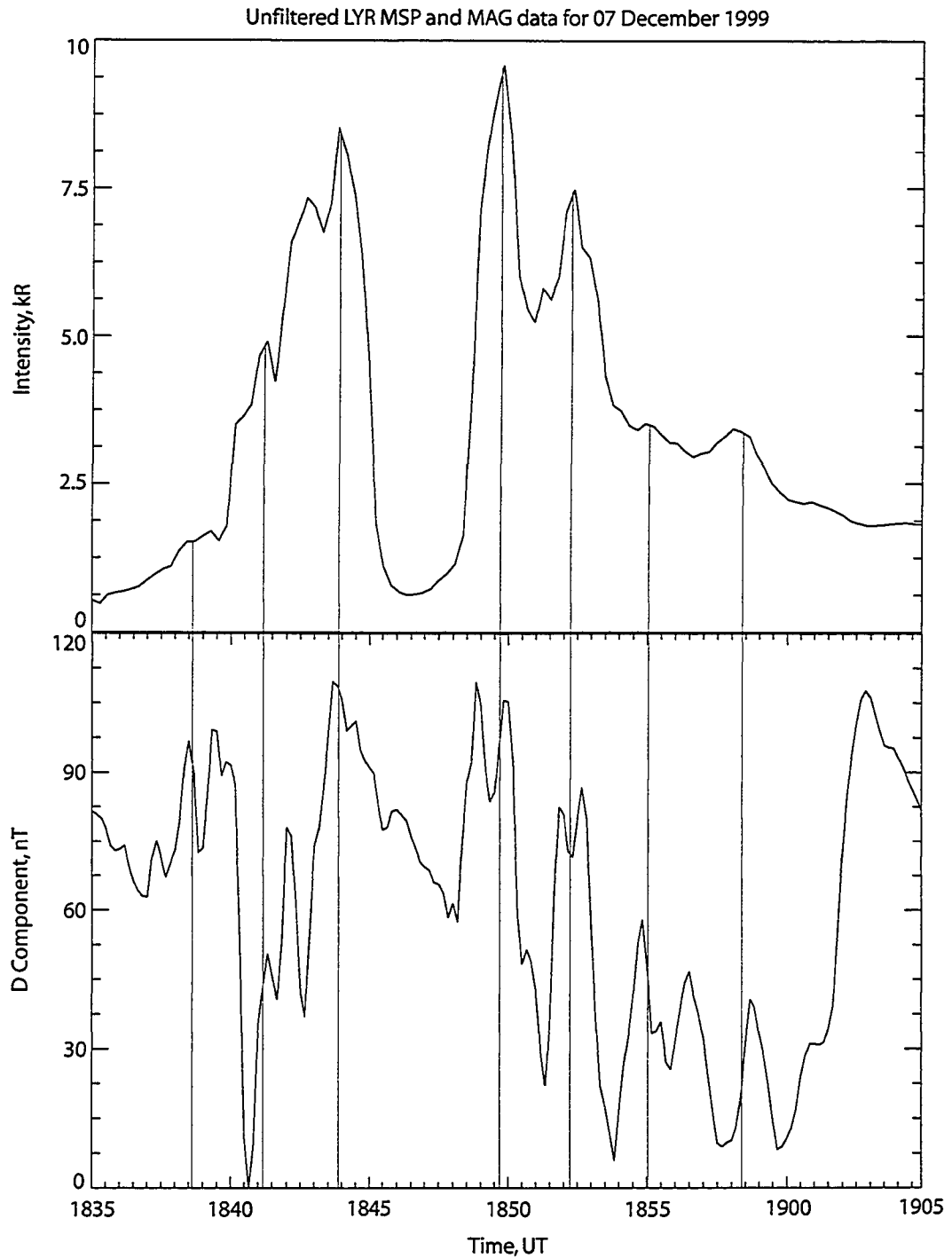


Figure 7.8: Slice through Longyearbyen MSP data from Figure 7.1 from the zenith in the 557.7 nm filter (top panel) and unfiltered D-component Longyearbyen magnetometer data (bottom panel) for the interval 1835 to 1905 UT on the 7^h December 1999. Red vertical lines indicate auroral intensifications that correspond with magnetic deflections.

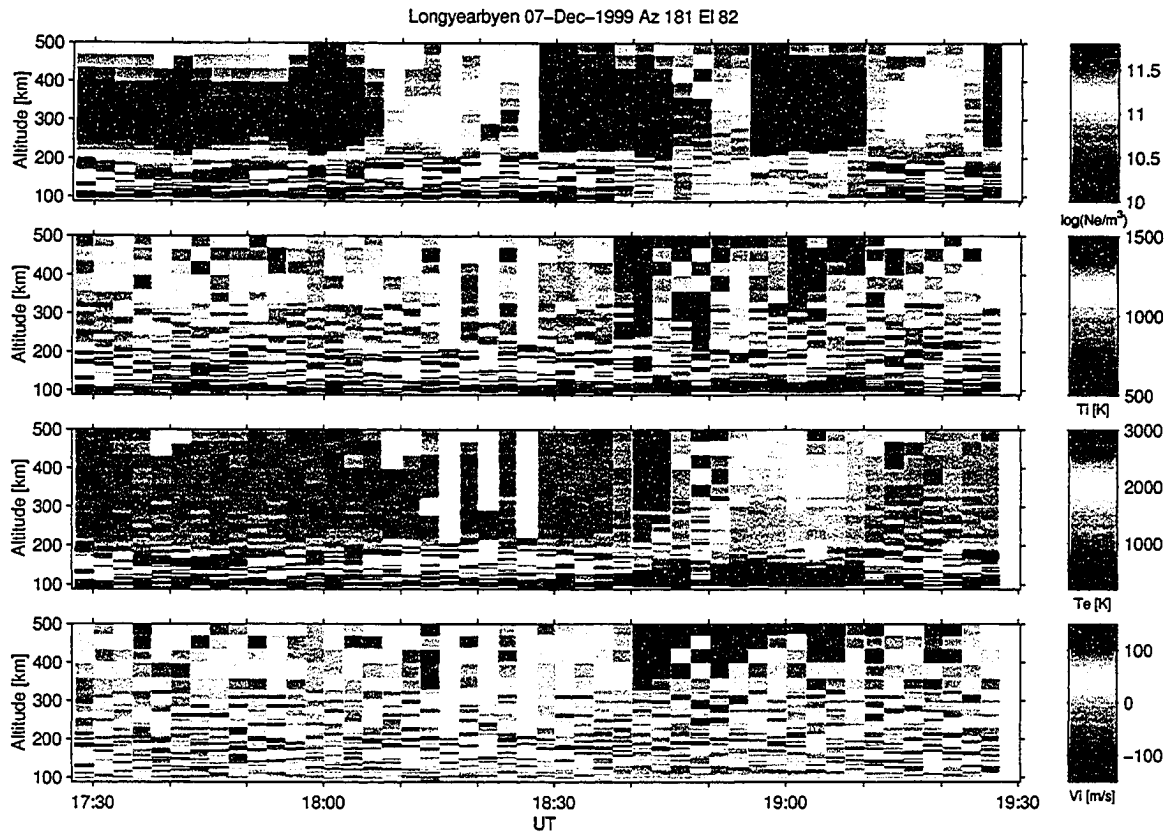


Figure 7.9: ESR field aligned data for the interval 1730 to 1930 UT on the 7th December 1999. From top to bottom, panels represent the logarithm of the electron density, the ion temperature, the electron temperature and the ion velocity. Blue in the ion velocity plot corresponds to motion towards the radar, with red corresponding to anti-Earthward motion.

Polar footprint at 1900 UT on 07 December 1999

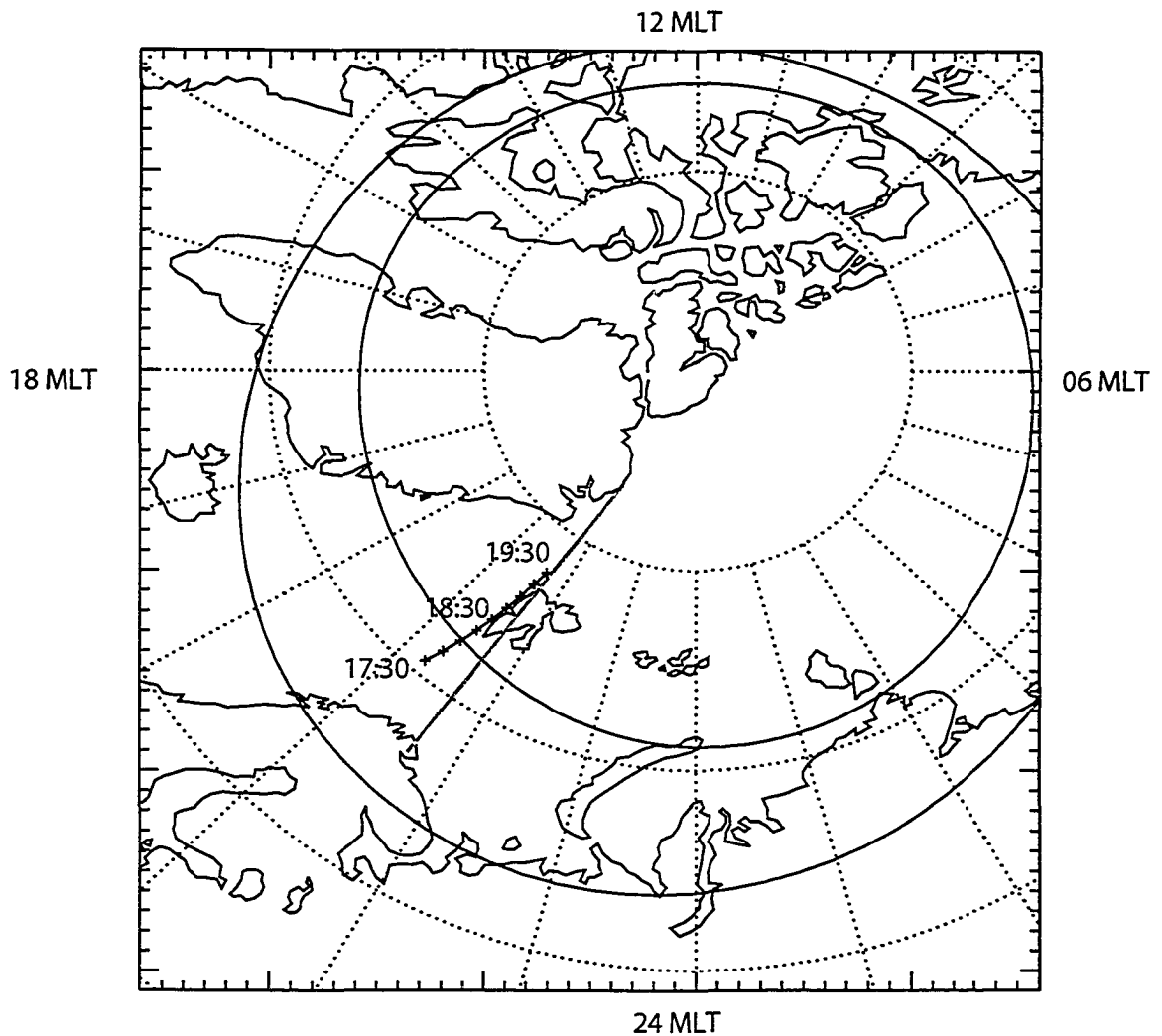
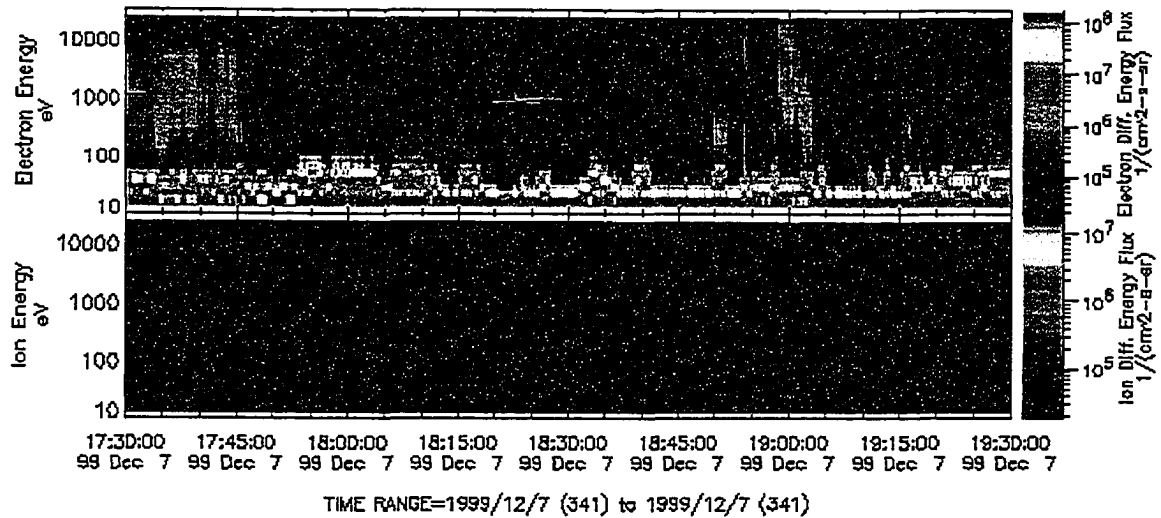


Figure 7.10: Polar ionospheric footprint for the interval 1730 to 1930 UT on the 7th December 1999 as determined from a Tsyganenko 1996 model. The grey line represents the field of view of the Longyearbyen MSP, and land masses and the Feldstein auroral oval for $K_p = 4$ are plotted for reference. Created by Jonathan Rae at the University of Alberta.



Please acknowledge data provider, J. Scudder at U of Iowa and CDAWeb when using these data.
 Key Parameter and Survey data (labels K0,K1,K2) are preliminary browse data.
 Generated by CDAWeb on Mon Mar 28 17:44:57 2004

Figure 7.11: Spectrograms from the HYDRA instrument on-board Polar for the interval 1730 to 1930 UT. Upper and lower panels show electron and ion fluxes between energies of 10 eV and 10 keV. Data courtesy of J. Scudder at U. of Iowa and produced via CDAWEB at <http://cdaweb.gsfc.nasa.gov>.

nighttime sector, and the transition between plasma regimes corresponds to Polar moving from the plasmashet region, through the plasmashet boundary layer (PSBL) and into the northern lobe. The HYDRA electron energy fluxes (top panel of Figure 7.11) also indicate that at around 1855 UT Polar was plunged into a region of hot plasma, then re-emerged into the lobe region after less than two minutes. As this corresponds to the time at which the MSP at Longyearbyen observed the first polewards expansion of the auroral oval, we suggest that this is the signature of the northwards expansion of the plasmashet, i.e., the fast moving plasmashet plasma washed over the slower moving spacecraft. Polar then experienced another region of hot plasma, corresponding to the second poleward motion of the auroral oval observed in the MSP data. The satellite stayed in this hot plasma region for around eight minutes. This second, fortunate configuration allows us to investigate whether energy transfer between the plasmashet (or PSBL) and the ionosphere is mediated by Alfvén waves, and whether the PBI auroral periodicity might be related to high altitude PSBL Alfvén wave periodicity.

Electric and magnetic field data from Polar between 1830 and 1930 UT on the 7th December 1999 are shown in Figure 7.12. The top three panels represent magnetic field data in a local field-aligned coordinate system, with the unit vectors in the y and z directions pointing in the azimuthal and field-aligned directions, respectively, and the unit vector in the x direction completing the orthogonal set. The bottom three panels correspond to the local electric field, in the same field-aligned coordinate system. All six timeseries are unfiltered.

The field-aligned coordinates were computed by first finding the direction of the local magnetic field for each data point. A running mean of duration twenty minutes, centered on each point, was taken and the direction of the average ambient magnetic field for the twenty minute interval was assumed to be the field-aligned direction at the centered point. The cross product of this direction and the vector pointing radially from the satellite to the Earth yielded the azimuthal direction, and finally the orthogonal set was completed by taking the cross product of the field-aligned and azimuthal directions. The transformation to field-aligned coordinates was then applied to the electric field data. The code used to perform the coordinate transformation was developed by Rae *et al.*, (2005, In Press) and was supplied by Jonathan Rae at the University of Alberta.

Figure 7.12 clearly shows that during the first, shorter entry into the PSBL, at 1855 UT, large amplitude magnetic and electric perturbations occurred, and during the later interval when Polar was in the PSBL region (between 1858 and 1906 UT) these large amplitude perturbations were again evident. The second, more extended interval allows us to examine the frequency characteristics of the observed waves in more detail, and it is clear that waves with a periodicity of around two minutes exist in this interval. These waves exhibit large scale oscillations, with magnetic perturbations of 6 nT and electric perturbations of around 100 mV/m. The magnetic perturbations are largest in the direction perpendicular to the local magnetic field (peak values of ~ 10 nT in the x and y directions compared to ~ 2 nT in the z direction) leading to the suggestion that they may be Alfvénic. The structure of the perturbations is non-sinusoidal, which may be due to interactions of the wave pulse with the plasma, or spatial variations being advected across the spacecraft in a non-stationary PSBL.

We may investigate the large-scale magnetic and electric field oscillations within the

7th Dec 1999, unfiltered

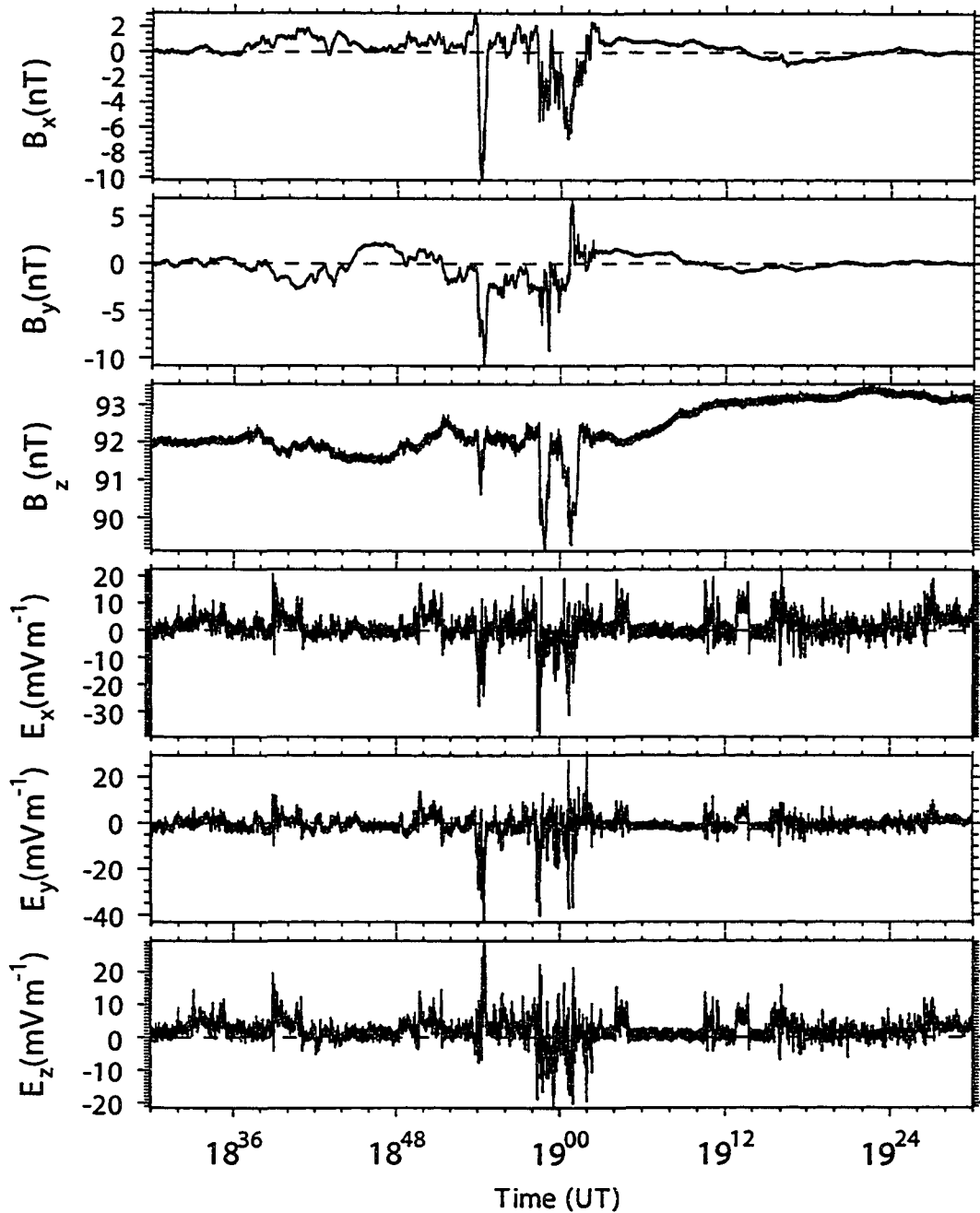


Figure 7.12: Polar magnetic (top three panels) and electric (bottom three panels) field data from 1830 to 1930 UT on the 7th December 1999. The data are presented in a local field-aligned coordinate system, with z representing the field aligned direction, y the approximately azimuthal direction and x the third direction of the orthogonal set, which is approximately radial in this case.

plasmashet/PSBL region by filtering the Polar data. The top six panels of Figure 7.13 display Polar magnetic and electric field data filtered between 1 and 10 mHz for the same interval and in the same coordinate system as Figure 7.12. The bottom three panels of Figure 7.13 show the Poynting flux in local field aligned coordinates, calculated using the relations

$$\begin{aligned}
\mu_0 S_x &= \delta E_y \cdot \delta B_z - \delta E_z \cdot \delta B_y \\
\mu_0 S_y &= \delta E_z \cdot \delta B_x - \delta E_x \cdot \delta B_z \\
\mu_0 S_z &= \delta E_x \cdot \delta B_y - \delta E_y \cdot \delta B_x.
\end{aligned}
\tag{7.1}$$

The Poynting flux measurements agree with the assertion that the waves during this interval are Alfvénic: the Poynting flux in the directions perpendicular to the background magnetic field (the x and y directions) are small compared to the Poynting flux in the field-aligned (z) direction. The Poynting flux measurements from the plasmashet and PSBL compare well with previous observations of large Poynting flux events in these regions that have been associated with electron acceleration and discrete auroral forms in the ionosphere [e.g., Keiling *et al.*, 2001; Wygant *et al.*, 2002].

Figure 7.14 displays Fourier power timeseries computed from the filtered data for the components B_x , B_y , E_x and E_y (upper, second, third and lower panels, respectively) in Figure 7.13 for the interval 1850 to 1910 UT on the 7th December 1999. The B_x component (which is directed perpendicularly to the plasmashet/PSBL) shows a broad spectral peak centered on 7-8 mHz, with the two electric field components also exhibiting the same periodicity with a smaller width spectral peak. The B_y component has a much smaller spectral peak at the same frequency. The z components were ignored in the FFT analysis as Alfvén wave power is not expected to occur in the field-aligned direction.

To investigate the high frequency properties of the observed wave fields we must remove any long period oscillations from the timeseries. Figure 7.15 displays Polar magnetic (top three panels) and electric (middle three panels) field data, and computed Poynting fluxes (bottom three panels) in local field-aligned coordinates. The magnetic field data clearly show a polarisation in the B_x (i.e., radial) component, with the electric field data seemingly showing no preferred polarisation direction. The Poynting flux during this inter-

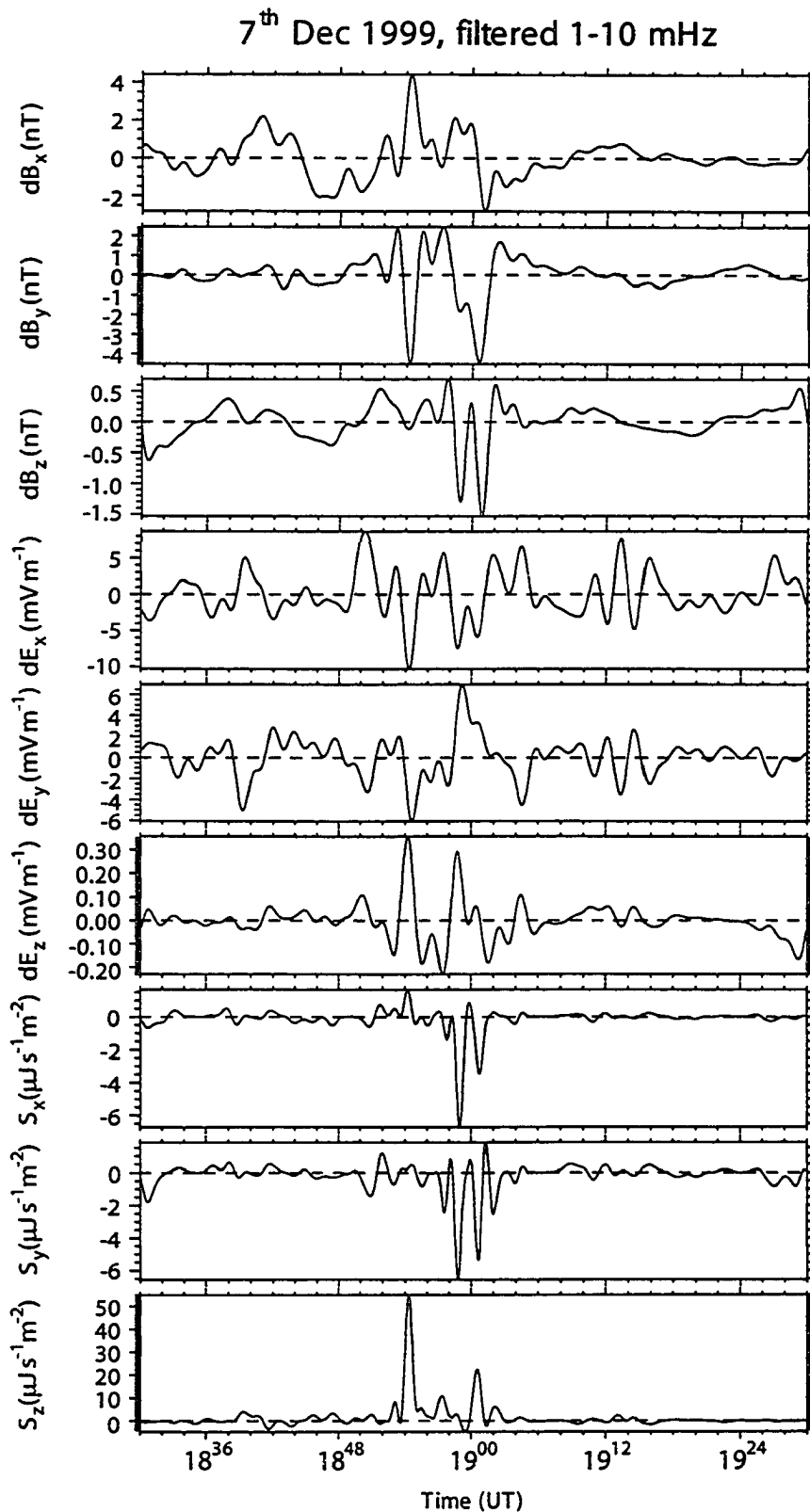


Figure 7.13: Polar magnetic field, electric field and Poynting flux data in field-aligned coordinates for the interval 1830 to 1930 UT on the 7th December 1999. Magnetic and electric field data are filtered between 1 and 10 mHz.

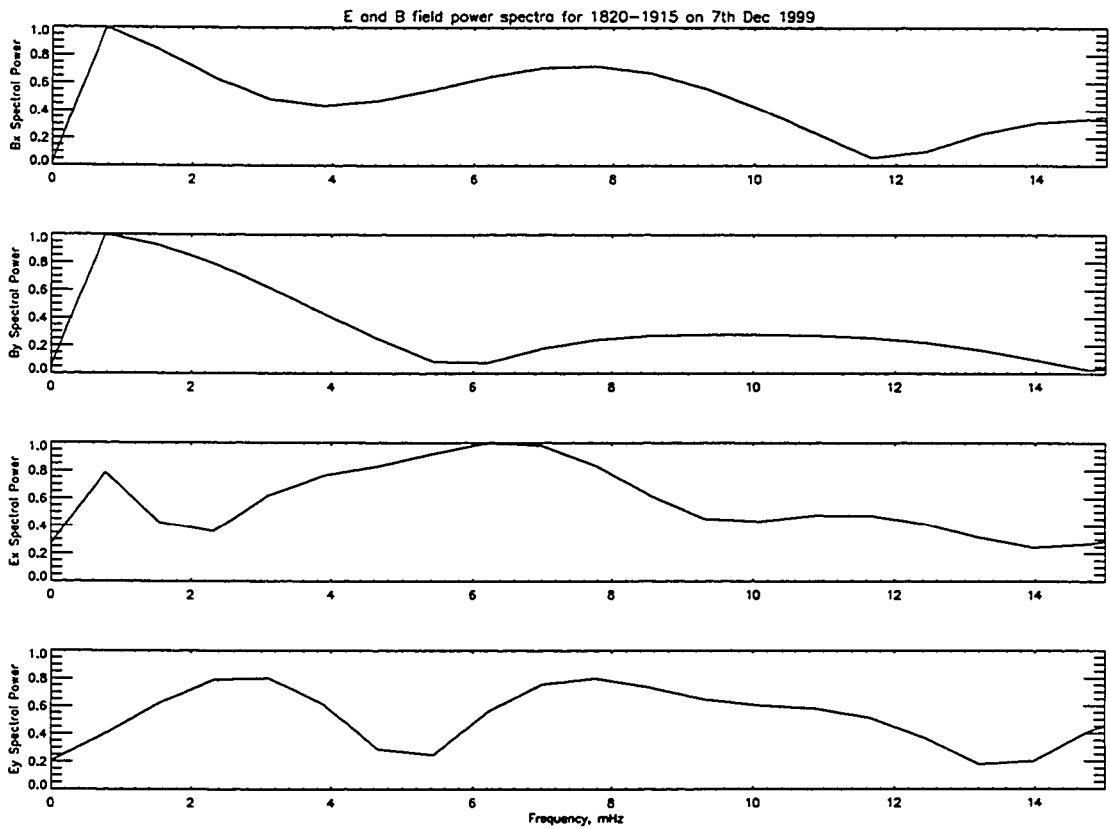


Figure 7.14: Spectral power for Polar B_x (top panel), B_y (second panel), E_x (third panel) and E_y (bottom panel) field data for the interval 1850 to 1910 UT on the 7th December 1999. The original data were filtered between 1 and 15 mHz, and x and y components are the quasi-radial and azimuthal directions in a local field-aligned coordinate system.

val oscillated between Earthward and anti-Earthward, seemingly in contrast to the purely Earthward directed Poynting flux of the lower frequency waves observed in Figure 7.13.

To understand the effects of the observed waves on the local plasma population, we may construct 2-D velocity distributions from the Polar HYDRA data. Figure 7.16 displays data from the HYDRA instrument on Polar for the interval 1850 to 1905 UT, when Polar passed into the PSBL/plasmashet region. The top three panels represent electron data from the Earthwards field-aligned, anti-Earthwards field-aligned and perpendicular directions, respectively. The lower plots, which represent 2-D electron distribution functions for selected times during the interval, clearly show that the distribution is not isotropic, with electrons predominantly moving in the field-aligned directions (note that due to the instrument characteristics, distributions are symmetric across the $y=0$ line).

7.3 Discussion

In order to ascertain whether it is possible for the waves shown in Figures 7.13 and 7.15 to be responsible for the electron precipitation observed in the MSP, ASC and ESR datasets (Figures 7.1, 7.3, 7.4 and 7.9 respectively), we must investigate their perpendicular scale sizes. As shown in Appendix B, Alfvén waves with perpendicular scale sizes that are of the order of the electron inertial length and/or the ion acoustic gyroradius may produce appreciable electric fields parallel to the background magnetic field, and thus cause and modulate particle precipitation into the ionosphere.

We use the technique of Wygant *et al.* (2002) and compare measured values of the local Alfvénic fields and plasma parameters with a local dispersion relation (described by Lysak, 1998). Using the relation $V_A = B_0/\sqrt{\mu_0\rho}$ with measured values of $B_0 = 92$ nT, $\rho = 5\times 10^{-22}$ kgm $^{-3}$ and with $\mu_0 = 4\pi\times 10^{-7}$ Hm $^{-1}$ at 1900 UT, the Alfvén speed in the PSBL was measured to be around 3.7×10^6 ms $^{-1}$. The measured electron thermal velocity was $1.3\pm 0.9\times 10^7$ ms $^{-1}$, as determined from $v_e = \sqrt{2kT_e/m_e}$ with the measured electron temperature, T_e , of $5.5\pm 0.4\times 10^6$ K from the TIDE instrument on Polar. These values are a good representation for the interval in which Polar was in the PSBL region, which corresponds to the time when the largest scale Alfvénic oscillations occurred. The error in the electron temperature was due to an averaging of the electron temperature over the entire

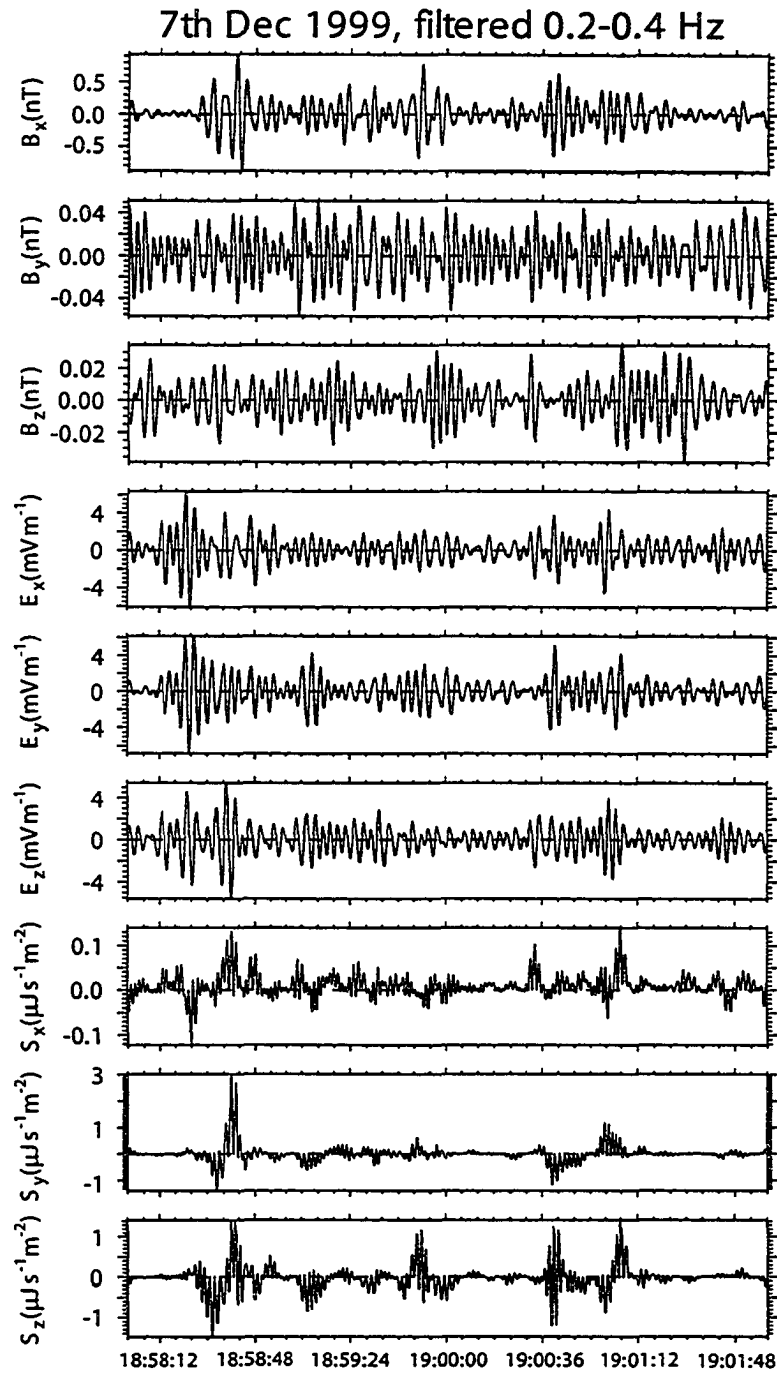


Figure 7.15: Polar magnetic field (top three panels), electric field (middle three panels) and Poynting flux (bottom three panels) data for the interval 1858 to 1902 UT on the 7th December 1999. Magnetic and Electric field data are filtered between 0.2 and 0.4 Hz, and all data are in a local field-aligned coordinate system.

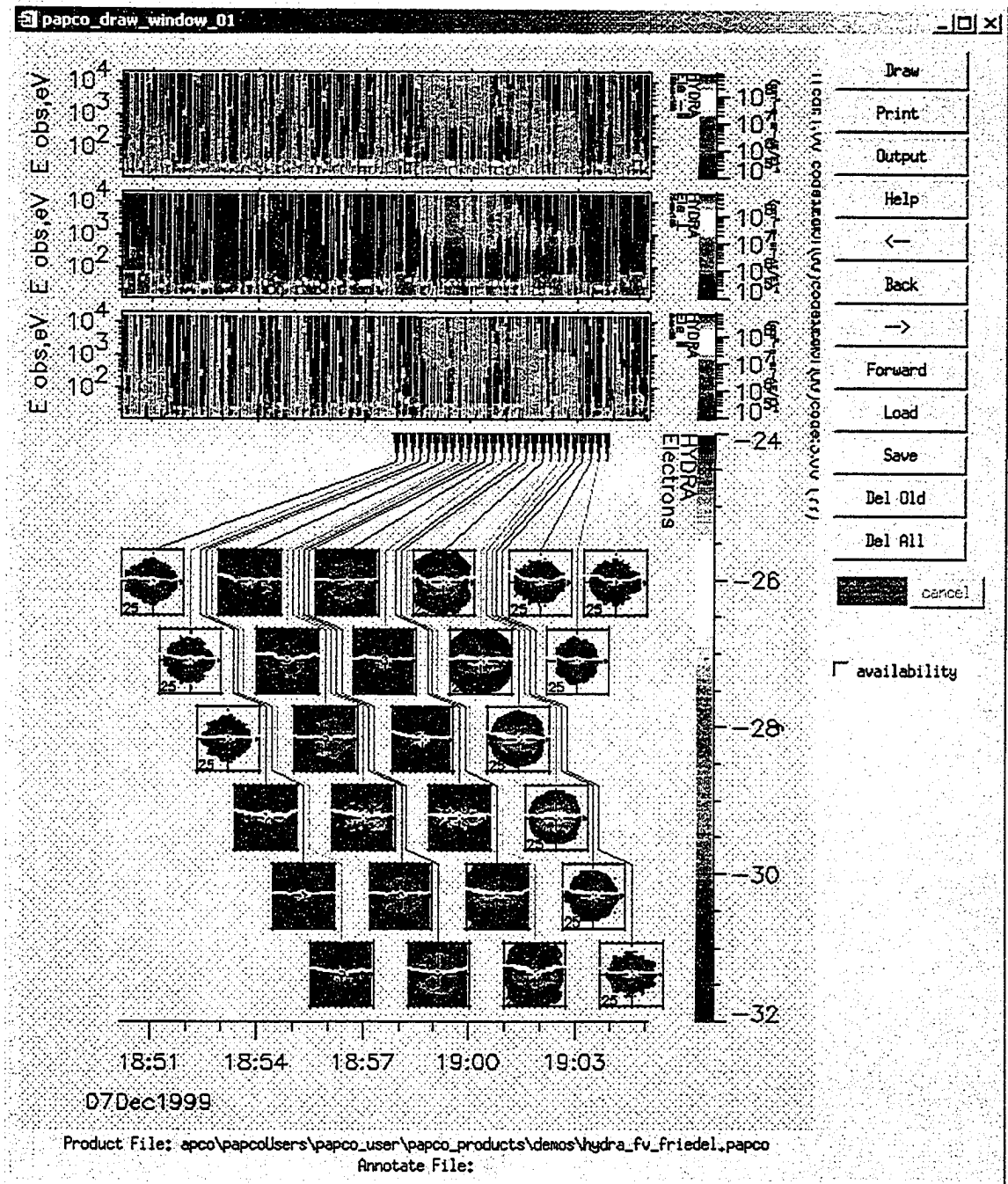


Figure 7.16: Polar HYDRA data for the interval 1850 to 1905 UT on the 7th December 1999. The top three panels represent electron fluxes in the Earthwards field-aligned, anti-Earthwards field-aligned and perpendicular directions respectively; lower plots represent 2-D velocity distributions for selected times during the interval with the upwards and downwards field-aligned directions corresponding to the negative and positive x -axis respectively. Plot produced by Reiner Friedel, Personal Communication, 2005.

interval that Polar was in the PSBL, between 1858 and 1906 UT, and an uncertainty of two standard deviations being taken to represent the error for this interval. Values of B_{\perp}/E_{\perp} were calculated for the magnetic and electric field perturbations in Figures 7.13 and 7.15 ($B_{\perp} = \sqrt{B_x^2 + B_y^2}$ and $E_{\perp} = \sqrt{E_x^2 + E_y^2}$). The range for $V_A B_{\perp}/E_{\perp}$ was found to be around 1 for the 2-minute periodicity waves, so that $E_{\perp}/B_{\perp} \simeq V_A$, consistent with that expected for a travelling Alfvén waves within the MHD regime. However, for the high frequency (~ 0.3 Hz) waves, $E_{\perp}/B_{\perp} = 0.3$ to 0.5 , so that the high frequency waves can not be described using the MHD approximations and they may have perpendicular scale sizes small enough to produce particle acceleration. It should be noted that in the analysis of Lysak (1998), the dispersion relation plotted in their Figure 1 and reproduced in our Figure 7.17 is for an Alfvén wave polarised in B_x and E_y (as imposed by the authors for simplicity), whereas the wave electric field observed in Figure 7.13 is not polarised in any single perpendicular direction with respect to our coordinate system. Since the wave is polarised in B_x we have therefore chosen to work with B_x and E_{\perp} in this analysis. This would have the effect of increasing the magnitude of the wave electric field by at most a factor of $\sqrt{2}$.

Figure 7.17 (taken from Lysak, 1998) displays the locus resulting from the observed values of v_e and B_{\perp}/E_{\perp} for the high frequency waves superimposed onto a local dispersion relation of the form of Equation B.21 [Lysak, 1998]. The left hand panel constrains the normalised value of k_{\perp} , which is between $0.6c/\omega_{pe}$ and $0.9c/\omega_{pe}$, i.e., $\lambda_{\perp} = 10$ to 15 km for the waves in the 0.2 to 0.4 Hz regime. The locus in the right hand panel of Figure 7.17 constrains $k_{\perp}E_z/k_{\parallel}E_x$ to between 0.7 and 0.8 , and using measured values of $E_x = 10$ mVm^{-1} and $E_z = 0.3$ mVm^{-1} with the calculated value of k_{\perp} , we obtain $k_{\parallel} = 0.016$ to 0.027 km^{-1} , so that $\lambda_{\parallel} = 230$ to 400 km. However, it should be noted that the satellite measurements of E_z in Figure 7.15 only corresponds to those oscillations in the 0.2 to 0.4 Hz band, and any even higher frequencies and large amplitude E_z variations have been removed by filtering.

Further, we need to compare the high frequency (0.2 - 0.4 Hz) wave scale sizes with the ion acoustic gyroradius, ρ_s and the electron inertial length, λ_e . For any appreciable parallel electric field to be generated by inertial Alfvén waves, the wave perpendicular scale size must be smaller than or of the order of either of these two quantities [e.g., Hasegawa, 1976;

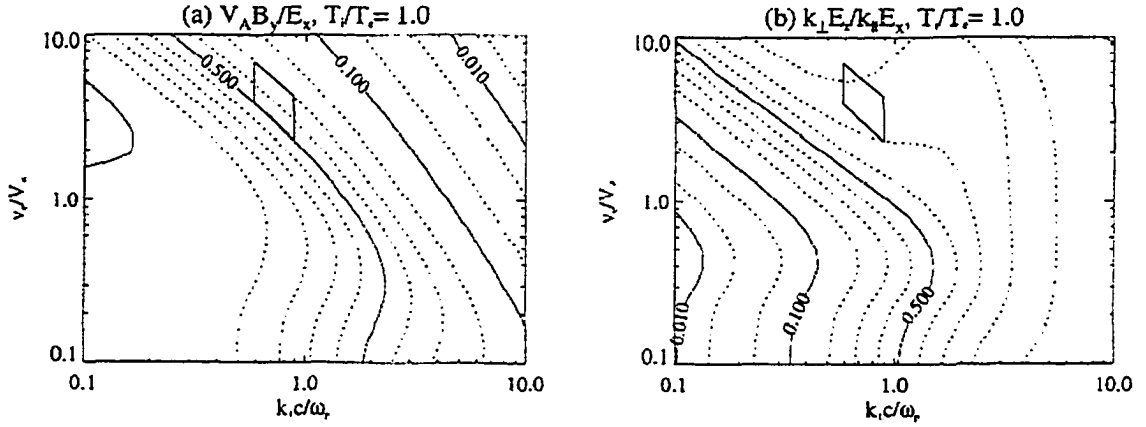


Figure 7.17: Taken from Lysak (1998). Normalised magnetic fields (left panel) and parallel electric fields (right panel) for the kinetic Alfvén wave dispersion relation. Fields are plotted as a function of the perpendicular wavenumber, k_{\perp} , and the electron thermal speed, v_e , normalised by the electron inertial length, c/ω_p , and the Alfvén speed, V_A , respectively. Overplotted in red in the left panel is the locus constructed from observed values of v_e and $V_A B_y/E_x$, so that a constraint on k_{\perp} can be made. The right panel illustrates this locus and the constraints it implies for $k_{\perp} E_z/k_{\parallel} E_x$.

Lysak, 1998; Lysak and Lotko, 2002; Lysak and Song, 2003]. Using data from the Polar satellite, it was found that $\rho_s = 10$ to 40 km, and that $\lambda_e = 17$ km. Thus the perpendicular scale size of the high frequency oscillations in the 0.2 to 0.4 Hz band are of the same order as both the ion acoustic gyroradius and the electron inertial length. This implies that these high frequency waves observed by Polar could produce an appreciable parallel electric field (see Equation B.36), and could have produced the auroral features observed in Figures 7.1, 7.3, 7.4 and 7.9 if this parallel field were maintained over an appreciable length of the field line.

Due to the 2-minute periodicity waves not falling into the kinetic regime, we must use another technique to estimate their perpendicular scale size. If we take the simplified version of Ohm's law

$$\mathbf{E}_{\perp} = -\mathbf{v} \times \mathbf{B}_0 \quad (7.2)$$

we may write

$$|\mathbf{v}| = \left| \frac{\mathbf{E}_\perp \times \mathbf{B}_0}{B^2} \right| = \frac{|\mathbf{E}_\perp|}{|\mathbf{B}_0|}. \quad (7.3)$$

If we assume that the wave velocity perturbations vary as $v = v_0 \cos(\omega t)$, we may integrate and write

$$\xi = \int v_0 \cos(\omega t) dt = \frac{v_0}{\omega} \sin(\omega t) \equiv \xi_0 \sin(\omega t) \quad (7.4)$$

so that $\xi_0 = v_0/\omega$, where ξ_0 is the wave perturbation displacement. Thus we may finally write

$$\xi_0 = \frac{|\mathbf{E}_\perp|}{|\mathbf{B}_0|\omega} \quad (7.5)$$

Using observed values of $|\mathbf{E}_\perp| = 5 \text{ mV/m}$, $|\mathbf{B}_0| = 92 \text{ nT}$ and $\omega = 2\pi \times 7.5 \times 10^{-3} \text{ rads/s}$ we obtain $\xi_0 \simeq 1200 \text{ km}$. The spacecraft velocity for this interval was approximately 2 km/s , so that in a wave period of ~ 130 seconds we may expect the satellite to move $\sim 260 \text{ km}$. Therefore the spacecraft might cross the region of wave displacement in approximately 4 wave cycles.

The scale size of the 2-minute period ULF waves at Polar may be compared to the latitudinal scale size of the auroral features observed on the ground by the MSP and ASC, allowing for a correction factor due to field line convergence. A Tsyganenko 1996 [Tsyganenko and Stern, 1996b] model was used to compute the separation of a perpendicular line segment, dl , along a meridian in space at the location of the Polar satellite when projected to an altitude of 110 km . This scale factor, for the purely radial convergence of field lines, was found to be approximately 10. Similarly, the separation of an azimuthal line segment, $d\phi$, was projected to the ionosphere using the same Tsyganenko model, and it was found that the azimuthal scale factor was approximately 5.9. Thus the area scale factor, which should be applied to e.g., Poynting flux measurements, was found to be 59, i.e., a Poynting flux of $1 \text{ Jm}^{-2}\text{s}^{-1}$ measured at Polar would correspond to a Poynting flux of $59 \text{ Jm}^{-2}\text{s}^{-1}$ at the ionosphere.

The latitudinal width of, for example, an east-west aligned auroral arc at an altitude of 110 km that was produced by a kinetic Alfvén wave in the PSBL would be purely determined by the radial scale size of the wave [e.g., Samson *et al.*, 1991]. Using the

radial scale size factor of 10, this implies that the auroral features of between 10 and 20 km in width map to a perpendicular wave scale size of 100 to 200km. This is larger than the measured values of either λ_e or ρ_s , consistent with the long period waves being in the MHD regime. Although the wave displacement (~ 1200 km) and the arc width mapped into the PSBL at Polar (~ 100 km) are of the same order of magnitude, they do not match exactly. However, this discrepancy may be due to the fact that auroral arcs may be produced at half or even quarter wave cycles, so that these observations are not inconsistent.

In order to quantify the amount of ionospheric heating produced by precipitating electrons that caused the PBIs in Figure 7.1, the technique of Vickrey *et al.* (1982), highlighted in Chapter 6, can be applied. In this case, the electron heating rate was found to be $8.1 \times 10^{-4} \text{ Js}^{-1}\text{m}^{-2}$, for the height range 100 to 120 km (the assumed emission height for 557.7 nm green line aurora). The maximum Poynting flux observed by the Polar satellite was $5 \times 10^{-5} \text{ Js}^{-1}\text{m}^{-2}$ directed Earthward, however, this Poynting flux needs to be modified due to the convergence of magnetic field lines as one moves from an altitude of $5 R_E$ at Polar to the E-region ionosphere. As discussed above, tracing an area in the magnetosphere at the Polar altitude to an ionospheric height of 110 km (the assumed altitude of emission of the 557.7 nm aurora) using a Tsyganenko 1999 model [Tsyganenko and Stern, 1996b] shows that the convergence of the magnetic field lines introduces a multiplication factor of around 59. Thus, the Poynting flux at the ionosphere due to the Alfvén waves shown in Figure 7.13 is $50 \mu\text{Js}^{-1}\text{m}^{-2} \times 59 = 3 \times 10^{-3} \text{ Js}^{-1}\text{m}^{-2}$ in the Earthward direction, i.e., the ULF waves contain more than enough energy to produce the aurora observed on the ground. These observations of large Poynting flux in the PSBL compare well with other results [e.g., Wygant *et al.* (2000); Keiling *et al.* (2001); Keiling *et al.* (2002); Wygant *et al.* (2002)], and the scale size calculations are similar to those of Wygant *et al.* (2002). These measurements are consistent with previous models of Alfvén wave production in the magnetotail propagating earthwards on PSBL field lines and producing discrete auroral forms [e.g., Allan and Wright, 1998; Wright *et al.*, 1999; Allan and Wright, 2000]. The Poynting flux in the higher frequency waves (Figure 7.15) is much smaller than that in the longer period waves, at around $1 \mu\text{Js}^{-1}\text{m}^{-2}$. Also, the Poynting flux of these high frequency oscillations was not primarily directed towards the Earth, indeed it appears that the average Poynting flux over the interval in Figure 7.15 is approximately zero, so that no net energy

is transferred Earthwards from these waves.

The timeseries in Figure 7.15 may be explained as Alfvénic turbulence [see e.g., Gurnett and Frank, 1977; Bonnell *et al.*, 1996; Wahlund *et al.*, 2003]. Low altitude (< 2000 km) BBELF emissions are thought to be generated via an instability occurring when current sheets have transverse scales of the order of the electron inertial length [Seyler and Xu, 2003]. Seyler and Xu (2003) used a 2-fluid simulation to parallel current structures, and found that their system became unstable to a local current convective interchange (CCI) mode. They reported that as the CCI mode grew, vortices were established in the plasma in the field-aligned direction (see Figure 1 of Seyler and Xu, 2003) which advect the plasma so as to reduce the current gradient. They also reported that the BBELF signature was similar to that of an inertial Alfvén wave (IAW) spectrum, in agreement with the earlier modelling work of Seyler and Wu (2001).

Wahlund *et al.* (2003) showed that Alfvénic turbulence (or BBELF emission) on auroral field lines at altitudes of 4-5 R_E was similar in its characteristics to that at lower altitudes, and they argued that the waves they observed could produce particle acceleration. In order to ascertain whether the high frequency oscillations in Figure 7.15 have the characteristics of Alfvénic turbulence, we employ a similar technique to Wahlund *et al.* (2003). Figure 7.18 displays the ratio of the spectral densities of the perpendicular electric to magnetic field oscillations for the intervals 1854 to 1906 UT (red line) and 1836 to 1848 UT (blue line) on the 7th December 1999. The earlier of these two intervals corresponds to when Polar was in the lobe region, where the plasma density is much lower than the PSBL or plasmashet, so that the Alfvén speed is much higher. The second interval corresponds to when Polar was in the PSBL/plasmashet, the interval in which the high frequency oscillations in Figure 7.15 were observed. If the observations in Figure 7.15 are similar to Alfvénic turbulence, then we expect the computed ratio of the spectral densities of E and B to follow from the Alfvén wave relation between E and B , namely

$$\frac{\delta E}{\delta B} = v_A \sqrt{\frac{(1 + k_{\perp}^2 \lambda_e^2)(1 + k_{\perp}^2 \rho_i^2)}{1 + k_{\perp}^2 \rho_s^2}} \quad (7.6)$$

where we have additionally retained the ion gyroradius term (ρ_i) as compared to Equation A.30 (see Seyler and Xu, 2003). In order to plot this ratio as a function of frequency, we need to convert between k_{\perp} and the observed frequency, ω . For these high frequency

waves, Doppler broadening effects mean that the observed frequency at Polar is given by $\omega = \omega_0 + \mathbf{k} \cdot \mathbf{v}$, where ω is the observed wave frequency, ω_0 is the frequency of the wave and \mathbf{v} is the plasma velocity relative to the spacecraft. Due to the slow relative bulk motion of the plasma, we assume that the plasma velocity, \mathbf{v} , is equal to the spacecraft speed, 1.96 km/s, and that as the spacecraft is moving northwards, approximately in the meridional plane, that this velocity is in the direction of k_{\perp} .

In the regime of the high frequency waves observed between 1854 and 1906 UT, the wave frequency, ω_0 , is small (~ 0.3 Hz) compared to the value of $\mathbf{k} \cdot \mathbf{v}$ (~ 1.3 s $^{-1}$), hence we approximate $\omega \simeq \mathbf{k} \cdot \mathbf{v}$, and hence plot the ratio of $\delta E / \delta B$ as a function of ω . To compare the computed values of $\delta E / \delta B$ with the dispersion relation for kinetic Alfvén waves in Equation 7.6 we plot theoretical values of $\delta E / \delta B$ from Equation B.36 as a function of ω using $k_{\perp} = \omega / v$. The black lines in Figure 7.18 represent the theoretical values of $\delta E / \delta B$ for a plasma with a temperature of $5.5 \pm 0.4 \times 10^6$ K and a mass density of 5×10^{-22} kgm $^{-3}$, with the top curve assuming a hydrogen only plasma, and the lower curve assuming an oxygen only plasma. Clearly, these two curves fit well with the observations from within the PSBL region (red curve), so that we can state that the high frequency oscillations observed in Figure 7.15 are most probably broadband emissions caused by a current-convective instability (CCI) mode, similar to those reported by Seyler and Xu (2003). This mechanism also accounts for the bi-directional field-aligned Poynting flux in the lower panel of Figure 7.15, which is probably due to the vortices produced by the CCI mode [Seyler and Xu, 2003].

It should be noted that the assumption that ω can be described purely by the Doppler broadening effect is valid for frequencies that are smaller than the product of \mathbf{k} and \mathbf{v} , like those in Figure 7.15, but in the instance of longer period waves with smaller k_{\perp} , as in Figure 7.13, then this probably does not hold. However, due to the identical periodicity in the ground-based magnetometer and optical data with the waves in space it is reasonable to assume that $\omega \simeq \omega_0$ for the 2-minute period waves.

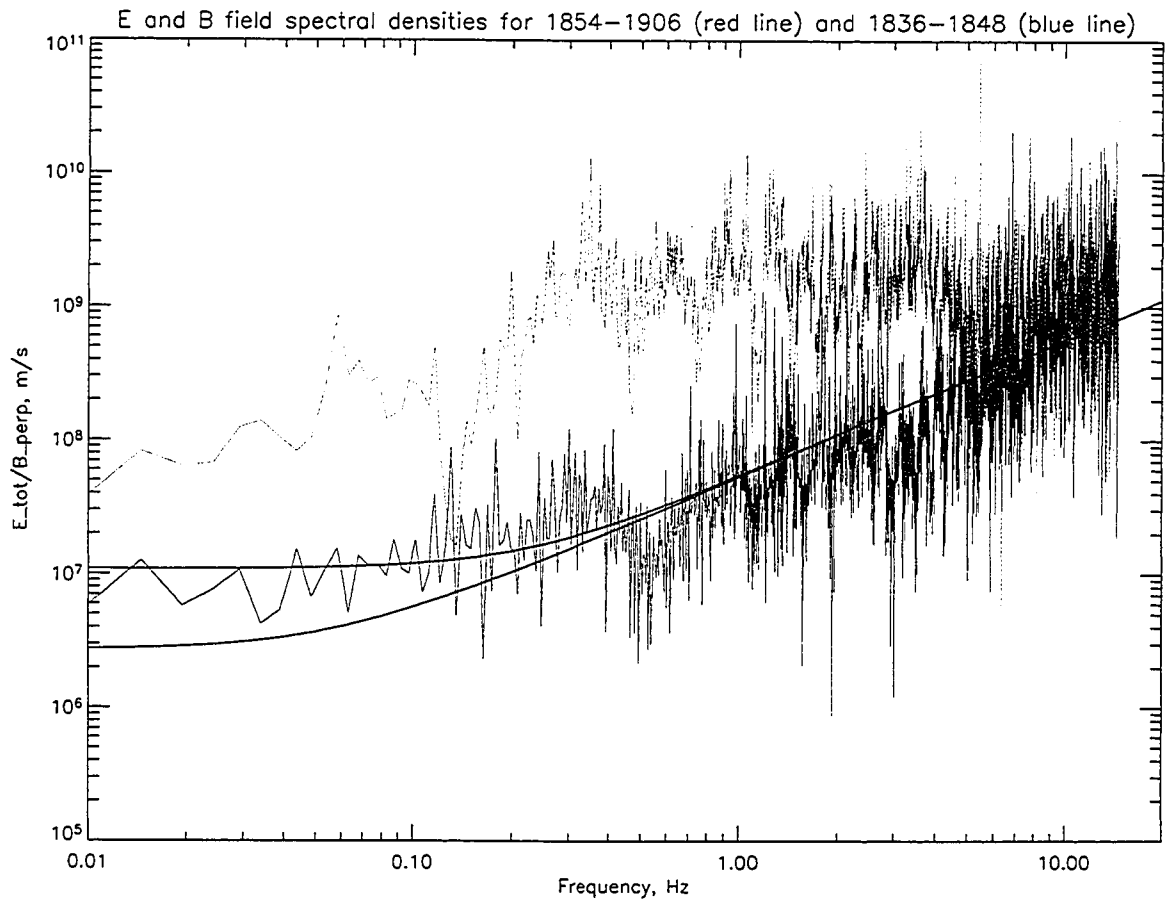


Figure 7.18: Ratio of the spectral densities of E_{tot} and B_{\perp} plotted versus frequency for the intervals 1854 to 1906 UT (red line) and 1836 to 1848 UT (blue line) on the 7th December 1999. Also plotted are theoretical curves for the ration of $\delta E/\delta B$ derived from Equation 7.6

7.4 Conclusions

We have presented multi-instrument observations of auroral poleward boundary intensifications in the dusk sector. Equatorwards propagating features were observed in MSP and ASC data in the recovery phase of a substorm, and incoherent scatter radar data was used to directly measure the ionospheric heating rate of $8.1 \times 10^{-4} \text{ Js}^{-1}\text{m}^{-2}$ due to the precipitating particles producing the auroral forms.

During the interval of PBI activity, the Polar satellite passed through the field of view of the ground based MSP, ASC and IS radar, passing from the lobe into the PSBL and plasmashet. Magnetic field data from Polar showed oscillations in the PSBL region, of the same periodicity as the repetition rate of the auroral features observed in the MSP. The Poynting flux of these waves in the 1 to 10 mHz regime was found to be of the same magnitude as those reported by Wygant *et al.* (2000), Keiling *et al.* (2001), Keiling *et al.* (2002) and Wygant *et al.* (2002)], and exclusively directed in the Earthward direction, providing $3 \times 10^{-3} \text{ Js}^{-1}\text{m}^{-2}$ when mapped down to the ionosphere. Clearly, the energy contained in the observed Alfvén waves was more than enough to produce the observed auroral emissions, even neglecting the observations of field-aligned electron and ion beams which may have been produced by the waves at a higher altitude.

Data from the Hydra instrument on Polar facilitated the production of two dimensional velocity space distributions, so that any possible electron beams could be investigated. The results from this analysis show that the electron distribution is in fact non-isotropic, although further work on the nature of any electron and/or ion beams present in the data needs to be completed. Indeed, the Polar HYDRA data allow a further analysis of the motion of the PSBL boundary, so that any plasma motion that is periodic in nature and is related to Alfvén waves on the boundary itself could be investigated

High frequency data from the Polar electric and magnetic field instruments showed significant wave energy between 0.2 and 0.4 Hz, with an associated bi-directional Poynting flux. We showed that these oscillations were most probably Alfvénic turbulence driven by a CCI mode, with typical polarisation characteristics that produce bi-polar Poynting flux [e.g., Seyler and Xu, 2003; Wahlund *et al.*, 2003]. High time resolution electric and magnetic field data allowed a comparison of the high frequency wave properties with a

local dispersion relation to be made, and the scale size of waves calculated. It was found that the perpendicular scale size of the waves in the 0.2 to 0.4 Hz band was of the order of the local ion acoustic gyroradius and electron inertial length, so that the conditions of MHD didn't apply and the waves could produce parallel electric fields and hence particle acceleration on auroral field lines.

These results are consistent with the idea that Alfvén waves that are excited in the magnetotail in the plasmashet and PSBL can propagate Earthwards and modulate particle precipitation on auroral field lines [e.g., Allan and Wright, 1998; Wright *et al.*, 1999; Allan and Wright, 2000], and that this modulation may occur at altitudes as high as $5 R_E$. The observations of identical periodicity in ground-based magnetometer and optical data and Polar magnetic and electric field data from the high altitude PSBL provides definitive evidence that Alfvén waves at altitudes of up to $\sim 6 R_E$ can be responsible for auroral particle precipitation. We have also shown that these Earthwards propagating Alfvén waves transfer similar amounts of energy per unit area into the ionosphere to that provided for example by substorms [Banks, 1977], and that Alfvén waves such as these on auroral field lines represent a major mechanism of energy transport from the magnetotail to near-Earth space and the ionosphere. We also showed that superimposed on top of these 2-minute period waves were small scale, high frequency oscillations that could produce parallel electric fields. We explain the presence of such small scale oscillations via a current-convective interchange (CCI) mode excited when current sheet structures have scale sizes on the order of the electron inertial length.

Further work needs to be carried out to fully characterise the plasma properties in the PSBL during this event, as in-situ measurements of ion and/or electron beams during the interval of the most intense wave activity would further cement the idea that high altitude acceleration of particles by Alfvén waves in the PSBL is a major method of production of auroral activity and PBIs.

Chapter 8

Further Work

Although we have highlighted the role of Alfvén waves in energy transport in the magnetosphere for differing magnetospheric events, further work is required to fully understand the role that MHD waves play. Further observations of particle driven FLR in all local time sectors are required, so that the distribution of such events in MLT may be investigated statistically, along with the rate of occurrence of such events. Also, multi-point observations in space would allow the FLR to be characterised in the Earth's magnetosphere as well as on the ground, so that the interaction between ring current ions and Alfvén waves may be directly observed.

Further observations of auroral poleward boundary intensifications in the dusk sector, similar to those in Chapter 5, are also required. We have highlighted the temporal coherence of PBIs with ground magnetic signatures, and postulated that Alfvén waves on stretched auroral field lines may produce such auroral phenomena, but no in-situ observations exist for any of the intervals we outlined. Clearly, in-situ satellite observations are necessary to confirm the production mechanism of these types of PBIs. Such observations would allow a full characterisation of the fast mode and Alfvén waves in space, and hence would determine whether any Alfvén waves that map to these types of PBIs in the Earth's ionosphere would be capable of producing particle acceleration. Further, multi-point measurements would allow the field-aligned current structure of any Alfvén waves to be investigated (the FAC is given by $\mathbf{j} = (\nabla \times \mathbf{B})/\mu_0$ from Maxwells equations), so that particle acceleration due to both the FAC structure and the perpendicular scale size of the waves may be compared.

Finally, more observations similar to those in Chapter 7 should be made, so that the

occurrence rate of large Poynting flux events associated with auroral PBIs may be investigated statistically. Multi-point in-situ observations would facilitate the investigation of the field aligned current structure associated with travelling Alfvén waves, and a comparison of this particle acceleration process with the particle acceleration due to the scale size of any Alfvén waves could be made. Further, to determine the altitude at which particle acceleration occurs, the 2-D velocity distributions of the plasma in the PSBL need to be analysed in detail. This will allow the determination of the altitude of the acceleration region, and allow further comparisons with the models of e.g., Allan and Wright (1998), Wright *et al.* (1999) and Allan and Wright (2000) to be made.

Bibliography

- Alfvén, H. (1942). Existence of electromagnetic-hydrodynamic waves. *Nature*, **150**, 405.
- Allan, W. and Poulter, E. M. (1992). ULF waves — Their relationship to the structure of the Earth's magnetosphere. *Reports on Progress in Physics*, **55**, 533–598.
- Allan, W. and Wright, A. N. (1998). Hydromagnetic wave propagation and coupling in a magnetotail waveguide. *J. Geophys. Res.*, **103**, 2359.
- Allan, W. and Wright, A. N. (2000). Magnetotail waveguides: Fast and Alfvén waves in the plasma sheet boundary layer and lobes. *J. Geophys. Res.*, **105**, 317.
- Allan, W., White, S. P., and Poulter, E. M. (1986). Impulse-excited hydromagnetic cavity and field-line resonances in the magnetosphere. *Planet. Space Sci.*, **34**, 371.
- Anderson, B. J., Engebretson, M. J., Rounds, S. P., Zanetti, L. J., and Potemra, T. A. (1990). A statistical study of Pc 3-5 pulsations observed by the AMPTE/CCE magnetic fields experiment. I - Occurrence distributions. *J. Geophys. Res.*, **95**, 10495–10523.
- Baddeley, L. J., Yeoman, T. K., Wright, D. M., Trattner, K. J., and Kellet, B. J. (2002). On the coupling between unstable magnetospheric particle populations and resonant high m ULF wave signatures in the ionosphere. *Ann. Geo.*, **23**, 567.
- Baker, D. N., Pulkkinen, T. I., Angelopoulos, V., Baumjohann, W., and McPherron, R. L. (1996). Neutral line model of substorms: Past results and present view. *J. Geophys. Res.*, **101**, 12975.
- Banks, P. M. (1977). Observations of Joule and particle heating in the auroral zone. *J. Atmos. Terr. Phys.*, **39**, 179.
- Banks, R. J. (1975). Complex Demodulation of Geomagnetic Data and the Estimation of Transfer Functions. *Geophys. J.R. astr. soc.*, **42**, 83–101.
- Blanchard, G. T., Lyons, L. R., and Samson, J. C. (1997). Accuracy of using 6300 Angstrom emissions to identify the magnetic separatrix on the nightside of Earth. *J. Geophys. Res.*, **102**, 9697–9703.
- Bonnell, J. *et al.* (1996). High-resolution sounding rocket observations of large-amplitude Alfvén waves. *Geophys. Res. Lett.*, **23**, 3297.
- Brekke, A., Feder, T., and Berger, S. (1987). Pc4 giant pulsations recorded in Tromsø, 1929-1985. *J. Atmos. Terr. Phys.*, **49**, 1027–1032.
- Cao, M., McPherron, R. L., and Russell, C. T. (1994). Statistical study of ULF wave occurrence in the dayside magnetosphere. *J. Geophys. Res.*, **99**, 8731–8753.

- Chen, L. and Hasegawa, A. (1974). A theory of long-period magnetic pulsations; 1, Steady state excitation of field line resonance. *J. Geophys. Res.*, **79**, 1024.
- Chi, P. J., Russell, C. T., Raeder, J., Zesta, E., Yumoto, K., Kawano, H., Kitamura, K., Petrinec, S. M., Angelopoulos, V., Le, G., and Moldwin, M. B. (2001). Propagation of the preliminary reverse impulse of sudden commencements to low altitudes. *J. Geophys. Res.*, **106**, 18,857.
- Chisham, G. (1996). Giant pulsations: An explanation for their rarity and occurrence during geomagnetically quiet times. *J. Geophys. Res.*, **101**, 24,755–24,763.
- Chisham, G. and Orr, D. (1991). Statistical studies of giant pulsations (Pgs) - Harmonic mode. *Planet. Space. Sci.*, **39**, 999–1006.
- Chisham, G., Mann, I. R., and Orr, D. (1997). A statistical study of giant pulsation latitudinal polarization and amplitude variation. *J. Geophys. Res.*, **102**, 9619–9629.
- Crooker, N. U. (1979). Dayside merging and cusp geometry. *J. Geophys. Res.*, **84**, 951.
- de la Beaujardiere, O. *et al.* (1994). Quiet-time intensifications along the poleward auroral boundary near midnight. *J. Geophys. Res.*, **99**, 287–298.
- Dent, Z. C. (2003). *ULF wave remote sensing of magnetospheric plasma density*. Ph.D. thesis, University of York.
- Dungey, J. W. (1961). Interplanetary magnetic fields and the auroral zone. *Phys. Rev. Lett.*, **6**, 47.
- Engebretson, M. J., Murr, D. L., Erickson, K. N., Strangeway, R. J., Klumpar, D. M., Fuselier, S. A., Zanetti, L. J., and Potemra, T. A. (1992). The spatial extent of radial magnetic pulsation events observed in the dayside near synchronous orbit. *J. Geophys. Res.*, **97**, 13741.
- Fejer, J. A. (1960). Scattering of radio waves by an ionized gas in thermal equilibrium. *Can. J. Phys.*, **38**, 1114.
- Glassmeier, K.-H. *et al.* (1999). Concerning the generation of geomagnetic giant pulsations by drift-bounce resonance ring current instabilities. *Ann. Geophys.*, **17**, 338–350.
- Greenwald, R. A., Weiß, W., Nielsen, E., and Thomson, N. R. (1978). STARE: A new auroral backscatter experiment in northern Scandinavia. *Radio Sci.*, **13**, 1021.
- Greenwald, R. A., Baker, K. B., Dudeney, J. R., Pinnock, M., Jones, T. B., Thomas, E. C., Villain, J.-P., Cerisier, J.-C., Senior, C., Hanuise, C., Hunsucker, R. D., Sofko, G., Koehler, J., Nielsen, E., Pellinen, R., Walker, A. D. M., Sato, N., and Yamagishi, H. (1995). Darn/superdarn: A global view of the dynamics of high-latitude convection. *Space Sci. Rev.*, **71**, 761–796.
- Gurnett, D. A. and Frank, L. A. (1977). A region of intense plasma wave turbulence on auroral field lines. *J. Geophys. Res.*, **82**, 1031.
- Hagfors, T. (1961). Density fluctuations in a plasma in a magnetic field, with applications to the ionosphere. *J. Geophys. Res.*, **66**, 1699.
- Hamlin, D. A., Karplus, R., Vik, R. C., and Watson, K. M. (1961). Mirror and azimuthal drift frequencies for geomagnetically trapped particles. *J. Geophys. Res.*, **66**, 1.

- Harten, R. and Clark, K. (1995). The design features of the ggs wind and polar spacecraft. *Space Sci. Rev.*, pages 23–40.
- Harvey, P., Mozer, F. S., Pankow, D., Wygant, J., Maynard, N. C., Sullivan, W., Anderson, P. B., Pfaff, R., Aggson, T., Pedersen, A., Falthammar, C. G., and Tanskannen, P. (1995). The Electric Field Instrument on the Polar satellite. In C. T. Russell, editor, *The Global Geospace Mission*. Kluwer Acad., Norwell, Mass.
- Hasegawa, A. (1976). Partilce Acceleration by MHD Surface Wave and Formation of Aurora. *J. Geophys. Res.*, **81**, 5083–5090.
- Henderson, M. G. *et al.* (1998). Are north-south auroral structures an ionospheric manifestation of bursty bulk flows? *Geophys. Res. Lett.*, **25**, 3737–3740.
- Hughes, W. J. (1994). Magnetospheric ULF waves: A tutorial with a historical perspective.
- Hughes, W. J. and Southwood, D. J. (1976a). An illustration of modification of geomagnetic pulsation structure by the ionosphere. *J. Geophys. Res.*, **81**, 3241–3247.
- Hughes, W. J. and Southwood, D. J. (1976b). The screening of micropulsation signals by the atmosphere and ionosphere. *J. Geophys. Res.*, **81**, 3234–3240.
- Hughes, W. J., Southwood, D. J., Mauk, B., McPherron, R. L., and Barfield, J. N. (1978). Alfvén waves generated by an inverted plasma energy distribution. *Nature*, **275**, 43–45.
- Jacobs, J. A., Kato, Y., Matsushta, S., and Troitskaya, V. A. (1964). Classification of geomagnetic micropulsations. *J. Geophys. Res.*, **69**, 180.
- Kabin, K. (2003). *Personal Communication*.
- Keiling, A. *et al.* (2001). Properties of large electric fields in the plasma sheet at 4-7 R_E measured with Polar. *J. Geophys. Res.*, **106**, 5779–5798.
- Keiling, A., Wygant, J. R., Cattell, C., Peria, W., Parks, G., Temerin, M., Mozer, F. S., Russell, C. T., and Kletzing, C. A. (2002). Correlation of Alfvén wave Poynting flux in the plasma sheet at 4-7 r_E with ionospheric electron energy flux. *J. Geophys. Res.*, **107**, 1132, doi:1029/2001JA900140.
- Kivelson, M. G. and Pu, Z. Y. (1984). The Kelvin-Helmholtz instability on the magnetopause. *Planet. Space Sci.*, **32**, 1335.
- Kivelson, M. G. and Russell, C. T. (1995). *Introduction To Space Physics*. Cambridge University Press, The Pitt Building, Trumpington Street, Cambridge, CB2 1RP, UK.
- Kivelson, M. G. and Southwood, D. J. (1985). Resonant ULF waves - A new interpretation. *Geophys. Res. Lett.*, **12**, 49–52.
- Kivelson, M. G. and Southwood, D. J. (1986). Coupling of global magnetospheric MHD eigenmodes to field line resonances. *J. Geophys. Res.*, **91**(10), 4345–4351.
- Lepping, R. P., Acuna, M., Burlaga, L., Farrell, W., Slavin, J., Schatten, K., Mariani, F., Ness, N., Neubauer, F., Whang, Y. C., Byrnes, J., Kennon, R., Panetta, P., Scheifele, J., and Worley, E. (1995). The wind magnetic field investigation. *Space Sci. Rev.*, **71**, 207.
- Lester, M., de La Beaujardiere, O., Foster, J. C., Freeman, M. P., Luehr, H., Ruohoniemi, J. M., and Swider, W. (1993). The response of the large scale ionospheric convection pattern to changes in the imf and sunstorms - Results from the SUNDIAL 1987 campaign. *Ann. Geophys.*, **11**, 556–571.

- Lui, A. (1996). Current disruption in the Earth's magnetosphere: Observations and models. *J. Geophys. Res.*, **101**, 13067.
- Lyons, L. R. *et al.* (1998). Near earth plasma sheet penetration and geomagnetic disturbances. In A. Nishida, S. W. H. Cowley, and D. N. Baker, editors, *New Perspectives on the Earth's Magnetotail*, page 241. AGU.
- Lyons, L. R., Nagai, T., Blanchard, G. T., Samson, J. C., Yamamoto, T., Mukai, T., Nishida, A., and Kokburn, S. (1999). Association between Geotail plasma flows and auroral poleward boundary intensifications observed by CANOPUS photometers. *J. Geophys. Res.*, **104**, 4485–4500.
- Lyons, L. R., Zesta, E., Xu, Y., Sanchez, E. R., Samson, J. C., Reeves, G. D., Ruohoniemi, J. M., and Sigwarth, J. B. (2002). Auroral poleward boundary intensifications and tail bursty flows: A manifestation of a large-scale ULF oscillation? *J. Geophys. Res.*, **107**, 1352, doi:10.1029/2001JA000242.
- Lysak, R. L. (1998). The relationship between electrostatic shocks and kinetic Alfvén waves. *Geophys. Res. Lett.*, **25**, 2089–2092.
- Lysak, R. L. and Carlson, C. W. (1981). Effect of microscopic turbulence on magnetosphere-ionosphere coupling. *Geophys. Res. Lett.*, **8**, 269.
- Lysak, R. L. and Lotko, W. (2002). Two-Fluid Shear-Alfvén Waves. In G. Paschmann, S. Haaland, and R. Treumann, editors, *Space Science Reviews*, volume 103. Kluwer Acad., Norwell, Mass.
- Lysak, R. L. and Song, Y. (2003). Kinetic theory of the Alfvén wave acceleration of auroral electrons. *J. Geophys. Res.*, **108**, 8005, doi:10.1029/2002JA009406.
- Mann, I. R. (1997). On the internal radial structure of field line resonances. *J. Geophys. Res.*, **102**, 27,109.
- Mann, I. R., Wright, A. N., and Cally, P. S. (1995). Coupling of magnetospheric cavity modes to field line resonances: A study of resonant widths. *J. Geophys. Res.*, **100**, 19,441.
- Mann, I. R., Voronkov, I., Dunlop, M., Donovan, E., Yeoman, T. K., Milling, D. K., Wild, J., Kauristie, K., Amm, O., Bale, S. D., Balogh, A., Viljanen, A., and Opgenoorth, H. J. (2002). Coordinated ground-based and cluster observations of large amplitude global magnetospheric oscillations during a fast solar wind speed interval. *Ann. Geophys.*, **20**, 405–426.
- Mathews, J. T., Mann, I. R., Rae, I. J., and Moen, J. (2004). Multi-instrument observations of ULF wave-driven discrete auroral arcs propagating sunwards and equatorwards from the poleward boundary of the duskside auroral oval. *Phys. Plas.*, **11**, 1250.
- Mathie, R. A. and Mann, I. R. (2001). On the solar wind control of Pc5 ULF pulsation power at mid-latitudes: Implications for MeV electron acceleration in the outer radiation belt. *J. Geophys. Res.*, **106**, 29783–29796.
- McComas, D. J., Bame, S. J., Barker, P., Feldman, W. C., Phillips, J. L., Riley, P., and Griffee, J. W. (1998). Solar Wind Proton Alpha Monitor (SWEPAM) for the Advanced Composition Explorer. *Space Sci. Rev.*, **86**, 563.
- McIlwain, C. E. (1961). Coordinates for mapping the distribution of magnetically trapped particles. *J. Geophys. Res.*, **66**, 3681–3691.

- Menk, F., Fraser, B., Waters, C., Ziesolleck, C., Feng, Q., Lee, S., and McNabb, P. (1994). Ground measurements of low-latitude magnetospheric field line resonances. In M. Engebretson, K. Takahashi, and M. Scholer, editors, *Solar Wind Sources of Magnetospheric ULF Waves*. American Geophysical Union.
- Milan, S. E., Sato, N., Masaki, E., and Moen, J. (2001). Auroral forms and the field-aligned current structure associated with field line resonances. *J. Geophys. Res.*, **106**, 25,825.
- Moen, J., Sandholt, P. E., Lockwood, M., Egeland, A., and Fokii, K. (1994). Multiple, discrete arcs on sunwards convecting field lines in the 14–15 MLT region. *J. Geophys. Res.*, **99**, 6113–6123.
- Myers, A. P. and Orr, D. (1990). ULF wave analysis and complex demodulation.
- Ogilvie, K. W., Chorney, D. J., Fitzenreiter, R. J., Hunsaker, F., Keller, J., Lobell, J., Miller, G. and Scudder, J. D., Sittler Jr, E. C., Torbert, R. B., Bodet, D., Needall, G., Lazarus, A. J., Steinberg, J. T., Tappan, J. H., Mavretic, A., and Gergin, E. (1995). SWE, a comprehensive plasma instrument for the Wind spacecraft. *Space Sci. Rev.*, **71**, 55–77.
- Ozeke, L. G. (2002). *Modelling the Generation and Properties of Guided Alfvén Waves in the Magnetosphere*. Ph.D. thesis, University of York.
- Ozeke, L. G. and Mann, I. R. (2001). Modelling the properties of high-*m* Alfvén waves driven by the drift-bounce resonance mechanism. *J. Geophys. Res.*, **106**, 15,583–15,597.
- Parker, E. N. (1958). Dynamics of the interplanetary gas and magnetic fields. *Astrophysical Journal*, **128**, 664–676.
- Poulter, E. M. and Allan, W. (1985). Transient ULF pulsation decay rates observed by ground based magnetometers - The contribution of spatial integration. *Planet. Space Sci.*, **33**, 607–616.
- Rae, I. J., Donovan, E. F., Mann, I. R., Fenrich, F. R., Watt, C. E. J., Milling, D. K., Lester, M., Lavraud, B., Wild, J. A., Singer, H. J., Rme, H., and Balogh, A. (In Press). Evolution and characteristics of global Pc5 ULF waves during a high solar wind speed interval. *J. Geophys. Res.*
- Risbeth, H. and Williams, P. J. S. (1985). The EISCAT Ionospheric Radar: the System and its Early Results. *Jl. R. Astr. Soc.*, **26**, 478.
- Ruohoniemi, J. M. and Baker, K. B. (1998). Large-scale imaging of high-latitude convection with Super Dual Auroral Radar Network HF radar observations. *J. Geophys. Res.*, **103**, 20,797–20,812.
- Russell, C. T. (1974). The Solar Wind And Magnetospheric Dynamics. In D. E. Page, editor, *Correlated Interplanetary and Magnetospheric Observations*, page 3. D. Reidel Publ. Co., Dordrecht, Holland.
- Russell, C. T., Snare, R. C., Means, J. D., Pierce, D., Dearborn, D., Larson, M., Barr, G., and Le, G. (1995). The GGS/Polar Magnetic Fields Investigation. In C. T. Russell, editor, *The Global Geospace Mission*. Kluwer Acad., Norwell, Mass.
- Saito, T., Yumoto, K., and Koyama, Y. (1976). Magnetic pulsation Pi2 as a sensitive indicator of magnetospheric substorm. *Planet. Space. Sci.*, **24**, 1025–1029.
- Samson, J. C., Jacobs, J. A., and Rostoker, G. (1971). Latitude-dependent characteristics of long-period geomagnetic micropulsations. *J. Geophys. Res.*, **76**, 3675.

- Samson, J. C., Hughes, T. J., Creutzberg, F., Wallis, D. D., Greenwald, R. A., and Ruohoniemi, J. M. (1991). Observations of a detached, discrete arc in association with field line resonances. *J. Geophys. Res.*, **96**, 15,683.
- Samson, J. C., Cogger, L. L., and Pao, Q. (1996). Observations of field line resonances, auroral arcs, and auroral vortex structures. *J. Geophys. Res.*, **101**, 17,373.
- Scudder, J., Hunsacker, F., Miller, G., Lobell, J., Zawistowski, T., Ogilvie, K., Keller, J., Chornay, D., Herrero, F., Fitzenreiter, R., Fairfield, D., Needell, J., Bodet, D., Googins, J., Kleitzing, C., Torbert, R., Vandiver, J., Bentley, R., Fillius, W., McIlwain, C., Wipple, E., and Korth, A. (1995). Hydra-A3 dimensional electron and ion hot plasma instrument for the Polar spacecraft of the GGS mission. *Space Sci. Rev.*, pages 459–495.
- Seyler, C. E. and Wu, K. (2001). Instability at the electron inertial scale. *J. Geophys. Res.*, **106**, 21,623.
- Seyler, C. E. and Xu, T. (2003). The relationship between field-aligned currents and low-frequency electromagnetic fluctuations. *Geophys. Res. Lett.*, **30**, 2106, doi:10.1029/2003GL018292.
- Shue, J.-H., Chao, J. K., Fu, H. C., Russell, C. T., Song, P., Khurana, K. K., and Singer, H. J. (1997). A new functional form to study the solar wind control of the magnetopause size and shape. *J. Geophys. Res.*, **102**, 9497.
- Smith, C. W., L'Heureux, J., Ness, N. F., Acuna, M. H., Burlaga, L. F., and Scheifele, J. (1998). The ACE Magnetic Fields Experiment. *Space Sci. Rev.*, **86**, 611.
- Southwood, D. J. (1974). Some features of field line resonances in the magnetosphere. *Planet. Space Sci.*, **22**, 482.
- Southwood, D. J. and Hughes, W. J. (1982). Theory of hydromagnetic waves in the magnetosphere. *Space Sci. Rev.*, **35**, 301–366.
- Southwood, D. J., Dungey, J. W., and Etherington, R. J. (1969). Bounce resonant interaction between pulsations and trapped particles. *Planet. Space Sci.*, **17**, 349–361.
- Stewart, B. (1861). On the great magnetic disturbance which extended from august 2 to september 7, 1859 as recorded by photography at the Kew observatory. *Phil. Trans. Roy. Soc. Lond.*, **11**, 407.
- Stone, E. C. (1989). The Advanced Composition Explorer. *Bulletin of the American Astron. Soc.*, **20**, 1077.
- Takahashi, K., Sato, N., Warnecke, J., Luehr, H., Spence, H. E., and Tonegawa, Y. (1992). On the standing wave mode of giant pulsations. *J. Geophys. Res.*, **97**, 10717–10732.
- Tsyganenko, N. A. and Stern, D. P. (1996a). Modelling the global magnetic field of the large-scale Birkeland current systems. *J. Geophys. Res.*, **101**, 27,187.
- Tsyganenko, N. A. and Stern, D. P. (1996b). Modelling the global magnetic field of the large-scale Birkeland current systems. *J. Geophys. Res.*, **101**, 27,187.
- Vickrey, J. F., Vondrak, R. R., and Matthews, S. J. (1982). Energy deposition by precipitating particles and Joule dissipation in the auroral ionosphere. *J. Geophys. Res.*, **87**, 5184.

- Viljanen, A. and Hakkinen, L. (1997). Image magnetometer network. In M. Lockwood, M. N. Wild, and H. J. Opgenoorth, editors, *Satellite-Ground Based Coordination Sourcebook*. ESA Publications.
- Wahlund, J.-E., Yilmaz, A., Backrud, M., Sundkvist, D., Vaivads, A., Winningham, D., André, M., Balogh, A., Bonnell, J., Buchert, S., Carozzi, T., Cornilleau, N., Dunlop, M., Eriksson, A. I., Fazakerley, A., Gustafson, G., Parrot, M., Robert, P., and Tjulin, A. (2003). Observations of auroral broadband emissions by CLUSTER. *Geophys. Res. Lett.*, **30**, 1563, doi:10.1029/2002GL016335.
- Walker, A. D. M. and Nielsen, E. (1984). Stare observations of an eastward propagating Pc5 pulsation with large azimuthal wavenumber. *Geophys. Res. Lett.*, **11**, 259–262.
- Wild, J. A. and Yeoman, T. K. (2000). CUTLASS HF radar observations of high-latitude azimuthally propagating vortical currents in the night side ionosphere during magnetospheric substorms. *Ann. Geophys.*, **18**, 640–652.
- Wilken, B., Weiß, W., Hall, D., Grande, M., Sørass, F., and Fennell, J. (1992). Magnetospheric Ion Composition Spectrometer onboard the CRRES spacecraft. *J. Spacecraft and Rockets*, **29**, 585.
- Wright, A. N. (1994). Dispersion and wave coupling in inhomogeneous MHD waveguides. *J. Geophys. Res.*, **99**, 159.
- Wright, A. N. and Allan, W. (1996). Structure, phase motion and heating within alfvén resonances. *J. Geophys. Res.*, **101**, 17,399–17,408.
- Wright, A. N., Allan, W., Elphinstone, R. D., and Cogger, L. L. (1999). Phase mixing and phase motion of Alfvén waves on tail-like and dipole-like magnetic field lines. *J. Geophys. Res.*, **104**, 10,159–10,175.
- Wright, D. M., Yeoman, T. K., Rae, I. J., Storey, J., Stockton-Chalk, A. B., Roeder, J. L., and Trattner, K. J. (2001). Ground-based and Polar spacecraft observations of a giant (Pg) pulsation and its associated source mechanism. *J. Geophys. Res.*, **106**, 10,837–10,852.
- Wygant, J. R. *et al.* (2000). Polar spacecraft based comparisons of intense electric fields and Poynting flux near and within the plasma sheet-tail lobe boundary to UVI images: An energy source for the aurora. *J. Geophys. Res.*, **105**, 18,675–18,692.
- Wygant, J. R. *et al.* (2002). Evidence for kinetic Alfvén waves and parallel electron energization at 4–6 R_E in the plasma sheet boundary layer. *J. Geophys. Res.*, **107**, 1201, doi:10.1029/2001JA900113.
- Yeoman, T. K. and Wright, D. M. (2001). ULF waves with drift resonance and drift-bounce resonance energy sources as observed in artificially induced HF radar backscatter. *Ann. Geophys.*, **19**, 159–170.
- Yumoto, K. and The CPMN Group (2001). Characteristics of Pi 2 magnetic pulsations observed at the CPMN stations: A review of the STEP results. *Earth, Planets and Space*, **53**, 981–992.
- Zesta, E., Hughes, W. J., and Engebretson, M. J. (2002a). Two-dimensional structure of auroral poleward boundary intensifications. *J. Geophys. Res.*, **107**, 1317, doi:10.1029/1999JA000386.

Zesta, E., Donovan, E., Lyons, L., Enno, G., Murphree, J. S., and Cogger, L. (2002b). The two dimensional structure of auroral poleward boundary intensifications. *J. Geophys. Res.*, **107**, 1350, doi:10.1029/2001JA000260.

Appendix A

Coordinate Systems

The two geocentric coordinate systems used in this thesis are geocentric solar ecliptic (GSE), and geocentric solar magnetospheric (GSM). The GSE coordinate system has an x-axis that points from the Earth to the Sun, with the y-axis lying in the ecliptic plane pointing duskwards and the z-axis perpendicular to the ecliptic plane completing the orthogonal set. Relative to an inertial coordinate system, the GSE system exhibits a yearly rotation.

The GSM coordinate system again has its x-axis pointing from the Earth to the Sun, but the y-axis is defined to be perpendicular to the Earth's dipole, so that the x-z plane contains the Earth's dipole axis. The positive z-axis is chosen to be in the same direction as the northern magnetic pole, and the difference between GSE and GSM coordinates is therefore a simple rotation.

Ground-based data are often transformed into corrected geomagnetic (CGM) coordinates. From any given point on the Earth's surface, the CGM x-axis points to the northern magnetic pole, the y-axis lies in the magnetic east-west direction and the z-axis points up vertically from the Earth's surface. These coordinates are often referred to as H, D, Z coordinates when analysing ground-based magnetometer data. A full description of geocentric coordinate systems can be found in e.g., Kivelson and Russell (1995).

Appendix B

Derivation Of E_{\parallel} For Kinetic Alfvén Waves

We follow the treatment of Lysak and Lotko (2002) and consider a two-fluid plasma in which electrons are the majority current carrier in the direction parallel to the local magnetic field, and ions carry any perpendicular currents. The justification for the separate parallel and perpendicular current carriers lies in the fact that in the parallel direction, the electric fields produced are likely to be small and transient in nature, so that the lower inertia of the electrons (due to their lower mass) causes them to respond much more quickly. In the perpendicular direction we note that the electron gyroradius is small compared to that of the ions, and so any large scale current disruption in the perpendicular direction must be mediated by the ions in the plasma. We also assume that the magnetic field is straight, uniform in space, and directed along the z axis.

Faradays law states that

$$\nabla \times \mathbf{E} = -\frac{\partial \mathbf{b}}{\partial t} \quad (\text{B.1})$$

where \mathbf{E} and \mathbf{b} are the wave perturbation electric and magnetic fields, respectively. Taking the parallel and perpendicular components of Equation B.1 yields

$$\frac{\partial \mathbf{b}}{\partial t} = -\left(\frac{\partial}{\partial z} [\hat{\mathbf{b}} \times \mathbf{E}_{\perp}] + \nabla_{\perp} \times \mathbf{E}_{\parallel} \right) \quad (\text{B.2})$$

where $\hat{\mathbf{b}}$ is the unit vector in the field aligned direction and the \perp and \parallel suffixes represent the perpendicular and parallel directions to the background magnetic field, respectively. If

we now examine the generalized Ohms law (Equation 2.25) and restrict ourselves to the z direction to find E_z , we obtain

$$E_z + (\mathbf{v}_e \times \mathbf{B})_z = \eta j_z + \frac{(\mathbf{j} \times \mathbf{B})_z}{n_e} - \frac{(\nabla \cdot \mathbf{P}_e)_z}{n_e} + \frac{m_e}{ne^2} \frac{\partial j_z}{\partial t}. \quad (\text{B.3})$$

The second term on the left hand side and the second term on the right hand side of Equation B.3 are both equal to zero, as $\mathbf{B} = B\hat{\mathbf{b}}$, so that the cross product of \mathbf{B} with another vector will have no component in the z direction. The first term on the right hand side of Equation B.3 is also zero, as we assume that any resistivity is caused by particle collisions, and that the plasma is collisionless (i.e., $\eta = 0$). We therefore obtain

$$\begin{aligned} E_z &= \frac{m_e}{ne^2} \frac{\partial j_z}{\partial t} - \frac{(\nabla \cdot \mathbf{P}_e)_z}{n_e} \\ &= \frac{m_e}{ne^2} \frac{\partial j_z}{\partial t} - \frac{1}{n_e} \frac{\partial P_e}{\partial z} \end{aligned} \quad (\text{B.4})$$

where we have assumed that the electron pressure is isotropic. For an isothermal electron plasma, electron continuity states that

$$\frac{\partial n_e}{\partial t} + n_0 \nabla \cdot \mathbf{v}_e = 0. \quad (\text{B.5})$$

Multiplying this through by the electron temperature, T_e , yields

$$\frac{\partial P_e}{\partial t} + n_0 T_e \frac{\partial v_{ez}}{\partial z} = 0 \quad (\text{B.6})$$

or

$$\frac{\partial P_e}{\partial t} = \frac{T_e}{e} \frac{\partial j_z}{\partial z}, \quad (\text{B.7})$$

where we have assumed that the electron velocity in the x and y directions is negligible and that $j_z = -n_e e v_{ez}$. We then take the time derivative of Equation B.4, which gives

$$\begin{aligned} \frac{\partial E_z}{\partial t} &= \frac{m_e}{ne^2} \frac{\partial^2 j_z}{\partial t^2} - \frac{1}{ne} \frac{\partial^2 P_e}{\partial z \partial t} \\ &= \frac{m_e}{ne^2} \frac{\partial^2 j_z}{\partial t^2} - \frac{T_e}{ne^2} \frac{\partial^2 j_z}{\partial z^2}. \end{aligned} \quad (\text{B.8})$$

We now consider the perpendicular component of the plasma motion, and assume that ions are the major current carriers in this direction. To compute the wave Equation in this regime, we begin by taking the time derivative of Equation B.2, which yields

$$\frac{\partial^2 \mathbf{b}}{\partial t^2} = -\frac{\partial}{\partial t} \left(\frac{\partial}{\partial z} [\hat{\mathbf{b}} \times \mathbf{E}_\perp] + \nabla_\perp \times \mathbf{E}_\parallel \right). \quad (\text{B.9})$$

We begin by examining the first term on the right hand side of Equation B.9. We know from the generalized Ohms law that

$$\mathbf{E}_\perp = -\mathbf{v}_\perp \times \mathbf{B}_0 \quad (\text{B.10})$$

where we have assumed a collisionless plasma, a slowly varying perpendicular current and that the electron pressure term may be neglected due to the ions carrying the perpendicular currents. Substitution into Equation B.9 yields

$$\begin{aligned} \frac{\partial}{\partial t} \left(\frac{\partial}{\partial z} [\hat{\mathbf{b}} \times \mathbf{E}_\perp] \right) &= \frac{\partial}{\partial t} \left(\frac{\partial}{\partial z} [\hat{\mathbf{b}} \times (-\mathbf{v}_\perp \times \mathbf{B}_0)] \right) \\ &= \frac{\partial}{\partial t} \left(\frac{\partial}{\partial z} [-(\hat{\mathbf{b}} \cdot \mathbf{B}_0)\mathbf{v}_\perp + (\hat{\mathbf{b}} \cdot \mathbf{v}_\perp)\mathbf{B}_0] \right) \\ &= \frac{\partial}{\partial z} \left[-\frac{\partial}{\partial t} (B_0 \mathbf{v}_\perp) \right] \end{aligned} \quad (\text{B.11})$$

as $\hat{\mathbf{b}} \cdot \mathbf{v}_\perp = 0$. The equation of motion (Equation 2.30) states that

$$\rho \frac{\partial \mathbf{v}}{\partial t} = \mathbf{j} \times \mathbf{B}_0 = \frac{\mathbf{B}_0 \cdot \nabla \mathbf{b}}{\mu_0} \quad (\text{B.12})$$

so we may write

$$\frac{\partial}{\partial t} \left(\frac{\partial}{\partial z} [\hat{\mathbf{b}} \times \mathbf{E}_\perp] \right) = -\frac{\partial}{\partial z} \left(\frac{B_0^2 \hat{\mathbf{b}} \cdot \nabla \mathbf{b}}{\mu_0 \rho} \right). \quad (\text{B.13})$$

Finally, we note that $\hat{\mathbf{b}} \cdot \nabla \mathbf{b} = \frac{\partial \mathbf{b}}{\partial z}$, which leaves us with

$$\begin{aligned}
\frac{\partial}{\partial t} \left(\frac{\partial}{\partial z} [\hat{\mathbf{b}} \times \mathbf{E}_\perp] \right) &= -\frac{\partial}{\partial z} \left(\frac{B_0^2}{\mu_0 \rho} \frac{\partial \mathbf{b}}{\partial z} \right) \\
&= -v_A^2 \frac{\partial^2 \mathbf{b}}{\partial z^2},
\end{aligned} \tag{B.14}$$

as the Alfvén speed remains constant with z . We now consider the second term on the right hand side of Equation B.9 by equating it to the curl of Equation B.8:

$$\begin{aligned}
\frac{\partial}{\partial t} (\nabla_\perp \times \mathbf{E}_\parallel) &= \nabla_\perp \times \frac{\partial E_z}{\partial t} \\
&= \nabla_\perp \times \left(\frac{m_e}{ne^2} \frac{\partial^2 j_z}{\partial t^2} - \frac{T_e}{ne^2} \frac{\partial^2 j_z}{\partial z^2} \right).
\end{aligned} \tag{B.15}$$

If we consider Ampère's law in the z direction, we may write $j_z = (\nabla \times \mathbf{b})_\parallel / \mu_0$, so that

$$\begin{aligned}
\frac{\partial}{\partial t} (\nabla_\perp \times \mathbf{E}_\parallel) &= \nabla_\perp \times \left(\frac{m_e}{ne^2} \frac{\partial^2}{\partial t^2} \left[\frac{(\nabla \times \mathbf{b})_\parallel}{\mu_0} \right] - \frac{T_e}{ne^2} \frac{\partial^2}{\partial z^2} \left[\frac{(\nabla \times \mathbf{b})_\parallel}{\mu_0} \right] \right) \\
&= \frac{m_e}{ne^2 \mu_0} \frac{\partial^2}{\partial t^2} (\nabla_\perp \times [\nabla \times \mathbf{b}]_\parallel) - \frac{T_e}{ne^2 \mu_0} \frac{\partial^2}{\partial z^2} (\nabla_\perp \times [\nabla \times \mathbf{b}]_\parallel)
\end{aligned} \tag{B.16}$$

assuming that n is uniform everywhere. Using the vector identity $\nabla \times (\nabla \times \mathbf{A}) = \nabla(\nabla \cdot \mathbf{A}) - \nabla^2 \mathbf{A}$ and noting that $\nabla \cdot \mathbf{b}$ must be zero everywhere, we obtain

$$\frac{\partial}{\partial t} (\nabla_\perp \times \mathbf{E}_\parallel) = \frac{T_e}{ne^2 \mu_0} \frac{\partial^2}{\partial z^2} (\nabla_\perp^2 \mathbf{b}) - \frac{m_e}{ne^2 \mu_0} \frac{\partial^2}{\partial t^2} (\nabla_\perp^2 \mathbf{b}). \tag{B.17}$$

We may now substitute Equations B.14 and B.17 into Equation B.9 to produce the two fluid Alfvén wave equation in the kinetic limit:

$$\begin{aligned}
\frac{\partial^2 \mathbf{b}}{\partial t^2} &= - \left(-v_A^2 \frac{\partial^2 \mathbf{b}}{\partial z^2} + \frac{T_e}{ne^2 \mu_0} \frac{\partial^2}{\partial z^2} (\nabla_\perp^2 \mathbf{b}) - \frac{m_e}{ne^2 \mu_0} \frac{\partial^2}{\partial t^2} (\nabla_\perp^2 \mathbf{b}) \right) \\
&= v_A^2 \frac{\partial^2 \mathbf{b}}{\partial z^2} + \frac{c^2}{\omega_{pe}^2} \frac{\partial^2}{\partial t^2} (\nabla_\perp^2 \mathbf{b}) - c^2 \lambda_D^2 \frac{\partial^2}{\partial z^2} (\nabla_\perp^2 \mathbf{b})
\end{aligned} \tag{B.18}$$

where we have introduced the electron plasma frequency, ω_{pe} , and the electron Debye length, λ_D . Equation B.18 is clearly reminiscent of the Alfvén wave equation in the MHD limit (given by $\frac{\partial^2 \mathbf{b}}{\partial t^2} = v_A^2 \frac{\partial^2 \mathbf{b}}{\partial z^2}$). The two additional terms on the right hand side of Equation B.18 can be neglected when the scale size of the Alfvén wave is large compared to the ion acoustic gyroradius, ρ_s (given by $\rho_s = c\lambda_D/v_A$), and the electron inertial length, λ_e (given by $\lambda_e = c/\omega_{pe}$). So for large scale size Alfvén waves the wave equation derived in the kinetic limit reverts back to the simple MHD wave equation.

We now examine the form of the dispersion relation in the kinetic limit. If we assume that the wave variations are of the form $\exp\{i(k_\perp x + k_\parallel z - \omega t)\}$, then we may Fourier analyze by substituting

$$\begin{aligned}\frac{\partial^2}{\partial t^2} &\rightarrow -\omega^2 \\ \frac{\partial^2}{\partial z^2} &\rightarrow -k_\parallel^2 \\ \nabla_\perp^2 &\rightarrow -k_\perp^2\end{aligned}$$

into the wave equation. We therefore obtain

$$-\omega^2 = -v_A^2 k_\parallel^2 + \frac{c^2}{\omega_{pe}^2} \omega^2 k_\perp^2 - c^2 \lambda_D^2 k_\parallel^2 k_\perp^2 \quad (\text{B.19})$$

$$\Rightarrow \omega^2 \left(1 + \frac{c^2}{\omega_{pe}^2} \omega^2 k_\perp^2\right) = v_A^2 k_\parallel^2 \left(1 + \frac{c^2 \lambda_D^2}{v_A^2} k_\perp^2\right) \quad (\text{B.20})$$

$$\Rightarrow \omega^2 = v_A^2 k_\parallel^2 \left(\frac{1 + \frac{c^2 \lambda_D^2}{v_A^2} k_\perp^2}{1 + \frac{c^2}{\omega_{pe}^2} k_\perp^2}\right) \quad (\text{B.21})$$

The dispersion relation is similar to the MHD wave dispersion relation, in that if we assume that the ion acoustic gyroradius and the electron inertial length are small compared to the wave scale size we revert back to the MHD limit. It is now possible to investigate the form of the perpendicular and parallel electric fields associated with the kinetic Alfvén wave, and we begin by considering the equation of motion

$$\begin{aligned}\rho \frac{\partial \mathbf{v}}{\partial t} &= \mathbf{j} \times \mathbf{B}_0 \\ &= \frac{\mathbf{B}_0 \cdot \nabla \mathbf{b}}{\mu_0}\end{aligned}\tag{B.22}$$

$$\begin{aligned}\Rightarrow \frac{\partial \mathbf{v}}{\partial t} &= \frac{\mathbf{B}_0 \cdot \nabla \mathbf{b}}{\mu_0 \rho} \\ &= \frac{B_0}{\mu_0 \rho} \hat{\mathbf{b}} \cdot \nabla \mathbf{b}\end{aligned}\tag{B.23}$$

If we now limit ourselves to the z direction and Fourier analyze as before, we obtain

$$\begin{aligned}-i\omega \mathbf{v} &= \frac{B_0}{\mu_0 \rho} \nabla_{\parallel} \mathbf{b} \\ &= \frac{B_0}{\mu_0 \rho} i k_{\parallel} \mathbf{b}\end{aligned}\tag{B.24}$$

so that

$$\begin{aligned}\mathbf{v} &= -\frac{B_0 k_{\parallel}}{\mu_0 \rho \omega} \mathbf{b} \\ &= -\frac{v_A k_{\parallel}}{\omega} \frac{1}{\sqrt{\mu_0 \rho}} \mathbf{b}.\end{aligned}\tag{B.25}$$

If we substitute in for $v_A k_{\parallel}/\omega$ from the dispersion relation (Equation B.21) we obtain

$$\mathbf{v} = \mp \sqrt{\frac{1 + k_{\perp}^2 \lambda_e^2}{1 + k_{\perp}^2 \rho_s^2}} \frac{1}{\sqrt{\mu_0 \rho}} \mathbf{b}\tag{B.26}$$

Finally, we note that $\mathbf{E}_{\perp} = -\mathbf{v} \times \mathbf{B}_0$ to obtain

$$\begin{aligned}\mathbf{E}_{\perp} &= \pm \frac{B_0}{\sqrt{\mu_0 \rho}} \sqrt{\frac{1 + k_{\perp}^2 \lambda_e^2}{1 + k_{\perp}^2 \rho_s^2}} \mathbf{b} \times \hat{\mathbf{b}} \\ &= \pm v_A \sqrt{\frac{1 + k_{\perp}^2 \lambda_e^2}{1 + k_{\perp}^2 \rho_s^2}} \mathbf{b} \times \hat{\mathbf{b}}\end{aligned}\tag{B.27}$$

We have now expressed the perpendicular magnetic field of the kinetic Alfvén wave in terms of the magnetic perturbation, \mathbf{b} . The top sign in Equation B.27 corresponds to waves propagating parallel to the background magnetic field, and the bottom sign corresponds to anti-parallel propagation. The two opposite signs exist due to the fact that the dispersion relation contains a term in k_{\parallel}^2 , so that the directionality of the vector \mathbf{k}_{\parallel} needs to be reconstructed via the positive and negative square roots in Equation B.26. We can now use Equations B.8 and B.21 along with Amperè's law to express the parallel electric field of the kinetic Alfvén wave in terms of its perpendicular electric field. Amperè's law states

$$\nabla \times \mathbf{b} = \mu_0 \mathbf{j} \quad (\text{B.28})$$

so that

$$j_z = \frac{(\nabla \times \mathbf{b})_z}{\mu_0}. \quad (\text{B.29})$$

In order to find an expression for E_{\parallel} we need to rearrange Equation B.27 so that we can substitute the wave magnetic field, \mathbf{b} , into Equation B.29. Equation B.27 states

$$\begin{aligned} \mathbf{E}_{\perp} &= \pm \frac{B_0}{\sqrt{\mu_0 \rho}} \sqrt{\frac{1 + k_{\perp}^2 \lambda_e^2}{1 + k_{\perp}^2 \rho_s^2}} \mathbf{b} \times \hat{\mathbf{b}} \\ \Rightarrow \mathbf{b} &= \pm \frac{\mathbf{E}_{\perp} \times \hat{\mathbf{b}}}{v_A \sqrt{K}} \end{aligned} \quad (\text{B.30})$$

where we have substituted $\sqrt{\frac{1 + k_{\perp}^2 \lambda_e^2}{1 + k_{\perp}^2 \rho_s^2}} = K$. Therefore

$$\begin{aligned} j_z &= \pm \frac{[\nabla \times (\mathbf{E}_{\perp} \times \hat{\mathbf{b}})]_z}{\mu_0 v_A \sqrt{K}} \\ &= \pm \frac{[\mathbf{E}_{\perp} (\nabla \cdot \hat{\mathbf{b}}) - \hat{\mathbf{b}} (\nabla \cdot \mathbf{E}_{\perp}) + (\hat{\mathbf{b}} \cdot \nabla) \mathbf{E}_{\perp} - (\mathbf{E}_{\perp} \cdot \nabla) \hat{\mathbf{b}}]_z}{\mu_0 v_A \sqrt{K}} \end{aligned} \quad (\text{B.31})$$

The only non-zero term in the numerator on the right hand side of Equation B.31 is $-\hat{\mathbf{b}} (\nabla \cdot \mathbf{E}_{\perp})$, so we may write

$$\begin{aligned}
j_z &= \mp \frac{[\hat{\mathbf{b}}(\nabla \cdot \mathbf{E}_\perp)]_z}{\mu_0 v_A \sqrt{K}} \\
&= \mp \frac{\nabla_\perp \cdot \mathbf{E}_\perp}{\mu_0 v_A \sqrt{K}}.
\end{aligned} \tag{B.32}$$

We now Fourier analyze Equation B.8 as before to yield

$$\begin{aligned}
\frac{\partial E_z}{\partial t} &= \frac{m_e}{ne^2} \frac{\partial^2 j_z}{\partial t^2} - \frac{T_e}{ne^2} \frac{\partial^2 j_z}{\partial z^2} \\
\Rightarrow i\omega E_z &= \frac{T_e}{ne^2} k_\parallel^2 j_z - \frac{m_e}{ne^2} \omega^2 j_z \\
\Rightarrow E_z &= \left(\frac{T_e}{ne^2} \frac{k_\parallel}{\omega} - \frac{m_e}{ne^2} \frac{\omega}{k_\parallel} \right) \frac{k_\parallel}{i} j_z
\end{aligned} \tag{B.33}$$

Using Equation B.32 to eliminate j_z , and substituting $k_\parallel/i = -ik_\parallel = -\partial/\partial z$ gives

$$E_z = \left(\frac{T_e}{\mu_0 ne^2} \frac{k_\parallel}{\omega v_A} \sqrt{K} - \frac{m_e}{\mu_0 ne^2} \frac{\omega}{k_\parallel v_A} \sqrt{K} \right) \left(-\frac{\partial}{\partial z} \right) (\mp \nabla_\perp \cdot \mathbf{E}_\perp) \tag{B.34}$$

We note that $\sqrt{K} = \omega/k_\parallel v_A$ from the dispersion relation, so that

$$E_z = \pm \left(\frac{T_e}{\mu_0 ne^2} - \frac{m_e}{\mu_0 ne^2} \frac{\omega^2}{k_\parallel^2 v_A^2} \right) \frac{\partial}{\partial z} (\nabla_\perp \cdot \mathbf{E}_\perp). \tag{B.35}$$

Finally we use the dispersion relation (Equation B.21) to substitute in for $\omega^2/k_\parallel^2 v_A^2$, and re-introduce the ion acoustic gyroradius, ρ_s , and the electron inertial length, λ_e to yield

$$E_z = \pm \left(\rho_s^2 - \lambda_e^2 \frac{1 + k_\perp^2 \lambda_e^2}{1 + k_\perp^2 \rho_s^2} \right) \frac{\partial}{\partial z} (\nabla_\perp \cdot \mathbf{E}_\perp). \tag{B.36}$$